Kinematic Study of the Evolution and Properties of Flame Surfaces in Turbulent Nonpremixed Combustion with Local Extinction and Reignition

Weirong Wang

A dissertation
submitted in partial fulfillment of the
requirements for the degree of

Doctor of Philosophy

University of Washington

2013

Reading Committee:

James J. Riley, Chair

John C. Kramlich, Chair

Ann M. Mescher

Program Authorized to Offer Degree:
Mechanical Engineering

University of Washington

Abstract

Kinematic Study of
the Evolution and Properties of Flame Surfaces in
Turbulent Nonpremixed Combustion with
Local Extinction and Reignition

Weirong Wang

Co-Chairs of the Supervisory Committee:
Professor James J. Riley
Mechanical Engineering

Professor John C. Kramlich
Mechanical Engineering

Turbulent nonpremixed combustion with local extinction and reignition is an important fundamental phenomenon that has many practical implications. The objective of the research reported in this thesis is to identify and understand the mechanisms that govern extinction and reignition by studying the kinematics of the stoichiometric mixture fraction isosurface (i.e., the flame surface). The configuration, area and the behavior of the flame surface can quantitatively describe the interaction of the flame with turbulent flow and thus the flame surface kinematics has a strong influence on the properties of the reactive scalars. One particular property of importance is the mean flame surface density Σ. This study contributes to the determination of Σ by proposing three approaches for its measurement through the use of direct numerical simulations (DNS) data for the case of incompressible and isotropic turbulence. These direct and indirect approaches proposed for the computation and modeling of the time evolution of Σ are 1) direct numerical measurement, 2) theoretical prediction from the concept of level crossings with the application of Rice's theorem[62], which leads to 3) two separate modeling approaches using statistical definitions and by balance equation of isoscalar surface area density. These approaches allow us to follow the growth of the surface due to local surface stretching by turbulence and its ultimate decrease due to

molecular destruction. The statistical model fairly accurately predicts the evolution of Σ. We are also able to determine values of the principal terms in the evolution equation for Σ, including the surface stretching term and the molecular destruction term. We find that the stretching and destruction term are approximately statistically independent of the isoscalar value of the surface. The difficulties in modeling of local flame extinction and reignition are demonstrated by evaluating the application of the steady-state flamelet (SFL) model. The transient effects (i.e., the lag of flame quenching behind fluctuations in the stoichiometric scalar dissipation rate χ_{st}) and the time lag of reignition relative to the relaxation of χ_{st} are not considered by the SFL model. These are demonstrated by showing the mixing and reactive quantities along the stoichiometric mixture fraction contour lines. With the knowledge of the flame surface evolution and its properties, the mechanisms of local extinction and reignition can be directly investigated by the dynamics of flame hole (i.e., an extinguished flame surface) expansion and collapse. The flame surface is first resolved as a mesh of triangular surfaces within the three-dimensional DNS volume that represents the stoichiometric surface. A criterion is developed on this flame surface mesh to identify instantaneously local quenched regions and distinguish these from burning surface regions. Next, a new methodology is developed to numerically identify contiguous extinguished stoichiometric surface elements such that the size of a single flame hole can be identified. The new methodology is tested and found to be accurate. This numerical algorithm can provide rich geometric information on local flame hole structure and along with knowledge of the local reacting properties for each individual flame hole. The statistics of the geometric properties of the flame holes are then obtained. During the reignition process, the area size distribution of flame holes was found to be roughly invariant with time which results in an approximate time invariant average hole area. This appears to be due to the loss of small flame holes with time while larger holes become smaller. To first order, this process appears to approximate a self-preserving size distribution.

TABLE OF CONTENTS

LIST OF FIGURES

LIST OF TABLES

ACKNOWLEDGMENTS

I want to express my sincere appreciation to Professor James Riley and Professor John Kramlich for their invaluable guidance, consistent support, patience, and general kindness that I have received over the course of my dissertation. I also like to sincerely thank Professor Ann Mescher for her numerous discussions, suggestions and enthusiasm on the subject. I would like to thank Professor Robert Breidenthal for his inspiring suggestions. And I also would like to thank Professor Dana Dabiri who was willing to participate in my committee in a short notice. I also want to thank my colleagues for sharing their comments on my work. Most of all I want to thank my parents and my husband for their supports and encouragements. There is one person I always feel thankful from deep inside. It was Professor George Kosály who accepted me into the PhD program. He was very supportive even when he was very sick. He will be always in my memory.

DEDICATION

to my father, mother and husband

Chapter 1

INTRODUCTION

1.1 Background

The problem of turbulent reacting flows has attracted considerable research interest over a long span of time. One important motivation comes from the broad range of applications in which turbulent reacting flows play a part, including the transport and reaction of pollutants in the air, and to turbulent combustion in industrial applications such as furnaces, boilers, gas turbines, Diesel engines etc.

Most studies initially set the approach to the problem depending on whether the fuel and oxidizer are initially premixed, nonpremixed or partially premixed before the start of the combustion process. A premixed flame is indicated if the fuel and oxidizer are completely mixed to the molecular level before combustion occurs. The premixed flame front propagates from hot burnt products into cold unburnt premixed reactants via diffusion of energy and free radicals. Common premixed combustion systems include the Bunsen burner, lean premixed gas turbines and spark-ignition engines. In nonpremixed combustion the fuel and oxidizer are initially in separate streams before they enter the reaction chamber. In nonpremixed combustion, a diffusion flame forms at the interface between the fuel and oxidizer. Consequently, the fuel and oxidizer react as they mix, and thus the reaction process is significantly affected by both molecular diffusion and turbulent mixing in the neighborhood of the reaction zone. Examples of this combustion mode can be found in Diesel engines, candles and pool fires. Partially premixed combustion is a combination of premixed and nonpremixed combustion. Among these three combustion modes, nonpremixed combustion is the most common in industrial systems due to its inherent safety (i.e., no flash back), and the self-regulating nature of the flames. This is the subject of the present research.

The primary challenge in understanding and modeling turbulent combustion is mastering the two-way coupling between the turbulence and chemical reaction. The turbulent

flow in itself is already a complicated physical phenomenon that is not yet a fully understood problem. When turbulence is coupled with combustion, the flow field is influenced through changes in properties such as density and viscosity as the gases burn and heat. An illustration of the density effect is the flow acceleration through the flame front that takes place in turbulent premixed combustion. The combustion itself is a complex process which is represented by a large number of elementary chemical reactions involving many species. The rate at which many of these reactions proceed is a highly non-linear function of temperature, often leading to narrow reaction zones and stiff numerical problems. For example, when a flame is stretched by a turbulent flow, the flame thickness decreases. The consequence of this stretching is to steepen the concentration gradients at the mixing layer, and thus increase the mixing. But carried further, this stretching will eventually cause chemical extinction by heat loss [67].

Flamelet extinction and subsequent reignition are phenomena which can often be observed in practical nonpremixed combustion processes, such as flame lift-off in high Reynolds number jet flames. The extinction and reignition have effects on the efficiency and stability of the combustion process. A quantitative understanding of this behavior is critical in developing qualitative combustion models for use in improving combustor efficiency and designing for reduced pollutant emissions. The physical mechanism governing this phenomena is the intensive interaction between the turbulence and the chemical reactions mentioned above. This phenomena can be characterized in terms of the strain rate at the flame surface, which is equivalent to the scalar dissipation rate of the mixture fraction, $\chi = 2D|\nabla Z|^2$. The mixture fraction, Z, being as a normalized value between 1 (in fuel stream) and 0 (in oxidizer stream), represents the level of mixing by a fuel-to-oxidizer ratio (the definition of Z is given in Chapter 3). Due to the definition of mixture fraction, the stoichiometric mixture fraction, denoted by Z_{st}, is considered as a tracer to locate the flame surface which is tracked through the isosurface of Z_{st}. These parameters, discussed later, represent the rate at which fuel and oxidizer are mixed. A high scalar dissipation value indicates that fuel and oxidizer must mix and react in a limited time. Very high scalar dissipation rates lead to the extinction of the flame sheet. Once extinguished, the flame can only be reignited by exposure to another flame. This is termed reignition. This extinction and reignition

behavior was studied in experiments performed by Barlow and Frank[54], who examined piloted methane/air jet diffusion flames at high strain rates. The experiment was designed to exhibit various extents of local extinction by changing the Reynolds number through a series of different jet velocities. The strain induces local extinction at locations close to the nozzle, but reignition occurs as the strain relaxes further downstream. Mastorakos et al.[13] performed experiments on nonpremixed and partially premixed turbulent counterflow flames. They estimated the critical strain rate needed to achieve extinction. In the current research, the extinction and reignition behavior is investigated in the context of initially nonpremixed reactants whose mixing evolves in a turbulent flow field.

Three-dimensional direct numerical simulation (DNS) as a research tool can provide insight into the problem of turbulent combustion with extinction and reignition. It uses a fine grid to resolve the full range of length and time scales contained in turbulent reacting flows. With the continued development of computer technology, high-performance computing has become capable of simulating flows with high levels of turbulence intensity (large Reynolds number). DNS plays an important role as a generator of benchmark data for studying the fundamental physics of the coupling between turbulence and chemistry, validating the models, and thus developing the predictive capabilities of models. In the current research, the DNS is used to study the evolution of an initially nonpremixed fuel and oxidizer field. The properties of the problem are selected so that the diffusion flame experiences extinction and reignition processes.

Diffusion flames concentrate at the interface where fuel and oxidizer are delivered in stoichiometric proportions. Hence, the flame surface is naturally considered to be formed at the interface where fuel and oxidizer are mixed in stoichiometric ratio. The fundamental understanding of the interactions between the flame surface and turbulence is important. The configuration, area and the behavior of the flame surface have a strong influence on the properties of the reactive scalars. For example, the effect of flame curvature on diffusion flames has been studied theoretically and experimentally. In the numerical study of H_2/Air diffusion flame performed by Lee[31], the flame-vortex interaction produces flame curvature. The curvature orientation towards the fuel stream or the air stream determines whether the flame becomes more intense or is weakened. In extreme cases, the flame can be-

come extinguished. In this regard, the geometrical and quantitative properties of the flame surface, such as the flame surface area, curvature, wrinkling, and orientation, are needed for a quantitatively description of flame behavior. One particular property of importance is the mean flame surface density (i.e., the flame surface area per unit volume). It has been proposed that the properties of chemical reaction depend on the local stretching of flame surface[43]. Reaction rate models based on mean flame surface density are among the most important models in nonpremixed turbulent combustion. These models are often cast in a laminar flamelet framework. The mean reaction rate is quantified as the product of the local reaction rate per unit flame surface, which depends on the local flamelet properties, times the mean flame surface density [67][17][20][5]. The turbulent flow field in turn also has important effects on the flame surface. The flame surface area is increased due to the flame wrinkling and folding by turbulence, and is decreased by molecular diffusion. The evolution of flame surface has been modeled by flame surface evolution equations. These equations include terms for production, destruction, and transport of flame surface. The development of these equations involve the use of a variety of ad hoc assumptions regarding the construction of the individual terms. Experimental measurements to test the fidelity of these assumptions are extremely challenging, and a such are not generally available. A portion of the work reported here is addressed at identifying values for these terms for the first time from DNS experiments. The study of the flame surface and its application have been of great interest to researchers. Thus, Chapter 4 develops a numerical, analytical and modeling tool to quantitatively analyze the evolution of flame surface area and the values of the terms that form the surface area evolution equation.

The main challenge of modeling turbulent diffusion flames lies in the nonlinear turbulence-chemistry interaction. The primary models at present include the flamelet model (Peters[42][49]), the conditional moment closure (CMC) (Klimenko and Bilger[7]), PDF methods (Pope[58]), and the linear eddy model (LEM) (Kerstein[4]). Among them, the flamelet model and CMC are often referred to as mixture fraction based models in which the conserved scalar, the mixture fraction, is used as independent variable. These modeling approaches are comprehensively reviewed by Peters[49] and Poinsot and Veynante[67].

As described above, the fluctuations of the scalar dissipation rate have significant effect

on local extinction and reignition. When the scalar dissipation rate fluctuates much higher above a critical value χ_q, local extinction occurs. This local extinction leads to the formation of flame holes (i.e., quenched holes) on the flame surface, within which the unburned reactants are mix by diffusion without reaction. As the turbulent strain rates decreases below the critical value, the quenched regions may be reignited by the surrounding hot flame elements. The reignition takes place through several different scenarios: (1) independent flamelet scenario (IFL); (2) edge flame propagation along the flame surface (EDGE); (3) engulfment scenario by hot neighboring gas (ENGULF)[64].

Flamelet models are generally acknowledged adequately handle flames where the scalar dissipation rate is below the quenching value, i.e., the continuous combustion regime. This situation is relatively easy to model since the flame behavior depends only on the local scalar dissipation rate and the local mixture fraction. The chemistry is calculated as a quasi-steady process against a slowly evolving turbulent flow field. Extinction can also be handled by the flamelet models via the assumption that the flame shifts to an extinguished mode if the scalar dissipation rate exceeds the critical value. This would be treated as an instantaneous process. In reality, both the extinction and reignition processes are inherently time unsteady, and thus they depend on the local history rather than just on the current conditions. This is made their modeling much more difficult. There have been a number of approaches proposed to close the reignition problem in particular. One of the goals of the present research is to provide data on the dynamics of reignition that can be used to propose and test high-fidelity models of reignition.

In our current DNS the scalar dissipation rate initially increases above the critical value due to the turbulent stretching, and this leads to the onset of local flame extinction. Later reignition occurs with the subsequent decrease in strain rate. Extinction represents a deviation from the burning states of the steady flamelet model, and reignition represents a gradual return to it [64]. In Chapter 5, the laminar steady flamelet model is applied to the diffusion flame with extinction and reignition, and evaluated with the DNS results. The comparison with the corresponding simulated data illustrates that the laminar steady flamelet model is capable of capturing the continuous burning and extinction, but not the reignition. The numerical technique for the quantitative description of the geometric properties of the flame

holes is developed and presented in that chapter.

1.2 Research Objectives

1.2.1 DNS for Extinction and Reignition

Direct numerical simulations (DNS) of turbulent diffusion flames are carried out by solving the governing equations for flow and scalar fields to provide insight into the fundamental process of turbulence-reaction interaction and to assist in the investigation of the mechanism of extinction and reignition. In the reacting flow simulations, the chemistry is represented by a single-step, irreversible, Arrhenius reaction. The DNS is specifically designed to exhibit extinction and reignition behavior. The physical problem and corresponding DNS are introduced in Chapter 3.

1.2.2 Measurement of Flame Surface Area: Numerical, Theoretical and Modeling Approaches; Evaluation of Governing Equation

In nonpremixed combustion, the flame surface forms at the stoichiometric interface between fuel and oxidizer. In other words, the flame surface in nonpremixed reacting flows can be approximated by an isolevel surface corresponding to the constant value of the passive scalar at stoichiometry, i.e., stoichiometric mixture fraction $Z = Z_{st}$. In nonpremixed combustion, for the purpose of both physical understanding and modeling, the turbulent mixing and the chemical reaction can be investigated to advantage in terms of the time evolution of the flame surface area.

Some studies have been devoted to the definition and measurement of a material surface area, and various approaches have been proposed from different perspectives.

In 1955, the area of a homogeneous random surface was measured by Corrsin's suggestion of the number of surface crossings[60]. A general definition of the mean surface density $\bar{\Sigma}$ (i.e., mean flame surface area per unit volume) was proposed by Pope, which is based on the fact that the one-point Eulerian probabilistic descriptor of a surface is the surface density function[57]. The definition is given as

$$\bar{\Sigma} = |\nabla Z|\delta(\bar{Z} - Z_{st}) = P(Z = Z_{st})\ \langle |\nabla Z||Z = Z_{st}\rangle, \tag{1.1}$$

where $\bar{()}$ and δ denote ensemble averaging and the Dirac function, respectively. $\langle|\nabla Z||Z = Z_{st}\rangle$ is the conditional average of $|\nabla Z|$ on $Z = Z_{st}$ and $P(Z = Z_{st})$ is the probability that the mixture fraction Z is at stoichiometric value[33]. Then, an exact balance equation for surface density was derived, and the statistics of the turbulence field in the unknown terms were modeled. Subsequently, the balance equation can be solved by a Monte Carlo method[57].

The algebraic expression definition of the flame surface density in nonpremixed combustion was determined from an algebraic expression as in Bray-Moss-Libby (BML) model for turbulent premixed combustion[34]. The algebraic expression in the BML model for premixed combustion was easily extended to nonpremixed combustion by introducing an indicator function in the form of Heaviside function. This extension was firstly presented by Kalmthout and Veynante[33]. In this algebraic expression, the Heaviside function needs to be determined by solving a balance equation of indicator function, and the flame wrinkling length scale needs to be modeled by considering the curvature effects and local strain rate on the flame surface.

In an alternative way, the mean surface density can be obtained by solving a balance equation. The balance equation was first derived from phenomenological consideration for nonpremixed turbulent combustion. It was proposed by Marble and Broadwell[20] and described in a coherent flame model. In the mixing region between two separate streams, the mean reaction rate is approximated as the product of the local reaction rate per unit flame surface, which associates with the local strained laminar flamelet embedded on the flame surface, times the mean flame surface density. The flame surface density based model can decouple the chemical reaction from the turbulence field.

Two alternatives exact, but unclosed, balance equations for the mean surface density was first developed by Kalmthout and Veynante[14][33]. The balance equation was derived from the definition of the mean surface density given in Eq.(1.1) and the governing equation of mixture fraction Z. The analysis of the terms intervening in the balance equation is performed in the context of a simulation of a homogeneous and isotropic two dimensional turbulent flow which is continuously injected at the mean convection velocity into a spatially developing, constant velocity, two dimensional mixing layer, where the reactive mixing layer

is the interface between a cold fuel flow and a hot oxidizer flow. Then, a closure for the balance equation was proposed and validated by using the direct numerical simulations.

In summary, a general definition was developed to approximate the mean surface to volume ratio of a material surface in a turbulent flow, but requires adjustments to be specifically applied to a nonpremixed turbulent reacting flow. The area of the flame front in premixed combustion can be predicted, and the definition can be extended to nonpremixed combustion but requires further models. In an alternative way, the surface area density can be obtained by solving the balance equation in which the terms needs further models.

The objective of current research is to contribute to the measurement of flame surface area by systematically proposing three different approaches, which include direct and indirect methods to accurately measure the flame surface area, with the use of data from direct numerical simulations of a three dimensional nonpremixed turbulent reacting flow. The flow field is described as an incompressible, homogeneous and isotropic turbulence. The reactive field is characterized by a single step Arrhenius type reaction rate. The four approaches are proposed as follows.

(1) Direct numerical measurement: The flame surface is generated by rendering an isosurface using DNS volumetric mixture fraction data Z at a specified isovalue Z_{st} using a marching cube triangulation algorithm. Accordingly, the area of the flame surface can be numerically calculated by using the geometric information yielded from the isosurface triangulation.

(2) Theoretical prediction: A theoretical formulation is developed from the concept of level crossings with the application of Rice's theorem. This theoretical formula leads to the following two different modeling approaches. The flame surface area predicted by the theoretical formula is assessed by comparing against the direct numerical results.

(3) Modeling approach using statistical definitions: The terms appearing in this theoretical formulation are modeled individually with the use of statistical definitions by assuming a homogeneous isotropic turbulent field which is the subject of current study. The flame surface area predicted by the model is assessed by comparing against the numerical results.

(4) Modeling approach by balance equation of isoscalar surface area density: The balance equation for the mean flame surface area density is derived based on the theoretical formulation of flame surface area in conjunction with invoking the governing equation of mixture

fraction. And then it is simplified for a homogeneous turbulent field. The balance equation provides an indirect way to calculate the time evolution of the flame surface area. The flame surface is described as a non-conserved property. Thus, the corresponding governing equation contains terms describing sources and sinks of flame surface. The terms in the governing equation for flame surface area are evaluated and analyzed via a *priori* testing using the numerical results. These are presented in Chapter 4.

The measurement study of the evolution of the flame surface area assists in understanding the topology of flame surface and plays a key role as the basis for investigating the mechanism of local extinction and reignition occurring on the flame surface.

1.2.3 Applicability of Steady Flamelet Model

The laminar steady flamelet model is compared with predictions from the DNS results by comparing the reaction rate predictions of two calculations on the stoichiometric mixture fraction isosurface. The steady laminar flamelet model can accurately predict the continuous burning state without extinction and reignition, and provides a valid criteria for defining extinction. The deviations between the model predictions and DNS demonstrates that the flamelet model fails to predict the reignition regime since it cannot take into account the interactions between the cold quenched regions (i.e., flame holes) and the local hot ignition sources, such as an edge flame with an intense reaction rate. Along the contour lines of stoichiometric mixture faction, the quantities for reactive scalars predicted by the flamelet model are displayed together with the ones obtained from DNS. The comparisons show the appearance of flame holes and the onset of edge flames surrounding the holes that are characterized by intense reaction rates. These results are presented in Chapter 5.

1.2.4 Quantitative Description of the Geometric Properties of Flame Holes

The flame holes are formed on the flame surface resulting from local quenching when the local scalar dissipation rate fluctuates beyond the critical value. These quenched regions are separated from the burning regions by edge flames that surround the holes. The mechanisms of the local extinction and reignition, especially the reignition scenario via edge flame

propagation, in diffusion flames can be easily described and investigated to advantage in terms of the topological configuration and properties of the flame holes.

The significance of the flame hole study in understanding the mechanism of diffusion flames is pointed out by Williams[17].

Buckmaster theoretically investigated the edge flame by using a one dimensional model. The simplified model approximates the governing equation for the dynamics of edge flame, in which the heat loss is modeled by algebraic functions[26]. In the studies of diffusion flame holes by Nayagam, Balasubramaniam and Ronney[70], they extended Buckmaster's model of one dimensional straight edge flame to account for the effects of flame curvature in a highly turbulent diffusion flame. The study selected a curved edge flame (interacting with vortices) surrounding an axisymmetric flame hole for investigation. The results showed the dependence of flame hole expansion or collapse on the initial radius and the relative value of Damköhler number compared to the value of steady edge flame. To be specific, the flame holes without a heat sink are not stable for any Damköhler number since 1) at small Damköhler number, the flame holes expand if the initial radius is large, but collapse if it is small, 2) at large Damköhler number, the flame holes collapse for any radius. The flame hole can be stable only when it is anchored by a heat sink for sufficiently large Damköhler number. Buckmaster and Jackson[29] numerically investigated the effects of curvature on edge flames and the time evolution of the flame hole expanding and collapse in a diffusion flame by solving two dimensional governing equations. The results showed that the edge flame propagation speed (i.e., speed of hole collapse) could be positive, negative or zero depending on the Damköhler number (referring to the S-curve response to different Damköhler numbers (Fig.(2.1))) and the instantaneous hole radius.

In the study of the collapse dynamics of a diffusion flame hole in a counterflow, Pantano and Pullin[46] showed that the final stage of the flame hole collapse has a self-similar structure and is controlled by the balance between the time rate of change of temperature and diffusion. And, due to the curvature term in the diffusion term of the governing equation, the rate of collapse in axisymmetric structure is larger than the one in planar structure, while these two structures are topologically identical. Furthermore, the dynamics of diffusion flame holes was investigated via a statistical approach by Pantano and Pullin[47].

In the approach, the edge flame propagation, which controls the dynamics of flame holes, was defined to be a function of the local Damköhler number. For small circular holes, the dynamics of marginal joint pdf of hole radius and scalar dissipation rate was investigated by modeling the fluctuations of scalar dissipation rate and the flow normal to the edge as stochastic processes. The corresponding transport equation for this joint pdf was derived with an assumption of flat flame surface. The results showed that the hole grows fast for sufficiently large scalar dissipation rate and collapse when scalar dissipation rate is small. And, the time scale of relaxation is much larger than the one at which the hole expands. Kim and his colleagues numerically simulated the partial quenching structure in a turbulent diffusion flame by using the modified method of flame hole dynamics (FHD)[32]. The simplest model of FHD is flame hole random-walk mapping (FHRWM) first proposed by Hartley[22], which uniformly divides the flame surface (i.e isosurface of stoichiometric mixture fraction) into a grid system. Each grid is classified into four groups due to both of its and its neighboring cell's burning state. In the model FHRWM, the edge flames were defined to move forward or backward grid by grid. This method is modified by including the level-set method which was specifically aimed to considered the effect of slow edge flame response near the quenching scalar dissipation rate. An improvement that was being undertaken is the inclusion of nonplanar virtual flame surface into FHD as the instantaneous flame surface is neither flat nor stationary. If this improvement can be accomplished, more realistic partial quenching properties will be obtained.

The dynamics of flame hole reignition was experimentally studied in a turbulent jet flame by Steinberg and his colleagues[3]. The flame was imaged using planar laser induced fluorescence (PLIF) of OH combustion radical, and, simultaneously, the velocity field was experimentally measured using particle image velocimetry (PIV). The entire reigniton process was captured. The temporal history of flame hole reignition due to a combination of edge flame propagation along flame surface and turbulent transport of burning flame segments in the normal direction to flame surface was experimentally measured. The time history of the contribution of each reignition mechanism was also obtained. The results showed that the edge flame propagation scenario is responsible for over 90% of reignition. The measured speed of edge flame propagation matches with the speed of highly-preheated

premixed flames.

In summary, the studies of flame holes is of importance for understanding the mechanisms and properties of the local extinction and reignition. The kinematics of the edge flame propagation, as a scenario of reignition, depend on the scale of the flame hole. And, the study of the dynamics of flame holes provides a means of investigating the edge flame propagation. The dynamics of flame holes has been investigated by theoretical and numerical approaches, but was performed in two dimensional space and required further assumptions for simplification, such as assuming a flat flame surface. In some studies, the interaction between edge flame and flow field was considered in terms of a curved edge flame.

These results motivate us to find a direct way to study the dynamics of the flame holes, which inspires us to develop an accurate numerical methodology to form the topological structures of flame holes on the stoichiometric mixture fraction isosurface in a three dimensional turbulent nonpremixed combustion. With the use of direct numerical simulation (DNS) data, the topological information of the flame holes formed by this numerical algorithm enables 1) the numerical measurement of the time evolution of flame hole expanding and collapse which leads to the statistical description of the dynamics of flame holes (i.e., scaling distribution and behavior), and 2) the quantitative study of the distribution behavior of the mixing and reactive scalars within each individual flame hole.

In current research, the flame surface rendering technique and the availability of the flame surface geometric properties described in Chapter 4 enable the development of an accurate numerical algorithm to form the topological structure of flame holes on the flame surface in three dimensional turbulent diffusion flames with local extinction and reignition. Subsequently, the numerical measurement of flame hole geometry statistics (e.g., hole size distribution and evolution) can be carried out using DNS data. These quantitative descriptions of flame hole formation patterns provide a direct and exact way to investigate and understand the dynamics of hole growth or shrinkage, and the mechanisms by which the holes are reignited. The numerical algorithms and statistical results are presented in Chapter 5.

Chapter 2

REVIEW OF THE FUNDAMENTALS

2.1 Nonpremixed Turbulent Combustion

In nonpremixed combustion, the fuel and oxidant are initially in separate streams and the reaction occurs as they mix, in other words, the burning and the mixing can happen simultaneously. In many practical nonpremixed combustion systems, the chemical time scale is much shorter than the diffusion time scale. Consequently the process of nonpremixed combustion tends to be controlled by the rate of mixing by molecular diffusion which results in the associated flame being called diffusion flame.

2.2 Flamelet Model

In this section, we review the concept of laminar diffusion flamelet modeling for nonpremixed combustion originally proposed by Williams[16]. The underlying assumptions and applications of the flamelet models are presented.

2.2.1 The Proposed Flamelet Model

Combustion with chemistry that is fast relative to the mixing rate is often encountered in industrial applications. This is due in part to two reasons: (1) decreasing the mixing time to the order of the chemistry time involves use of a large hydrodynamic mixing power which is too expensive; (2) flames that are mixing controlled tend to be more stable, and are of predictable size and shape. The equilibrium chemistry approach that is valid in the limit of infinitely fast chemistry has been widely and successfully used in the modeling of nonpremixed flames. The equilibrium approach simplifies the problem in that the thermochemistry is reduced to one conserved scalar, the mixture fraction Z. It implies that all the instantaneous variables such as the concentration of the major species, temperature and density can be uniquely predicted by the mixture fraction on the basis of the infinitely

fast chemistry assumption. This nonpremixed combustion approach then comes down to solving the a problem of mixing. For hydrogen diffusion flames, the equilibrium approach provides good predictions for major species and temperature due partly to the very fast chemistry of the H_2/O_2 system, but the free radicals O, OH, and H are underpredicted since the radical chain branching leads to superequilibrium radical concentrations during fuel consumption[25]. For hydrocarbon diffusion flames, the equilibrium model overpredicts the concentrations of species CO and H_2. Jones and Priddin predicted the gas composition and temperature field in gas-turbine combustion chambers using the equilibrium assumption. They found that CO and H_2 are overestimated since, in the fuel-rich region of mixture, the equilibrium approach predicts concentration peaks of CO and H_2 that are absent in the experimental data [76][43].

The equilibrium assumption (i.e., much longer mixing time than chemical time) may be locally invalid due to the presence of considerable diffusion time scales variation in turbulent combustion. Local quenching occurs when the diffusion time scales approach or become shorter than the chemical time scales. A further decrease in diffusion time scale results in the lift-off and eventually the blow-out of the flame. In these circumstances, the equilibrium approach fails and the non-equilibrium processes need to be taken into account[43]. It will be seen from this that the mixture fraction as the single independent variable is not sufficient to predict the temperature and the mass fractions of major species, so an additional parameter is needed to account for the non-equilibirum and finite-rate chemistry effects. This suggests the development of the laminar flamelet model. Here, the scalar dissipation rate, a quantity reflecting mixing rate, is included as an additional parameter to scale the extent of departure from equilibrium. The laminar flamelet model was introduced by Williams[16] and developed for nonpremixed turbulent flame by Peters[43]. The flamelet model allows for the simultaneous consideration of mixing rate and chemistry rate.

2.2.2 Concept of Flamelet Model

The flamelet concept views the turbulent nonpremixed flame as an ensemble of discrete small flames which can be viewed as strained laminar diffusion flamelets embedded within the turbulent flow field. Nonpremixed combustion is well known to largely take place in narrow bands which sit where fuel-rich and oxidizer-rich bodies touch, i.e., in the vicinity of stoichiometric surfaces. The key parameter is the strain rate acting on this interface since it governs how quickly fuel and oxidizer are brought into contact. This mixing rate is traditionally represented by the scalar dissipation rate. Thus, the local instantaneous mixing rate(χ_{st}) and the local mixture fraction(Z) are the two parameters that govern the flamelet model. To be specific, the reactive scalars in the model depend only on these two independent variables χ_{st} and Z. In the flamelet model, the thin reactive-diffusive flame structure of each individual flamelet is locally one-dimensional in mixture fraction Z space. This implies that a coordinate is attached to the surface of stoichiometric mixture fraction that points toward the normal direction. Each laminar flamelet structure that is subjected to various degrees of stretching can be characterized by the instantaneous local strain rate that is expressed in terms of the scalar dissipation rate at the stoichiometric condition, χ_{st}. Different scalar dissipation rates correspond to different flamelet structures. The strain rate varies as a function of time and position in the flow field, and thus each flamelet structure specified by the local strain rate can be identified and examined individually.

2.2.3 Assumptions of the Flamelet Model

The underlying assumption of the flamelet approach is the length scale separation between the thin chemical scales and the larger scales in the inertial range of turbulence. For fast chemistry, the thickness of the reaction zone in the flamelet structure is small when compared to the smallest turbulent scale. It follows that the inner structure of the flamelet will not be distorted by the turbulent eddies and can be considered as being embedded in a laminar sublayer. The turbulent flame can thus be treated as an ensemble of laminar flamelets in the turbulent flow field. On the other hand, the thinner reaction layer has no effect on the flow field. Therefore, fast chemistry, leading to sufficient small length scale of reaction zone

thickness compared to the smallest turbulent scale, is the fundamental assumption required for applying the laminar flamelet structure in turbulent combustion[49]. This assumption is justified in many practical situations. Nevertheless, the validity of this assumption based on the comparison of the reaction zone thickness with the Kolmogorov scale will be numerically assessed by means of the flamelet structure attached to flame surface with the use of DNS data, the details will be presented in chapter 3. In addition, the unity Lewis number is another underlying assumption used in current research.

2.2.4 Advantages of the Flamelet Model

From a computational perspective, the advantage of the flamelet model is that it decouples the numerical calculations of the non-equilibrium chemical process from that of the turbulent flow. The flamelet concept divides the combustion calculations into two parts which are performed independently:

(1) The flamelet structure is pre-computed and tabulated into the flamelet library with mixture fraction Z and the stoichiometric scalar dissipation rate χ_{st} as two independent variables prior to the calculation of the flow field. The flamelet structure described by the flamelet library involves the detailed chemical mechanism.

(2) The level of turbulent mixing that provides the passive scalars (i.e., Z and χ_{st}) are determined by resolving the flow field. In the current study, the mixture fraction field is adequately resolved by DNS, and the scalar dissipation rate can be numerically evaluated.

In this way, (1) the approach considerably decreases the computational cost since the pre-built flamelet library provides efficient access; (2) the offline calculation of chemistry allows use of a computationally intensive chemical reaction mechanism for more complicated and detailed chemistry. In the flamelet model, the interactions between the chemistry and the turbulence are achieved through these two key parameters, Z and χ_{st}. The quantities of interest, i.e., the species and the temperature, can be completely determined by these two parameters from the flamelet library through the linear interpolation scheme.

2.2.5 Limitations of Steady Flamelet Model

In the current research, the flamelet structure is assumed to be steady state, this is, the so-called steady laminar flamelet approach (SFL). However, this SFL model is limited by the fact that the assumption concerning an instantaneous response of flamelet structure to changes of scalar dissipation rate might be invalid. And thus the SFL approach cannot capture strong non-equilibrium effects such the extinction and very fast mixing [24]. This transient effect has been shown experimentally by carrying out an unsteady analysis for both diffusion and premixed flame in counter flow geometry [68], and has also been demonstrated in the simulations of unsteady flamelets[53]. In Chapter 5, this unsteady effect will be shown by the comparisons between the SFL model predictions and the DNS results. The increased amount of extinction make the application of flamelet model less justified.

2.2.6 S-shaped curve

The key mechanism of turbulent combustion is the interaction between turbulence and chemistry, which can be scaled by a non-dimensional parameter referred to as the Damköhler's second similarity group number, Da. It represents the ratio of characteristic flow and chemical reaction time scales, and is defined as

$$Da = \frac{t_{flow}}{t_{chemistry}}. \tag{2.1}$$

The various combustion regimes that result from the competition between flow and reaction are illustrated using a S-shaped curve through the Damköhler number by Fendell[18][19]. Equivalently, the results of turbulence-reaction interaction(e.g., ignition, chemical equilibrium and flame extinguishment) can also be graphically depicted by the characteristic S-shaped curve in terms of the stoichiometric scalar dissipation rate χ_{st}, since the Damköhler number can be considered as the non-dimensionalization of χ_{st}. As shown in Fig.(2.1), the S-shaped curve displays the non-monotonic change of the stoichiometric flamelet temperature $T_{fl}(Z_{st})$ with the stoichiometric scalar dissipation rate χ_{st}. The S-curve is generated by solving the unsteady flamelet equation with chemical parameters specifically used for case R2 in current research; the corresponding time-dependent equation and numerical implementation will be derived and explained in Section 3.6. The segments of S-curve identify

different combustion regimes: the upper steady burning (SFL) branch, the lower steady non-burning branch (reactants mixing with frozen chemistry), and the unstable central (USFL) branch. The critical state of extinction can be identified by the upper right turning point of the S-curve, designated by the quenching value of dissipation rate χ_q.

In a physical sense, when the flame is stretched, the width of the flame zone decreases, which thereby causes the concentration gradients at stoichiometric surface to increase. This results in an increase in the mass and heat transfer at interface between the reactants. In other words, the scalar dissipation rate at stoichiometric condition χ_{st} characterizes the rate of strain acting on the flame zone, and represents the mass diffusion of species and the rate of heat conduction occurring at the flame[43].

At the left endpoint of steady burning branch, when χ_{st} approaches zero, $\chi_{st} \rightarrow 0$, the laminar flamelet structure approaches the chemical equilibrium state, and the corresponding temperature is at the maximum value. However, the rate at which the reactants diffuse into the reaction zone for sustaining the chemical reaction is so low that the rate of reaction is limited to be close to zero.

Along the steady burning branch, with the increase of the stoichiometric scalar dissipation rate, the stoichiometric flame temperature decreases and the reaction rate increases. The higher rate of scalar dissipation implies the shortest turbulent mixing time, which leads to less complete reaction and therefore a decrease in temperature. A larger strain rate replenishes more reactants into the reaction zone, which accelerates the rate of reaction. But in the meantime, a similar consideration applies to the mass and heat transfer occurring at the interface, the temperature is depressed by more heat loss that is caused by the mass diffusion of hot products away from, the mass diffusion of cold reactants into, and the heat diffusion from, the flame zone.

A steady burning flame is sustained until χ_{st} increases beyond a critical limit, denoted as the quenching point χ_q, at upper right turning point. The highly nonlinear dependence of Arrhenius-type reaction rate constant on temperature ($exp(-\frac{E}{RT})$) shows an exponential decay of reaction rate with decrease of temperature. When the critical state is reached, the temperature is so low that the chemical kinetics are inhibited to the point of flame extinguishment.

Any state with a temperature above or below the middle unstable branch will be rapidly driven to the upper or lower stable states, respectively[49]. The flamelet experiences an extinction from the stable burning to stable extinguished state, or reignition along a vertical projection onto the S-shaped curve.

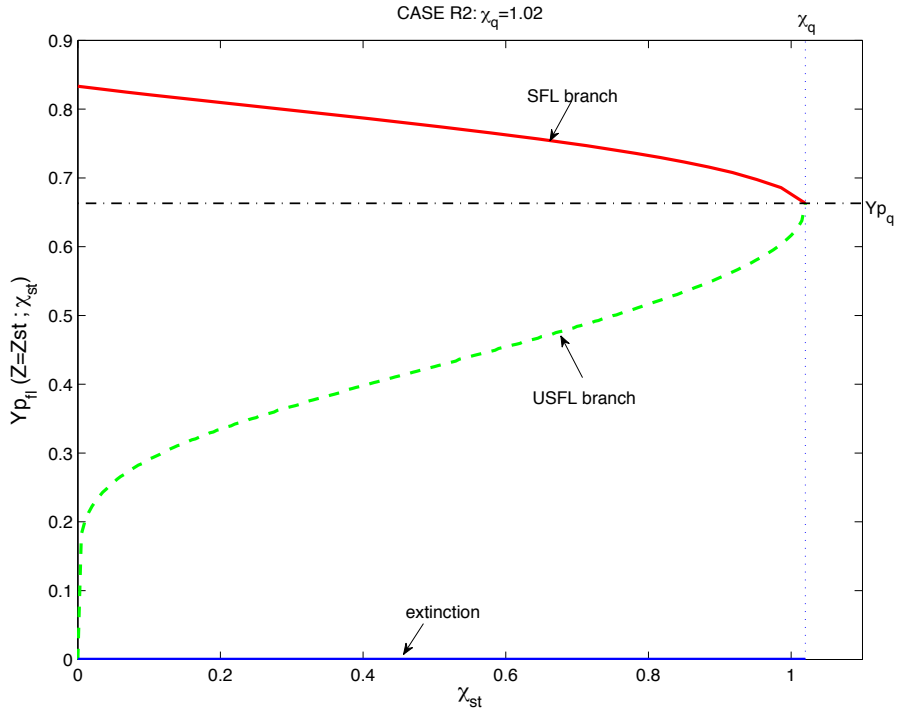

Figure 2.1: Solutions of flamelet equation for diffusion flame. The stoichiometric temperature as a function of the scalar dissipation rate at $Z = Z_{st} = 0.5$. The upper and lower branches represent the stable burning and non-burning states from the solutions of the steady flamelet equation, respectively, and the middle branch is unstable.

2.3 Flame Surface Area

The analytical measurement of the flame surface density (i.e., flame surface area per unit volume) can be obtained by an algebraic expression or by solving its balance equation[67]. The evolution equation of the flame surface density was first proposed by Marble and Broadwell[20]. Later, an exact balance equation for the surface density function was deduced mathematically based on a geometry approach by Pope[57], and Candel and Poinsot[61].

The flame surface approach has advantages for some kinds of turbulent combustion. The Coherent Flame Model (CFM) developed by Marble and Broadwell[20] describes the turbulent nonpremixed flame in terms of the flame surface density concept together with the laminar flamelet assumption. It decouples the complex interactions between the chemical reaction and the turbulent flow.

2.4 Extinction and Reignition

2.4.1 Extinction Mechanisms

Extinction occurs when the temperature decreases dramatically, thereby slowing the chemical kinetics and consequently inhibiting the reaction. The reasons that lead to the temperature drop include the dilution of reactants with fresh gas, contact with a cold interface, or heat diffusion or convection away from the reaction zone exceeding the heat production of chemical reaction. The last possibility is related to the high concentration gradients of reactants (characterized in terms of scalar dissipation rate) due to the flame stretch effect which results from the high strain rate [13]. The increase of scalar gradients leads to an increase in diffusive mixing, and an increase in heat loss. The extinction event in response to high fluctuations in scalar dissipation rate was discussed previously. In addition to this extinction mechanism, there are other mechanisms that can lead to the onset of flame extinction. One extinction mechanism is flame shortening. As the local flame wrinkling increases during the flame surface growth by turbulent straining, the adjacent flame elements move so close that they consume the intervening reactants and thus mutually annihilate each other [20]. This mutual annihilation of neighboring flame fronts due to the high degree of local flame wrinkling is called flame shortening. The other extinction mechanism is attributed to the excessive lateral heat diffusion occurring at the location where the local curvature of flame surface is large. This mechanism (heat diffusion in the direction tangential to the local flame surface) is similar to the way flames are quenched by higher fluctuations of scalar dissipation rate due to flame stretch (heat diffusion in the direction normal to the local flame surface).

These extinction mechanisms are related to the geometric interpretation of the effects of the flame surface on the local extinction. Thus, the geometric characteristics of the flame

surface can provide valuable information to understand the extinction mechanisms.

2.4.2 Reignition Mechanisms

When the scalar dissipation rate decreases below the critical quenching value, reignition occurs. There are three major reignition scenarios identified in turbulent nonpremixed combustion [64]:

(1) IFL: This reignition scenario is expected to happen if the excursion of the scalar dissipation rate beyond the critical quenching value is small and of short duration. This extent of fluctuation will not bring about significant drop in temperature and thus the flame element can reignite independently to a burning state without assistance from the neighboring burning flame segments. An alternative way to characterize this process is that the excursion beyond the critical scalar dissipation rate is too small to cause complete flame extinction.

(2) EDGE: When the excursion of scalar dissipation rate beyond the critical quenching value is large and lasts for a period of time, the temperature drops excessively and the quenched holes forms on the flame surface. An edge flame develops surrounding the flame holes and separates the nonburning region from the burning flame. The structure, behavior and propagation of edge flame depends on the scalar dissipation rate at the edge flame. When the value of the scalar dissipation rate at the edge flame is higher than χ_q, the intense heat and mass diffusion prevent the edge flame from propagating into the premixed, quenched region. A receding edge flame thus expands the flame hole, something that is considered an extinction process. When the value of scalar dissipation rate at the edge flame is lower than χ_q, the edge flame propagates into the quenched region via the diffusion of heat into adjacent nonburning premixed reactants, which is considered an ignition mechanism. When the scalar dissipation rate at the edge flame is much less than χ_q, the edge flame exhibits a tribrachial structure[27].

(3) ENGULF: The local extinguished region can be reignited by a neighboring burning flame element via turbulent transport of heat in the direction normal to the local quenched stoichiometric isosurface. This scenario is expected to occur when the flame surface has a sufficiently high degree of wrinkling such that the neighboring burning and nonburning

flame elements are close enough to interact with each other. This scenario is also called 'flame-flame' interaction [30].

Chapter 3

NUMERICAL SIMULATION

3.1 Introduction

The physical feature of extinction and reignition resulting from the imbalance between the mixing and reaction in nonpremixed reacting flames is investigated in the current research. In this chapter, the description of turbulent reacting flow field and the numerical techniques employed to study the mechanism underlying the extinction and reignition is presented and discussed.

3.2 Physical Description of Research Problem

The investigation of extinction and reignition is explored in the context of diffusion flames by performing the direct numerical simulation (DNS) of a non-premixed chemical reaction occurring in a flow field characterized by incompressible homogeneous decaying isotropic turbulence. The simulated turbulent, chemically reacting flow can be described by five quantities: three velocity components, one conserved scalar (mixture fraction) and one reactive scalar (mass fraction of product).

The chemical mechanism employed in DNS is characterized by a single-step, irreversible, reaction whose rate constant is expressed as an Arrhenius function of temperature,

$$F + rO \rightarrow (1 + r)P \tag{3.1}$$

where F, O and P represent the fuel, the oxidizer and the product, respectively. The stoichiometric ratio, r, denotes the mass ratio of air to fuel that measures the mass of oxidant required to completely burn off a unit mass of fuel.

The mixing between the reactants is a fundamental process in nonpremixed combustion. The mixture fraction Z is introduced as a conserved scalar indicative of the degree of mixing between the fuel and the oxidizer, which provides insight into the process of non-premixed

combustion. For a two-feed problem, it is a nondimensional variable normalized so as to vary between $Z = 0$ in the pure oxidizer stream and $Z = 1$ in pure fuel stream, and given as

$$Z = \frac{rY_F - Y_O + Y_{O\infty}}{rY_{F\infty} + Y_{O\infty}} = \frac{rY_F - Y_O + 1}{r + 1}. \tag{3.2}$$

Here Y_F, Y_O and Y_P denote the mass fractions of fuel, oxidizer and product, respectively. $Y_{F\infty}$ and $Y_{O\infty}$ corresponds to the mass fractions of fuel and oxidizer in pure unburnt fuel and oxidizer streams, respectively. Here both $Y_{F\infty}$ and $Y_{O\infty}$ equal unity. The normalization is exemplified by

$$\begin{aligned} \text{In pure fuel stream} &: Y_F = Y_{F\infty}, \quad Y_O = 0 \quad \rightarrow \quad Z = 0 \\ \text{In pure oxidizer stream} &: Y_F = 0, \quad Y_O = Y_{O\infty} \quad \rightarrow \quad Z = 1 \end{aligned} \tag{3.3}$$

According to the concept of mixture fraction Z and stoichiometric ratio r, the stoichiometric mixture fraction Z_{st} quantifies the relative amount of oxidant and fuel at the flame surface where $rY_F - Y_O$ vanishes. Thus, Z_{st} is a good tracer to dictate the approximate position of the flame surface. Substituting $rY_F - Y_O = 0$ into Eq.(3.2) yields the definition of Z_{st} as

$$Z_{st} = \frac{1}{r + 1}. \tag{3.4}$$

In current study, r is taken as unity, which leads to $Z_{st} = 0.5$. Another important quantity is the scalar dissipation rate χ measuring the gradients of reactant concentrations on both sides of flame surface, which is defined as follows.

$$\chi = 2D|\nabla Z|^2. \tag{3.5}$$

It scales the feeding rate of reactants and thus can be interpreted as the inverse of characteristic mixing time scale.

3.3 Governing Equations

The simulated velocity field evolves according to the incompressible, Navier-Stokes equations which are derived from the conservation of mass and momentum equations. The governing equations for the five quantities charactering the turbulent reacting flow field are written as follows in vector notation.

Conservation of mass (also known as Continuity equation) for an incompressible flow field:

$$\nabla \cdot \mathbf{u} = 0 \tag{3.6}$$

Conservation of momentum (Navier-Stokes equation) for an incompressible flow field:

$$\frac{\partial \mathbf{u}}{\partial t} = -\nabla(\frac{p}{\rho} - \frac{|\mathbf{u}|^2}{2}) - \mathbf{w} \times \mathbf{u} + \nu \nabla^2 \mathbf{u} \tag{3.7}$$

where p and ρ respectively denotes the hydrostatic pressure and density, $|\mathbf{u}|^2/2$ is related to the dynamic pressure, $\mathbf{w} \equiv \nabla \times \mathbf{u}$ represents the vorticity vector, and ν, the kinematic viscosity in unit $[L^2/T]$, is assumed to be a temperature-independent constant in space and time.

The conservation equation of mixture fraction Z is:

$$\frac{\partial Z}{\partial t} = -\mathbf{u} \cdot \nabla Z + D \nabla^2 Z \tag{3.8}$$

while the conservation equation of species mass fraction Y_i is:

$$\frac{\partial Y_i}{\partial t} = -\mathbf{u} \cdot \nabla Y_i + D \nabla^2 Y_i - \omega_i \tag{3.9}$$

where Y_i indicates the mass fraction of species i ($i = F, O, P$). D is the molecular diffusion coefficient, which is assumed to be identical for all reacting species and heat. The Schmidt number $Sc = \nu/D$ of conserved scalar and reactive scalar are assumed to be the same and equal to 0.7 in current study. Once ν is given, D can be determined accordingly using $D = \nu/Sc$, and is therefore also considered as a temperature-independent constant in space and time.

It is well known that, in a real flame, the density and kinematic viscosity can change when subjected to a temperature change caused by the heat released in a chemical reaction. The change in temperature affects the kinematic viscosity and hence the Reynolds number. But, in the current DNS, these effects of temperature on the flow properties, i.e., density, kinematic viscosity and the specific heat, are ignored, so that these parameters are kept constant in space and time.

3.4 Direct Numerical Simulations(DNS) and Resolution Considerations

3.4.1 DNS

With the enormous progress during recent decades in computer technology and the advances in numerical methodologies, direct numerical simulation (DNS) emerges as a new approach and an important and reliable tool in the study of turbulent combustion. The advantages of DNS over the laboratory experiments include easily achieved information from the simulated results and conveniently altered parameters. In DNS, the entire range of flow and chemical scales are completely resolved without the use of any modeling. The spatially and temporally resolved turbulent reacting flow fields provide complete and unique information as a tool to improve the understanding of physical process in turbulence-chemistry interactions, and to facilitate the development and the evaluation of models by means of a *priori* or a *posteriori* tests. However, the high resolution of simulated fields is associated with the high demands on computational capacity and computing time, even at low Reynolds number. In recent years, with the advent of powerful supercomputers, higher Reynolds numbers become feasible on massively parallel computers.

A series of three dimensional direct numerical simulation (DNS) runs of fully developed homogeneous decaying isotropic turbulence with chemical reactions is carried out on uniformly distributed grid points in a cubic computational domain with periodic boundaries.

The DNS is performed to resolve three velocity components, one conserved scalar and one reacting scalar by solving the set of governing equations. The algorithm of the numerical solution is a Fourier-based pseudospectral approach[71][64] which has been a favored numerical method in solving nonlinear partial differential equations with periodic boundaries as it provides an appropriate tradeoff between the accuracy and the computational cost. In the Navier-Stokes and scalar equations, the spatial derivative terms are calculated in Fourier space, while the convective terms and the reaction terms are computed in physical space. The pseudospectral algorithm involves the use of a Fast Fourier Transform(FFT) between the physical and wavenumber space(converts a quantity from physical to spectral space in a forward FFT, and from spectral to physical space in a backward FFT). The implementation of the FFT is performed using FFTW which is a widely used free software

developed by MIT. The time discretization is carried out by employing the second-order Adams-Bashforth scheme, except in the first time step a first order forward Euler method is utilized.

In physical space, the dimensions of the 3D computational domain are $L \times L \times L$, where L, the computational domain size, is taken to equal 2π. The boundary conditions are periodic as required by the Fourier series representation. The cube is spatially discretized by uniformly distributed grid points of number $N \times N \times N$ in the x_1-, x_2- and x_3-directions, respectively. The locations of the grid points ordered in Cartesian coordinates are defined as $\mathbf{x} = (x_i, x_j, x_k) = (i\Delta, j\Delta, k\Delta)$, where $i, j, k = 0, 1, ..., N-1$, and the uniform mesh width Δ is L/N. In spectral space, it can be discretized because the physical domain is periodically bounded. The discrete wavenumber vector is defined as $\mathbf{k} = (k_1, k_2, k_3) = (l_1 k_{min}, l_2 k_{min}, l_3 k_{min})$, where k_1, k_2 and k_3 are respectively the wave numbers in the x_1-, x_2- and x_3-directions, and the wavenumbers are stored in the order $l_1, l_2, l_3 = 0, 1, ..., \frac{N}{2} - 1, -\frac{N}{2}, -\frac{N}{2} + 1, ..., -1$ but replacing term $-\frac{N}{2}$ with 0 for odd derivatives because of a loss of symmetry. The minimum nonzero wavenumber k_{min} is taken to be $2\pi/L = 1$.

Dealiasing in Pseudospectral Method

The aliasing errors associated with the pseudospectral method need to be specified with care. In the pseudospectral scheme, the bilinear product in the convective term is calculated in physical space instead of computing through the convolution in wavenumber space. The aliasing errors thus induced can be reduced by different methods, i.e., the truncation method or phase-shift scheme[51][10]. A commonly employed dealiasing method is the wavenumber truncation in which the amplitudes of all the Fourier modes beyond the cutoff wave number k_{max} are reset to zero in spectral space. The cutoff wave number is traditionally given following the 2/3 dealiasing rule that ensures the results being aliased free. In the pseudospectral solver for the current DNS, the radius of spherical-filter mask, k_{max}, is set to $(15/32)N$ instead of performing the traditional 2/3 rule. This eliminates the most serious aliasing errors while allowing for more resolution. Once the number of grid points N is specified, the cutoff wave number k_{max} and hence the smallest resolved length scale

can be determined.

3.4.2 Determination of Some Statistical Quantities

Statistical quantities pertaining to the velocity and scalar fields at a particular time t are defined here.

The energy spectrum $E(\kappa,t)$ shows how kinetic energy is distributed as a function of wavenumber κ. The kinetic energy spectrum in the wave number bin n, $e_u(n,t)$, represents the kinetic energy contained in a spherical wavenumber shell of radius n with thickness k_{min}. The calculation is performed by summing the square of the modulus of the complex Fourier coefficients of all the nodes whose wave number amplitudes $|\mathbf{k}|$ are in the n-th bin, such that $(n-k_{min}/2) \leq |\mathbf{k}| < (n+k_{min}/2)$, where $|\mathbf{k}| = \sqrt{{k_1}^2 + {k_2}^2 + {k_3}^2}$ is the magnitude of the 3D wavenumber vector $\mathbf{k} = (k_1, k_2, k_3)$ as previously defined.

$$\begin{aligned} e_u(n,t) &= \sum_{(n-k_{min}/2)\leq|\mathbf{k}|<(n+k_{min}/2)} \frac{1}{2}\hat{u}_i(\mathbf{k},t)\hat{u}_i^*(\mathbf{k},t) \\ &= \frac{1}{k_{min}} \int_{(n-k_{min}/2)\leq\kappa<(n+k_{min}/2)} E(\kappa,t)d\kappa \end{aligned} \tag{3.10}$$

where $n = 0, 1, ..., n_{max}$(n_{max} is the largest integer less than k_{max}), $\hat{u}_i(\mathbf{k},t)$ is the Fourier coefficient of the velocity component $u_i(\mathbf{x},t)$ at wavenumber vector $\mathbf{k}$, and $\hat{u}_i^*(\mathbf{k},t)$ is its complex conjugate. As above mentioned, the minimum nonzero wavenumber k_{min} is taken to be 1. Then, Eq.(3.10) can be rewritten as

$$e_u(n,t) = \int_{(n-k_{min}/2)\leq\kappa<(n+k_{min}/2)} E(\kappa,t)d\kappa \tag{3.11}$$

The total kinetic energy $E_{ke}(t)$ can thus obtained by summing the energy spectrum $e_u(n,t)$ over all shells in spectral space, which yields the same result as the one computed by summing the kinetic energy over all grid points in physical space.

$$\begin{aligned} E_{ke}(t) &= \frac{1}{N^3}\sum_{\mathbf{x}} \frac{1}{2}u_i(\mathbf{x},t)u_i(\mathbf{x},t) = \int_{\kappa} E(\kappa,t)d\kappa \\ &= \sum_{|\mathbf{k}|\leq k_{max}} \frac{1}{2}\hat{u}_i(\mathbf{k},t)\hat{u}_i^*(\mathbf{k},t) \end{aligned}$$

$$= \sum_{n=0}^{n_{max}} \int_{(n-k_{min}/2)\leq\kappa<(n+k_{min}/2)} E(\kappa,t)d\kappa$$
$$= \sum_{n=0}^{n_{max}} e_u(n,t) \tag{3.12}$$

The root mean square velocity(r.m.s.):

$$u^{'}(t) = \sqrt{\frac{1}{3}\frac{1}{N^3}\sum_{\mathbf{x}} u_i(\mathbf{x},t)u_i(\mathbf{x},t)} = \sqrt{\sum_{\mathbf{k}} \frac{1}{3}\hat{u}_i(\mathbf{k},t)\hat{u}_i^*(\mathbf{k},t)} \tag{3.13}$$

The energy dissipation rate ε:

$$\varepsilon(t) = \sum_{\mathbf{k}} \nu|\mathbf{k}|^2\hat{u}_i(\mathbf{k},t)\hat{u}_i^*(\mathbf{k},t) \tag{3.14}$$

The integral length scale l, the taylor microscale λ and the Kolmogorov microscale η_k can be determined respectively as follows:

$$l(t) \equiv \frac{3\pi}{4}\frac{\sum_{\mathbf{k}} \frac{1}{2|\mathbf{k}|}\hat{u}_i(\mathbf{k},t)\hat{u}_i^*(\mathbf{k},t)}{E_{ke}(t)} \tag{3.15}$$

$$\lambda(t) \equiv [\frac{15\nu u^{'2}(t)}{\varepsilon(t)}]^{1/2} \tag{3.16}$$

$$\eta_k \equiv (\frac{\nu^3}{\varepsilon})^{1/4} \tag{3.17}$$

The Reynolds number based on integral length scale and Taylor microscale are defined respectively as:

$$Re_l \equiv u^{'}l/\nu \qquad Re_\lambda \equiv u^{'}\lambda/\nu \tag{3.18}$$

The velocity derivative skewness S is defined as: (take the derivative of x component velocity with respect to x direction for instance)

$$S \equiv \frac{\langle(\frac{\partial u}{\partial x})^3\rangle}{\langle(\frac{\partial u}{\partial x})^2\rangle} \tag{3.19}$$

The quantities defined in above governing equations are extracted from DNS data at each grid point. Due to the initialization procedure (see below), the resolved field under consideration is statistically homogeneous. Then, based on the ergodic hypothesis, the statistics measured by probability or averaging over grid points within the volume, indicated by $\langle\cdot\rangle$, is approximately equal to be equivalent to the statistics of an ensemble average.

3.4.3 Velocity Field

Velocity Field: Numerical Resolution

The velocity field is evolved by performing DNS of incompressible homogeneous decaying isotropic turbulence. In DNS, all relevant spatial scales are resolved, from the smallest scales related to the Kolmogorov scale up to scales significantly larger than the integral scale. The spatial resolution requirements can therefore be dictated by these two extreme ends of the length scales: (1) The largest energy containing scale should not be influenced by the boundaries of computational domain; (2) The smallest dissipative scale needs to be adequately resolved on the computational grid, and can thus reveal the mechanism of the mixing process. The spatial and temporal numerical constraints required to adequately resolve the velocity field are imposed as follows:

(1) The integral length scale of turbulence l, the largest scale which contains the most of energy, should be significantly smaller than the size of the computational domain L (i.e., l/L must be less than a criteria) in order to reduce the impact of boundary conditions on the integral length scale and to have better statistics. The ratio constraint of the size of integral scale l to the size of the domain L can be expressed in terms of lk_{min} as L and k_{min} are linked by $2\pi/L = k_{min}$. de Bruyn Kops and Riley[37] finds that, for a simulation of decaying, isotropic turbulence, the large scale resolution requirement $lk_{min} < 0.3$ is to be met so that the large eddies can be accurately resolved and can evolve correctly with negligibly energy transfer to larger scales. In the current study, this large scale constraint is relaxed to $lk_{min} \simeq 1$ [64].

(2) The smallest relevant scale in the flow is related to the Kolmogorov microscale of the turbulence, η_k, at which the kinetic energy of the eddies can be dissipated to heat by viscosity. The resolution of this small-scale motion requires a sufficiently small ratio of computational grid spacing to the dissipative scale, Δ/η_k, where Δ can be expressed in terms of k_{max} as $\Delta = \frac{15}{32}\frac{L}{k_{max}}$ ($\Delta = L/N$ and $k_{max} = \frac{15}{32}N$ as previously defined). Consequently, the constraint can be formed as $k_{max}\eta_k > 1$ [69]. It ensures that the maximum wavenumber k_{max}, equivalently the number of grid points N, is sufficiently large (i.e., the mesh size is sufficiently small) to resolve the smallest relevant scales of turbulence, at the order of

Kolmogorov scale η_k. The Kolmogorov scale η_k increases with time in fully-developed turbulence, and therefore the constraint $k_{max}\eta_k$ increases accordingly, which results in a more favorable numerical resolution.

(3) The timestep size Δt is estimated based on the Courant number C_n, which is given as

$$C_n = u^{'}\Delta t/\Delta. \tag{3.20}$$

The Courant number must be less than a constant near unity for a stable calculation. It is chosen to be 0.0426 in the present research.

It is noteworthy to mention that these numerical constraints impose restrictions not only on the DNS, but also on the velocity initialization procedure introduced in the following section.

Velocity Field: Initialization

The initial velocity field for the simulations is incompressible, homogeneous, isotropic and periodic in the computational domain. It is produced with an intent to mimic the flow conditions in the laboratory experiments. To achieve this aim, the velocity field is initialized with an attempt to attain the highest possible Reynolds number within the context of the numerical constraints. The simulated velocity field is initialized in wave space using a two-stage numerical procedure[64][74][72] that is composed of the following steps:

Stage I: Prescribed Energy Spectrum The velocity field is initialized in wave space from a prescribed kinetic energy spectrum function, $E_0(\kappa)$, which can be given in different forms, such as an exponential shaped form introduced by Orszag [56][64] or a modified laboratory data form [75]. In the current simulation, the lab form is employed and defined as

$$E_0(\kappa) = \left(\frac{3u_0^2}{2}\right)\left(\frac{32}{\pi k_m}\right)\frac{\kappa^4}{(1+\kappa^2)^4}, \tag{3.21}$$

where κ represents the wave number magnitude and k_m is the wave number containing the maximum energy. The unknown parameters, u_0 and k_m, in this predefined energy spectrum function are dictated by the numerical constraints. In addition, the level of the rms velocity of the resulting velocity field should be small enough for numerical stability and large enough for strong turbulent velocity fluctuations (or, equivalently, the high Reynolds

number). Here, the value of the rms velocity is around $\mathcal{O}(1)$. The velocity field is evolved according to the incompressible Navier-Stokes Eq.(3.7) until the fully-developed turbulence undergoing the full spectrum decay is achieved, which can be specified by the following termination conditions:

(1) All the turbulent length scales, i.e., the integral length scale l, the Taylor microscale λ, and the Kolmogorov microscale η_k, increase with time.

(2) The velocity-derivative skewness has peaked and has settled to an approximately constant value of -0.5 which is a typical experimental value.

The chronological details of the statistical properties of turbulence are demonstrated using the results from the case R2 and R3 as shown in Fig.(3.1) and Fig.(3.2). Fig.(3.1) shows the time evolution of the energy spectra $E(n)$ in stage I for case R3 from the initial prescribed spectrum (Eq.(3.21)) to fully-developed state. The energy spectra initially decay(grow) at small(large) wavenumbers during time $t = 0 \sim 0.97$ (top panel in Fig.(3.1)) because of going through an adjustment, then undergoes a full spectrum decay between time $t = 0.97$ to $t = 2.09$ (bottom panel in Fig.(3.1)). The time evolution of the rms velocity, velocity integral scale, velocity Taylor scale and velocity-derivative skewness in stage I for case R2 and R3 are presented in Fig.(3.2). Note that the simulation is terminated when both of the above criteria are reached. In the comparisons shown in the figure, the lower Reynolds number the flow field (case R2), the more rapidly the rms velocity starts to decrease, and the shorter time the velocity length scales take to start increasing. This is because smaller Reynolds number leads to smaller length scale separation between the energy containing scales and the dissipation scales. The Fourier modes of velocity are initialized using a random number generator for normal distribution with zero mean (the random variables with normal distribution are generated by transforming the uniformly distributed random variables based on the fundamental transformation law of probabilities). This results in a zero velocity-derivative skewness at the initial time as shown in the bottom-right panel of Fig.(3.2), and hence no initial spectral transfer[37]. With the temporal evolution of velocity, the skewness builds up from zero to a typical experimental value around -0.5 [64][65].

At the end of stage I, the Reynolds number reach a lower value as the fully developed flow decays. In order to generate a higher Reynolds number initial flow field, the energy

spectrum from the end of stage I needs to be reenergized in the following stage II.
Stage II: Self-similar Energy Spectrum The turbulent kinetic energy spectrum evolves in a self-similar manner. Accordingly, the energy spectrum can be defined based on a self-similar scaling law for a decaying kinetic energy spectrum as [64]

$$E(\kappa) = u'^2 l F(\kappa l), \tag{3.22}$$

where u' is the rms velocity defined in Eq.(3.13) and l is the integral length scale. The new reenergized energy spectrum $\tilde{E}(\kappa)$ can be expressed in term of the energy spectrum from the end of stage I, $E(\kappa)$, as

$$\tilde{E}(\kappa) = \tilde{u'}^2 \tilde{l} F(\kappa \tilde{l}) = \tilde{u'}^2 \tilde{l} F(\kappa l[\tilde{l}/l]) = \frac{\tilde{u'}^2 \tilde{l}}{u'^2 l} E(\kappa[\tilde{l}/l]). \tag{3.23}$$

The new kinetic energy spectrum can be computed when $\tilde{u'}$ and $\tilde{l}$ are specified. $\tilde{u'}$ and $\tilde{l}$ are chosen, in a similar manner as in stage I, such that the the numerical constraints are satisfied and a higher Reynolds number can be achieved. The velocity field generated from this rescaled energy spectrum is advanced according to Eq.(3.7) until the specified termination conditions, the same ones used in Stage I, are met. The values of the rms velocity and the length scales, at the time when self-similar decay is attained, will not necessarily reach the level required for being the initial velocity. Thus, an iterative procedure is need for generating an initial velocity field with desired values of Reynolds number and length scales.

3.4.4 Conserved Scalar Field

Since the nonpremixed flame is the subject being considered, i.e., the fuel and oxidant are initially supplied from two separated streams, the initial mixture fraction field is designed to be segregated blobs of fuel and oxidant ($Z = 1$ and $Z = 0$). The fuel blobs ($Z = 1$) occupy about half of the computational domain, with oxidant ($Z = 0$) occupying approximately the other half, thus the mixing layer between them is very thin. As a result of this arrangement, the mean value of mixture fraction $\langle Z \rangle$ is close to 0.5, and this average value is invariant over time.

The mixture fraction field is initialized in blob-like shape using the scheme developed by Eswaran and Pope[69]. There are two parameters required in the initialization, K_c and K_s:

(1)K_c: The initial field is created such that the pdf of the mixture fraction conforms to a double-delta distribution. This shape of pdf is in accordance with the segregation of blobs that the fuel and oxidant blobs respectively fill nearly half of the computational domain. But a desired double-delta distribution is associated with jump discontinuities resulting in steep gradients at the interfaces between the fuel and oxidant blobs that cannot be numerically resolved. Next a filtering operation with an associated cutoff wavenumber K_c is performed in spectral space by rescaling the higher wavenumber modes to spatially smooth the double-delta distribution. But from another perspective, considering the study of extinction, the parameter K_c needs to produce sufficiently large steepness, and hence high enough level of initial χ. In the current DNS, allowing a trade-off between the numerical resolution and the degree of extinction, K_c is taken as 8.0.

(2)K_s: This parameter controls the size of the blobs. The K_s is chosen such that the integral length scales of the conserved scalar field and velocity field are at comparable levels. Here K_s is taken as 1.7. Thus, the resulting initial Z field is considered to be composed of $''$large blobs$''$.

The conserved scalar field initialized in blobs is injected into the turbulent field when it is fully developed undergoing full spectrum decay; due to the method of initialization the initial scalar blobs are spatially homogeneous and isotropic. The Z field evolves due to the transport Eq.(3.8). The time history of the statistics of the scalar dissipation rate at stoichiometric conditions for a series of simulations R2-R7 with increasing Reynolds number(see Section 3.4.6 for a detailed introduction about the simulated cases) are shown in Fig.(3.3) and Fig.(3.4). As can be seen from the figures, during the whole simulation time, the mean value, $\langle\chi_{st}\rangle$, remains smaller than χ_q, with a maximum $\langle\chi_{st}\rangle/\chi_q$ of around 0.5, whereas the profiles that envelopes 99% of the fluctuations of χ_{st} are far above the critical quenching value. The fluctuations of χ_{st} beyond χ_q caused by the turbulence, together with the high activation energy chemistry, result in the occurrence of local extinction.

3.4.5 Reactive Scalar Field

For a diffusion flame with one-step chemistry, the reaction rate of the product, ω_P, can be defined due to Arrhenius law as

$$\omega_P = (r+1)A_f \; exp(\frac{-\beta}{\alpha})exp[\frac{-\beta(1-Y_P)}{1-\alpha(1-Y_P)}](Y_F Y_O - \frac{1}{K}{Y_P}^{r+1}), \tag{3.24}$$

where the chemical parameters A_f, α, β and K denote the pre-exponential factor, nondimensional adiabatic temperature, Zeldovich number and equilibrium constant for reversible chemistry, respectively.

Regarding the choice of chemical parameter β, it is found by de Bruyn Kops[36] that the choice of Zeldovich number β depends on the spatial resolution of DNS. As examined by Sripakagorn[64], whose DNS were configured in the same manner as the present research, large values of β exhibits strong dependence of reaction rate on β through the activation temperature, and results in abrupt occurrence of extinction. Nevertheless, the large value of β requires high spatial resolution demands, and leads to thin reaction zone which will impact the numerical resolution. Considering all these factors, β is chosen to be 4 in current study. Furthermore, the dependence of the quenching value χ_q on the choice of A_f and β will be analyzed at the end of Section 3.6.2.

For the quantities Y_F and Y_O entering in the reaction rate term, since the total mass is conserved in reacting flow, the sum of the mass fractions of all reacting species must be unity.

$$Y_F + Y_O + Y_P = 1 \tag{3.25}$$

With the knowledge of Z and Y_P, due to above Eq.(3.25) and the definition of mixture fraction, it is sufficient to determine the mass fractions of fuel and oxidizer in terms of Z and Y_P as

$$\begin{aligned} Y_F(Z, Y_P) &= Z - Z_{st} Y_P \\ Y_O(Z, Y_P) &= (1-Z) - (1-Z_{st}) Y_P \end{aligned} \tag{3.26}$$

Thus, it is quite obvious that the reaction rate ω_P depends only on Z and Yp. This means that the mixture fraction Z and mass fraction of product Y_P, respectively, as conserved

scalar and reactive scalars, are sufficient and appropriate for characterizing the reacting field.

The normalized temperature θ is defined as

$$\theta = \frac{T - T_\infty}{T_f - T_\infty}, \tag{3.27}$$

where T_f and T_∞ are the adiabatic flame temperature and ambient temperature of both unburnt fuel and oxidant, respectively. The normalized temperature equals the mass fraction of product, $\theta = Y_P$. Except when mentioned explicitly, Y_P will be referred to as temperature throughout the study.

The reactive field Y_P is initialized using the steady flamelet model, which will be introduced in Section 3.6.2. Then, the temperature evolves according to the governing Eq.(3.9). The time history of the average of temperature at stoichiometric conditions, $\langle Y_{P_{st}} \rangle$, is exhibited in Fig.(3.5). It can be seen that at the initial time, as seen in Fig.(3.4), all the fluctuations of χ_{st} stay well below the critical quenching value χ_q, which implies that the whole flame surface has burning steady flamelet solutions. The initial mixture fraction fields are identical for various simulated cases. Thus, the increasing $\langle Y_{P_{st}} \rangle$ at the initial time that appears in the increasing Reynolds number cases from R2 to R7 in Fig.(3.5) can be attributed to the effect of the decrease in ν (i.e., the decrease in diffusion coefficient D and hence the decrease in χ) on the steady flamelet burning solutions. During the early simulation time, the high fluctuations of χ_{st} exceeding the critical quenching value due to flame stretching, as seen in Fig.(3.4), leads to the local extinctions. Accordingly, Fig.(3.5) shows that the conditional temperature $\langle Y_{P_{st}} \rangle$ decreases with time. As time proceeds, the stoichiometric scalar dissipation rate is relaxed as the molecular mixing overcomes the turbulent stretching, as seen in Fig.(3.4), corresponds to the increase of $\langle Y_{P_{st}} \rangle$ as exhibited in Fig.(3.5). This implies that the reignition prevails during the later simulation time.

3.4.6 Simulated Cases

A series of simulated cases with increasing Reynolds number are created through decreasing the kinematic viscosity ν by a factor of 1/2, but all at $Sc = 0.7$. Therefore, the diffusion coefficient $D = \nu/Sc$ also decreases proportionally. The initial conditions of both the large

Simulations	N^3	ν	η_k	λ	l	$u^{'}$	ε
$R2$	256^3	$1.000E{-}02$	$3.242E{-}02$	$3.634E{-}01$	$8.825E{-}01$	$8.927E{-}01$	$9.054E{-}01$
$R3$	256^3	$5.000E{-}03$	$1.999E{-}02$	$2.765E{-}01$	$8.823E{-}01$	$8.928E{-}01$	$7.822E{-}01$
$R4$	512^3	$2.500E{-}03$	$1.224E{-}02$	$2.073E{-}01$	$8.828E{-}01$	$8.930E{-}01$	$6.958E{-}01$
$R5$	512^3	$1.250E{-}03$	$7.311E{-}03$	$1.497E{-}01$	$8.936E{-}01$	$9.039E{-}01$	$6.837E{-}01$
$R6$	1024^3	$6.250E{-}04$	$4.215E{-}03$	$9.839E{-}02$	$8.836E{-}01$	$8.938E{-}01$	$7.738E{-}01$
$R7$	1024^3	$3.125E{-}04$	$2.536E{-}03$	$7.112E{-}02$	$8.824E{-}01$	$8.925E{-}01$	$7.381E{-}01$

Table 3.1: Parameters of the velocity field at initial time.

Simulations	$u^{'}/l$	l/η_k	Re_λ	Re_l	$k_{max}\eta_k$
$R2$	1.0115	$2.722E{+}01$	$3.244E{+}01$	$7.879E{+}01$	3.890
$R3$	1.0120	$4.413E{+}01$	$4.937E{+}01$	$1.575E{+}02$	2.399
$R4$	1.0116	$7.211E{+}01$	$7.405E{+}01$	$3.153E{+}02$	2.938
$R5$	1.0115	$1.222E{+}02$	$1.082E{+}02$	$6.462E{+}02$	1.755
$R6$	1.0116	$2.096E{+}02$	$1.407E{+}02$	$1.264E{+}03$	2.023
$R7$	1.0114	$3.480E{+}02$	$2.031E{+}02$	$2.520E{+}03$	1.217

Table 3.2: Parameters of the velocity field at initial time.

scale of velocity l and the r.m.s. velocity $u^{'}$ are almost identical across the various cases. The related parameters of the initial velocity fields are listed in Table.(3.1) and (3.2). The chemical parameters are the same for different simulated cases, which are given in Table (3.3).

The code developed for higher Reynolds number cases is based on a parallel algorithm that invokes the Message Passing Interface(MPI) on the Fortran90 interface. The initialization and the DNS for case R4,R5 and R6,R7 are implemented on 32 and 128 processors on the IBM P690+/P655+ named ″Iceberg″ at the Arctic Region Supercomputing Center(ARSC), respectively.

r	A_f	α	β	K
1	$8.0E{+}04$	0.87	4	100

Table 3.3: Chemical parameters of the reactive field.

3.5 Flame Surface Area: Numerical Measurement

3.5.1 Isosurface Rendering

The flame surface is identified by the isosurface of the stoichiometric mixture fraction corresponding to $Z = Z_{st}$. The rendering of this isosurface plays a crucial role in determining the isosurface area, and in visualizing and understanding the structure of the volumetric scalar field. In recent decades, many efficient algorithms of isosurface extraction have been developed, such as marching cubes[38] and span space[77]. Essentially, the isosurface extraction algorithm is composed of two stages. For an elemental cube, the two stages are described in below.

For stage 1, each vertex of the cube is assigned an index that is one of two states of classification as either being smaller than($<$), or larger than or equal to($\geq$) the isovalue.

$$\text{if } Z < Z_{iso} \quad : \quad \text{vertex state index=0} \tag{3.28}$$

$$\text{if } Z \geq Z_{iso} \quad : \quad \text{vertex state index=1} \tag{3.29}$$

For stage 2, comparing the states of the pairs of vertices on each cube edge can tell which edges are cut across by the isosurface. The specified intersection points on cube edges serving as vertices can create one or more triangular meshes that form the isosurface segments cutting through the cube. There are 8 vertices in a cube and each has 2 possible states, therefore there are $2^8 = 256$ possible cases that an isosurface can intersect the cube. Two of these are trivial, where all the of 8 vertices have the same states. This implies that the cube does not intersect with isosurface. After listing the 8 vertices of the cube in counterclockwise order, by enumerating all possible permutations of the states of 8 vertices and considering the symmetries(complementarities and rotations) of the cube, the 254 possible

intersections are reduced to 14 unique patterns, which are listed in a look-up table for future calculations. The location of the intersection point along the edge (i.e., the vertices of the triangular meshes) can be determined by linear interpolation of the scalar values at the two vertices forming the edge.

The above described 2-stage algorithm can process one elemental cube at a time. So it is repeatedly implemented on each cube over the entire volume.

Under the consideration of the degree of adaptivity in terms of the rendering time and the practicality, the Matlab built-in function *isosurface* is utilized to extract the isosurface from the volumetric conserved scalar data Z at a specified isovalue [41].

3.5.2 Numerical Calculation of Isosurface Area

The numerical method employed to calculate the isosurface area using the outputs from the isosurface rendering algorithm is presented here.

The Matlab *isosurface* extraction scheme triangulates the isosurface into triangular meshes as shown in Fig.(3.6) using a spherical surface triangulation. The triangulation algorithm produces a set of triangular faces made up by connecting each of the spaced data points (i.e., vertices of the triangles) that are generated by interpolation. Accordingly, it exports this geometric information in the form of an $H \times 3$ matrix of faces and an $M \times 3$ matrix of vertices, where H and M are the number of faces and vertices, respectively. The vertex matrix specifies the 3D Cartesian coordinates of M vertices, and the face matrix designates the indices of three vertices defining each of H triangular faces. Each row of face matrix represents a triangular mesh defined by indices into the M-by-3 matrix of 3D vertex coordinates. Subsequently the area of each triangular mesh can be calculated by using Heron's formula in terms of the lengths of its three sides, which are computed from the coordinates of the three vertices. Accordingly, the total area of the flame surface is the sum of the areas of all triangle meshes in the stoichiometric isosurface, and the result is given in the units of the input data. This is regarded here as the 'exact solution'. The detailed numerical procedure for determining the isosurface area by using the Matlab *isosurface* output information is illustrated in Appendix A.

The accuracy of this numerical algorithm must be assessed before attempting an application to a turbulent diffusion flame. The relative error between the numerical and analytical surface area is plotted in Fig.(3.7) for spherical surfaces of different radii (top panel) and prolate spheroid surfaces of different semi-major diameters(bottom panel), respectively. The cubical domain employed in this test, with a sphere or a spheroid inscribed within it, is set to have a side length of 2π, which is the same as our computational domain for a convenient comparison thereby the inscribed sphere and prolate are scaled to the same units. As shown in the figure, the relative error between the numerical and the analytical results is less than 3% and decreases with the decrease of surface curvature(or, equivalently, the surface area). This indicates that the numerical algorithm adopted in the current research for predicting the isosurface area can achieve good accuracy, and the accuracy of this scheme is improved with a decrease in surface curvature.

Accordingly, in Fig.(3.8), the average of the squared curvature of the spherical surfaces and the prolate spheroid surfaces are plotted in the same manner as in Fig.(3.7). Also, the time evolution of the average of the squared curvature of the flame surface formed in the diffusion flame of interest is plotted in Fig.(3.9). The surface curvature is defined in Section 4.8 as $\nabla \cdot \vec{n}$ where $\nabla \cdot$ is the surface divergence and $\vec{n}$ is the normal vector pointing outward. A comparison of Fig.(3.8) with Fig.(3.7), illustrates that a decrease in curvature corresponds to a decrease in numerical error. This allows us to estimate the numerical error based on curvature. So, in order to estimate the possible accuracy in the numerical determination of flame surface area, it is instructive to compare the curvature of flame surface (i.e., around 75 as shown in Fig.(3.9)) with the one from the spherical surface(Fig.(3.8)), in conjunction with Fig.(3.7). The comparison reveals that the possible relative error is around 0.7%.

3.6 Flamelet Modeling of Nonpremixed Combustion

3.6.1 Unsteady flamelet equation

The turbulent nonpremixed flame can be viewed as an ensemble of discrete small flames, i.e., laminar diffusion flamelets, that are distinguished by the degree to which they are locally strained by the turbulent flow. Each flamelet is time dependent and locally approximately

one-dimensional. The structure of a one-dimensional flamelet originates at the flame surface, i.e., the isosurface of stoichiometric mixture fraction Z_{st}, and varies in the direction normal to it.

The corresponding time-dependent one-dimensional flamelet equation (for simplicity hereafter referred to as "flamelet equation") can be derived by systematically applying a Crocco-type coordinate transformation to the governing equation of mass fraction that transforms the equation from temporal-spatial space to temporal-mixture fraction space[49][43]. The derivation proceeds in three steps.

First, a new coordinate system is introduced via the coordinate transformation of the Crocco-type. As shown in Fig.(3.10), the coordinate system is locally oriented so that the original three-dimensional orthogonal coordinates (x_1, x_2, x_3) for the flamelet originate at point O on the surface of stoichiometric mixture, the direction x_1 and x_2 lie within the surface $Z = Z_{st}$, and x_3 is in the direction normal to the surface. The new three-dimensional orthogonal coordinates are denoted by (Z_1, Z_2, Z) in which Z_1 and Z_2 are respectively equal to x_1 and x_2, but x_3 is replaced by the mixture fraction Z that is in the direction locally normal to the surface of the stoichiometric mixture. This implies that the new coordinate is locally attached to a point on the surface of stoichiometric mixture. Note that here the mixture fraction Z is introduced as a new independent variable.

Next, the coordinate transformation of the Crocco-type is performed so that the governing equation for mass fraction Y_i is transformed from the old coordinates (t, x_1, x_2, x_3) to the new coordinates (τ, Z_1, Z_2, Z) by adopting the following transformation techniques. The Crocco-type coordinate transformation defines

$$(t, x_1, x_2, x_3) \quad \rightarrow \quad (\tau, Z_1, Z_2, Z(x_1, x_2, x_3, t)), \tag{3.30}$$

where $\tau = t$, $Z_1 = x_1$ and $Z_2 = x_2$. Accordingly, due to the transformation rules, the first and the second derivatives in old coordinate can be expressed in terms of the new coordinate by using the chain rule, as

$$\begin{aligned} \frac{\partial}{\partial t} &= \frac{\partial}{\partial \tau} + \frac{\partial}{\partial Z}\frac{\partial Z}{\partial t} \\ \frac{\partial}{\partial x_i} &= \frac{\partial}{\partial Z_i} + \frac{\partial}{\partial Z}\frac{\partial Z}{\partial x_i}, \quad (i = 1, 2) \end{aligned}$$

$$\frac{\partial}{\partial x_3} = \frac{\partial}{\partial Z}\frac{\partial Z}{\partial x_3} \tag{3.31}$$

$$\begin{aligned}
\frac{\partial^2}{\partial {x_i}^2} &= \frac{\partial^2}{\partial {Z_i}^2} + 2\frac{\partial^2}{\partial Z \partial Z_i}\frac{\partial Z}{\partial x_i} + \frac{\partial^2}{\partial Z^2}(\frac{\partial Z}{\partial x_i})^2 + \frac{\partial}{\partial Z}\frac{\partial^2 Z}{\partial {x_i}^2}, \quad (i = 1, 2) \\
\frac{\partial^2}{\partial {x_3}^2} &= \frac{\partial^2}{\partial Z^2}(\frac{\partial Z}{\partial x_3})^2 + \frac{\partial}{\partial Z}\frac{\partial^2 Z}{\partial {x_3}^2}
\end{aligned} \tag{3.32}$$

Inserting the above transformation relations Eq.(3.31) and Eq.(3.32) into the balance equation for the mass fraction $Y_i(t, x_1, x_2, x_3)$, Eq.(3.9), and then simplifying it through the elimination of all terms containing $\partial Y_i/\partial Z$ because of the conservation equation for mixture fraction, Eq.(3.8), yields the governing equation for $Y_i(\tau, Z_1, Z_2, Z)$ as

$$\frac{\partial Y_i}{\partial \tau} = \underbrace{\frac{\chi}{2}\frac{\partial^2 Y_i}{\partial Z^2}}_{I} - \underbrace{(u_1\frac{\partial Y_i}{\partial Z_1} + u_2\frac{\partial Y_i}{\partial Z_2})}_{II} + \underbrace{D(\frac{\partial^2 Y_i}{\partial {Z_1}^2} + \frac{\partial^2 Y_i}{\partial {Z_2}^2})}_{III} + \underbrace{2D(\frac{\partial^2 Y_i}{\partial Z \partial Z_1}\frac{\partial Z}{\partial x_1} + \frac{\partial^2 Y_i}{\partial Z \partial Z_2}\frac{\partial Z}{\partial x_2})}_{IV} + \underbrace{\omega}_{V}, \tag{3.33}$$

where $\chi = 2D|\nabla Z|^2$ denotes the instantaneous scalar dissipation rate. It should be noted that the rate of change of a quantity with respect to the old coordinate, $\partial/\partial t$, differs from the one with respect to the new coordinate, $\partial/\partial \tau$. In the original governing Eq.(3.9), $\partial/\partial t$ is evaluated from the observer fixed at a point in space (x_1, x_2, x_3), but in the transformed governing Eq.(3.33), $\partial/\partial \tau$ is evaluated from the comoving observer fixed on the isosurface of the mixture fraction.

Finally, the transformed balance Eq.(3.33) is further simplified under the assumption that the gradients of the mixture fraction across the stoichiometric surface are large relative to those parallel to the surface. The simplification is performed by neglecting the transport terms in tangential directions (i.e., derivatives with respect to Z_1 and Z_2) since they are much smaller when compared to the terms in the direction normal to the flame surface (i.e., derivatives with respect to Z).

$$\frac{\partial}{\partial Z_1}, \frac{\partial}{\partial Z_2} \ll \frac{\partial}{\partial Z}; \quad \frac{\partial^2}{\partial {Z_1}^2}, \frac{\partial^2}{\partial {Z_2}^2}, \frac{\partial^2}{\partial Z \partial Z_1}, \frac{\partial^2}{\partial Z \partial Z_2} \ll \frac{\partial^2}{\partial Z^2} \tag{3.34}$$

As a result of the above assumptions, terms II, III and IV on the RHS of Eq.(3.33), which respectively represent the lateral convection, lateral diffusion and curvature, are neglected. Under these simplifications, the transformed balance equation for mass fraction

$Y_i(\tau, Z_1, Z_2, Z)$ is simplified to a time-dependent one-dimensional equation with time t and mixture fraction Z as the only independent variables, which is the so-called flamelet equation. Note that, for clarification purposes, the notation used to denote a flamelet variable is distinguished from the one in DNS by adding a subscript 'fl'.

$$\frac{\partial Y_{i,fl}}{\partial t} = \frac{\chi}{2}\frac{\partial^2 Y_{i,fl}}{\partial Z^2} + \omega(Z, Y_{i,fl}). \tag{3.35}$$

The scalar dissipation rate χ in front of the diffusion term can be modeled by assuming a counterflow-like geometry[2][43].

$$\chi = \frac{a_s}{\pi} F(Z) \tag{3.36}$$

$$F(Z) = exp\{-2[erf^{-1}(2Z-1)^2]\} \tag{3.37}$$

Here $erf^{-1}(\cdot)$ is the inverse error function, and a_s is the flamelet strain rate (velocity gradient at the stagnation point) and serve as a shape factor to control the mixture fraction profile along the axis of flamelet. It can be related to the scalar dissipation rate at stoichiometric mixture by applying Eq.(3.36) to stoichiometric condition $Z = Z_{st}$.

$$\chi_{st} = \frac{a_s}{\pi} F(Z_{st}) \tag{3.38}$$

And hence, Eq.(3.36) can be rewritten in terms of χ_{st} as

$$\chi(Z,t) = \chi_{st}(t)\frac{F(Z)}{F(Z_{st})} \tag{3.39}$$

Then the flamelet Eq.(3.35) can be recast as

$$\frac{\partial Y_{i,fl}}{\partial t} = \frac{1}{2}\chi_{st}(t)\frac{F(Z)}{F(Z_{st})}\frac{\partial^2 Y_{i,fl}}{\partial Z^2} + \omega(Z, Y_{i,fl}), \tag{3.40}$$

where $\chi_{st}(t)$ represents the local instantaneous scalar dissipation rate at the stoichiometric mixture and acts as an external stoichiometric parameter dominating the flamelet structure. The reaction mechanism used here in the flamelet model is a one-step, irreversible, Arrhenius-type reaction, which is the same reaction scheme as employed in the DNS.

In summary, the flamelet equation describes the interaction between diffusion influenced by the turbulent flow and the chemical reaction. The local flamelet structure is characterized by the local instantaneous scalar dissipation rate at stoichiometric mixture, χ_{st}, which

represents the degree of local stretching and quantifies the non equilibrium effects. Once the parameter χ_{st} is specified, the local flamelet structure can be determined in mixture fraction space Z. Thus, the flamelet model defines the species mass fraction can or temperature as a function of Z and time t.

$$Y_{i,fl} = Y_{i,fl}(Z,t) \tag{3.41}$$

The boundary conditions at $Z = 0, 1$ and the initial condition are defined by equilibrium states as:

$$B.C.: \quad Y_{i,fl}(Z=0,t) = Y_{i,eq}(Z=0); \qquad Y_{i,fl}(Z=1,t) = Y_{i,eq}(Z=1) \tag{3.42}$$

$$I.C.: \quad Y_{i,fl}(Z,t=0) = Y_{i,eq}(Z) \tag{3.43}$$

3.6.2 Steady Laminar Flamelet Library

The governing equation of the steady flamelet model (SFL) can be obtained directly by omitting the time derivative term on the LHS of Eq.(3.40)[43](the subscript ″sfl″ refers to the steady flamelet).

$$\frac{1}{2}\chi_{st}(t)\frac{F(Z)}{F(Z_{st})}\frac{\partial^2 Y_{i,sfl}}{\partial Z^2} + \omega(Z, Y_{i,sfl}) = 0 \tag{3.44}$$

As introduced in above section, the χ_{st} serves as an external control parameter identifying the influence of turbulent flow on flamelet structure. Once χ_{st} is specified, the steady flamelet structure can be completely solved in mixture fraction Z space. The χ_{st} has dimension of inverse time and can be interpreted as the inverse of a characteristic diffusion time scale. In the limit $\chi_{st} \to 0$, the corresponding solution approaches equilibrium. With the increase of χ_{st} caused by the turbulent stretching, the non-equilibrium effects increase. When χ_{st} exceeds the critical value χ_q, the diffusion flamelet is extinguished from the perspective of SFL model. The steadily burning solutions do not exist when χ_{st} is beyond this quenching value χ_q. It follows that a series of discrete values of χ_{st} ranging from 0 to χ_q are employed to make a family of steady flamelet solutions from equilibrium to extinction which are tabulated into the SFL library. The functional dependence of the steady flamelet solution on mixture fraction Z parameterized by χ_{st} is given in the form

$$Y_{i,sfl} = Y_{i,sfl}(Z;\chi_{st}). \tag{3.45}$$

The steady flamelet solutions are obtained as the long-time asymptotic stationary solutions to the unsteady flamelet balance Eq.(3.40). The detailed numerical schemes are illustrated as follows:

(1) The common approach for solving the steady equation is to solve the corresponding unsteady equation until the time-asymptotic solution converges to a stationary solution, rather than directly solve the steady equation.

(2) The unsteady flamelet Eq.(3.40) is solved by the fractional-step method. The diffusion term is updated using the Crank-Nicolson technique, while the reaction term is advanced using the 2nd order Adam-Bashforth method. The mixture fraction space is discretized into 300 uniform bins and a total of 31 steady flamelets are calculated with χ_{st} varying from a very small value 0.0001 to quenching value χ_q in uniform intervals.

(3) The initial and the boundary conditions used in solving the unsteady flamelet equation are defined in Eq.(3.43).

The above-described numerical algorithm can be exemplified by a single case of a particular value of χ_{st} in the range $0 \simeq \chi_q$, say 0.986. The chemical parameters used in this example are the ones of case R2. The time history of corresponding temperature-profile evolution, $Y_{P,fl} = Y_{P,fl}(t, Z; \chi_{st} = 0.986)$, at the same time steps from initial equilibrium state to asymptotic steady state is depicted in Fig.(3.11). As shown in the figure, the temperature profile converges towards a unique state that is considered as the steady-state solution.

A tabulated set of SFL temperature profiles is shown schematically in Fig.(3.12), where $Y_{P,sfl}(Z; \chi_{st})$ is plotted for a series values of χ_{st} varying from 0.0001 to $\chi_q = 1.02$. Also plotted in dashed line is the equilibrium chemistry which is the limit case when χ_{st} approaches 0. It can be seen that the steady state profiles monotonically decrease with increasing strain rate (decreasing the Damköhler number).

3.6.3 S-curve

The solutions of the flamelet model can be diagrammed as an S-curve, which is shown in Fig.(2.1). The S-curve is formed by plotting the maximum temperature (i.e., temperature

at stoichiometric mixture) as a function of χ_{st}. The upper and the lower branches are respectively the stable burning and non-burning branches corresponding to the solutions of the steady flamelet equation, while the middle branch is unstable. The turning point between the upper and middle branches corresponds to the critical quenching value χ_q. This S-curve will be used as a reference point for the investigation of the applicability of steady flamelet model in chapter 5.

3.6.4 Steady flamelet model applied in turbulent nonpremixed combustion

The S-curve demonstrates that there are multiple states corresponding to a certain χ_{st} value; therefore the one-parameter χ_{st} is not sufficient to uniquely determine a state. In the application of the steady flamelet model, only the stable burning and non-burning states are considered according to the value of χ_{st}. To be specific, the stable burning and non-burning states are uniquely identified while $\chi_{st} \leq \chi_q$ and $\chi_{st} > \chi_q$, respectively. This guarantees the uniqueness, i.e., a unique flamelet state for a unique value of χ_{st}.

3.6.5 Choice of χ_q

As mentioned above, the behavior of extinction and reignition is characterized in conjunction with the quenching limit value χ_q, which depends on the chemical reaction mechanism. The choice of χ_q is based on the consequences of generating adequate amount of extinction. The appropriate value for the critical quenching value χ_q is selected such that extinction is exclusively induced by the local fluctuations of χ_{st}. This implies that the level of χ_q needs to be larger than $\langle\chi_{st}\rangle$ and much smaller than the fluctuations, as shown in Fig.(3.3) and Fig.(3.4).

In order to generate adequate values for χ_q, it is instructive to numerically investigate the dependence of χ_q on the chemical parameters A_f and β, which is performed using the burning solution of the steady flamelet model. The functional dependence of χ_q on A_f and β is illustrated in Fig.(3.13). For $\beta = 4$, the preexponential factor A_f is chosen to be $8.0E{+}04$ in order to make the critical quenching value $\mathcal{O}(1)$.

3.6.6 Numerically validate the flamelet assumption

The scale separation assumption for flamelet model presented in Section2.2.3 will be numerically evaluated in this section. As we know, turbulent nonpremixed combustion involves a wide range of length scales. The chemical reaction is most intense mainly within a thin layer in the vicinity of the flame surface which is called the reaction zone, and the behavior of the diffusion flame is determined primarily by the chemistry occurring within this reaction zone. If this reaction zone is smaller than the smallest turbulent length scale, namely Kolmogorov length scale η_k, then the turbulent eddies can only impact the flame at larger scales but could not penetrate into the flamelet structure to distort and break up the flame. So, the reaction zone of the flame can remain intact and the flame can be considered as being sustained within a local laminar flow field [49]. Here an assessment of this assumption is numerically explored by means of scales comparison which is conducted for case R2. Next, the method used to quantify the length scale of the reaction zone in a diffusion flame will be explained. Finally, the comparison between the obtained chemical length scale and the smallest turbulent length scale will be examined to evaluate the flamelet assumption.

The length scales relevant to the chemical reaction in a diffusion flame can be derived to advantage by the use of steady laminar diffusion flamelet structure. The reaction zone locates in the vicinity of the flame surface, and the flamelet is a locally one-dimensional structure embedded on the flame surface. Thereby the flamelet structure in conjunction with the geometric information as a result of the flame surface triangulation leads to the approximation of the reaction zone thickness. The detailed description of a numerical algorithm to compute the approximate reaction zone thickness l_r is given by the following steps:
(1) The stoichiometric isosurface is extracted from the volumetric data of the mixture fraction field by triangulation along with exporting the vertex 3D coordinates, the same strategy as previously introduced in Section3.5.
(2) For one particular triangular mesh on the surface, say the ii-th (ii=$1, 2, ..., H$) mesh, the scalar dissipation rate, χ, of the three vertices defining this mesh can be obtained by trilinear interpolation on the cubic 3D grid DNS results due to the vertex 3D coordinates. The vertices are distributed on the flame surface, therefore the quantities at the vertices are

considered naturally to be the ones at stoichiometry, χ_{st}. Then, the mean value theorem for the double integral of χ_{st} over this mesh is applied to yield a mean value serving as the representative to this triangular mesh, and thus, denoted as $\chi_{st_{ii}}$ (the subscript ii indicates that the quantity is associated with the ii-th triangular mesh on the surface)(Appendix B).
(3) The steady laminar flamelet structure attached to the ii-th triangular mesh is characterized by $\chi_{st_{ii}}$ associated with this mesh. The SFL temperature profile as a function of mixture fraction is established by interpolating the SFL library based on $\chi_{st_{ii}}$, and subsequently the reaction rate profile as a function of mixture fraction can be determined due to Arrhenius Eq.(3.24). Then, the mixture fraction space Z is converted into physical space x using the relation [67]

$$x = \sqrt{\frac{2D}{\pi \chi_{st_{ii}}}} erf^{-1}(1 - 2Z), \tag{3.46}$$

which is uniquely characterized by $\chi_{st_{ii}}$. The domain size length of 2π is used in this development. Thus the transformation maps a mixture fraction space function to a physical space function.
(4) As schematically represented in Fig.(3.14), the peak value of the reaction rate profile in physical space locates at the flame surface (i.e., $x = 0$ in physical space corresponding to $Z = Z_{st}$ in mixture fraction space), the reaction zone thickness l_r can be numerically estimated from a range where the reaction rates decrease to 50% of its peak value.
(5) Repeatedly performing above numerical scheme to each triangular mesh and area-weighted averaging the results over all meshes lead to the mean thickness of the reaction zone along the flame surface, $\langle l_r \rangle_s$.

Before entering into the analysis of the outcome of the length scales comparison aimed at testing the assumption of flamelet approach, there are two things worth noting here. First, the flamelet approach is based on an asymptotical concept, i.e., the asymptotic limit of fast chemistry and asymptotically thin reaction zone. The asymptotical concept is capable of predicting the basic behavior and tendencies rather than of resolving accurate quantities. Therefore, the length scales comparison on the basis of exact quantitative results may be misleading: flamelet behavior may well be exhibited when the assumption is not quite satisfied; but on the other hand, it may also break down even if the assumption is satisfied

but local conditions are unfavorable. Second, the scales in this context represent statistical average quantities, therefore the comparison using these scales can only provide an estimate that the flamelet assumption is probably valid[35]. The resulting surface averaged reactive length scale against the turbulent Kolmogorov scale for case R2 is demonstrated in Fig.(3.15). As seen in the figure, although the reaction zone thickness is larger than the Kolmogorov scale over the whole simulation time, they are approximately in the same order of magnitude. The flame thickness l_r is not necessarily smaller than the value of η_k. As demonstrated in the figure of the dissipation spectrum and cumulative dissipation given by Pope([59],pg.237), the pattern of the quantities shows that the dissipative scales responsible for most of the dissipation are considerably larger than the Kolmogorov scale. Even though the thickness l_r is larger than the scale η_k, the flamelet approach can capture important physical properties, such as the extinction, and may have good agreement with DNS results.

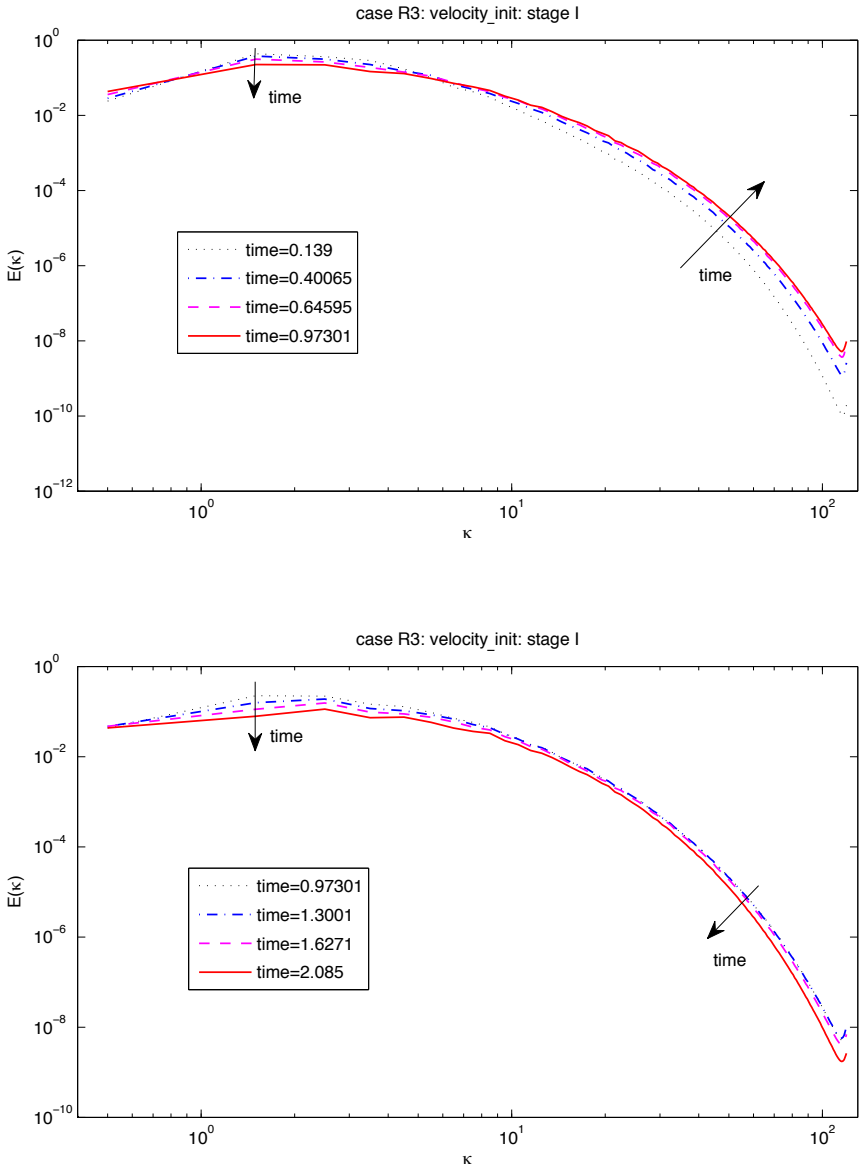

Figure 3.1: The time evolution of the energy spectra $E(\kappa)$(log-log scale) in velocity initialization stage I for case R3, initialized with the prescribed spectrum Eq.(3.21). Top panel: the energy spectra adjusts between $time = 0.14$ and $time = 0.97$. Bottom Panel: the full energy spectrum decay between $time = 0.97$ and $time = 2.09$.

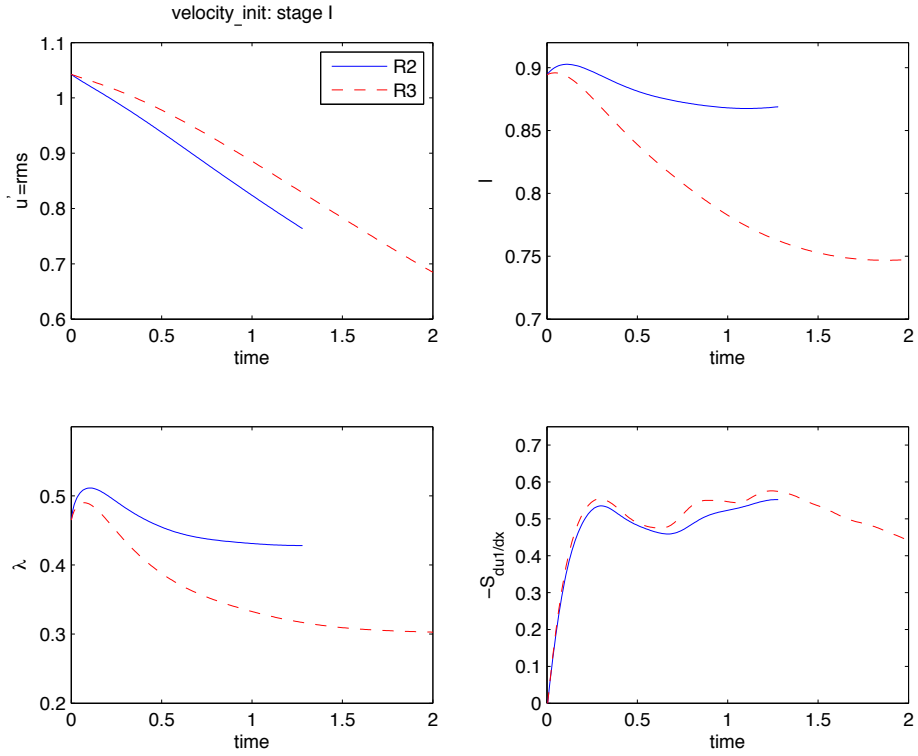

Figure 3.2: The time evolution of the rms velocity(left upper), integral length scale(right upper), Taylor length scale(left bottom) and skewness of velocity-derivative(right bottom) in velocity initialization stage I for case R2(solid) and R3(dashed), initialized with the prescribed spectrum Eq.(3.21). The simulations evolve until the specified termination conditions(i.e., a self-similar decay of fully-developed turbulence) are met.

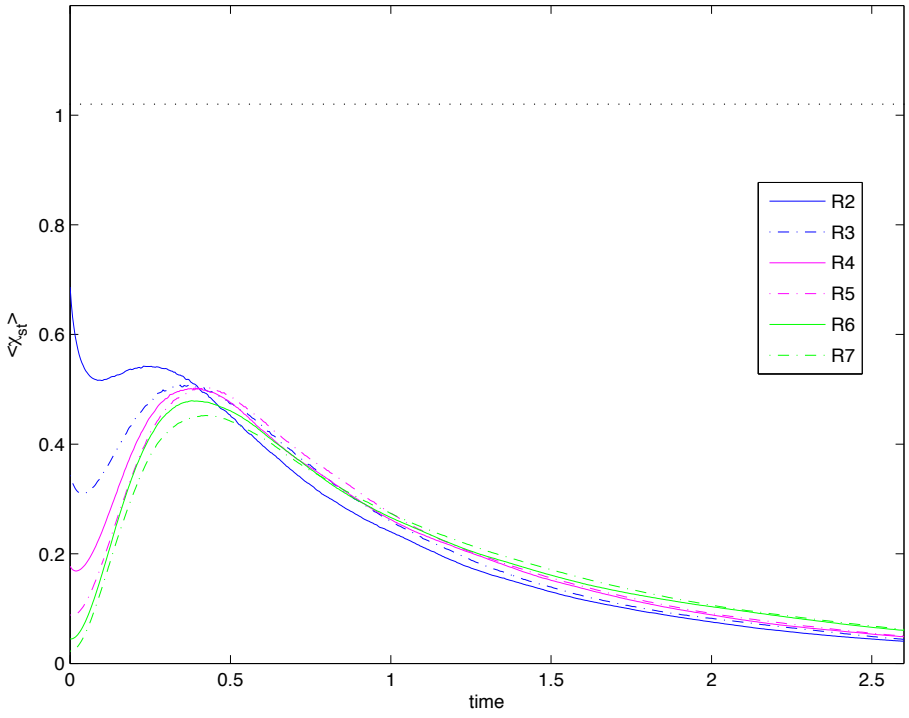

Figure 3.3: The time evolution of the average of scalar dissipation rate at $Z = Z_{st} = 0.5$ for the series of simulations R2-R7 with increasing Reynolds number. The horizontal dotted line corresponds to the quenching value $\chi_{st} = \chi_q = 1.02$.

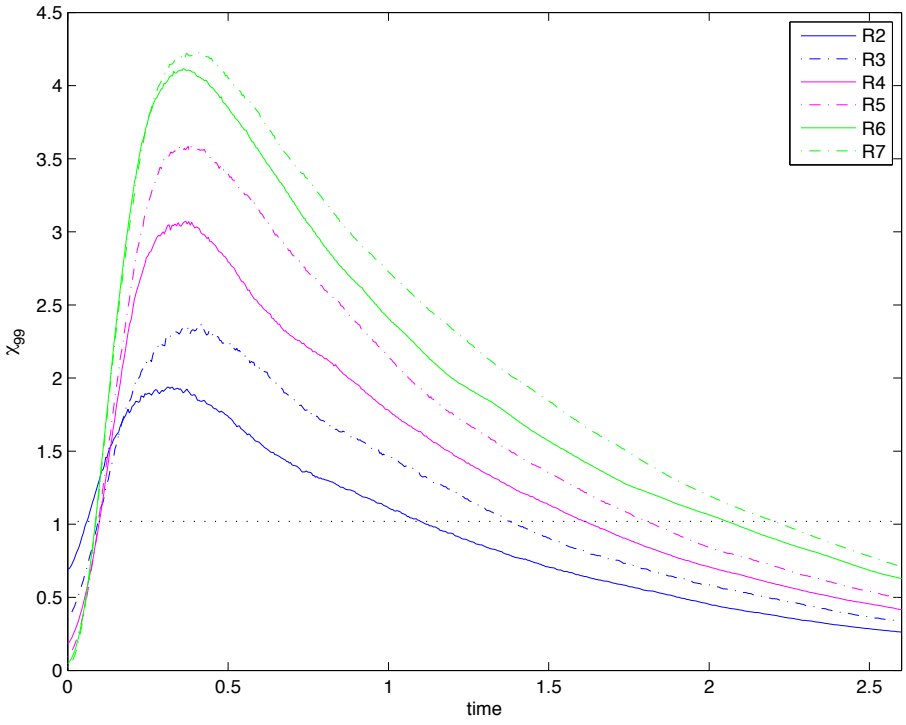

Figure 3.4: The time evolution of the envelope that contains 99% of the fluctuations of χ_{st} for the series of simulations R2-R7 with increasing Reynolds number. The horizontal dotted line corresponds to the quenching value $\chi_{st} = \chi_q = 1.02$.

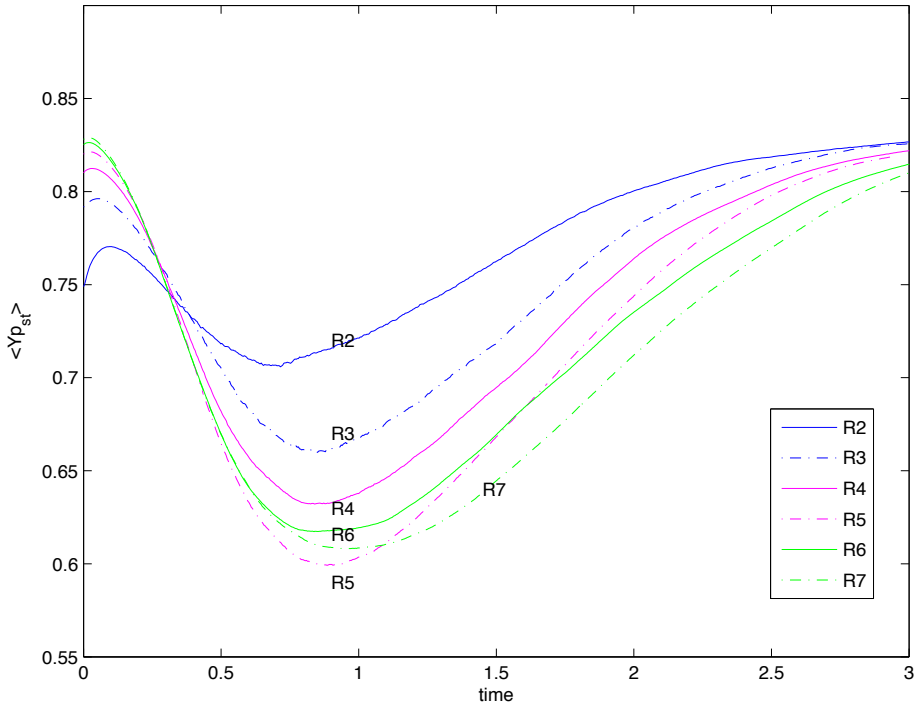

Figure 3.5: The time evolution of the conditional average of temperature on the stoichiometric mixture fraction for the series of simulations R2-R7 with increasing Reynolds number.

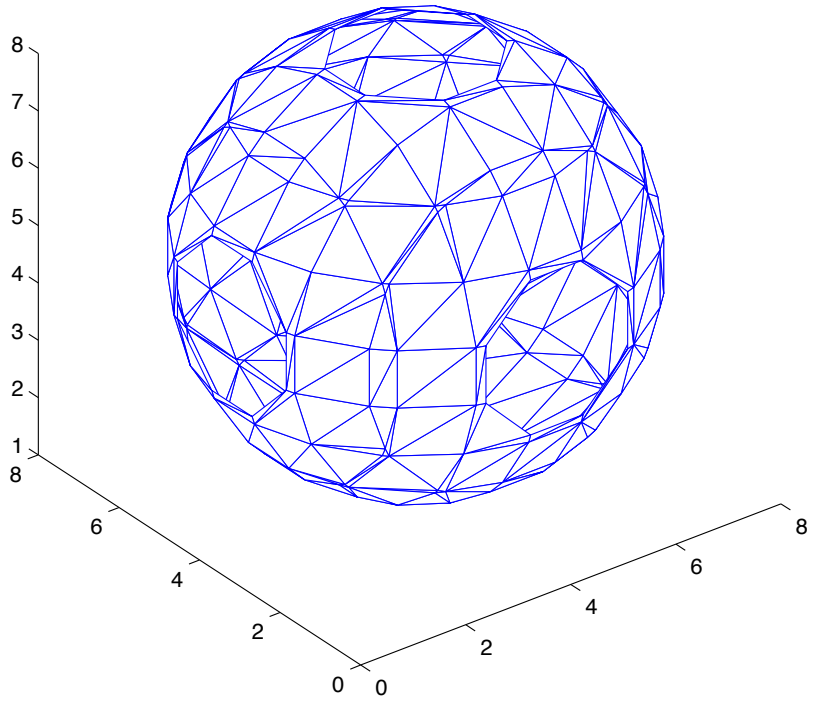

Figure 3.6: Surface triangulation of a sphere.

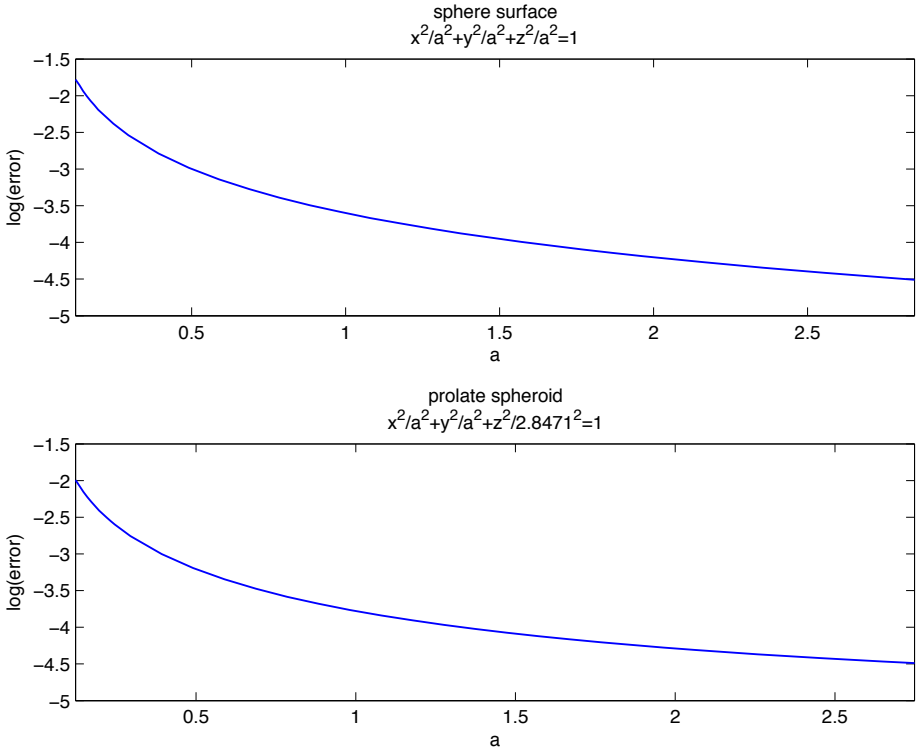

Figure 3.7: Relative error (in logged units) in the numerical determination of the surface area of sphere (top panel) and prolate spheroid (bottom panel) as a function of radius and equatorial radius, respectively. Both sphere and prolate spheroid are inscribed in a cubical domain with side length 2π which is the same as the computational domain employed in DNS.

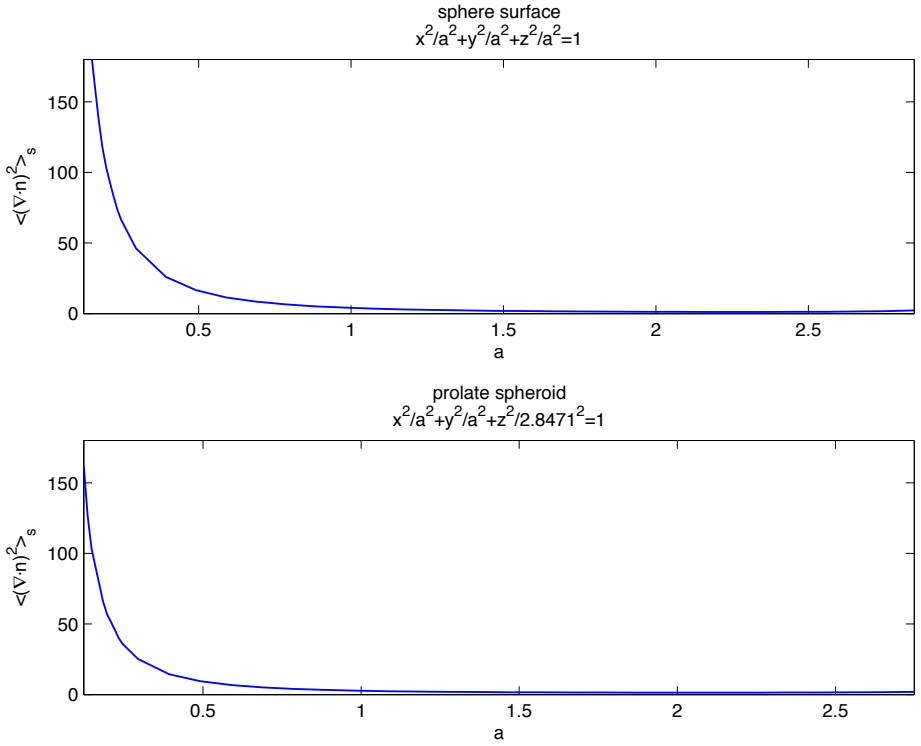

Figure 3.8: The mean surface curvature as a function of the radius of the spherical surface(top panel) and the equatorial radius of the prolate spheroid surface(bottom panel), respectively.

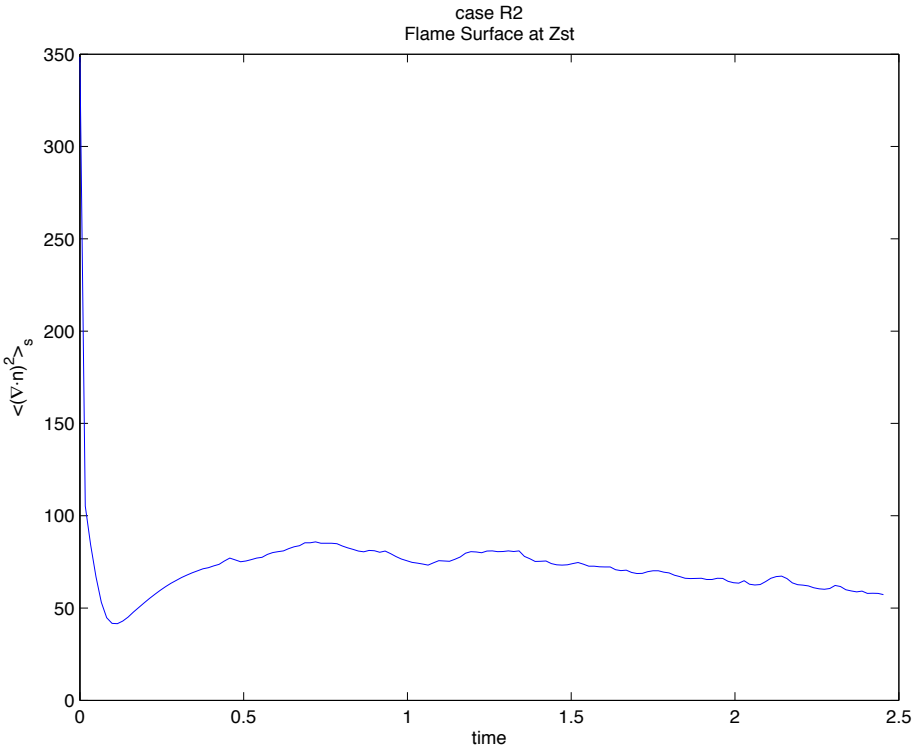

Figure 3.9: The time evolution of the average of squared curvature of the flame surface. The flame surface is generated by isosurface rendering from a volumetric DNS data resolved in a computational domain with side length 2π.

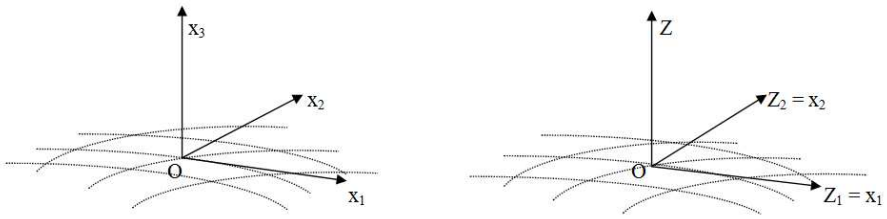

Figure 3.10: The local 3D coordinate system attached to a point O fixed on the surface of stoichiometric mixture fraction Z_{st}. Original(left) and new coordinate system(right).

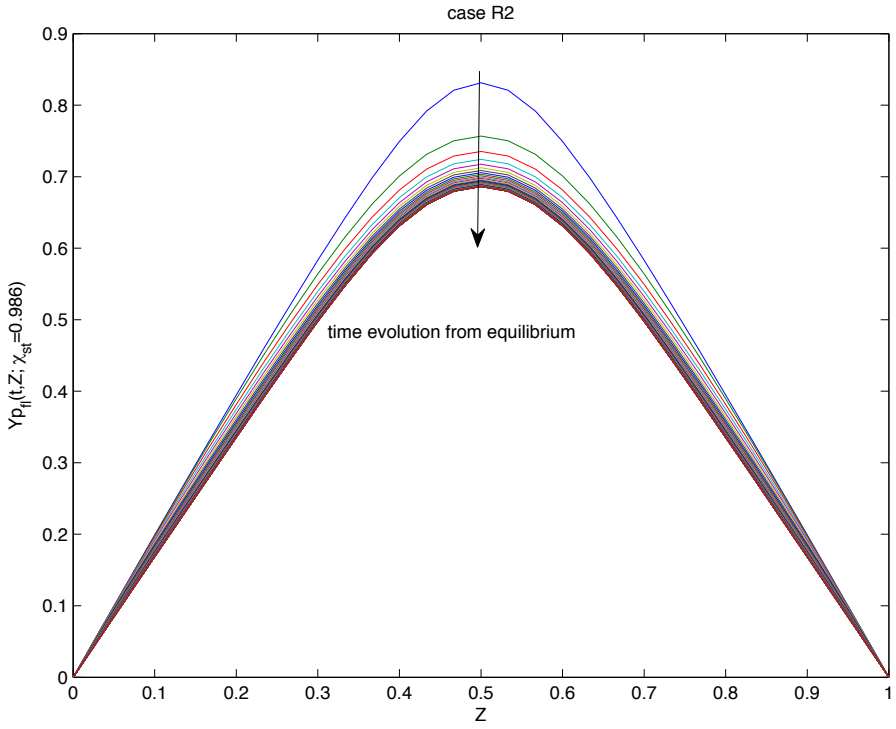

Figure 3.11: The time evolution of temperature profile in terms of mixture fraction Z for a particular value $\chi_{st} = 0.986$ at same time steps. The chemical parameters used in this example are the ones of case R2.

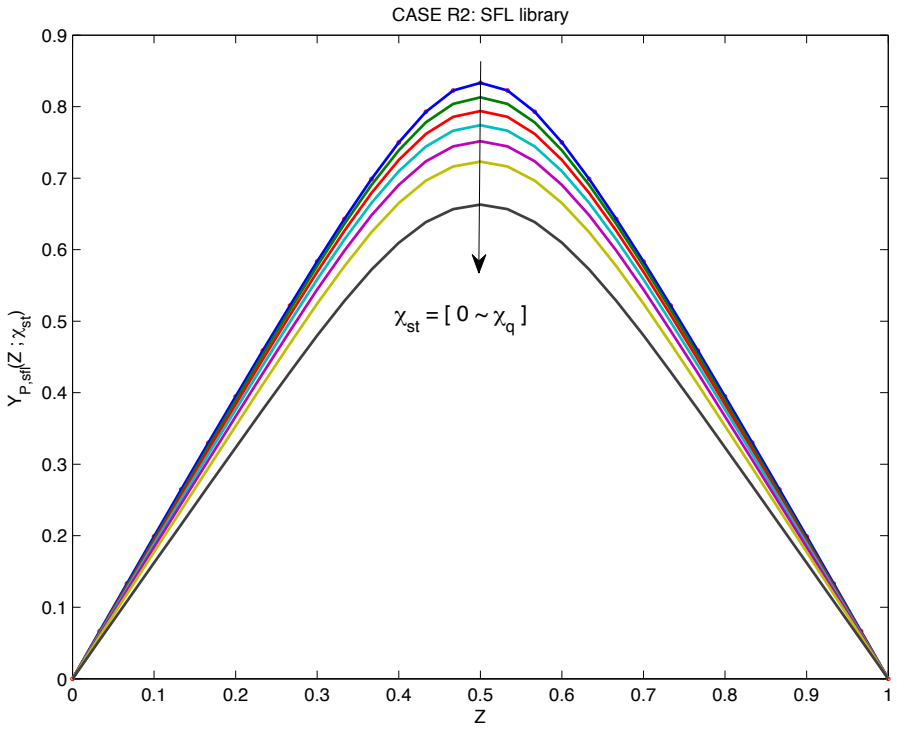

Figure 3.12: The steady-state temperature profiles from the SFL library as a function of Z and parameterized by a set of χ_{st} varying from $1.0E{-}04$ to quenching value 1.02 with uniform step size 0.17. The set of χ_{st} used here in the figure is a subset out of the entire family of χ_{st} in the SFL library for visualization purposes. The solid line with circles at the very top of the curves represents the equilibrium chemistry. Note that the temperature profile at the smallest $\chi_{st} = 1.0E{-}04$ and the equilibrium temperature profile almost lie over each other.

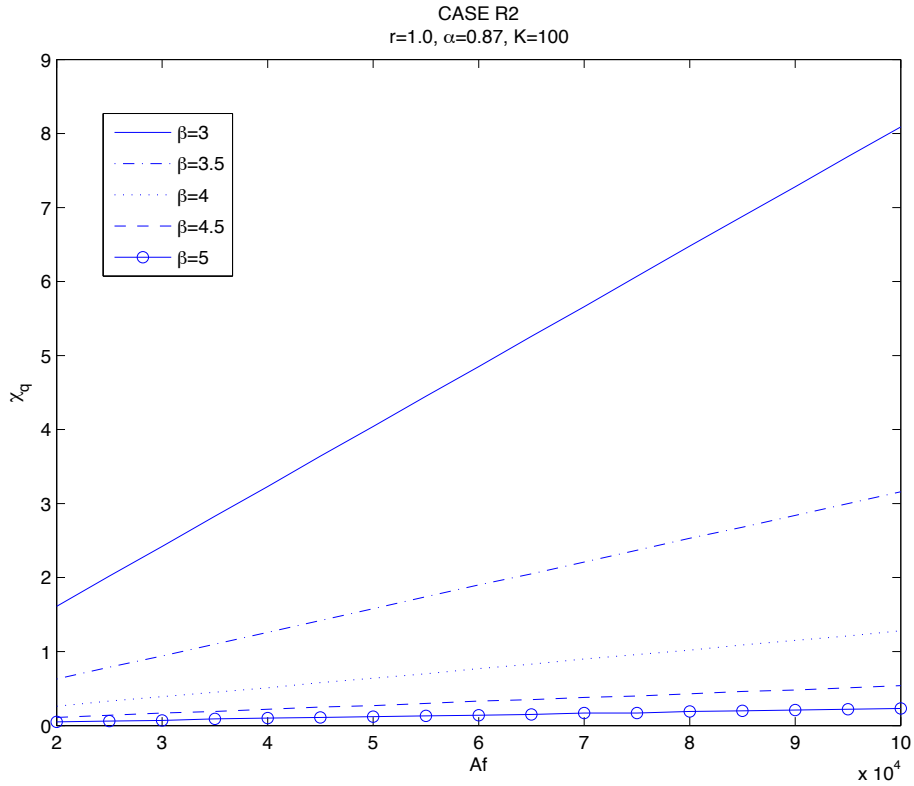

Figure 3.13: The quenching limit value χ_q is plotted as a function of A_f for various values of β.

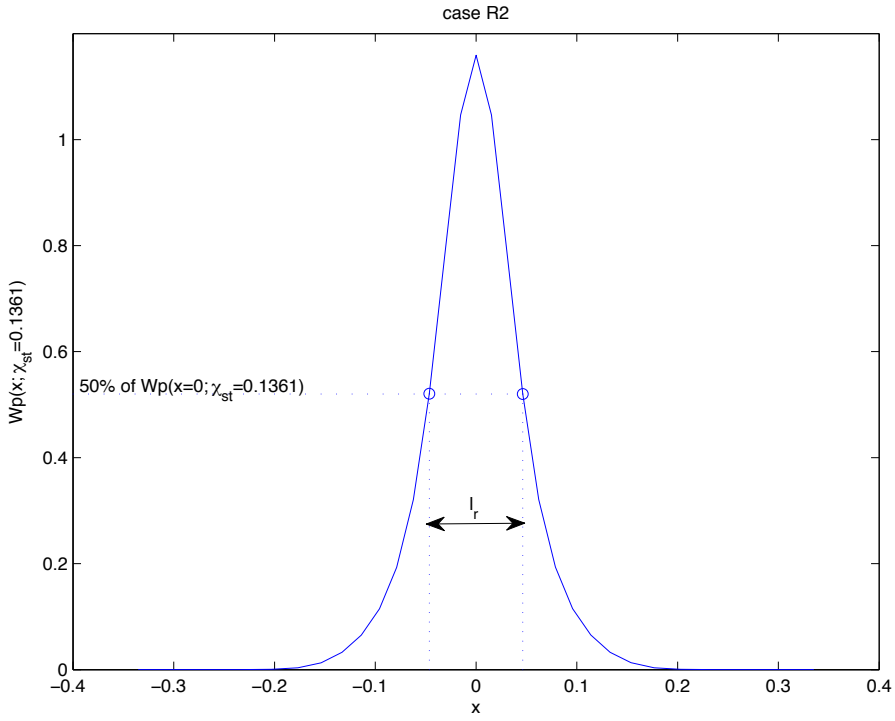

Figure 3.14: The reaction rate profile predicted using a steady flamelet library concept for χ_{st} taking(for example) 0.1361 is plotted as a function of physical space.

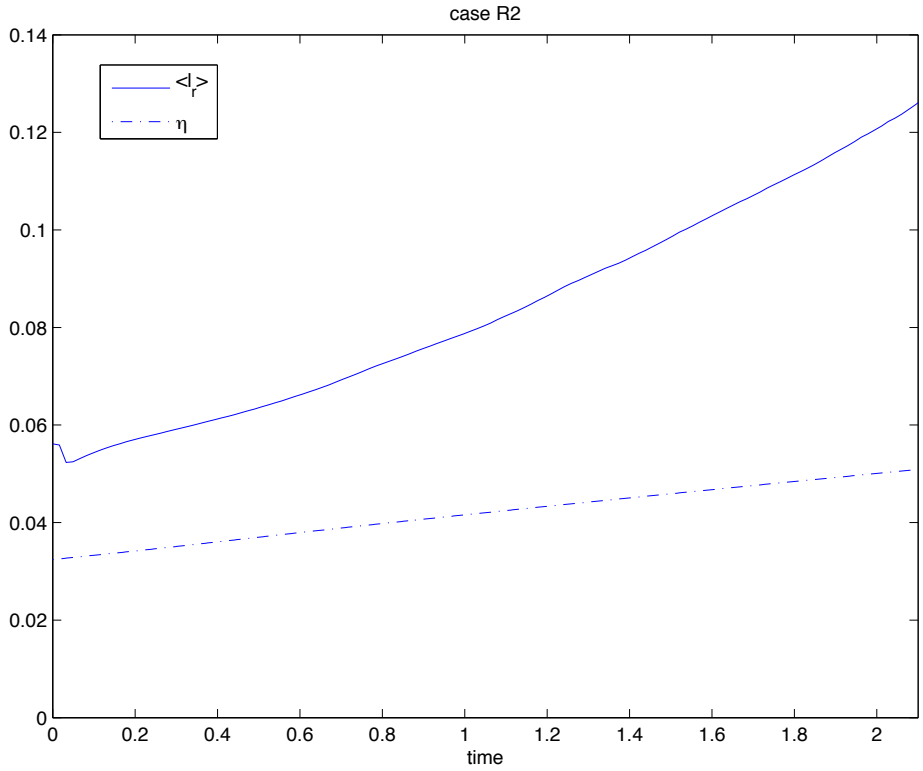

Figure 3.15: The time evolution of the flame surface averaged reaction zone thickness(solid) against the Kolmogorov scale(dash-dot) for case R2.

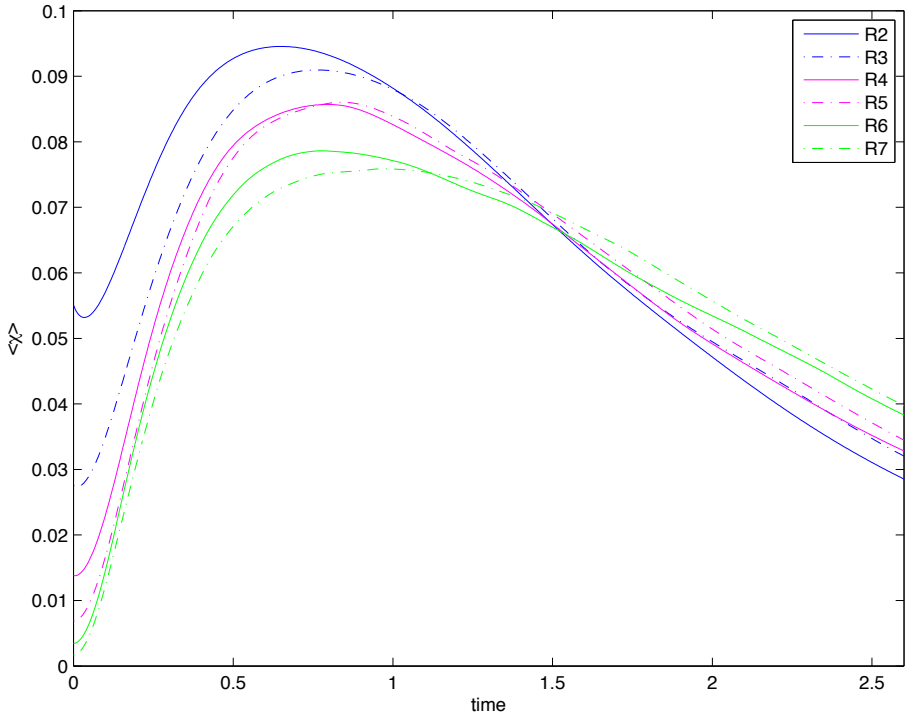

Figure 3.16: The time evolution of the average of scalar dissipation rate.

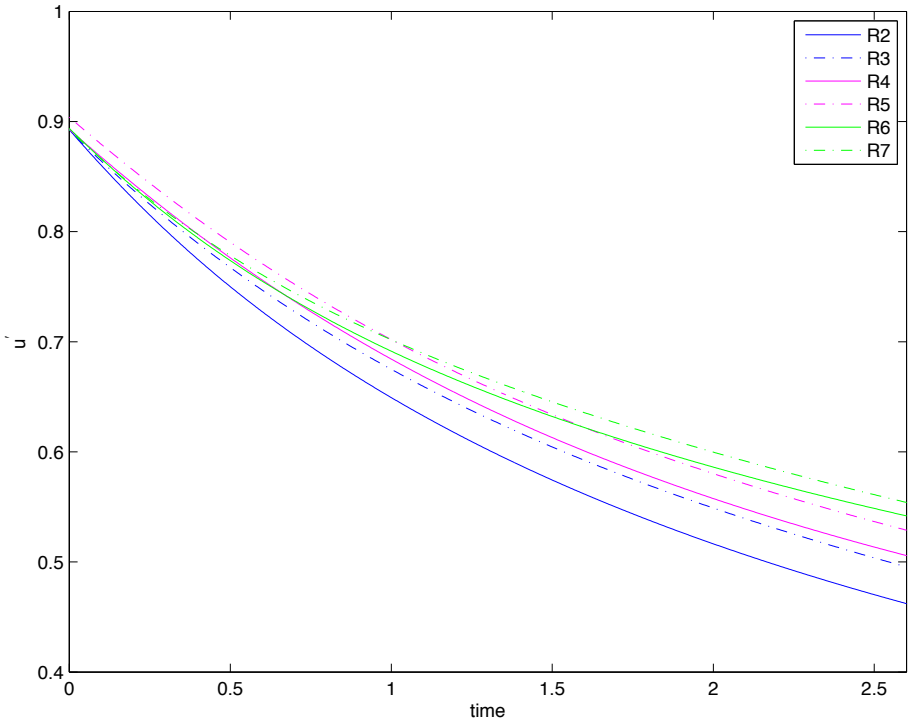

Figure 3.17: The time evolution of the rms velocity in a series of simulations with different viscosities.

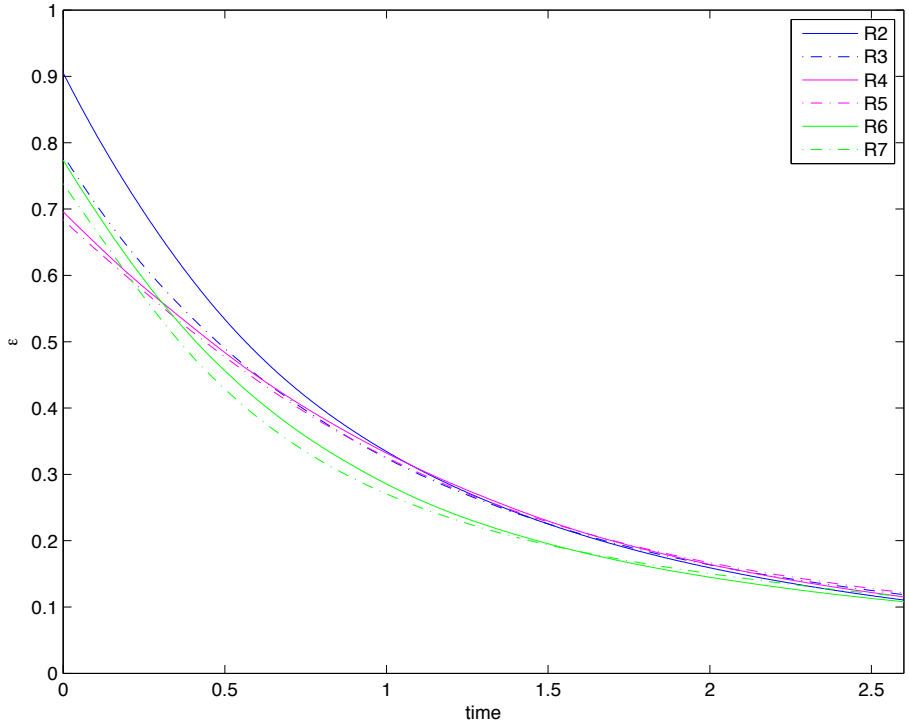

Figure 3.18: The time evolution of the energy dissipation rate in a series of simulations with different viscosities.

Chapter 4

FLAME SURFACE MODELING BY LEVEL CROSSING

The flame surface is indicated by the isosurface of mixture fraction at $Z = Zst$. In this chapter, the tasks revolving around the area of flame surface are as follows: (1) A theoretical formulation for predicting the area of isosurface(i.e., flame surface) is developed from the concept of level crossing; (2) The corresponding model for approximating each term in the theoretical formulation is proposed; (3) The model evaluation and verification are carried out by comparing the predictions with the numerical results; (4) The balance equation for isosurface area is numerically assessed and analyzed.

4.1 Flame Surface Area: Numerical Approach

As presented in chapter3(Section3.5), the numerical strategy based on the intrinsic function *isosurface* available in Matlab is adopted to extract and determine the area of the flame surface. The obtained numerical results are considered as the 'exact solution' which will be used to examine and investigate the proposed models by comparing with the predictions in this chapter.

4.2 Level Crossing: Numerical Approach

The level crossing measures how often a line through the scalar field data crosses the stoichiometric value of mixture fraction. More frequent crossing corresponds to higher density of flame surface. This brings up an idea that the level crossing can be utilized to quantify the area of flame surface[60].

The mathematical theory underlying the level crossing problem is associated with a random process. Therefore, interpreting the scalar field data as a random process is of great help in conveniently applying the theory to the analysis of the level crossing problem. Section 4.2.1 explains how to view a scalar field from the perspective of a random process.

Section 4.2.2 introduces a numerical approach to quantify the level crossing. A mathematical formulation of the relationship between the level crossing and the flame surface area is developed in Section 4.2.3.

4.2.1 Level Crossing: Introduction

The 3D mixture fraction field $Z(x_1, x_2, x_3)$ is treated as a spatial random process for the purpose of current study. A uniform 3D grid-based scalar field can be imagined as an ensemble of functions of one dimension in space; the random process considered in the current study is accordingly a family of one-dimensional discrete-space functions which evolve in this spatial dimension. The scalar field in a 3D cartesian coordinate system (x_1, x_2, x_3) is assumed to be spatially isotropic, therefore we arbitrarily choose the axis x_1 to be the argument of a one-dimensional spatial function. The underlying idea is that the spatial dimension x_1 is thought to be the spatial argument of a random function, and the x_2 and x_3 dimensions serve as indices to various ensemble members of a random process. It implies $Z(x_1; x_j, x_k)$ denotes the spatial evolution along the direction x_1 of a unique realization which is specified by a given position (x_j, x_k), and thus the number of ensemble members is correspondingly $N \times N$. From the perspective of a random process, the scalar field can be simply described as a discrete-space random process denoted by $\{Z(x_1)\}$, $0 \leq x_1 \leq L$, without the explicit dependence on x_2 and x_3 for notational convenience.

4.2.2 Level Crossing: Numerical Approach

The level-crossing problem quantifies how often a random process crosses the level value and is applied to approximate the area of the flame surface which lies along the stoichiometric isosurface. In this sense, it leads naturally to set the threshold value of level crossing to be the stoichiometric mixture fraction Z_{st}.

For a 3D grid-based scalar field, $\mathbf{n}_{z_{st}}(L; x_j, x_k)$ denotes the number of points where $Z(x_1; x_j, x_k)$ crosses the level Z_{st} in the interval of length $[0, L]$ along a particular line of points which is oriented in x_1 direction and specified by the position (x_j, x_k). It can be numerically calculated by comparing the value of Z at every two neighboring grid points $x_{i,j,k}$

and $x_{i+1,j,k}$ sequentially along x_1 axis. If either of these two conditions: 1) $Z(x_{i,j,k}) \geq Z_{st}$ and $Z(x_{i+1,j,k}) < Z_{st}$, 2) $Z(x_{i,j,k}) < Z_{st}$ and $Z(x_{i+1,j,k}) \geq Z_{st}$, is satisfied, one crossing is counted. This scheme can be represented by an indicator function $I\{\cdot\}$ which equals 1 if its argument is true and 0 otherwise[66].

$$\mathbf{n}_{z_{st}}(L; x_j, x_k) = \sum_{i=0}^{N-2} I\Big\{[Z(x_{i,j,k}) \geq Z_{st}, Z(x_{i+1,j,k}) < Z_{st}] \cup [Z(x_{i,j,k}) < Z_{st}, Z(x_{i+1,j,k}) \geq Z_{st}]\Big\} \tag{4.1}$$

Then applying the same numerical scheme to all the lines parallel to the x_1-axis over the entire domain, and adding up the results gives the total number of crossings as

$$\mathbf{N}_{z_{st}} = \sum_{k=0}^{N-1} \sum_{j=0}^{N-1} \mathbf{n}_{z_{st}}(L; x_j, x_k). \tag{4.2}$$

For comparison, the time evolution of the total number of crossings appear as solid, dashed and dash-dot lines in Fig.(4.1), corresponding to the calculations performed along the x_1, x_2 and x_3 directions respectively. A fairly good agreement among the three results corroborates that the total number of crossings are nearly identical regardless of whether to operations are performed along the x_1-, x_2- or x_3-axis, this is due to the approximately isotropic property of the mixture fraction field Z. Hence, unless otherwise stated, it will be assumed that the calculation is performed in x_1-direction throughout the present study. Nonetheless, due to the minor deviations between various directions, it is a stringent consideration that the statistics computed along x_2- and x_3-direction will also be presented in the following analysis to show the statistical accuracy of the results in different directions.

From the perspective of a random process, we generalize the definition of $\mathbf{n}_{z_{st}}(L; x_j, x_k)$ derived for a particular realization $Z(x_1; x_j, x_k)$ to any realization, and use a general and standard notation $\mathbf{n}_{z_{st}}(L)$ to represent the number of crossings of level Z_{st} by a random process $\{Z(x_1)\}$ during the interval of length L. Accordingly, the expected number of level crossings, denoted by $E\{\mathbf{n}_{z_{st}}(L)\}$, is determined numerically by dividing the total number of crossings, from Eq.(4.2), by the number of realizations as

$$E\{\mathbf{n}_{z_{st}}(L)\} = \frac{\mathbf{N}_{z_{st}}}{N^2} = \frac{1}{N^2} \sum_{k=0}^{N-1} \sum_{j=0}^{N-1} \mathbf{n}_{z_{st}}(L; x_j, x_k). \tag{4.3}$$

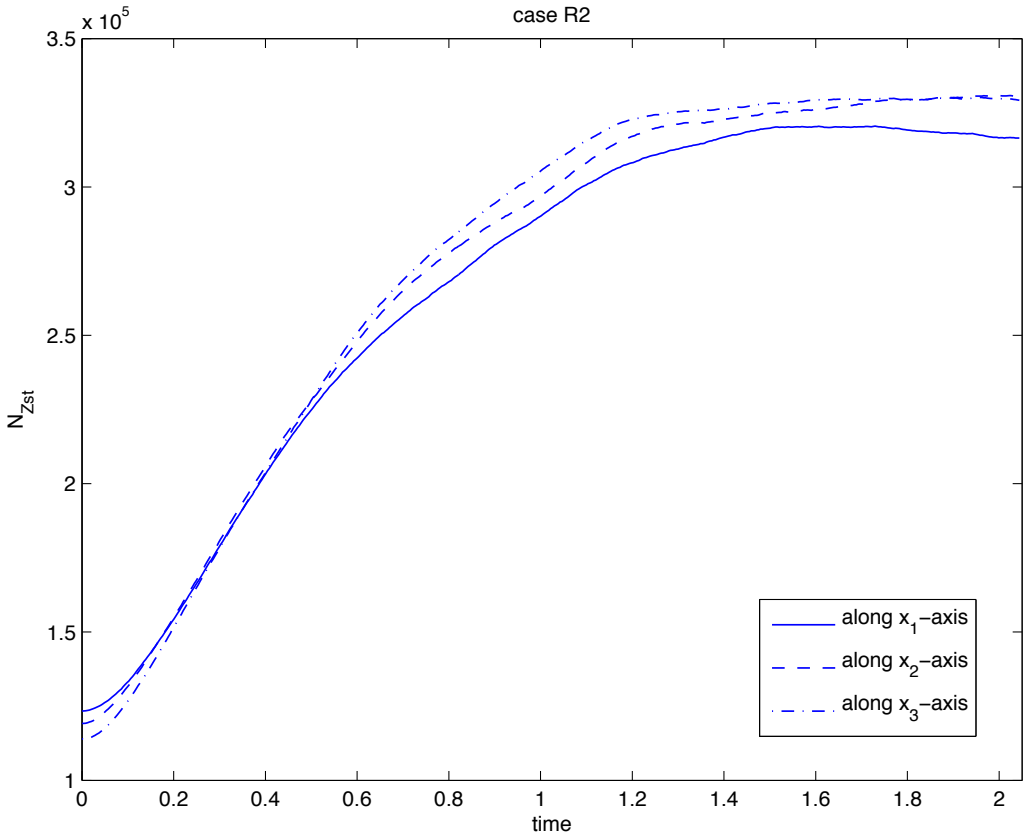

Figure 4.1: The time evolution of total number of crossings calculated along x_1-(solid),x_2-(dashed) and x_3-direction(dash-dot), respectively.

4.2.3 Flame surface area prediction in terms of level-crossing number

As described above, it is instructive to develop an algebraic formula to predict the area of flame surface A from the concept of level crossing. The explorations will proceed in three stages. First, a two dimensional case (i.e., line case) will be studied as a motivating example to illustrate how the length of a projected line is related to the number of crossings. Then, the same technique will be extended to formulate the relationship between the projected area of a surface and the number of crossings in three dimensions. Finally, the ratio of the surface area to its projected area will be determined with the knowledge of the statistical distribution of the projection angle.

To begin with consider a simple plane case. A smooth curve and a more tortuous line

inscribed into a square domain with side length $L_x = L_y$ are sketched in the top left and top right panel of Fig.(4.2), respectively. It graphically compares and demonstrates that the length of the projection of the line onto x-axis is proportional to the number of crossings made by the traverse vertical grid line across the plane $N_{c,y}$. Take the smooth curve depicted in the top left panel for example, the square domain of side length L_x is subdivided by N_x equally spaced vertical grid lines parallel to y-axis, at $\Delta x = L_x/N_x$ intervals. In this case, the projection of the curve l onto x-axis is l_x. For the i-th differential section of the line of length Δl_i, focus on the circled section enlarged in the bottom panel of Fig.(4.2), the projection of this line segment onto the x-axis is denoted by Δl_{x_i}. Consequently, the total length of the projection of the curve can be obtained by summing over all N_s differential line segments as

$$l_x = \sum_{i=1}^{N_s} \Delta l_{x_i}. \tag{4.4}$$

If the vertical grid lines has a high enough density that, for the $i-$th segment Δl_i, the number of crossings (i.e., crossings made by the traverse y axes) associated with this segment, n_{c,y_i}, can be proportional to Δl_{x_i} as

$$\frac{\Delta l_{x_i}}{L_x} = \frac{n_{c,y_i}}{N_x}. \tag{4.5}$$

Substituting Eq.(4.5) into Eq.(4.4) yields

$$l_x = \sum_{i=1}^{N_s} L_x \frac{n_{c,y_i}}{N_x} = \frac{L_x}{N_x} \sum_{i=1}^{N_s} n_{c,y_i} = \Delta x \, N_{c,y}, \tag{4.6}$$

where $N_{c,y} = \sum_{i=1}^{N_s} n_{c,y_i}$ denotes the total number of crossings counted along y-axis in the plane. This expression shows that the projected length of a line onto x-axis, l_x, is proportional to its crossing number $N_{c,y}$ by a factor of grid spacing $\Delta x = L_x/N_x$.

In order to extend the above relationship to three dimensional case, it is advantageous to recast Eq.(4.6) in terms of projected line length per unit area as

$$\frac{l_x}{L_x L_y} = \frac{\Delta x \, N_{c,y}}{L_x L_y} = \underbrace{\frac{\Delta x}{L_x}}_{1/N_x} \frac{N_{c,y}}{L_y} = \frac{1}{L_y} \frac{N_{c,y}}{N_x}, \tag{4.7}$$

where N_x is the number of grid points in x-direction (or, equivalently, the number of y axes

in the plane). Therefore, $N_{c,y}/N_x$ represents the average number of crossings per vertical grid line (i.e., y-axis) of length L_y.

Similarly, the projected length of line l onto y-axis, l_y, per unit area can be given in terms of the total number of crossings as

$$\frac{l_y}{L_x L_y} = \frac{1}{L_x}\frac{N_{c,x}}{N_y}, \tag{4.8}$$

where $N_{c,x}$ denotes the total number of crossings made by the traverse x axes in the plane and N_y is the number of grid points in y-direction (or, equivalently, the number of x axes in the plane). Therefore, $N_{c,x}/N_y$ represents the average number of crossings per horizontal grid line (i.e., x-axis) of length L_x.

Accordingly,

$$l_y = \frac{L_y}{N_y} N_{c,x} = \Delta y \, N_{c,x}. \tag{4.9}$$

Next, the relationship derived in above two dimensional case will be adapted to the surface area in a three dimensional domain which is the subject of current research as introduced in Chapter 3. The relationship between the projected line length per unit area and the average number of crossings, Eq.(4.8), can be directly extended to yield the relationship between the projected area per unit volume and the average number of crossings as

$$\frac{A_{yz}}{L_x L_y L_z} = \frac{1}{L_x}\frac{N_{c,x}}{N_y N_z}, \tag{4.10}$$

where A_{yz} denotes the the projected area of flame surface onto the $x_2 - x_3$ plane and $N_{c,x}$ denotes the total number of crossings made by the traverse x_1 axes over the whole computational domain. Same as above introduced, $N_{c,x}/(N_y N_z)$ represents the average number of crossings per x_1-axis of length L_x.

Accordingly,

$$\begin{aligned} A_{yz} &= \frac{1}{L_y} N_y \frac{L_z}{N_z} N_{c,x} = \Delta y \Delta z \, N_{c,x} \\ &= (\frac{L}{N})^2 N_{c,x} = \Delta x^2 \, N_{c,x}, \end{aligned} \tag{4.11}$$

where $L_x = L_y = L_z = L$ is the length of each side of our computational domain and $N_x = N_y = N_z = N$ is the number of grid points in each coordinate direction. Consequently,

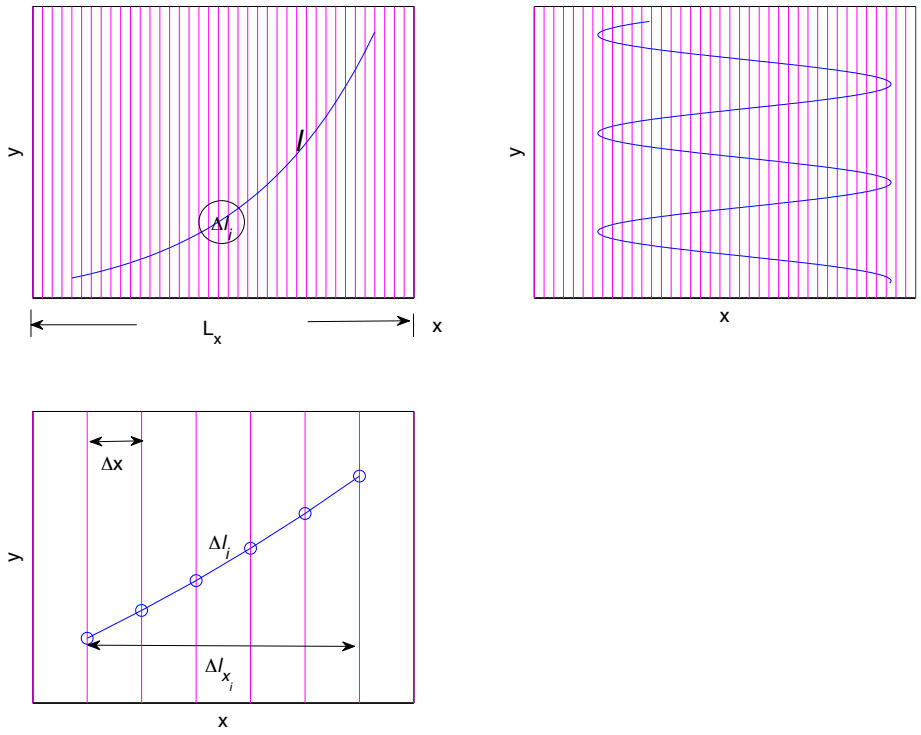

Figure 4.2: Diagram of a two dimensional case that a curve lies inside a square. It illustrates how the length of the projection of a line is related to its crossing number. A square plane with side length L_x inscribed, respectively, with a smooth curve(top left) and a more tortuous line(top right). The solid circle surrounding the $i-$th differential segment of the line in top left panel is enlarged in bottom left panel to show the details.

$\Delta x = \Delta y = \Delta z$ is the grid spacing. Because of isotropy, the same procedure can be carried out in the y and z directions.

When considering the stoichiometric isosurface (i.e., flame surface), the stoichiometric mixture fraction Z_{st} is taken to be the level value for measuring crossings. Accordingly, the total number of level crossings measured along x_1-direction is denoted by $\mathbf{N}_{z_{st}}$. The projected area of flame surface onto the $x_2 - x_3$ plane is denoted by A_P. The above relation Eq.(4.11) can be recast as

$$A_P = (\frac{L}{N})^2 \mathbf{N}_{z_{st}} = \frac{(2\pi)^2}{N^2} \mathbf{N}_{z_{st}} = \Delta x^2 \mathbf{N}_{z_{st}}, \tag{4.12}$$

where L is equal to 2π as introduced in Chapter 3. This relationship formula is consistent with the one derived from above planar case, Eq.(4.9), when squaring the line scale factor Δx to area scale factor Δx^2. The total number of level crossings measured along x_1-direction $\mathbf{N}_{z_{st}}$ is considered to be mathematically equivalent to the projected area of flame surface onto the $x_2 - x_3$ plane, A_P. Since these two quantities are expressed in different units, a conversion factor is required for rescaling their units to be interpreted on the same scale.

Finally the ratio of flame surface area A to its projected area A_P is investigated. For a differential flame surface area dA, its projected area onto the $x_1 - x_2$ plane dA_P is given by

$$dA_P = dA|cos\Phi|, \tag{4.13}$$

where Φ is the angle between the direction of projection and the normal to surface element. The surface area A and its projected area A_P are linked by summing over all the differential areas

$$A_P = A\left\langle|cos\Phi|\right\rangle, \tag{4.14}$$

where $\langle\cdot\rangle$ denotes an volumetric average. For the isotropic case, the averaged quantity $\langle|cos\Phi|\rangle$ can be determined based on a spherical coordinate system in the following way. In a spherical coordinate system, as depicted in Fig.(4.3)[12], defining the polar angle $\Phi(0 \leq \phi \leq \pi)$ and the azimuthal angle $\Theta(0 \leq \theta < 2\pi)$ in the usual manner, consider the probability of particular values of Φ and Θ occurring as $p(\phi, \theta)$. It follows that the probability of Φ being in the range ϕ and $\phi + d\phi$ and Θ being in the range θ and $\theta + d\theta$ is defined as

$$\mathbf{P}(\phi \leq \Phi < \phi + d\phi; \theta \leq \Theta < \theta + d\theta) = p(\phi, \theta)d\phi d\theta. \tag{4.15}$$

Now assuming that any point on a sphere has equal chance, then the probability $P(\phi \leq \Phi < \phi + d\phi; \theta \leq \Theta < \theta + d\theta)$ will be proportional to the surface area swept out at point (ϕ, θ) by $(d\phi, d\theta)$ which is denoted by dA_s.

$$\mathbf{P}(\phi \leq \Phi < \phi + d\phi; \theta \leq \Theta < \theta + d\theta) = k_1 dA_s, \tag{4.16}$$

where k_1 is a constant of proportionality. The infinitesimal spherical surface area dA_s spanned from ϕ to $\phi + d\phi$ and from θ to $\theta + d\theta$ at radius R is given by $R^2 sin\phi d\phi d\theta$. So,

the probability can be formulated as

$$\mathbf{P}(\phi \leq \Phi < \phi + d\phi; \theta \leq \Theta < \theta + d\theta) = k_1 R^2 sin\phi d\phi d\theta = K sin\phi d\phi d\theta, \tag{4.17}$$

where K is a constant of proportionality obtained by combining coefficients. Therefore, comparing Eq.(4.15) with Eq.(4.17) gives

$$p(\phi, \theta) = K sin\phi. \tag{4.18}$$

The constant K can be solved by the normalization relationship

$$\int_0^{2\pi} \int_0^{\pi} p(\phi, \theta)\, d\phi d\theta = 1, \tag{4.19}$$

which gives $K = 1/4\pi$, so that

$$p(\phi, \theta) = \frac{sin\phi}{4\pi}. \tag{4.20}$$

With the knowledge of the probability, the averaged value $\langle |cos\Phi| \rangle$ can be determined by integrating over all possible directions since the flame surface is created from an isotropic flow field in our study.

$$\begin{aligned} \langle |cos\Phi| \rangle &= \int_0^{2\pi} \int_0^{\pi} p(\phi, \theta) |cos\phi| d\phi d\theta \\ &= 2 \int_0^{2\pi} \int_0^{\pi/2} \frac{sin\phi}{4\pi} cos\phi d\phi d\theta \\ &= \int_0^{\pi/2} sin\phi cos\phi d\phi \\ &= -\frac{1}{2} [cos\phi]^2 \Big|_0^{\pi/2} = \frac{1}{2}. \end{aligned} \tag{4.21}$$

The derivations we have performed thus far suffice to formulate the flame surface area A in terms of the total number of crossings $N_{z_{st}}$ by substituting Eq.(4.21) into Eq.(4.14) and combining with Eq.(4.12). The final formulation is written as

$$A = 2\, \frac{L^2}{N^2}\, \mathbf{N}_{z_{st}} = 2\, \Delta x^2\, \mathbf{N}_{z_{st}}. \tag{4.22}$$

The justification of this linear relationship, Eq.(4.22), and the verification of the associated proportional constant coefficient, $2\, L^2/N^2 = 2\, \Delta x^2$, proceed through Fig.(4.4), which

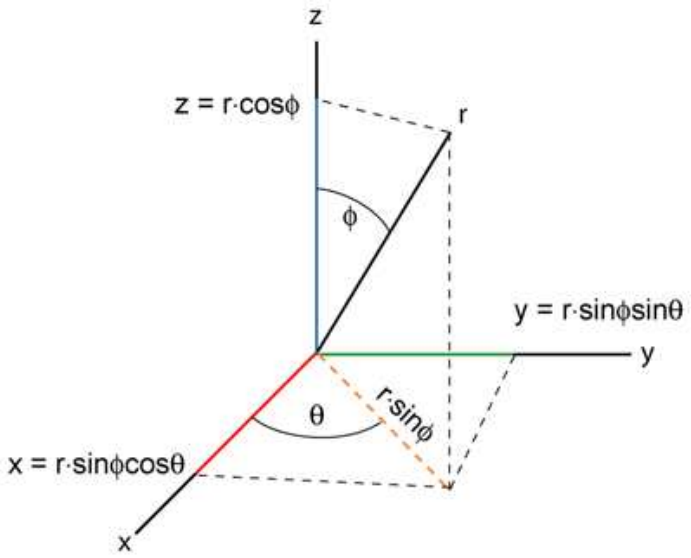

Figure 4.3: The spherical coordinate system.

exhibits and confirms the postulated linear relationship between the area and the total number of crossings, and proves the value of the coefficient via the slope of the line. In this figure, the total number of crossings $N_{z_{st}}$ measured along x_1-, x_2- and x_3-direction are plotted, respectively, against the flame surface area A to show that the area A can be predicted by using $N_{z_{st}}$ counted along any of three directions. Note that here both the flame surface area A and the total number of crossings $N_{z_{st}}$ are obtained directly from DNS data.

Furthermore, Eq.(4.22) can be alternatively expressed in terms of the expected number of level crossings that will be of practical use when we come to probing the modeling the flame surface area. Substituting Eq.(4.3) into Eq.(4.22) recasts the flame surface area A in terms of the expected number of level crossings as

$$A = 2\,\frac{L^2}{N^2}\,N^2\,E\{\mathbf{n}_{z_{st}}(L)\} = 2\,L^2\,E\{\mathbf{n}_{z_{st}}(L)\}. \tag{4.23}$$

4.3 Level Crossing and Flame Surface Area: Theoretical Approach

Based on the analysis above, the expected number of crossings $E\{\mathbf{n}_{z_{st}}(L)\}$ plays a major role in approximating the area of flame surface. Although it can be numerically calculated from the DNS data as described in Section 4.2.2, a theoretical approach is necessary to

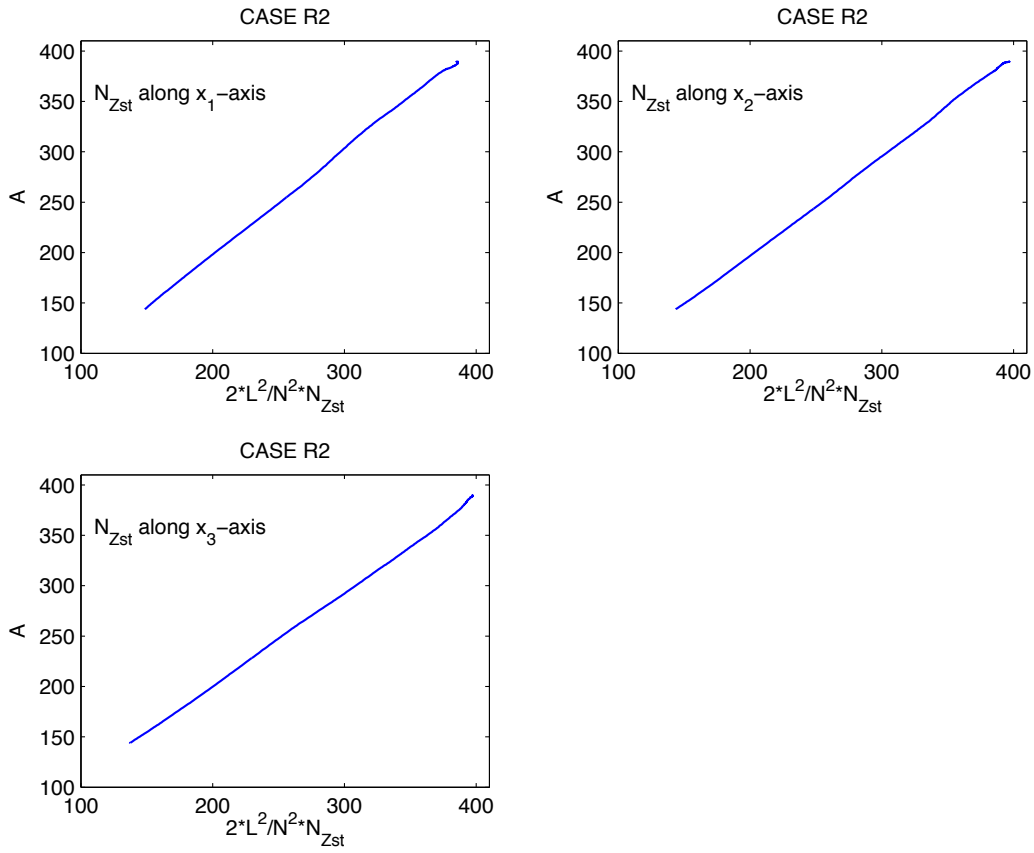

Figure 4.4: The time evolution of the rescaled total number of crossings versus the flame surface area. $N_{z_{st}}$ is counted along x_1-(top left), x_2-(top right) and x_3-direction(bottom left), respectively. Note that the scale of the area is set to 2π which is the length of computational domain in DNS.

be developed to estimate it with the aim of providing a mathematical framework for the subsequent modeling of the flame surface area.

For a mixture fraction field being considered as a random process, if the gradient $\partial Z/\partial x_1$ exists, then a theorem of S.O.Rice[62][63] can be applied to determine the expected value of $\mathbf{n}_{z_{st}}(L)$ as

$$E\{\mathbf{n}_{z_{st}}(L)\} = L\, P_Z(Z_{st})\, \langle |Z^{'}(x_i)| \mid Z(x_i) = Z_{st} \rangle, \tag{4.24}$$

where L equals the size of our computational domain 2π and $Z^{'} = \partial Z/\partial x_1$ is the local derivative of mixture fraction Z with respect to x_1 axis. The second and the third terms

represent the probability density function (PDF) of the discrete random variable $Z(x_i)$ and the conditional mean of the absolute value of its derivative, respectively. In the theory of stochastic processes, the random variable $Z(x_i)$ should be a collection of samples from all realizations of a random process at a fixed position $x_1 = x_i$. However, in the present study, the spatial random process actually refers to a homogeneous and isotropic field, therefore, the ensemble statistics are exchangeable with the volume statistics. It means that the sample space of the above-mentioned random variable can be extended to consist of DNS data from the entire computational domain. Accordingly, dropping the dependence on x_i, the Eq.(4.24) can be recast as

$$E\{\mathbf{n}_{z_{st}}(L)\} = L\, P_Z(Z_{st})\, \langle |Z^{'}| \mid Z = Z_{st} \rangle, \tag{4.25}$$

where the second term is the PDF of the mixture fraction Z at a specific value $Z = Z_{st}$ and the third term is the volume averaged $|Z^{'}|$ conditioned on the stoichiometric surface Z_{st}.

The theoretical prediction is assessed by comparing the expected crossing number solved by Eq.(4.25) to the one obtained numerically from DNS data due to Eq.(4.3). For the number of crossings, the numerical measurement and the theoretical prediction containing local derivative $Z^{'}$ both depend on the direction in which the computations are taken, so the comparison between the numerical and the theoretical results is performed in x_1-, x_2- and x_3-direction, respectively. As can be seen in Fig.(4.5), the theoretical approach achieves very good agreement with the numerical results in each respective direction that the calculation is performed, therefore it is considered to provide an accurate theoretical formula for the subsequent modeling and be appropriate irrespective of the direction considered.

Consequently, the theoretical approach to the flame surface area is then of the form

$$\begin{aligned} A &= (2L^2)\, E\{\mathbf{n}_{z_{st}}(L)\} \\ &= (2L^3)\, P_Z(Z_{st}) \langle |Z^{'}| \mid Z = Z_{st} \rangle, \end{aligned} \tag{4.26}$$

and the comparison with the area obtained numerically from DNS is displayed in Fig.(4.6). Note that the surface area A is a unique value, independent of direction. But the theoretical prediction involving local derivative $Z^{'}$ is direction-dependent. Therefore, the theoretical results achieved in different directions are all presented. As seen in the figure, the good agree-

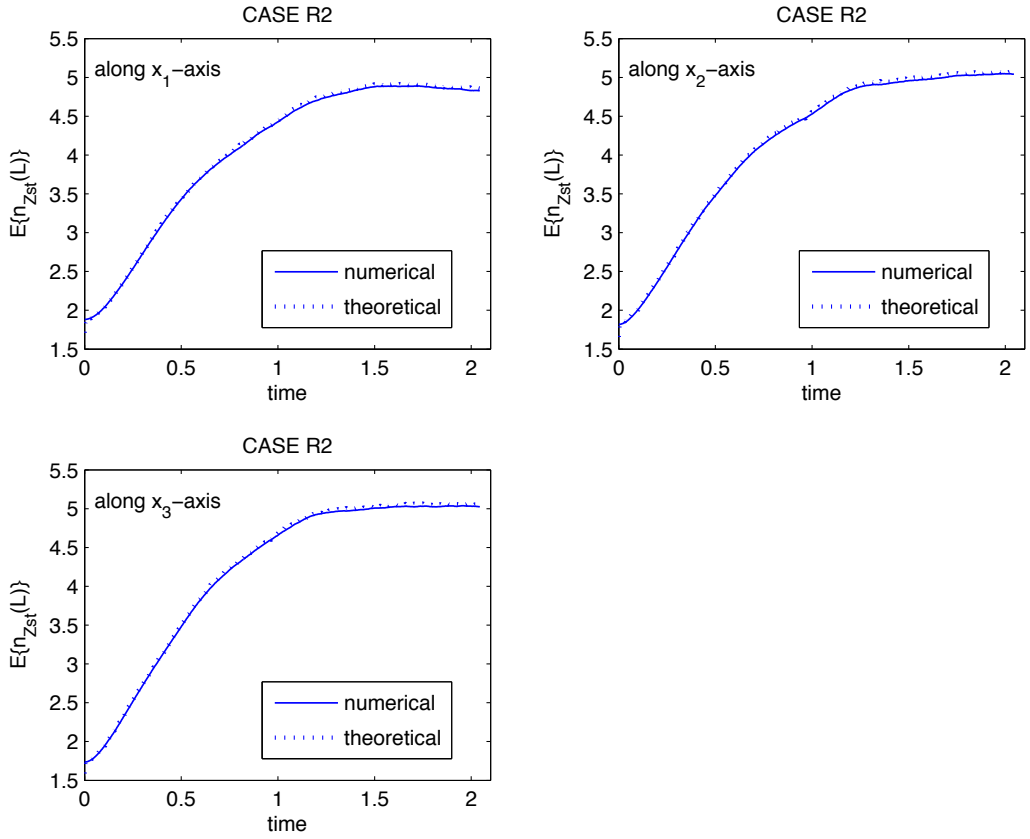

Figure 4.5: The time evolution of expected number of crossings obtained numerically from DNS due to Eq.(4.3)(solid) is compared with the one predicted by Rice's theorem Eq.(4.25)(dotted) where $P_Z(Z_{st})$ and $\langle |Z^{'}| \mid Z = Z_{st} \rangle$ are directly from DNS. Both the numerical and the theoretical results are computed with respect to x_1(top left), x_2(top right) and x_3(bottom left) directions, respectively.

ment once again substantiates the above argument that the theoretical formula provides an appropriate framework to enable probing of models even though some slight deviations are found between different directions. Note that the minor deviations found here are consistent with the ones found in Fig.(4.1).

In the following sections, the second and third terms will be modeled and tested by DNS data.

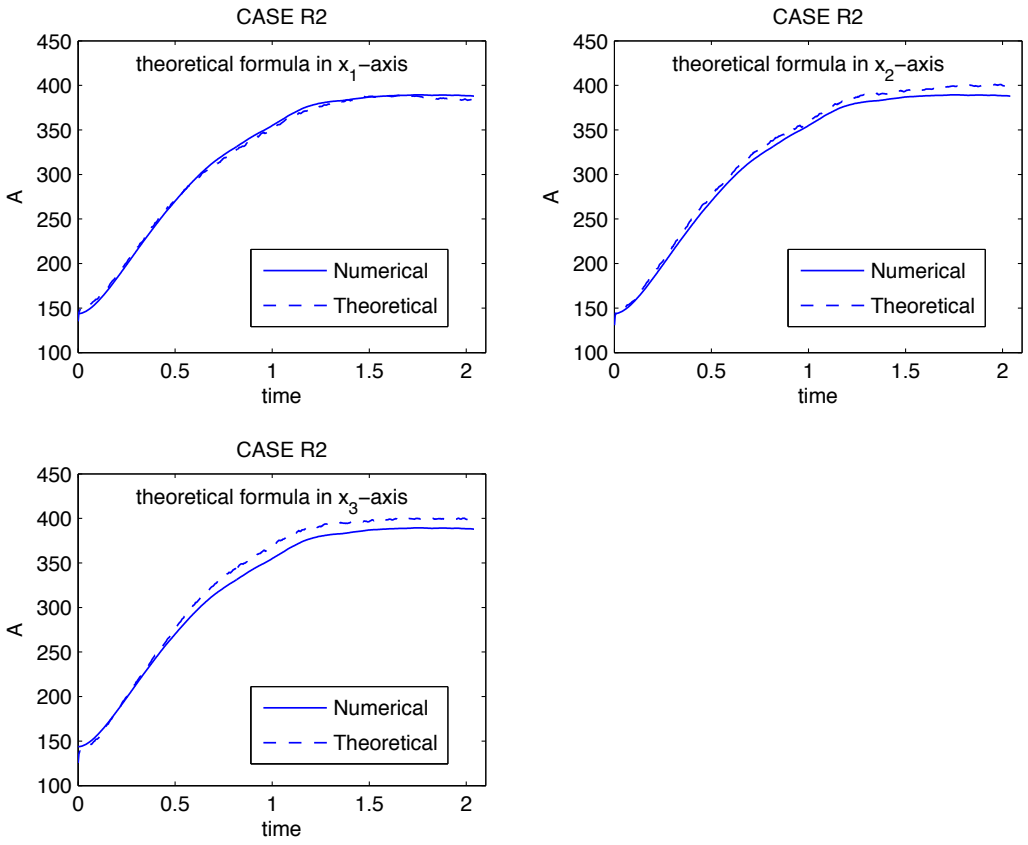

Figure 4.6: The time evolution of flame surface area obtained numerically from DNS(solid) is compared with the one determined by a theoretical formula Eq.(4.26)(dashed) where $P_Z(Z_{st})$ and $\langle |Z^{'}| \mid Z = Z_{st} \rangle$ are directly from DNS. Each succeeding panel (left to right, top to bottom) represents the derivative $Z^{'}$ intervening in theoretical formula with respect to x_1-, x_2- and x_3-direction.

4.4 Flame Surface Area: Modeling $P_Z(Z = Z_{st})$

In a two-feed system where the mixture fraction Z varies between $Z = 0$ and $Z = 1$, a β-distribution is widely used to model the PDF of mixture fraction in nonpremixed turbulent combustion[11],[49],[45]. $P_Z(Z = Z_{st})$ is the PDF in terms of the stoichiometric mixture fraction, which can be approximately by a β function as

$$P_Z(Z = Z_{st}) = f_\beta\left(Z = Z_{st}; \alpha, \beta\right) = \frac{\Gamma\left(\alpha + \beta\right)}{\Gamma\left(\alpha\right)\Gamma\left(\beta\right)} \, Z_{st}^{\alpha-1} \, \left(1 - Z_{st}\right)^{\beta-1}, \tag{4.27}$$

where $\Gamma()$ is the gamma function. The shape parameters α and β are related to the volume averaged mean $\langle Z \rangle$ and variance $\langle Z''^2 \rangle$ by

$$\begin{cases} \alpha &= \langle Z \rangle \left[\dfrac{\langle Z \rangle}{\langle Z''^2 \rangle} (1 - \langle Z \rangle) - 1 \right] \\ \beta &= \alpha (\dfrac{1}{\langle Z \rangle} - 1) \end{cases} \tag{4.28}$$

It follows that the PDF of Z can be specified uniquely by its mean and variance, and thus $P_Z(Z_{st})$ can be expressed as $P_Z(Z_{st}) = f_\beta(Z = Z_{st}; \langle Z \rangle, \langle Z''^2 \rangle)$.

The time evolution of $P_Z(Z_{st})$ approximated by the proposed model with $\langle Z \rangle$ and $\langle Z''^2 \rangle$ taken from DNS data is compared in Fig.(4.7) with the one evaluated numerically using DNS data. The model predicts almost exact results until a slight overprediction occurs at time$\approx$ 1.35.

4.5 Flame Surface Area: Modeling $\langle |Z^{'}| \mid Z = Z_{st} \rangle$

In this section, we seek to develop a model for the third term in Eq.(4.26), $\langle |Z^{'}| \mid Z = Z_{st} \rangle$. In order to simplify the notations used in the following explorations, let Q and $|Q|$ denote the conditional random variable $(Z^{'} \mid Z = Z_{st})$ and its absolute value $(|Z^{'}| \mid Z = Z_{st})$, respectively. Accordingly, the conditional average of the absolute value, $\langle |Z^{'}| \mid Z = Z_{st} \rangle$, is denoted succinctly as $\langle |Q| \rangle$.

4.5.1 Presume the PDF of Q to be a normal distribution with zero mean

As we know, determining the expectation of a random variable requires knowledge of its PDF, so we start with by prescribing a probability distribution model for the random variable Q by presuming it to be a normal distribution with zero mean.

$$P_Q(q) = \frac{1}{\sigma\sqrt{2\pi}} exp\left(-\frac{(q-\mu)^2}{2\sigma^2}\right) = \frac{1}{\sigma\sqrt{2\pi}} exp\left(-\frac{q^2}{2\sigma^2}\right) \tag{4.29}$$

Here $\mu = \langle Q \rangle$ is assumed to be zero because of isotropy, the selection of the initial conditions for Q and the choice of Z_{st}. σ^2 is the variance of Q.

In order to assess the suitability of the assumed PDF approach, the following two tests are performed: (1) The time evolutions of μ (i.e., mean value of Q, $\langle Q \rangle$), calculated with

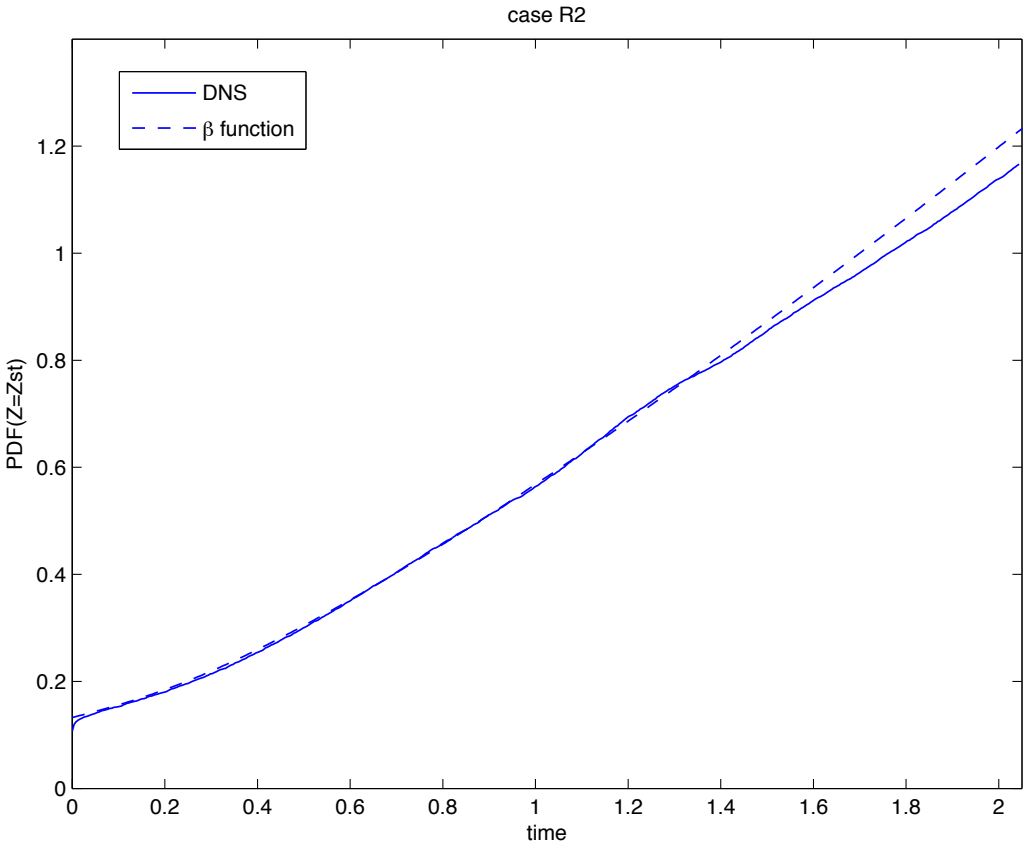

Figure 4.7: The time evolution of $P_Z(Z_{st})$ obtained directly from DNS(solid) is compared with the $\beta-$PDF approach(dashed) where two parameters $\langle Z \rangle$ and $\langle Z''^2 \rangle$ are taken from DNS.

respect to each direction by using DNS data, is respectively displayed in Fig.(4.8). As shown in the figure, in all three directions, they exhibit the same behavior that the fluctuations in time are around zero within the range $[-0.0175, +0.0175]$. It is seen that a zero mean is an adequate assumption for this statistical quantity regardless of the direction of computation. (2) The PDF of Q modeled by Eq.(4.29) with $\mu = 0$ and variance σ^2 taken from DNS data is presented in Fig.(4.9) for times $t = 0.07$,0.25,0.72, and 1.72. The PDF numerically estimated by using DNS data is also included in Fig.(4.9) at these same times for reference. The comparisons demonstrate that the normal distribution with zero mean appears to be a reasonable approximation. Nevertheless, a minor non-Gaussian tail can be observed by

a closer study of the bottom two plots in Fig.(4.9), it is a typical phenomenon attributed to the spatial intermittency effect in velocity field of turbulent flow. The intermittency in turbulence refers to the strong oscillations of small scales (i.e., scalar gradients), and the non-Gaussian behavior is a typical manifestation of this "spotty" structure [8][15].

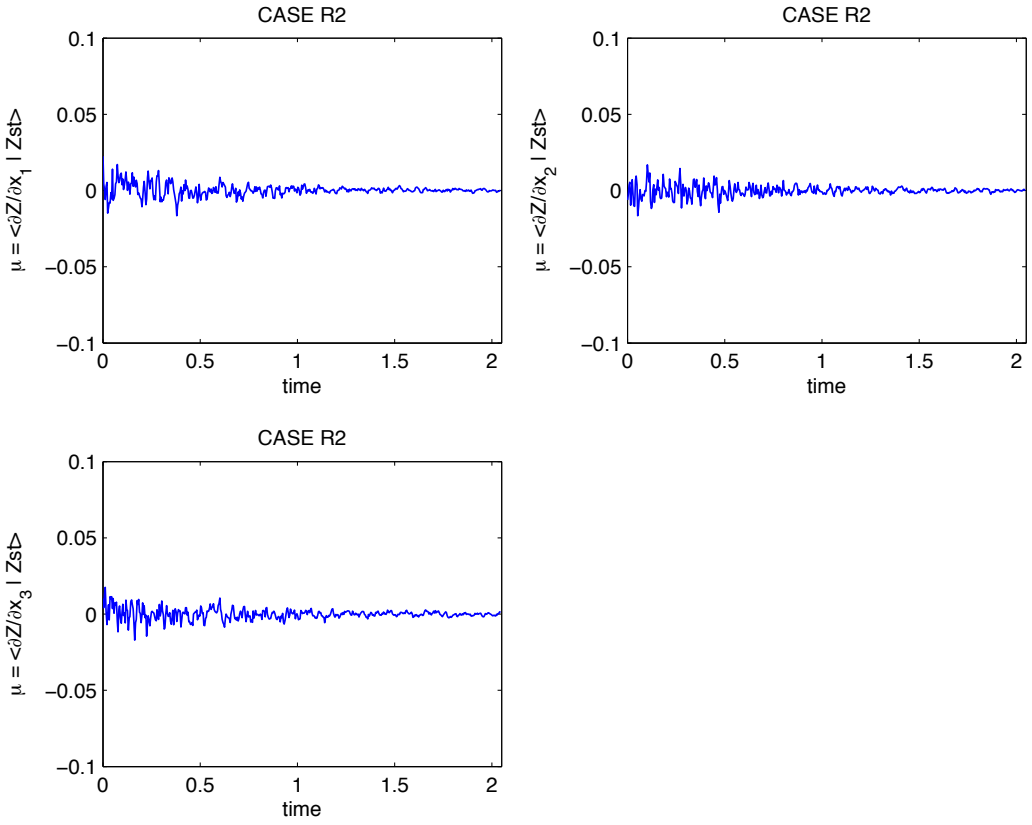

Figure 4.8: The time evolution of mean value of Q, $\langle Q \rangle$, calculated from DNS. From top to bottom and left to right, the panels correspond to Q with respect to x_1-, x_2- and x_3-direction, respectively.

4.5.2 Model $\langle |Q| \rangle$ in terms of σ

Once the PDF of Q is specified, the expectation of the absolute value of Q, $|Q|$, can be determined based on probability theory as

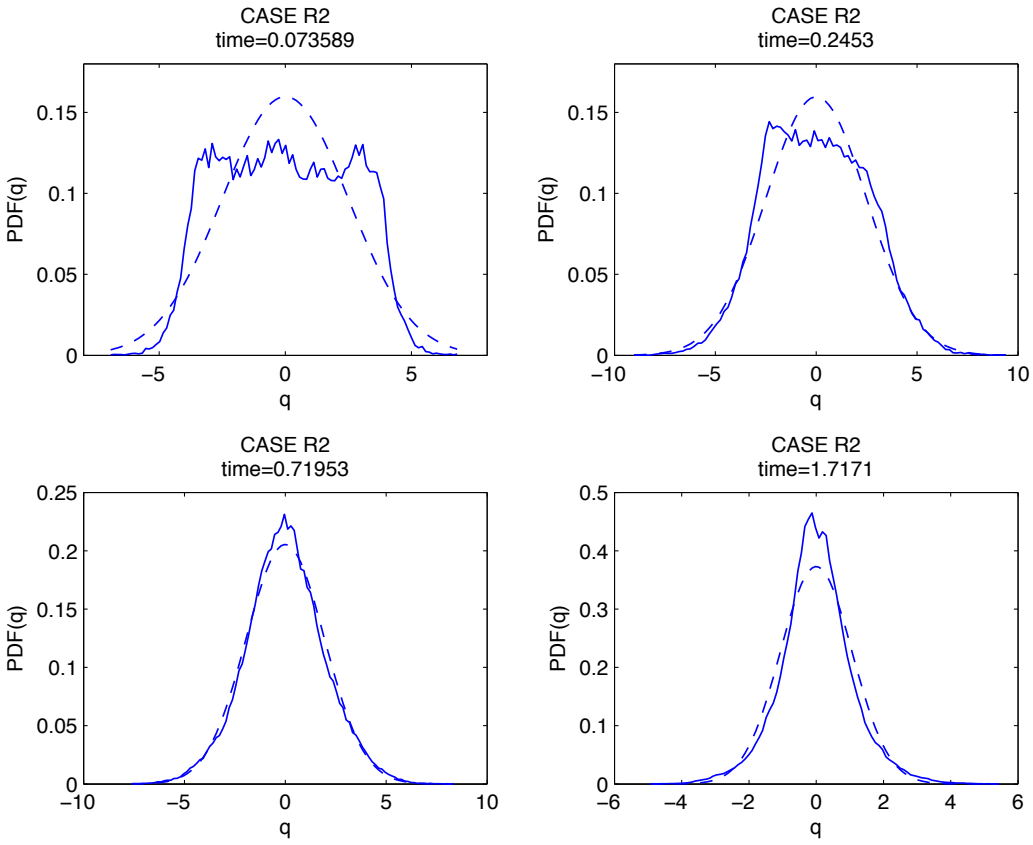

Figure 4.9: PDF of Q obtained directly from DNS(solid) and from the normal distribution approximation with $\mu = 0$ and σ^2 taken from DNS(dashed) correspond to simulation times: time=0.07(left upper), 0.25(right upper), 0.72(left bottom) and 1.72(right bottom), respectively.

$$\begin{aligned}
\langle |Q| \rangle &= \int_{-\infty}^{+\infty} |q| P_Q(q)\, dq \\
&= \int_{-\infty}^{+\infty} |q| \frac{1}{\sigma\sqrt{2\pi}} exp\left(-\frac{q^2}{2\sigma^2}\right) dq \\
&= 2\int_{0}^{+\infty} q \frac{1}{\sigma\sqrt{2\pi}} exp\left(-\frac{q^2}{2\sigma^2}\right) dq \\
&= \sigma\sqrt{\frac{2}{\pi}}
\end{aligned} \tag{4.30}$$

The $\langle |Q| \rangle$ approximated by the model expressed in the above equation with σ directly

taken from DNS is indicated by a solid line as shown in Fig.(4.10). Also illustrated for comparison is the one estimated by DNS data, which corresponds to a dashed line. Each individual panel of the figure corresponds to a particular direction in which the calculations are performed. As can be seen, the performance of the model is the same irrespective of direction. The model underpredicts the quantity $\langle |Q| \rangle$ during early simulation times, and there are deviations around time $t \approx 0.07$ which gives a maximum error of 8%. As time proceeds, the extent of underprediction tends to decrease until the overprediction occurs around time $t \approx 0.5$. The overprediction persists at later times and the errors of overprediction remain relatively the same order of magnitude, which give about 6%. The deviations between the model and the DNS results stem solely from the presumed PDF shape of Q, since the two input parameters required by the model, i.e., the first and the second moments of variable Q, are accurate and independent of the PDF shape of Q.

The expected value of a function of Q, $|Q|$, with respect to the probability density function $P_Q(q)$ is hereby defined as a function depending upon its variance σ^2. The procedure for determination of this variance will be illustrated in the subsequent section.

4.5.3 Model $\langle |Q| \rangle$ in terms of $\langle \chi_{st} \rangle$

The term σ^2, the variance of Q, is defined as

$$\sigma^2 = \langle (Q - \mu)^2 \rangle = \langle Q^2 \rangle. \tag{4.31}$$

As mentioned at the outset, take x_1-direction for instance because of isotropy, $\langle Q^2 \rangle$ represents $\langle (\partial Z/\partial x_1)^2 \mid Z = Z_{st} \rangle$, which is exactly the same as the x_1-direction component of the averaged scalar dissipation rate conditioned on stoichiometry, $\langle \chi_{st} \rangle$. This motivates the use of $\langle \chi_{st} \rangle$ as a point of departure for the determination of σ^2.

As we know, $\langle \chi_{st} \rangle$ is defined by

$$\langle \chi_{st} \rangle = 2D_f \left[\langle (\frac{\partial Z}{\partial x_1})^2 \mid Z = Z_{st} \rangle + \langle (\frac{\partial Z}{\partial x_2})^2 \mid Z = Z_{st} \rangle + \langle (\frac{\partial Z}{\partial x_3})^2 \mid Z = Z_{st} \rangle \right], \tag{4.32}$$

where D_f is the molecular diffusivity of Z.

The property of isotropic turbulence (i.e., the statistical quantities are invariant under rotations of the coordinate system) determines that the conditional means of the mixture

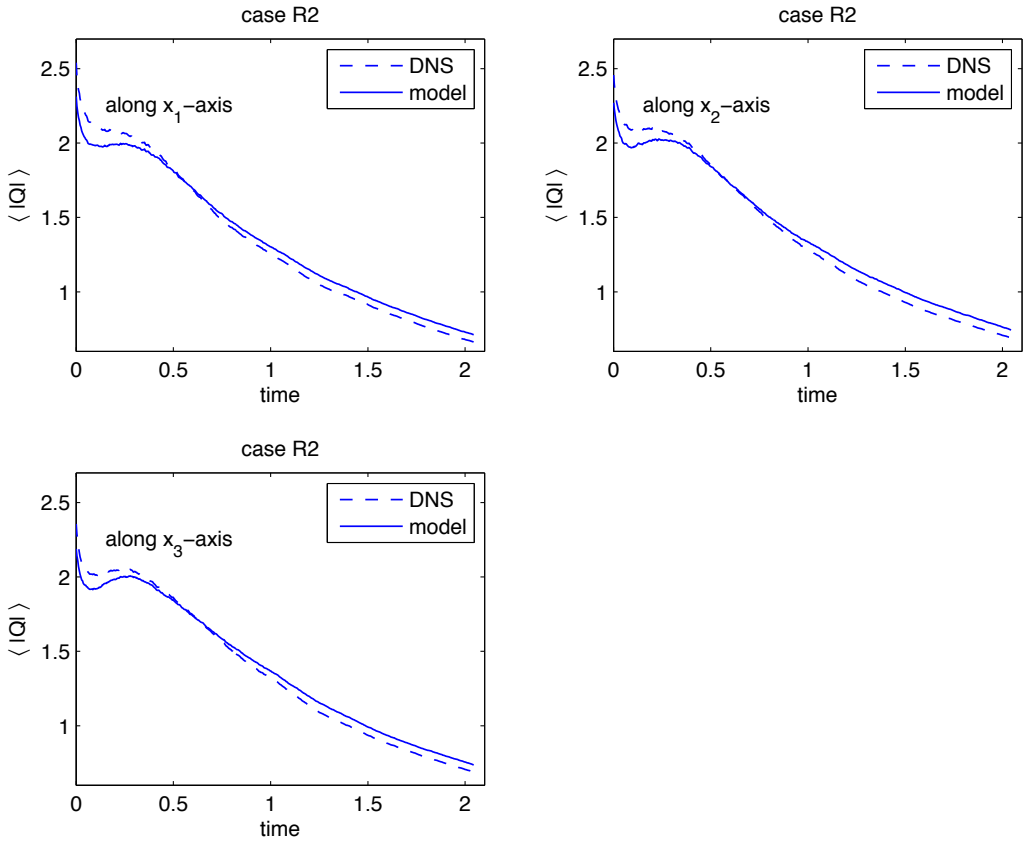

Figure 4.10: The time evolution of $\langle |Q| \rangle$ obtained numerically from DNS(dashed) and the one determined by model Eq.(4.30)(solid) with σ taken directly from DNS. Each succeeding panel (left to right, top to bottom) corresponds to the computations (i.e., numerical determinations of $\langle |Q| \rangle$ and σ) performed in x_1-, x_2- and x_3-direction, respectively.

fraction gradients with respect to various directions should be identical. All the three components of $\langle \chi_{st} \rangle$ calculated from DNS are individually depicted against each other in Fig.(4.11), which indicates that they are approximately invariant with respect to direction. Therefore, we can say that

$$\langle (\frac{\partial Z}{\partial x_1})^2 \mid Z = Z_{st} \rangle = \langle (\frac{\partial Z}{\partial x_2})^2 \mid Z = Z_{st} \rangle = \langle (\frac{\partial Z}{\partial x_3})^2 \mid Z = Z_{st} \rangle. \tag{4.33}$$

As a direct consequence, the expression of $\langle \chi_{st} \rangle$ is reduced to

$$\langle \chi_{st} \rangle = 6 D_f \langle (\frac{\partial Z}{\partial x_1})^2 \mid Z = Z_{st} \rangle. \tag{4.34}$$

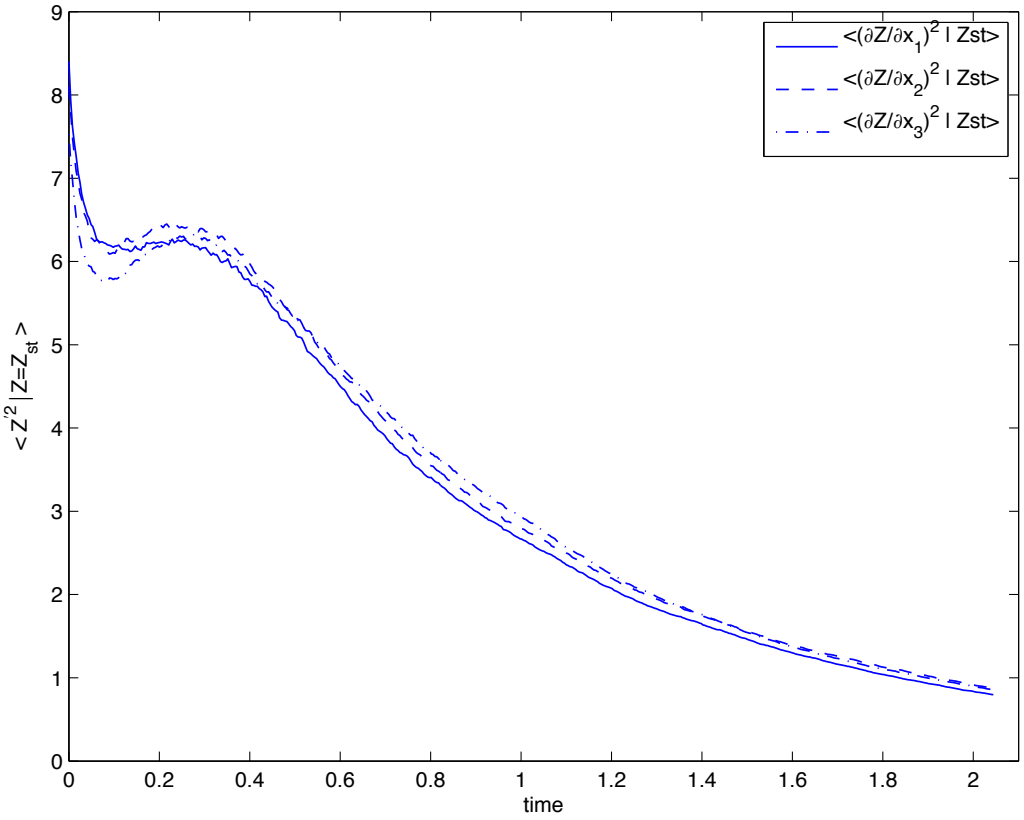

Figure 4.11: The time evolution of three components of $\langle \chi_{st} \rangle$ with respect to x_1(solid), x_2(dashed) and x_3(dash-dot) directions, respectively.

Combining Eq.(4.31) and Eq.(4.34), the parameter σ^2 can be written in terms of $\langle \chi_{st} \rangle$ as

$$\sigma^2 = \frac{1}{6D_f} \langle \chi_{st} \rangle. \tag{4.35}$$

Fig.(4.12) presents a comparison of σ^2 predicted from Eq.(4.35) and the ones computed in three different directions by using DNS data. As can be seen, the $\langle \chi_{st} \rangle$ can be used to approximate σ^2 measured with respect to any direction because of isotropy. It should be mentioned that the determination of σ^2 does not invoke the prescribed PDF shape of Q, so the well-approximated variance of Q is irrelevant to the choice of its presumed PDF shape.

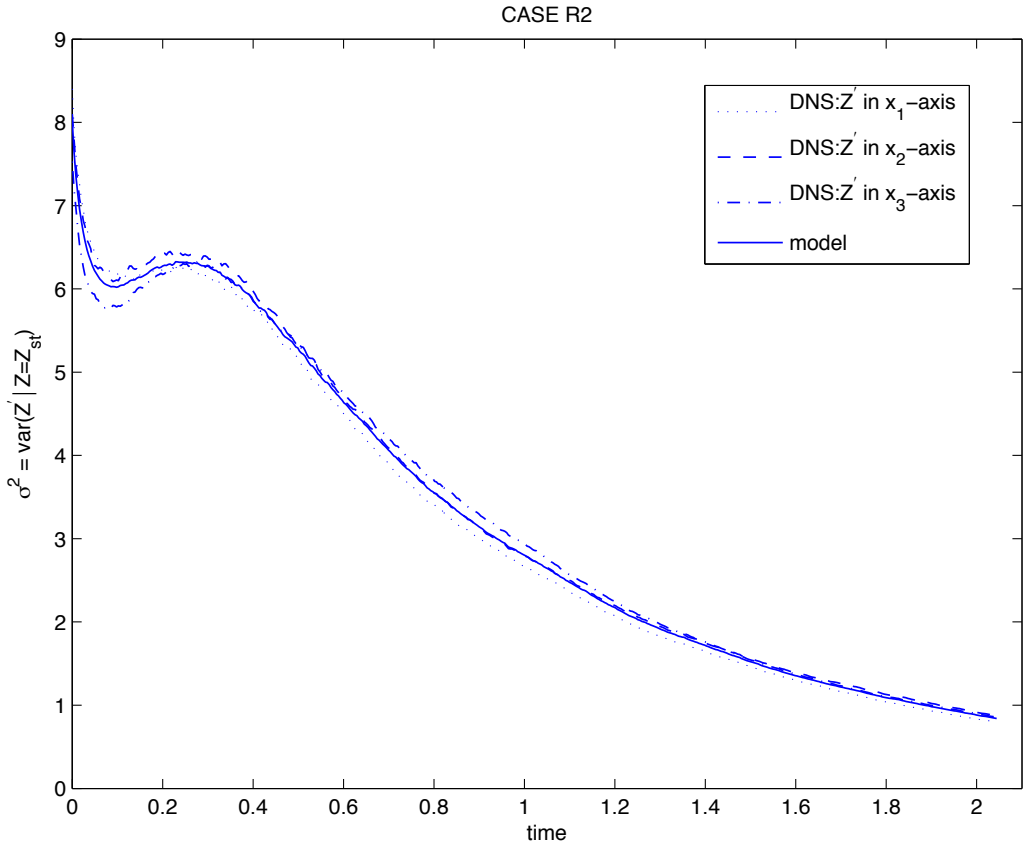

Figure 4.12: The time evolution of σ^2 calculated using DNS data with respect to x_1-(dotted), x_2-(dashed) and x_3-direction(dash-dot), and the one approached by model Eq.(4.35)(solid).

Then, substituting it into Eq.(4.30), the $\langle|Q|\rangle$ can be given in terms of $\langle\chi_{st}\rangle$ as

$$\langle|Q|\rangle = \sqrt{\frac{\langle\chi_{st}\rangle}{3\pi D_f}}. \tag{4.36}$$

The $\langle|Q|\rangle$ predicted by the model Eq.(4.36) with input parameter $\langle\chi_{st}\rangle$ taken from DNS is indicated by a solid line as shown in Fig.(4.13). Also included for comparisons are the ones numerically estimated with respect to three different directions by using DNS data. By comparing Fig.(4.13) with Fig.(4.10), both models exhibit deviations from actual results in same behavior. It means that the modeled $\langle|Q|\rangle$ due to Eq.(4.36) with variance σ^2 approximated by $\langle\chi_{st}\rangle$ can reproduce the one predicted due to Eq.(4.30) with σ^2 taken from DNS in quite good agreement. This corroborates earlier statement that the prediction

of σ^2 using $\langle \chi_{st} \rangle$ is accurate regardless of direction due to isotropy. As shown in this figure, the discrepancies resulting from the comparison between the predicted and actual $\langle |Q| \rangle$ are attributed only to the presumed normal distribution of Q.

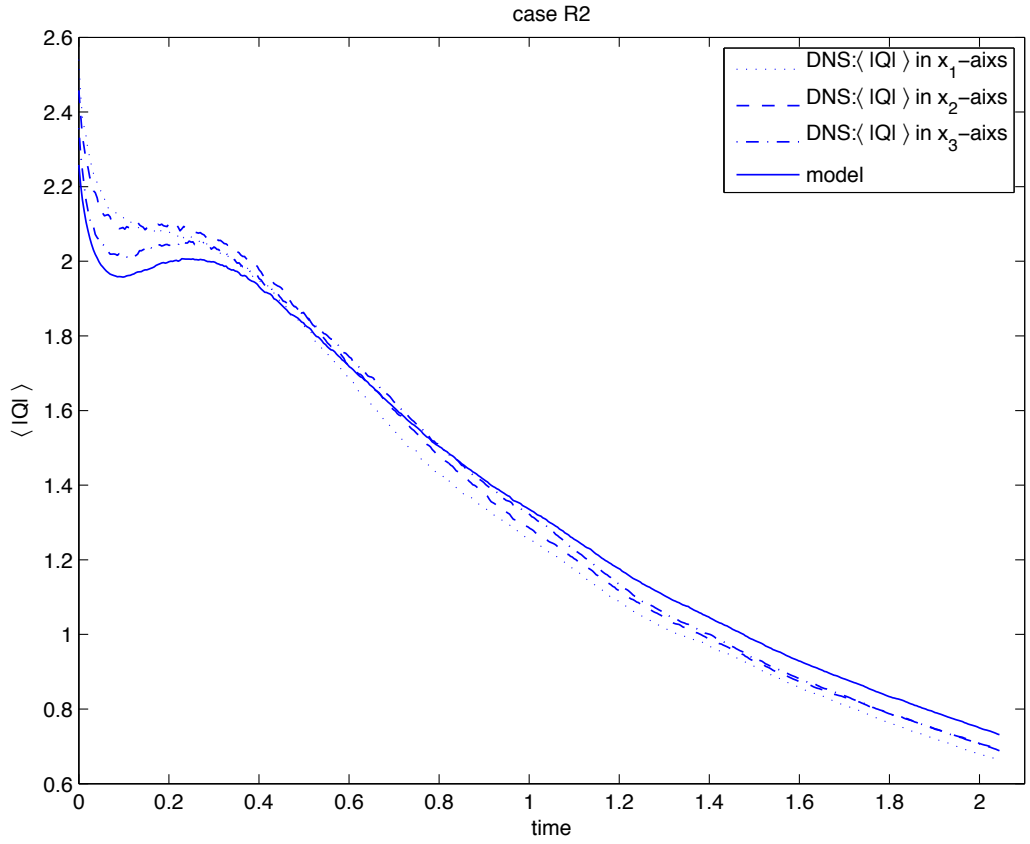

Figure 4.13: The time evolution of $\langle |Q| \rangle$ numerically obtained from DNS with respect to x_1-(dotted), x_2-(dashed) and x_3-direction(dash-dot), respectively. And the one predicted by model Eq.(4.36) in terms of $\langle \chi_{st} \rangle$(solid).

In summary, the flame surface area can be predicted with $\langle Z \rangle$, $\langle Z''^2 \rangle$ and $\langle \chi_{st} \rangle$ by substituting Eq.(4.27) and Eq.(4.36) into Eq.(4.26) as follows:

$$A = 2L^3 \, f_\beta(Z = Z_{st}; \langle Z \rangle, \langle Z''^2 \rangle) \sqrt{\frac{\langle \chi_{st} \rangle}{3\pi D_f}} \tag{4.37}$$

The flame surface area modeled by Eq.(4.37) is plotted in Fig.(4.14) together with the 'exact result' obtained using the scheme described in Section 3.5. During early times in

simulations, the observed minor deviations are only caused by the underprediction of $\langle|Q|\rangle$, which is due to the presumed PDF shape of Q since the second term, i.e., $P_Z(Z = Z_{st})$, can be more adequately modeled. As time proceeds, the deviations between the modeled and the 'exact' results are due to: (a) a slight overprediction of modeled $P_Z(Z = Z_{st})$, and (b) overprediction of modeled $\langle|Q|\rangle$, which becomes more pronounced. We realize that specifying a more appropriate PDF shape of variable Q can significantly improve the flame surface area model.

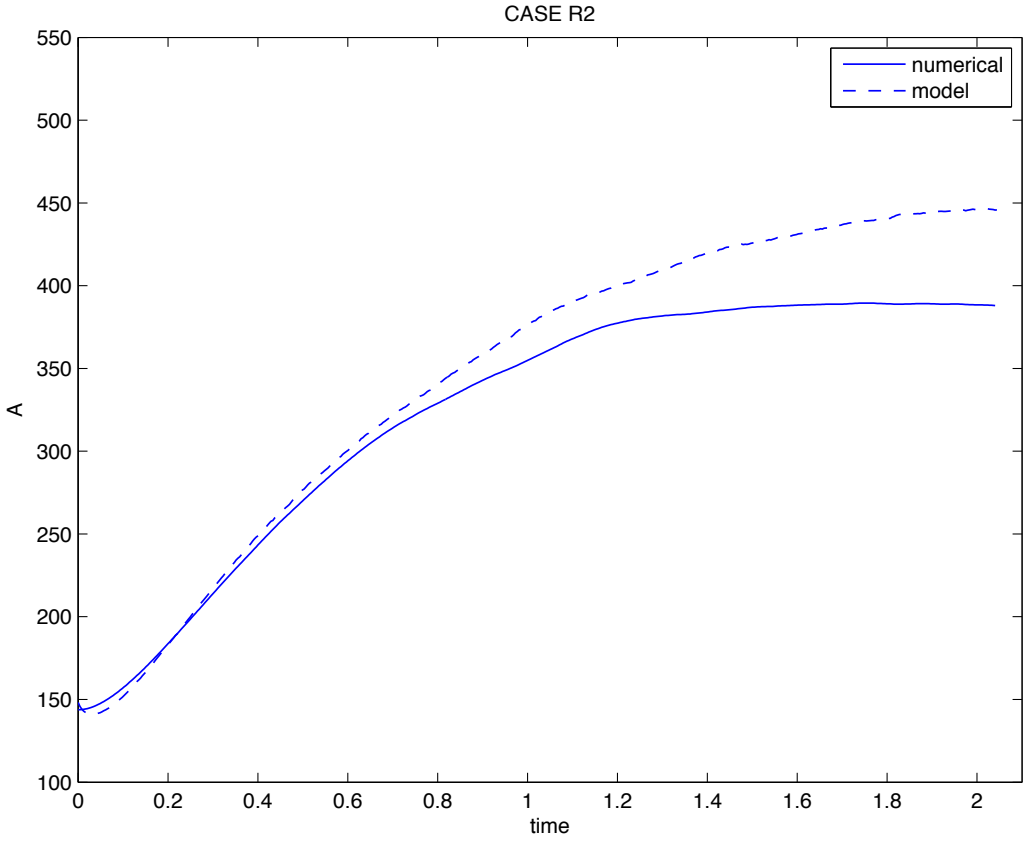

Figure 4.14: The time evolution of flame surface area obtained from DNS(solid) is compared with the one modeled by Eq.(4.37)(dashed) where the required parameters $\langle Z\rangle$, $\langle Z''^2\rangle$ and $\langle\chi_{st}\rangle$ are taken from DNS.

4.5.4 A further model for $\langle|Q|\rangle$ in terms of $\langle\chi\rangle$

Due to Eq.(4.37), $\langle\chi_{st}\rangle$ is one of the required input parameters for modeling the flame surface area. Cook et al.[6] related this conditional mean scalar dissipation rate to the unconditional mean scalar dissipation rate based on the flamelet structure.

$$\langle\chi_{st}\rangle = \frac{\langle\chi\rangle f(Z_{st})}{\int_{Z=0}^{1} f(Z)P_Z(Z)\,dZ} \tag{4.38}$$

Here

$$\begin{cases} f(Z) &= exp(-2\left[erfc^{-1}(2Z)\right]^2) \\ P_Z(Z) &= \text{presumed as a } \beta\text{-distribution,} \end{cases}$$

where $erfc^{-1}(\cdot)$ is the inverse of error function, $erfc(\cdot)$.

The modeled $\langle\chi_{st}\rangle$ as well as the one taken from DNS are plotted in Fig.(4.15). The model tends to underpredict $\langle\chi_{st}\rangle$ by 4% during early simulation times. As time proceeds, the model can almost make an exact prediction.

Given $\langle\chi_{st}\rangle$ in terms of $\langle\chi\rangle$, the consistent form of $\langle|Q|\rangle$ is expressed as

$$\langle|Q|\rangle = \sqrt{\frac{1}{3\pi D_f}\frac{\langle\chi\rangle f(Z_{st})}{\int_{Z=0}^{1} f(Z)P_Z(Z)\,dZ}}. \tag{4.39}$$

If we substitute the expression for $\langle\chi_{st}\rangle$ directly into Eq.(4.37), the modeling of the flame surface area can be recast in terms of $\langle Z\rangle$, $\langle Z''^2\rangle$ and $\langle\chi\rangle$ as

$$A = 2L^3\, f_\beta(Z = Z_{st};\langle Z\rangle,\langle Z''^2\rangle)\sqrt{\frac{1}{3\pi D_f}\frac{\langle\chi\rangle f(Z_{st})}{\int_{Z=0}^{1} f(Z)f_\beta(Z;\langle Z\rangle,\langle Z''^2\rangle)\,dZ}}. \tag{4.40}$$

In Fig.4.16, both the time evolution of flame surface area modeled by Eq.(4.40) and the one obtained numerically from DNS data are plotted. Comparing with Fig.4.14, we observe that using $\langle\chi_{st}\rangle$ predicted by the model based on $\langle\chi\rangle$ rather than taken directly from DNS can increase the underpredictions during early simulation times but reduce the overpredictions in later times. It results from the underprediction of $\langle|Q|\rangle$ corresponding to the underprediction of $\langle\chi_{st}\rangle$ with the use of $\langle\chi\rangle$.

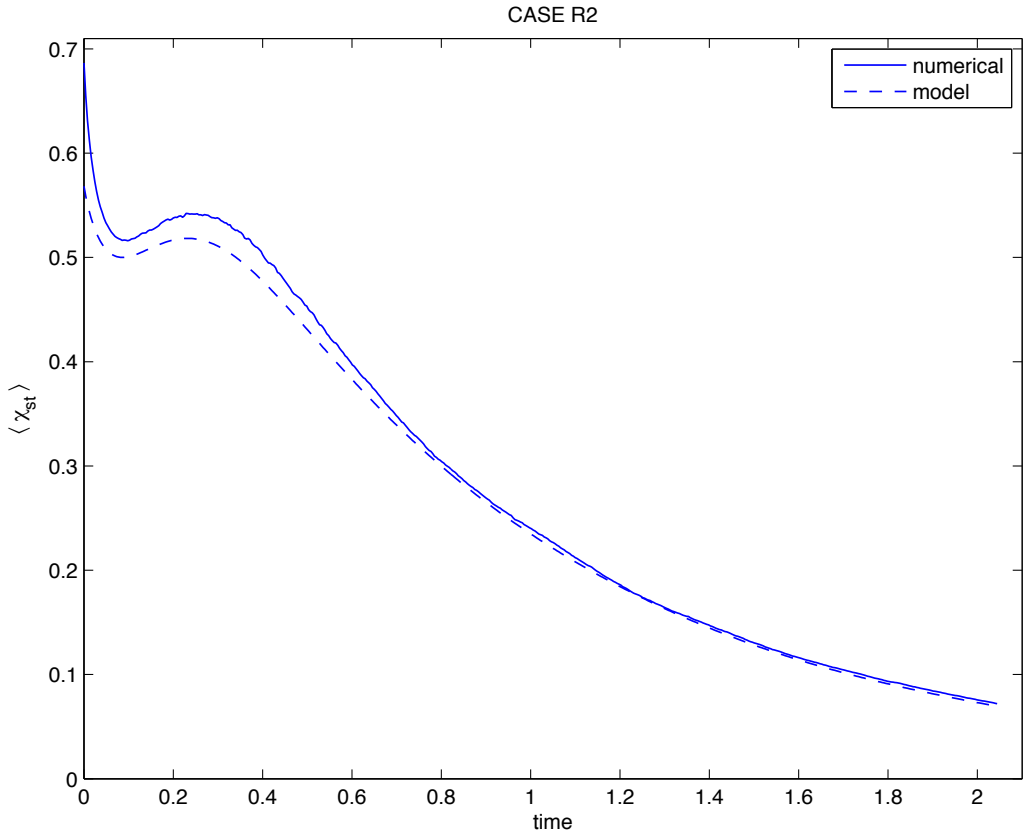

Figure 4.15: The mean scalar dissipation rate conditioned on $Z = Z_{st}$, $\langle \chi_{st} \rangle$, versus time. The solid line indicates the result calculated directly from DNS, and the dashed line represents the one approximated by the model with $\langle Z \rangle$, $\langle Z''^2 \rangle$ and $\langle \chi \rangle$ taken from DNS.

4.6 Test With Higher Reynolds Number Case R4

In this section, the flame surface area model will be tested in higher Reynolds number case (i.e., case R4). The previous proposed modeling procedures that are presented through case R2 will be equally applied to case R4, and then the validation of the model for higher Reynolds number and the influence of the small scales on the model will be investigated by comparing with the available DNS data and the previous model results obtained from case R2.

The theoretical approach to flame surface area, Eq.(4.26), is recovered and applied to case R4 as displayed in Fig.4.17. The upper two curves in the figure correspond to the case

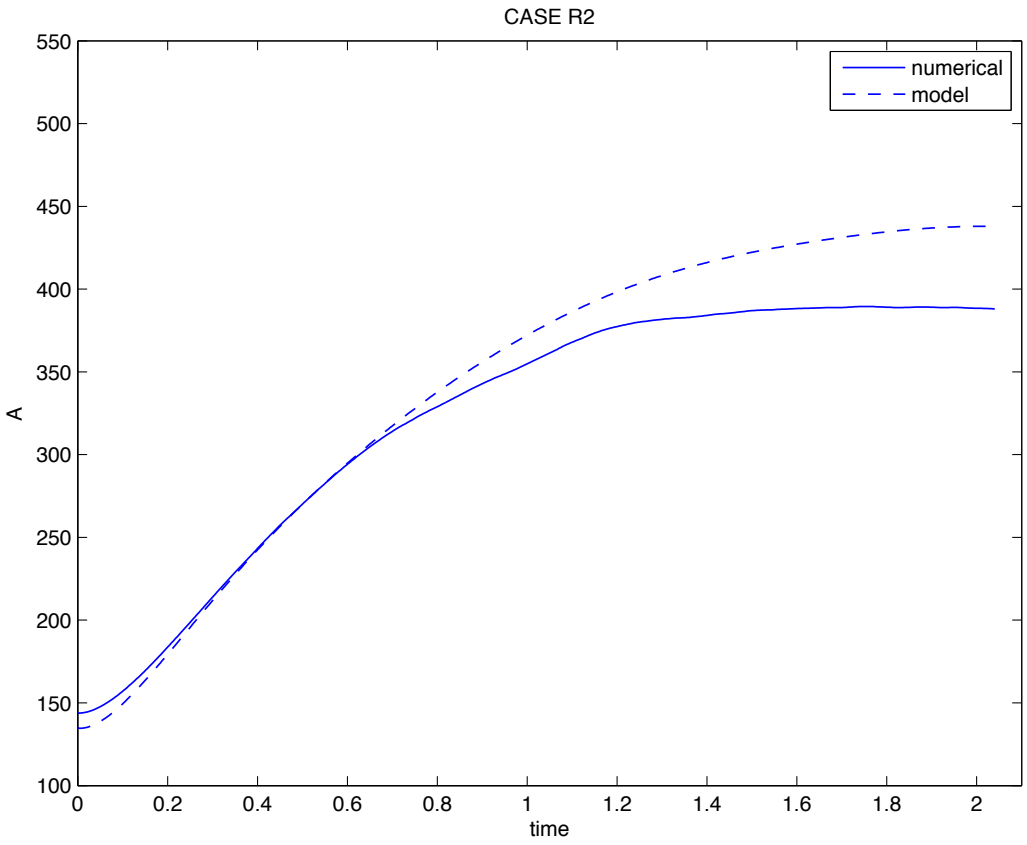

Figure 4.16: The time evolution of flame surface area obtained from DNS(solid) is compared with the one modeled by Eq.(4.40)(dashed) where the required parameters $\langle Z \rangle$, $\langle Z''^2 \rangle$ and $\langle \chi \rangle$ are taken from DNS.

R4, and the lower two curves generated based on case R2 are also included for reference. From the figure, there are two findings worth mentioning: (1) The theoretical formula can certainly provide a very accurate estimate of flame surface area even in higher Reynolds number case. (2) The different area show up between different cases can be attributed to the effect of Reynolds number. The flame surface area is increased by the more intense turbulence with greater stretching, folding and wrinkling.

The presumed β distribution for approximation $P_Z(Z_{st})$ as expressed in Eq.(4.27) is applied to case R4. The numerical and modeled profiles for both cases are given in Fig.4.18. The assumed β distribution model is shown to work even better for higher Reynolds number

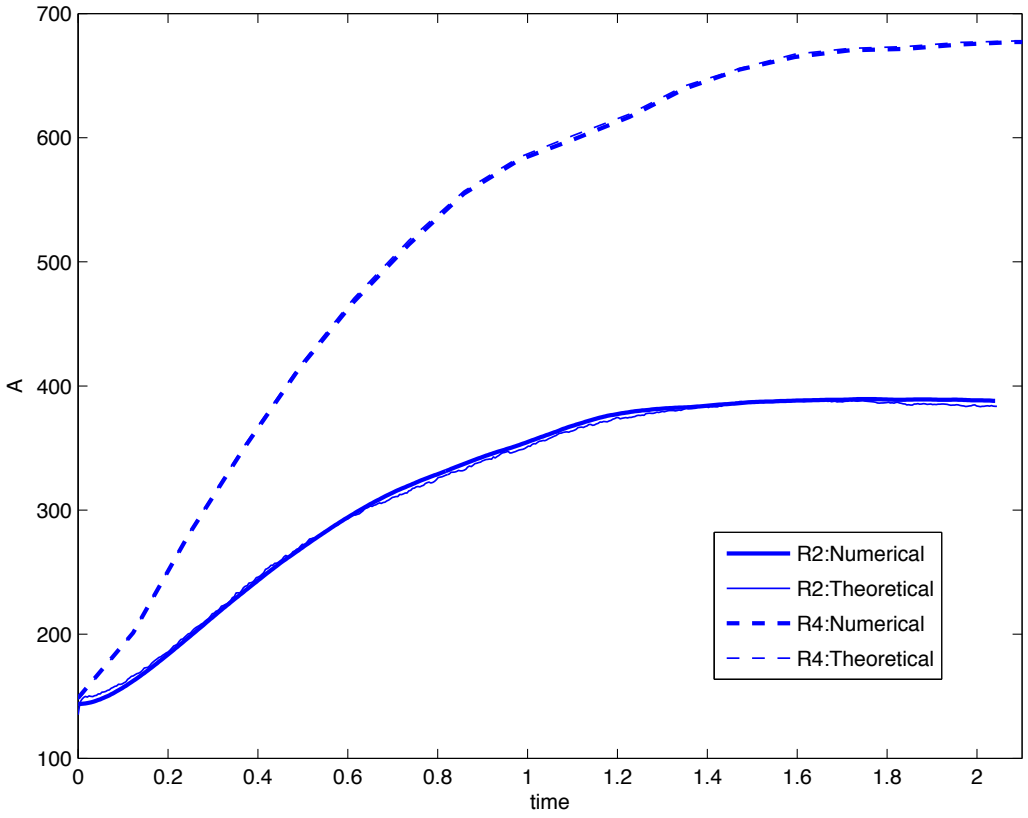

Figure 4.17: The time evolution of flame surface area: case R2(lower two curves): DNS(bold solid), theoretical formula(normal solid); case R4(upper two curves): DNS(bold dashed), theoretical formula(normal dashed). The required parameters $P_Z(Z_{st})$ and $\langle|Z^{'}|\,|\,Z = Z_{st}\rangle$ in theoretical formula Eq.(4.26) are directly taken from DNS.

flow field.

The Eq.(4.36) and Eq.(4.39) for predicting $\langle|Q|\rangle$ are applied to case R4 and assessed against available DNS data. Also, the results from case R2 are included in the same figure for reference with the aim of investigating the impact of small scales on the model. As demonstrated in Fig.4.19, the difference between two predictions is unnoticeable that confirms the appropriateness of the $\langle\chi_{st}\rangle$ model given by Eq.(4.38), but the deviation between the prediction and the numerical values increases with increasing Reynolds number. As previously discussed, the deviation in modeling the term $\langle|Q|\rangle$ can be traced back to the deviation between the shape of PDF of Q and the presumed normal distribution. The

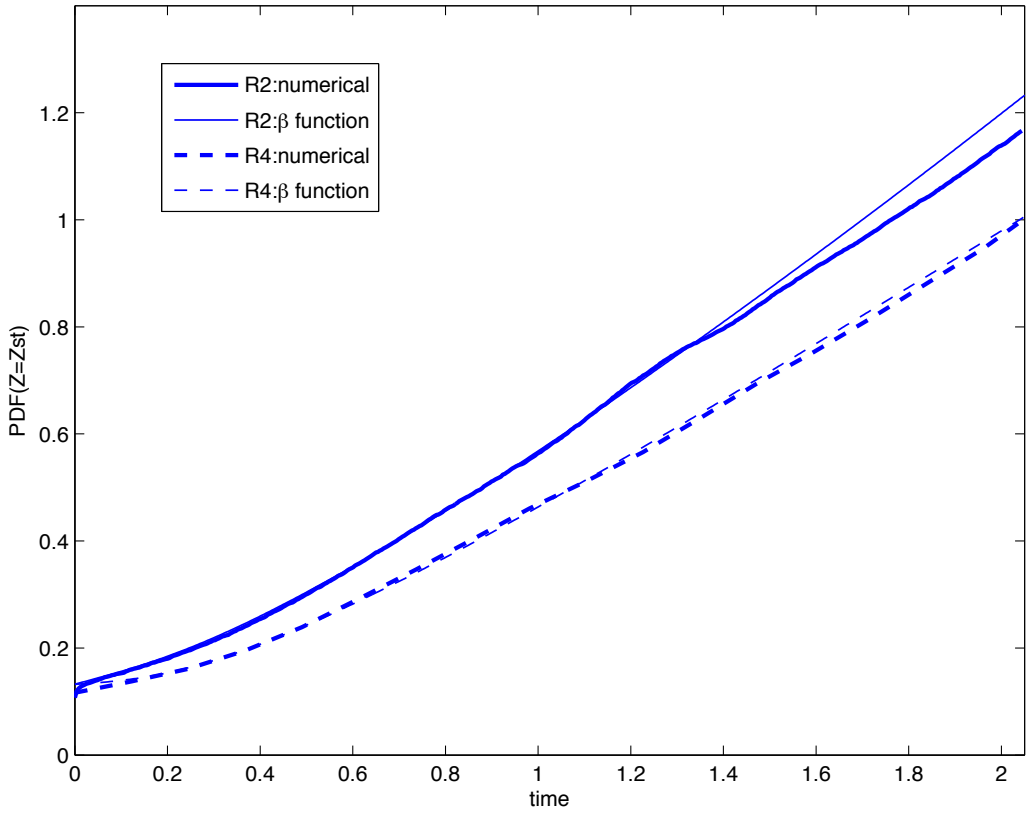

Figure 4.18: The time evolution of $P_Z(Z_{st})$: case R2(upper two curves): DNS(bold solid), $\beta-$PDF approach(normal solid); case R4(lower two curves): DNS(bold dashed), $\beta-$PDF approach(normal dashed). The requirement parameters $\langle Z \rangle$ and $\langle Z''^2 \rangle$ are taken from DNS.

non-Gaussian tails in PDF of scalar gradients is stronger with increasing Reynolds number. The implication of this intermittency on the area prediction will be explored subsequently.

Likewise, the model Eq.(4.37) and Eq.(4.40) are employed to predict the flame surface area for case R4. The model formula is composed of two terms, $P_Z(Z_{st})$ and $\langle |Q| \rangle$, the accurate prediction of $P_Z(Z_{st})$ model implies that the appropriateness of $\langle |Q| \rangle$ model is responsible for the accuracy of the area prediction. As shown in Fig.4.20, the difference between two predictions and the deviation between the prediction and DNS results agree with the conclusions when examining the model for $\langle |Q| \rangle$.

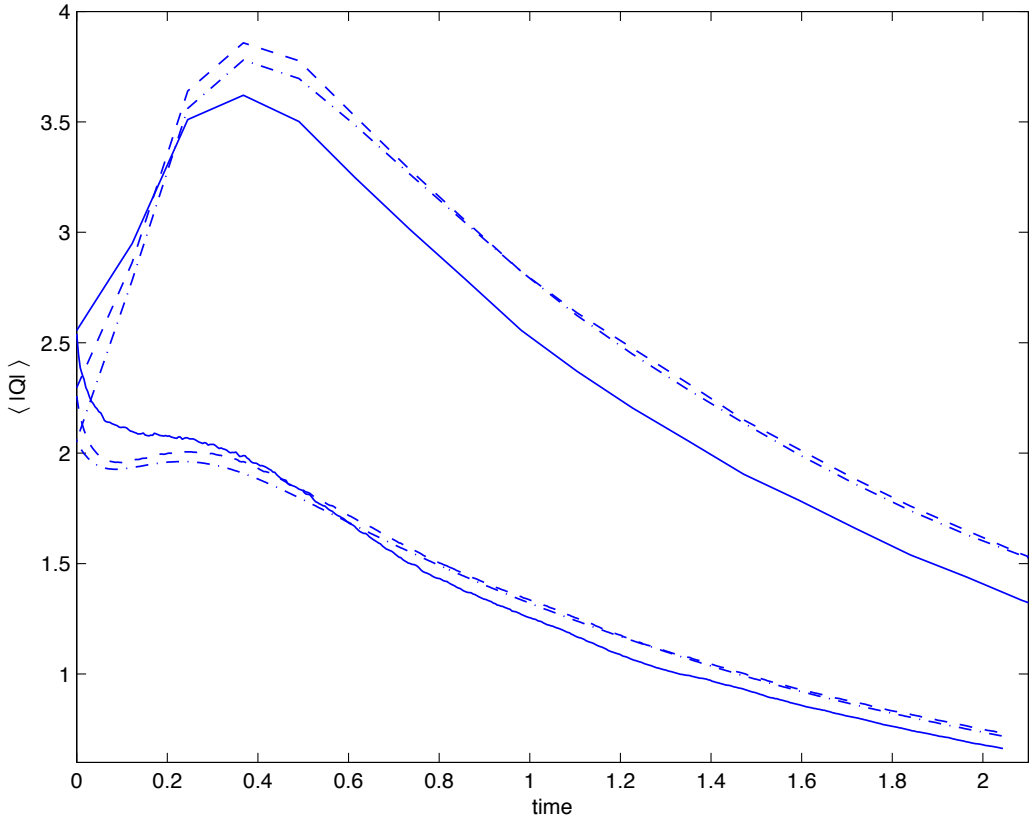

Figure 4.19: The time history of $\langle|Q|\rangle$: case R2(lower three curves), case R4(upper three curves). DNS(solid), prediction from Eq.(4.36)(dashed) where $\langle\chi_{st}\rangle$ is taken from DNS, prediction from Eq.(4.39)(dash-dot) where $\langle Z\rangle$, $\langle Z''^2\rangle$ and $\langle\chi\rangle$ are taken from DNS.

4.7 An Alternative Model for $\langle|Z^{'}|\mid Z=Z_{st}\rangle$

Before exploring an alternative model for $\langle|Q|\rangle$, due to the isotropic turbulence, a relationship between $\langle|\partial Z/\partial x_1|\mid Z=Z_{iso}\rangle$ and $\langle|\nabla Z|\mid Z=Z_{iso}\rangle$ is proposed as

$$\langle|\frac{\partial Z}{\partial x_1}|\mid Z=Z_{iso}\rangle=\frac{1}{2}\langle|\nabla Z|\mid Z=Z_{iso}\rangle, \tag{4.41}$$

where $\langle\cdot\mid Z=Z_{iso}\rangle$ represents the area weighted average conditioned on isosurface specified by any constant value of Z_{iso}.

This relationship is validated through comparison of the time evolution of $\langle|\partial Z/\partial x_1|\mid Z=Z_{iso}\rangle$ with the one of $0.5\langle|\nabla Z|\mid Z=Z_{iso}\rangle$ by using DNS data as shown in Fig.4.21. The comparison is performed for a series of Z_{iso} values ranging from 0.1 to 0.5 with step size 0.1.

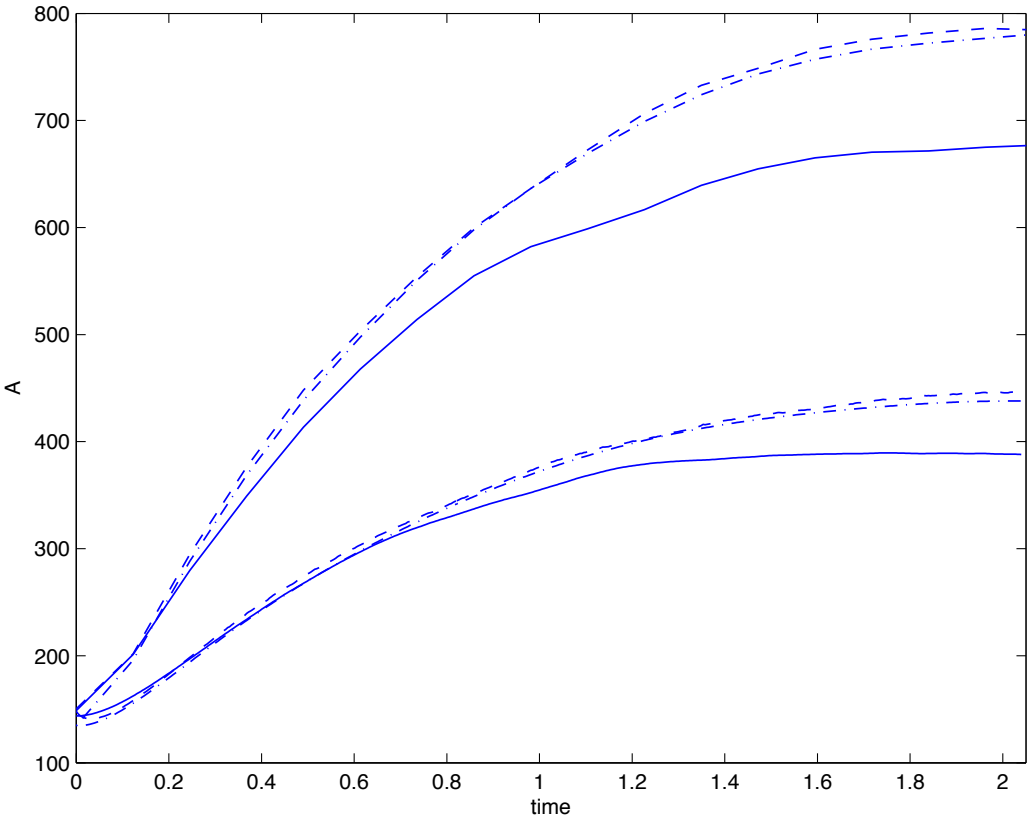

Figure 4.20: The time evolution of flame surface area: case R2(lower three curves), case R4(upper three curves). DNS(solid), prediction from Eq.(4.37)(dashed), prediction from Eq.(4.40)(dash-dot).

The lower and upper ten curves correspond to the case R2 and R4, respectively. From the figure, the constant coefficient 1/2 of the proposed relationship holds for isosurface specified by any constant value of Z_{iso} and any Reynolds number case as long as it is in an isotropic turbulent field. This relationship provides a solid basis for the further modeling. To be more specific, the relationship Eq.(4.41) applied to flame surface (i.e., $Z_{iso} = Z_{st} = 0.5$) yields

$$\langle |Q| \rangle = \frac{1}{2} \langle |\nabla Z| \mid Z = Z_{st} \rangle. \tag{4.42}$$

For notational convenience, R and S are introduced and defined as

$$R \quad = \quad (|\nabla Z|^2 \mid Z = Z_{st}) = \frac{\chi_{st}}{2D_f}$$

$$S = (|\nabla Z| \mid Z = Z_{st}) = +\sqrt{R}. \tag{4.43}$$

Then, the relationship given in Eq.(4.42) can be expressed as

$$\langle |Q| \rangle = \frac{1}{2}\langle S \rangle. \tag{4.44}$$

Thus, $\langle |Q| \rangle$ can be determined accordingly once $\langle S \rangle$ is predicted.

In previous section, the development for modeling $\langle |Q| \rangle$ starts with a presumed normal distribution with zero mean for Q. But it is well known that a lognormal distribution is generally assumed for stoichiometric scalar dissipation rate from both experimental observations and numerical simulations. And R, defined as $(|\nabla Z|^2 \mid Z = Z_{st})$ in present analysis, is proportional to the scalar dissipation rate with a constant coefficient of $2D_f$. So it is more relevant to assume that R is a lognormal distribution. In this section, from both modeling and physics standpoints, the modeling for $\langle |Q| \rangle$ will be developed by starting with a presumed lognormal distribution of R. In this regard, the R is assumed to be a lognormal distribution, and then $\langle S \rangle$ is determined in terms of the statistical moments of R , which will ultimately be $\langle |Q| \rangle$.

The probability distribution model for the random variable R is presumed to be a lognormal distribution as

$$P_R(r; m, a) = \frac{1}{r \cdot a \cdot \sqrt{2\pi}}\, exp\left(-\frac{(\ln r - m)^2}{2a^2}\right),\ r > 0. \tag{4.45}$$

Here the parameters m and a are mean and standard deviation of random variable R's natural logarithm, respectively. Subsequently, the shape parameter m and a needs to be determined in terms of the statistical moments of R. Due to the probability theory, the n-th moments of lognormally distributed variable R is defined as

$$\langle R^n \rangle = exp(nm + \frac{1}{2}n^2a^2) \tag{4.46}$$

To be specific, the first and second moments of log normally distributed variable R are as follows:

$$\begin{aligned} \langle R \rangle &= exp(m + \frac{1}{2}a^2) = \frac{\langle \chi_{st} \rangle}{6D_f} \\ \langle R^2 \rangle &= exp(2m + 2a^2) \end{aligned} \tag{4.47}$$

Consequently, the shape parameter m and a can be determined in terms of the first and second moments of R as

$$\begin{aligned} exp(m) &= \frac{exp(2m+a^2)}{exp(m+a^2)} = \frac{\langle R\rangle^2}{\langle R^2\rangle^{1/2}} \\ exp(a^2) &= \frac{exp(2m+2a^2)}{exp(2m+a^2)} = \frac{\langle R^2\rangle}{\langle R\rangle^2} \end{aligned} \tag{4.48}$$

The presumed lognormal distribution for R as described by Eq.(4.45) with shape parameters m and a^2 (i.e., $\langle R\rangle$ and $\langle R^2\rangle$) taken from DNS data is evaluated through comparing against the one numerically estimated by using DNS data. The comparisons are carried out at four selected simulation times of case R2 and R4, respectively, as shown in Fig.(4.22) and Fig.(4.23). The comparisons demonstrate that the lognormal distribution appears to be a good approximation except the minor deviations in the tail due to the turbulent intermittency. And, the deviation becomes significant in higher Reynolds number case R4.

Let $S = g(R) = +\sqrt{R}$ be a strictly increasing function of R with inverse function $R = g^{-1}(S) = S^2$. Then the probability density function for random variable S can be derived by applying the change-of-variable rule (i.e., transformation formula) on the lognormal density function of R.

$$\begin{aligned} P_S(s;\hat{m},\hat{a}) &= P_R[g^{-1}(s)]\cdot|\frac{d}{ds}g^{-1}(s)| \\ &= P_R(s^2)\cdot|\frac{d}{ds}s^2| = P_R(s^2)\cdot|2s| \\ &= \frac{|2s|}{s^2\cdot a\cdot\sqrt{2\pi}}\ exp\left(-\frac{(\ln s^2 - m)^2}{2a^2}\right) \\ &= \frac{2}{|s|\cdot a\cdot\sqrt{2\pi}}\ exp\left(-\frac{(2\ln s - m)^2}{2a^2}\right) \\ &= \frac{1}{|s|\cdot(a/2)\cdot\sqrt{2\pi}}\ exp\left(-\frac{(\ln s - m/2)^2}{2(a/2)^2}\right) \\ &\quad \text{let} \quad \hat{m} = \frac{m}{2}; \quad \hat{a} = \frac{a}{2} \\ &= \frac{1}{|s|\cdot\hat{a}\cdot\sqrt{2\pi}}\ exp\left(-\frac{(\ln s - \hat{m})^2}{2\hat{a}^2}\right) \\ &\quad \text{since} \quad s > 0 \\ &= \frac{1}{s\cdot\hat{a}\cdot\sqrt{2\pi}}\ exp\left(-\frac{(\ln s - \hat{m})^2}{2\hat{a}^2}\right) \end{aligned} \tag{4.49}$$

From above derivations, the probability density function for S is a lognormal distribution with mean $\hat{m}$ and standard deviation $\hat{a}$. Accordingly, the expected value of S (or equivalently $\langle|Q|\rangle$) can be determined in terms of $\hat{m}$ and $\hat{a}$ due to probability theory as

$$\langle S\rangle = exp(\hat{m} + \frac{1}{2}\hat{a}^2). \tag{4.50}$$

Equivalently, the expected value of S can also be recast in terms of m and a through $\hat{m} = m/2$ and $\hat{a} = a/2$ as

$$\langle S\rangle = exp(\hat{m} + \frac{1}{2}\hat{a}^2) = exp[\frac{m}{2} + \frac{1}{2}(\frac{a}{2})^2]. \tag{4.51}$$

Accordingly, substituting Eq.(4.48) in Eq.(4.51), $\langle S\rangle$ can be determined in terms of the first and the second moments of R as

$$\begin{aligned}
\langle S\rangle &= exp[\frac{m}{2} + \frac{1}{2}(\frac{a}{2})^2] \\
&= exp[\frac{m}{2} + \frac{1}{8}a^2] = exp[\frac{m}{2} + \frac{1}{4}a^2 - \frac{1}{8}a^2] \\
&= exp[\frac{1}{2}(m + \frac{1}{2}a^2) - \frac{1}{8}a^2] \\
&= exp[\frac{1}{2}(m + \frac{1}{2}a^2)]exp(-\frac{1}{8}a^2) \\
&= \langle R\rangle^{1/2}\left[\frac{\langle R^2\rangle}{\langle R\rangle^2}\right]^{-1/8}
\end{aligned} \tag{4.52}$$

Finally, $\langle|Q|\rangle$ is predicted in terms of the first and the second moments of R as

$$\langle|Q|\rangle = \frac{1}{2}\langle S\rangle = \frac{1}{2}\langle R\rangle^{1/2}\left[\frac{\langle R^2\rangle}{\langle R\rangle^2}\right]^{-1/8}. \tag{4.53}$$

Then, the performance of the alternative model prediction Eq.(4.53) for $\langle|Q|\rangle$ is compared with the previous model predictions Eq.(4.36) and Eq.(4.39) with respect to the results obtained directly from DNS. Note that the first two moments of R as the required shape parameters in the alternative model are taken directly from DNS. As shown in Fig.(4.24), the discrepancies between the alternative model and the DNS keep roughly invariant with time. In comparison with the previous model for $\langle|Q|\rangle$, the alternative model prediction starting with the presumed lognormal distribution of R performs better than the model

starting with the presumed normal distribution of Q, and the improvement is more prominent in higher Reynolds number case.

Substituting the model predictions for $P_Z(Z = Z_{st})$(Eq.(4.27)) and $\langle|Q|\rangle$(Eq.(4.53)) into Eq.(4.26), the flame surface area A can be approximated as

$$A = L^3 \, f_\beta(Z = Z_{st}; \langle Z\rangle, \langle Z''^2\rangle) \, \langle R\rangle^{1/2} \left[\frac{\langle R^2\rangle}{\langle R\rangle^2}\right]^{-1/8}. \tag{4.54}$$

The performance of the alternative model Eq.(4.54) is compared with the previous model predictions Eq.(4.37) and Eq.(4.40) with respect to the flame surface area A taken directly from DNS. As shown in Fig.(4.25), the advantage of alternative model over previous model is obvious, especially for higher Reynolds number case.

4.8 Governing Equation for Flame Surface Area

The discussion presented so far has revolved around the flame surface. For a diffusion flame, the flame surface is identified by the stoichiometric isolevel surface that corresponds to one particular isoscalar value $Z_{iso} = Z_{st}$, so the numerical measurement and the theoretical formulation for the flame surface area A presented in previous section 3.5 and 4.3 can be applied not only to flame surface but to an isosurface specified by any constant value of Z_{iso}. In this section, these approaches with DNS data are employed to numerically investigate the balance equation for isosurface area per unit volume Σ_{iso} where the isosurface is specified by mixture fraction isolevel with any constant value of Z_{iso}.

4.8.1 Time evolution of mean isosurface area density Σ_{iso}

First, applying the algorithm described in section3.5 for numerically extracting and calculating the flame surface area A in Matlab environment, with respect to simulations R2 and R4, the time evolution of the isosurface area per unit volume Σ_{iso} extracted from the DNS volume data is plotted in Fig.(4.26) as a function of time for seven specific isovalues, $Z_{iso} = 0.01, 0.05, 0.1, 0.2, 0.3, 0.4$, and 0.5, respectively. Note that only half range of the mixture fraction is necessary since the isosurface area is symmetric with respect to the mixture fraction value 0.5 due to the scheme to initialize Z.

At the initial time, the mixture fraction field is artificially designed to be blobs of fuel and oxidant ($Z = 1$ and $Z = 0$). The fuel blobs ($Z = 1$) occupy about half of the computational domain, with oxidant ($Z = 0$) occupying approximately the other half, the mixing layer between them is very thin. Take case R2 for example, as shown in Fig.(4.27), for surfaces corresponding to mixture fraction isolevel values $0.03 < Z_{iso} < 0.97$, the surface areas have almost the same magnitude. But for isosurface with isovalue of 0.01, the surface area has a remarkably large value. For isosurfaces in the region close to pure oxidant/fuel(i.e., $Z_{iso} = 0.01$), the high wavenumber spectral truncation scheme, which is used in initializing Z for the purpose of smoothing out the steep spatial gradients from a jump discontinuity between $Z = 0$ and 1, results in the occurrence of fluctuations at Z values close to 0 and 1. These fluctuations persist due to the Gibbs phenomenon and are responsible for the layers of slices which can be observed from the 3D visualization of isosurface at $Z_{iso} = 0.01$, as exhibited on top left plot in Fig.(4.28). Accordingly, this can explain the initial larger area of the isosurface corresponding to $Z_{iso} \leq 0.01$ as seen in Fig.(4.27). Consequently, as seen in Fig.(4.26), all time evolution curves of each case start out with almost the same small magnitude except for isovalue $Z_{iso} = 0.01$.

For both cases with different Reynolds numbers, the mixing by molecular diffusion contributes to minimize the variance of mixture fraction. Therefore, as mixing proceeds, the mixture fraction takes on values approaching the stoichiometry, so the maximum area corresponds to the stoichiometric surface Z_{st}, and the farther away the isovalue Z_{iso} is from Z_{st}, the earlier its isosurface area starts to decrease. For the time evolution curves corresponding to mixture fraction isovalues $Z_{iso} \neq 0.5$, the initial increase followed by a decrease is due to the imbalance between turbulent stretching and molecular diffusion, which will be further investigated through the analysis of the balance equation for mean isosurface area density Σ_{iso} in the following section. Comparing these two Reynolds number cases, the higher the Reynolds number, the larger the resulting isosurface area due to the stronger turbulence.

4.8.2 Balance equation for mean isosurface area density Σ_{iso}

The behaviors of the time evolution of mean isosurface area density change with different isoscalar values as shown in Fig.(4.26). In this section, the balance equation governing the time evolution of Σ_{iso} is derived and extensively investigated. The theoretical approach for predicting the time evolution of flame surface area A as presented in previous section 4.3 can be generalized to isosurface specified by any isovalue of Z_{iso} and serve as the basis for developing the balance equation for Σ_{iso}.

Accordingly the theoretical formulation of flame surface area A as described by Eq.(4.26) can be generalized to give the definition for area A_{iso} of isosurface with any isovalue Z_{iso} as:

$$A_{iso} = (2L^3)\ P_Z(Z_{iso})\langle |Z^{'}| \mid Z = Z_{iso}\rangle. \tag{4.55}$$

Equivalently, the mean area of isosurface with any isovalue Z_{iso} per unit volume, Σ_{iso}, can thus be defined as:

$$\Sigma_{iso} = \frac{A_{iso}}{L^3} = 2\ P_Z(Z_{iso})\langle |Z^{'}| \mid Z = Z_{iso}\rangle. \tag{4.56}$$

Substituting the relationship Eq.(4.41) into above Eq.(4.56), the expression for isosurface area density Σ_{iso} is recast as

$$\Sigma_{iso} = P_Z(Z_{iso})\langle |\nabla Z| \mid Z = Z_{iso}\rangle. \tag{4.57}$$

This definition has the same formulation as the mean flame surface density Σ, but in a little different notation, which is formulated through the concept of probability density function (pdf) as [40],[67]:

$$\Sigma = \overline{|\nabla Z|\delta(Z - Z_{st})} = \overline{|\nabla Z| \mid Z = Z_{st}}\ p(Z_{st}) \tag{4.58}$$

where δ is the Dirac-delta function, $\overline{()}$ represents the ensemble average and $\overline{|\nabla Z| \mid Z = Z_{st}}$ denotes the average of ∇Z conditioned on the stoichiometric surface $Z = Z_{st}$.

The transport equation for the mean flame surface density Σ was first proposed by Marble and Broadwell from empirical and phenomenological arguments[20]. Starting from the definition of Σ as expressed by Eq.(4.58), together with the governing equation of mixture

fraction(3.8), an exact balance equation for mean flame surface density Σ in an nonpremixed turbulent combustion was derived theoretically by Van Kalmthout and Veynante[14]. As the formula of mean isosurface area density Σ_{iso}(4.57) is the same as the one of mean flame surface density Σ (Eq.(4.58)), the balance equation for Σ can be applied equally to isosurface area density Σ_{iso} as (written in indicial notation):

$$\underbrace{\frac{\partial \Sigma_{iso}}{\partial t}}_{I} + \underbrace{\frac{\partial \bar{u}_i \Sigma_{iso}}{\partial x_i}}_{II} + \underbrace{\frac{\partial \langle u_i{}' \rangle_s \Sigma_{iso}}{\partial x_i}}_{III} = \underbrace{\left\langle \frac{\partial u_i}{\partial x_i} - n_i n_j \frac{\partial u_i}{\partial x_j} \right\rangle_s \Sigma_{iso}}_{IV} + \underbrace{\left\langle w \frac{\partial n_i}{\partial x_i} \right\rangle_s \Sigma_{iso}}_{V} - \underbrace{\frac{\partial \langle w n_i \rangle_s \Sigma_{iso}}{\partial x_i}}_{VI} \tag{4.59}$$

where n_i is the i-th component of the unit vector $\vec{n}$, which is normal to the local instantaneous mixture fraction isosurface Z_{iso} and points towards the oxidizer, $\vec{n} = -\nabla Z/|\nabla Z|$. The surface curvature is given by the divergence of the normal vector $\vec{n}$ as $\nabla \cdot \vec{n}$. The turbulent velocity u_i is composed of its mean and its fluctuating component as $u_i = \bar{u}_i + u_i{}'$. w is the diffusion velocity of the isosurface, defined as

$$w = D_f \frac{\nabla^2 Z}{|\nabla Z|} \tag{4.60}$$

w denotes the relative propagating velocity of the isosurface with respect to the fluid flow due to the diffusion, and is in the direction of scalar gradient (i.e., parallel to the unit normal vector $\vec{n}$)[23]. The introduction of w will be of particular practical use in modeling the time development of Σ_{iso}. The term $\langle \rangle_s$ denotes an isosurface averaging operator, weighted with the local value of $|\nabla Z|$, and is defined for any quantity Q as

$$\langle Q \rangle_s = \frac{\overline{Q|\nabla Z|\delta(Z - Z_{iso})}}{\overline{|\nabla Z|\delta(Z - Z_{iso})}} \tag{4.61}$$

For the numerical implementation, it is convenient to estimate $\langle Q \rangle_s$ by an area-weighted average, with the use of geometric information generated from the isosurface triangulation.

$$\langle Q \rangle_s = \frac{\sum\limits_{ii} Q_{ii} \Delta A_{ii}}{\sum\limits_{ii} \Delta A_{ii}} = \frac{\sum\limits_{ii} Q_{ii} \Delta A_{ii}}{A_{iso}} \tag{4.62}$$

where ΔA_{ii} refers to the elemental area of the $ii-$th triangular face on the triangulated isosurface and the summation is performed over all the triangular faces. The quantity Q_{ii}

represents the value of Q for the $ii-$th triangular face, which is obtained by using the mean value theorem for the surface integral of the quantity Q over the $ii-$th triangular face ((Appendix B)), in which the quantity Q of the three vertices bounding the $ii-$th face is computed by trilinear interpolation on 3D grid DNS results.

The first 4 terms in Eq.(4.59) correspond, respectively, to the unsteady effect(I), the convection by mean turbulent flow(II), the turbulent diffusion(III) and the contribution of isosurface production from the tangential strain rate due to the flow field(IV). The terms (V) and (VI) are the flame surface displacement due to the combined effects of curvature and flow[14].

For homogeneous turbulent flow, which is the subject of current study, the above balance equation(4.59) simplifies to

$$\underbrace{\frac{\partial \Sigma_{iso}}{\partial t}}_{I} = \underbrace{\left\langle -n_i n_j \frac{\partial u_i}{\partial x_j} \right\rangle_s \Sigma_{iso}}_{IV} + \underbrace{\left\langle w \frac{\partial n_i}{\partial x_i} \right\rangle_s \Sigma_{iso}}_{V}. \tag{4.63}$$

Dividing both sides of Eq.(4.63) by the mean isosurface area density Σ_{iso} yields:

$$\underbrace{\frac{1}{\Sigma_{iso}} \frac{\partial \Sigma_{iso}}{\partial t}}_{I} = \underbrace{\left\langle -n_i n_j \frac{\partial u_i}{\partial x_j} \right\rangle_s}_{IV} + \underbrace{\left\langle w \frac{\partial n_i}{\partial x_i} \right\rangle_s}_{V}. \tag{4.64}$$

In the following, the results extracted from the DNS data of case R2 and R4 are employed to evaluate the Σ_{iso}-balance equation, and to analyse and validate the proposed models for the terms involved in the equation, respectively.

The equation(4.64) that governs the evolution of mean isosurface area density Σ_{iso} can be assessed by comparing the LHS with the RHS of equation at all simulation times through the data produced by the DNS. The time discretization on LHS of equation(4.64) is numerically calculated with the second-order central difference scheme. The behavior of the LHS(solid line) and the sum of all terms on the RHS(dash-dot line) of Eq.(4.64) are displayed in Fig.(4.29) as a function of time for different isosurfaces specified at isovalues $Z_{iso} = 0.01$, 0.1, 0.3, and 0.5, respectively. Although the two sides of the equation do not exactly match each other, they track each other quite closely given some confidence in the numerical accuracy of the results. The terms on RHS involve the area-weighted average on the isosurface, which

requires interpolating the vertices that form the triangulation of the isosurface based on 3D uniform grid points. The interpolation scheme applied in current research is trilinear interpolation; the errors in this may explain the deviation between the two curves in each case.

In Fig.(4.30), the term(IV) appearing in Eq.(4.64), denoted by strain rate a_T, is shown as function of time for the seven isosurfaces $Z_{iso} = 0.01$, 0.05, 0.1, 0.2, 0.3, 0.4, and 0.5 in case R2 and R4, respectively. Note that the scale of the vertical axis range is fixed across two panels in the figure for the purpose of comparison. For both cases, it can be observed that the strain rate acting on the surface is positive and thus can be considered as a source term to increase the isosurface area. At initial time, the scalar initialized in blobs is injected into a fully developed turbulent field, so the correlation between scalar and flow field is very weak, which results in a strain rate close to zero as seen in Fig.(4.30). The maximum strain rate occurs at the stoichiometric isosurface, but the average strain rate across the entire mixing layer (i.e., $0.2_{iso} \leq 0.5$) appears to be roughly constant. The differences between the curves corresponding to various isolevel surfaces are almost unnoticeable. Comparing these two cases, the magnitude of term(IV) in higher Reynolds number case is larger due to the stronger local turbulent stretching.

In Fig.(4.31), the term(V) in Eq.(4.64), corresponding to the curvature-induced isosurface displacement, is plotted in the same way as a_T in Fig.(4.30). For both cases, the curvature term takes on a negative value during the entire simulation time and can therefore be regarded as a sink term, therefore decreasing the isosurface area. In comparing these two cases, the term(V) has larger magnitude in higher Reynolds number case.

The imbalance between the surface generation term(IV) and surface consumption term(V) yields a surface area growth followed by a decrease, and is responsible for the deviations between the area densities across different isovalues. Comparing Fig.(4.30) with Fig.(4.31), it is recognized that, even though the deviations between the curves corresponding to different isolevel surfaces are very slight, the deviation between the curves of term(V) is relatively larger than the one of term(IV) (referring to the scale of the vertical axis). It implies that the deviation between the curves of term(V) is the major reason to be responsible for the difference in the behavior of the time evolutions of Σ_{iso} of isosurfaces with different isolevel

values.

The characteristics of local diffusion velocity are exemplified by the area-weighted statistics of the local diffusion velocity conditioned on isosurface in oxidizer(i.e., $Z_{iso} < 0.5$), central region(i.e., $Z_{iso} = 0.5$), respectively, as plotted in Fig.(4.32). As can be seen, except the isosurface close to region of pure oxidizer(i.e., $Z_{iso} = 0.01$), the variances are almost time invariant and the differences between variances are unnoticeable. In nonpremixed flame, the local isosurfaces in oxidizer and fuel regions diffuse away from the central region(i.e., $Z_{iso} = 0.5$), but in opposite directions. The local isosurface in oxidizer(fuel) region moves relative to the flow field with a positive(negative) speed towards the pure oxidizer(fuel) region. It is intuitive to consider that (1)the local diffusion velocity at isosurface $Z_{iso} = 0.5$ is close to zero[33], (2)the local diffusion velocity is symmetric with respect to the zero-velocity at central region. As shown in Fig.(4.32), the variance is small and hence the average value provides a good predictor of the characteristics of local diffusion velocity. In this sense, the above arguments can be evidenced directly by plotting the area-weighted average of the local diffusion velocity conditioned on isosurface in oxidizer(i.e., $0.1 \leq Z_{iso} < 0.5$), fuel(i.e., $0.5 < Z_{iso} \leq 0.6$) and central region(i.e., $Z_{iso} = 0.5$), respectively, as displayed in Fig.(4.33). As can be seen in the figure, for both cases, for isosurface $Z_{iso} = 0.5$, the average value being almost zero over entire simulation time corroborates the above argument that the flame surface identified by $Z_{iso} = 0.5$ has zero local diffusion velocity. The magnitude of diffusion velocity is symmetric around $Z_{iso} = 0.5$ and depends roughly linearly on the isosurface difference between the region and the central isosurface as $C\,(0.5 - Z_{iso})$, here C roughly equals 0.42. In addition, the average of local diffusion velocity is time invariant, especially for isosurfaces within the mixing layer.

The area-weighted statistics of the local curvature conditioned on isosurface are displayed in Fig.(4.34), the same way as for Fig.(4.32). In theory, for an isosurface corresponding to any particular isovalue of Z, the surface average of curvature should be zero in a field of isotropic turbulence that has no preferential direction. But the minor discrepancies resulting from the nonzero surface averaging values are found in the top two panels of Fig.(4.34). The discrepancies are caused by the numerical error involved in the surface averaging scheme. As time proceeds, the deviations become more pronounce. And, the closer an isosurface

is to the pure oxidant/fuel region, the larger the discrepancies grow. The reason is that the isosurfaces in these regions away from the center reduce considerably with time and ultimately disappear. For the variance of curvature, it increases at first and then levels off. Comparing these two cases, the variance of curvature is larger in a higher Reynolds number field, but the averages have the same order of magnitude.

In the following, the models for term(IV) and term(V) will be presented. Note that the models are mainly concerned with mixture fraction isosurfaces not far from the stoichiometric surface (i.e., $0.2 \leq Z_{iso} \leq 0.8$) since the isosurfaces close to pure oxidant/fuel regions tend to vanish in time and therefore cannot yield sufficient statistics to provide any conclusive evidence of the adequacy of the model. So the isosurfaces at isovalues $0.2 \leq Z_{iso} \leq 0.8$ will be mainly considered when evaluating the appropriateness of the model.

The performance of the model proposed for strain rate term a_T is assessed by a comparison against DNS results. For a homogeneous and isotropic turbulent field, a_T may be modeled from the inverse of a turbulent time scale based on Kolmogorov timescale as [14][21]

$$a_T = \gamma \sqrt{\frac{\varepsilon}{\nu}}. \tag{4.65}$$

where constant γ is set as $\gamma = 0.27$ and 0.25 for case R2 and R4 respectively, which is estimated based on fitting the model predictions to DNS results. ε and ν are, respectively, the turbulent dissipation rate and fluid kinematic viscosity. The model for strain rate term is evaluated with respect to the DNS results as shown in Fig.(4.35). It can be seen that the model predictions are in fairly good agreement with the DNS data except for early simulation times. As exhibited in Fig.(4.30), the strain rate term a_T is roughly invariant at different isolevel surfaces, so the model with a universal constant γ can cover the cases corresponding to various isosurfaces, especially the isosurfaces within mixing layer ($Z_{iso} = 0.2 \sim 0.5$).

Regarding modeling term(V), from a modeling perspective, it is useful to mathematically recast the diffusion velocity w by splitting it into two components that represent the contribution of curvature and normal molecular diffusion, respectively[14].

$$w = D_f \frac{\nabla^2 Z}{|\nabla Z|} = -D_f \nabla \cdot \vec{n} + D_f \frac{\nabla Z \cdot \nabla |\nabla Z|}{|\nabla Z|^2} \tag{4.66}$$

Accordingly, the term(V) can be written as (in vector notation):

$$\langle w\nabla\cdot\vec{n}\rangle_s = \underbrace{-D_f\Big\langle(\nabla\cdot\vec{n})^2\Big\rangle_s}_{a} + \underbrace{D_f\Big\langle\frac{\nabla Z\cdot\nabla|\nabla Z|}{|\nabla Z|^2}\nabla\cdot\vec{n}\Big\rangle_s}_{b} \tag{4.67}$$

As shown in Fig.(4.36), the term(b) in Eq.(4.67) remains almost at zero in time and can be neglected in comparison with term(a), which reduces term(V) to Eq.(4.68) below. The surface average quantity, term(b), being close to zero may be understood by interpreting the energy spectrum of its two components, $\frac{\nabla Z\cdot\nabla|\nabla Z|}{|\nabla Z|^2}$ and $\nabla\cdot\vec{n}$, respectively. As seen in Fig.(4.37), these two components are not expected to be well correlated with one another since the peaks in their respective energy spectrum occur at different wavenumbers.

$$\langle w\nabla\cdot\vec{n}\rangle_s = -D_f\Big\langle(\nabla\cdot\vec{n})^2\Big\rangle_s \tag{4.68}$$

As observed in Fig.(4.34), the behavior of the variance of curvature appears to be invariant with time and with isosurface. It implies that the mean curvature square appearing in the model for term(V) can be approximated by a constant, with a value of approximately 92(800) for case R2(R4) i.e.,

$$\begin{aligned}\text{case R2} \quad &: \quad \Big\langle(\nabla\cdot\vec{n})^2\Big\rangle_s = 92\\ \text{case R4} \quad &: \quad \Big\langle(\nabla\cdot\vec{n})^2\Big\rangle_s = 800\end{aligned} \tag{4.69}$$

Accordingly, a simple model for term(V) can be presented based on statistical analysis of DNS results as

$$\begin{aligned}\text{case R2} \quad &: \quad \langle w\nabla\cdot\vec{n}\rangle_s = -92D_f\\ \text{case R4} \quad &: \quad \langle w\nabla\cdot\vec{n}\rangle_s = -800D_f\end{aligned} \tag{4.70}$$

As shown in Fig.(4.31), the time evolution of term(V) almost maintains at a constant negative value regardless of different isosurfaces except a gradual decrease from zero in early simulation time. It implies that using a constant mean curvature square to approximate term(V) should be appropriate. The model for term(V) is assessed with respect to the DNS results which is displayed in Fig.(4.38). As can be seen from the figure, except for early simulation times and the isosurfaces near pure fuel/oxidant regions, the predicted value from the model is in good agreement with the DNS results.

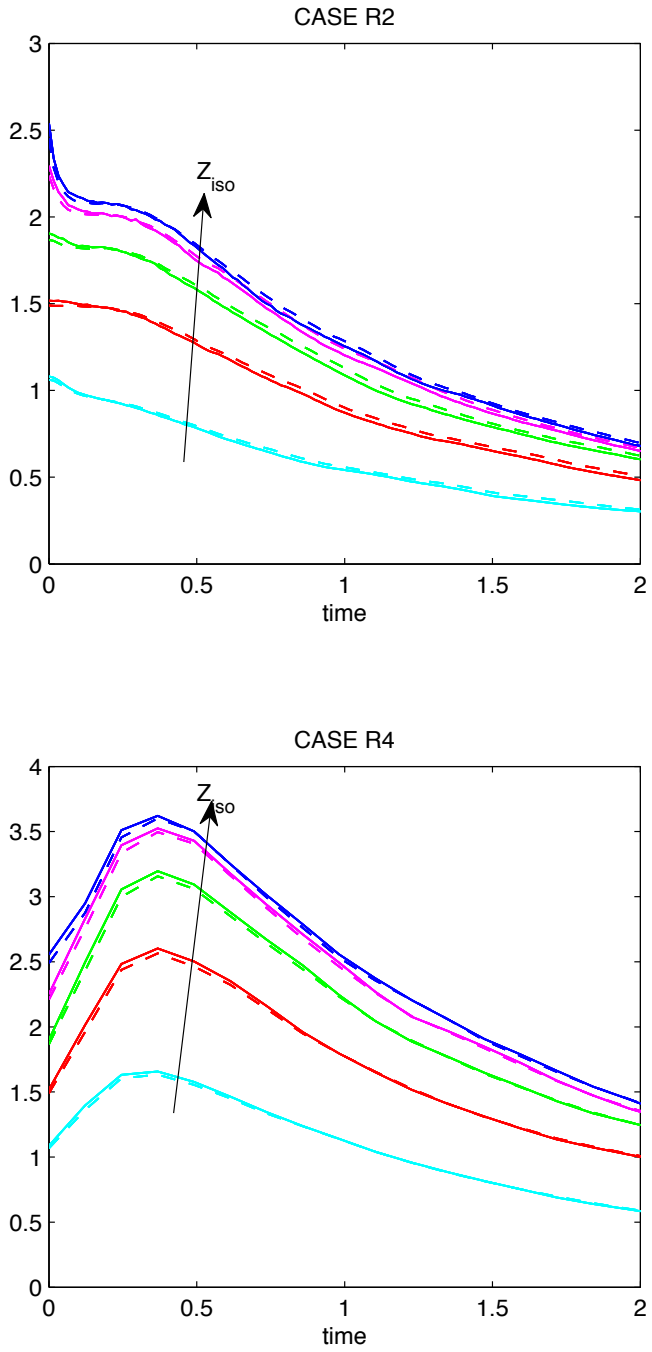

Figure 4.21: The time evolution of $|\frac{\partial Z}{\partial x_1}| \mid Z = Z_{iso}$(solid line) is compared with the one of $0.5\langle|\nabla Z| \mid Z = Z_{iso}\rangle$(dashed line) for a series of isovalues: $Z_{iso} = 0.1$(cyan), 0.2(red), 0.3(green), 0.4(magenta) and 0.5(blue) by using DNS data of case R2(top panel) and R4(bottom panel). The farther away the isovalue Z_{iso} is from Z_{st}, the smaller the iso-surface averaged gradient of mixture fraction is.

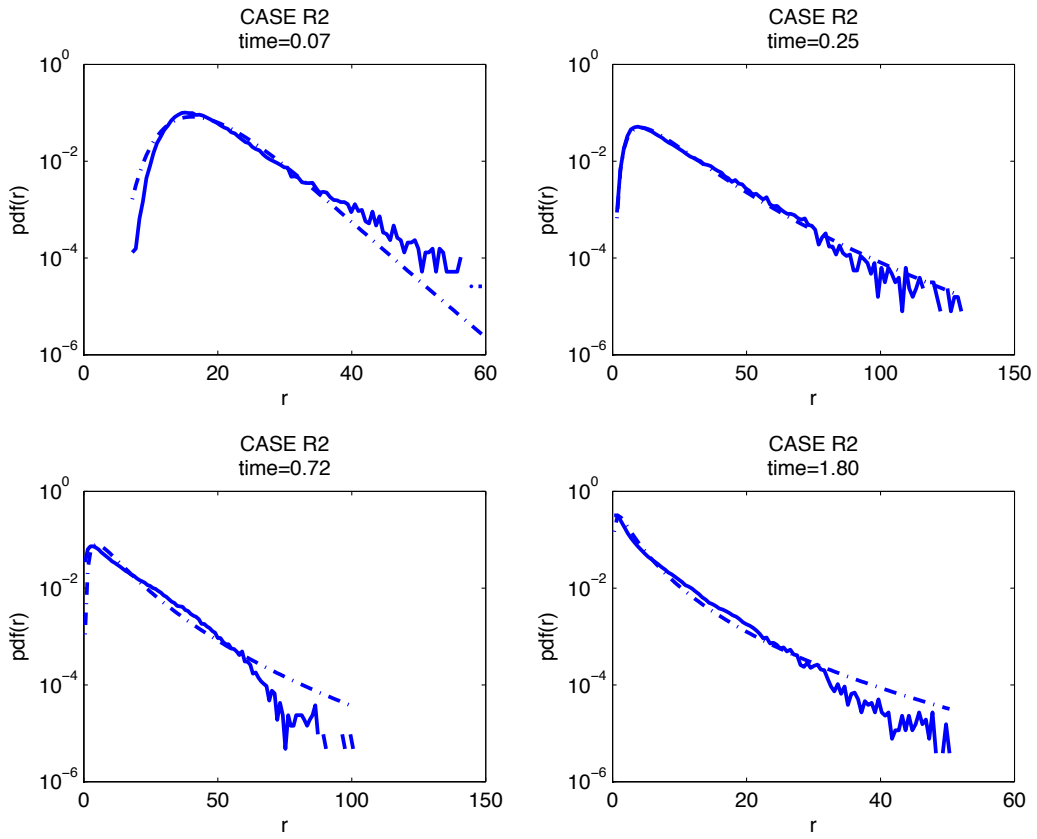

Figure 4.22: For case R2, PDF of R obtained directly from DNS(solid) and from the lognormal distribution approximation(dash-dot) correspond to simulation times: time=0.07(left upper), 0.25(right upper), 0.72(left bottom) and 1.80(right bottom), respectively. For model prediction, the required shape parameters m and a are computed in terms of $\langle R \rangle$ and $\langle R^2 \rangle$ taken directly from DNS. The PDF is plotted on log-linear scale for comparison details especially in the tail of the distribution.

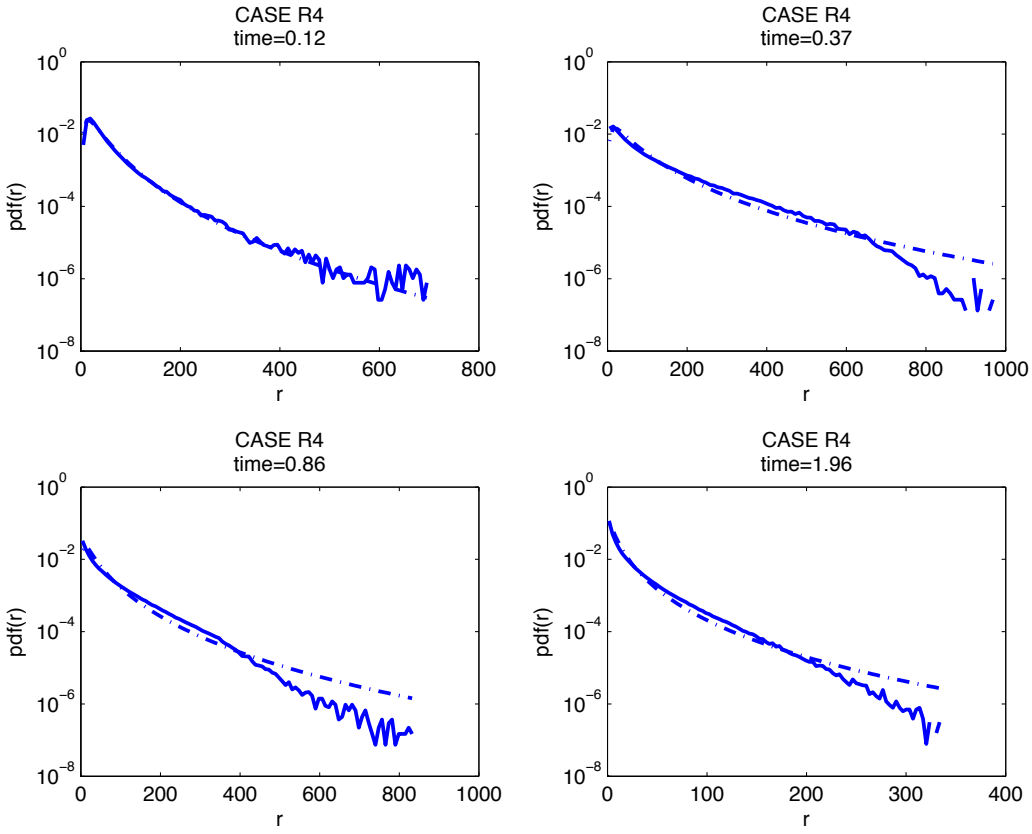

Figure 4.23: For case R4, PDF of R obtained directly from DNS(solid) and from the lognormal distribution approximation(dash-dot) correspond to simulation times: time=0.12(left upper), 0.37(right upper), 0.86(left bottom) and 1.96(right bottom), respectively. For model prediction, the required shape parameters m and a are computed in terms of $\langle R \rangle$ and $\langle R^2 \rangle$ taken directly from DNS. The PDF is plotted on log-linear scale for comparison details.

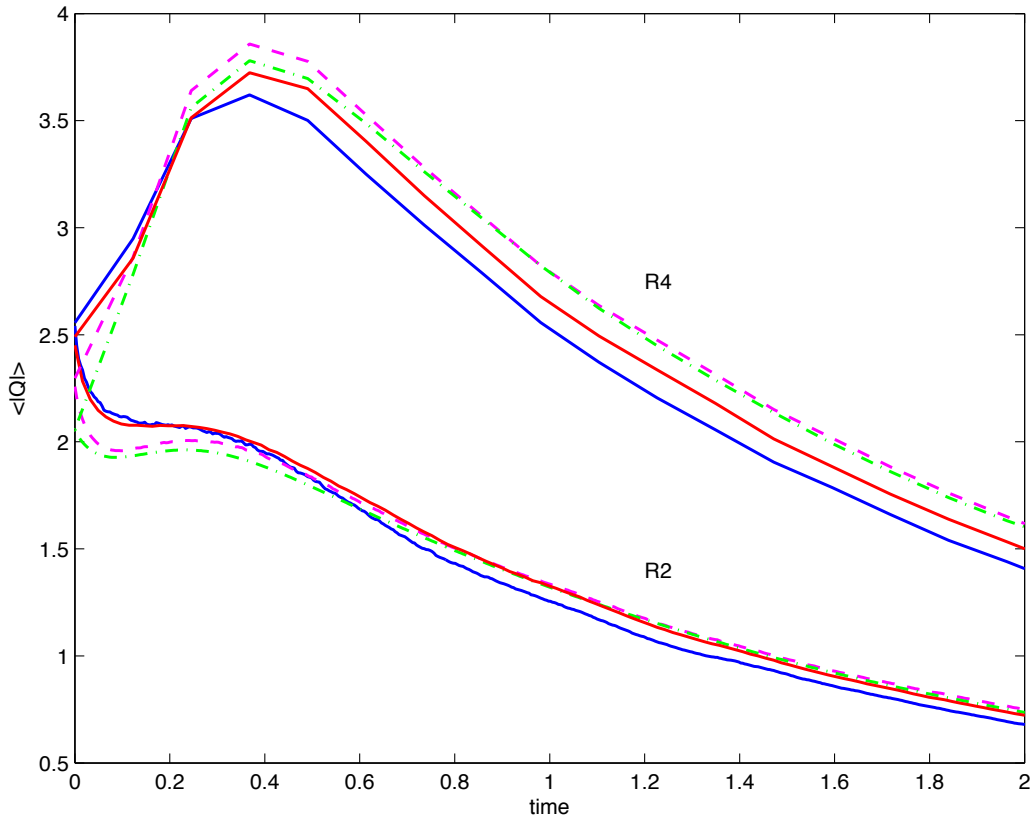

Figure 4.24: The time evolution of $\langle |Q| \rangle$ predicted by Eq.(4.53)(red solid line) is compared with the ones predicted by Eq.(4.36)(magenta dashed line) and Eq.(4.39)(green dash-dot line) with respect to the results obtained directly from DNS(blue solid line). The required shape parameters $\langle R \rangle$ and $\langle R^2 \rangle$ for model Eq.(4.53) are directly taken from DNS. The curves correspond to previous model prediction Eq.(4.36) and Eq.(4.39) are processed in the same manner as Fig.(4.19). The lower and upper four curves represent the results of case R2 and R4, respectively.

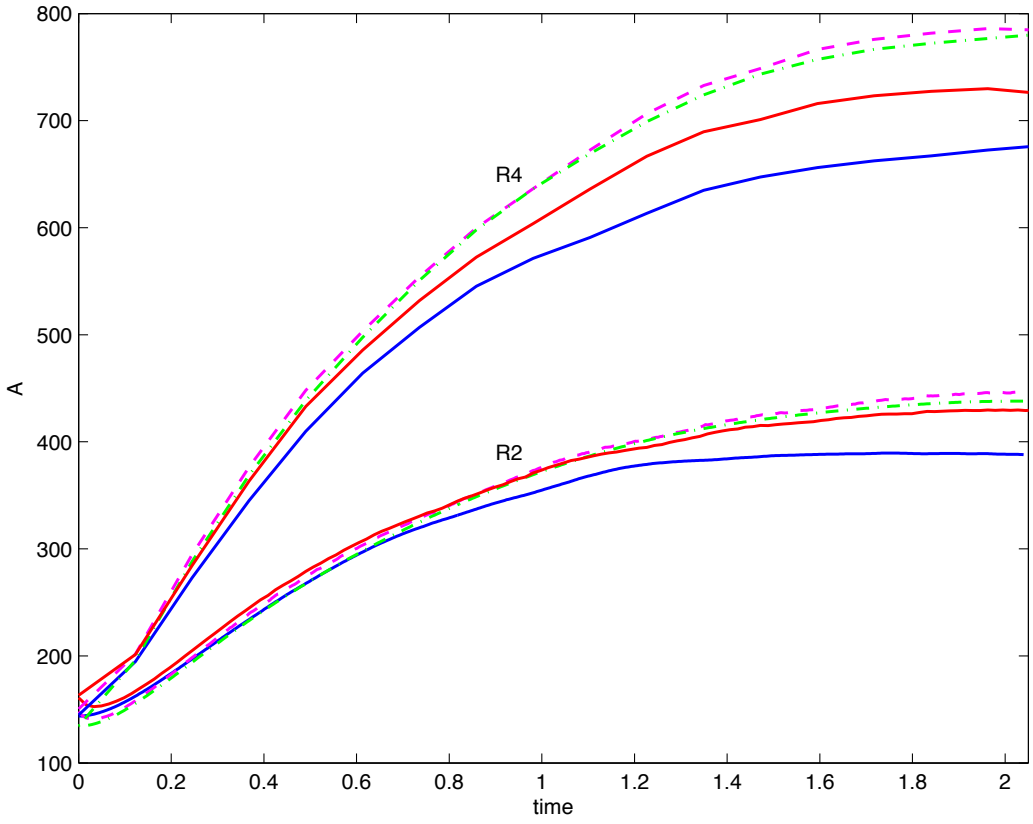

Figure 4.25: The time evolution of flame surface area A predicted by Eq.(4.54)(red solid line) is compared with the ones predicted by Eq.(4.37)(magenta dashed line) and Eq.(4.40)(green dash-dot line) with respect to the results obtained directly from DNS(blue solid line). The required shape parameters $\langle R \rangle$ and $\langle R^2 \rangle$ for model Eq.(4.54) are directly taken from DNS. The curves correspond to previous model prediction Eq.(4.37) and Eq.(4.40) are processed in the same manner as Fig.(4.20). The lower and upper four curves represent the area of case R2 and R4, respectively.

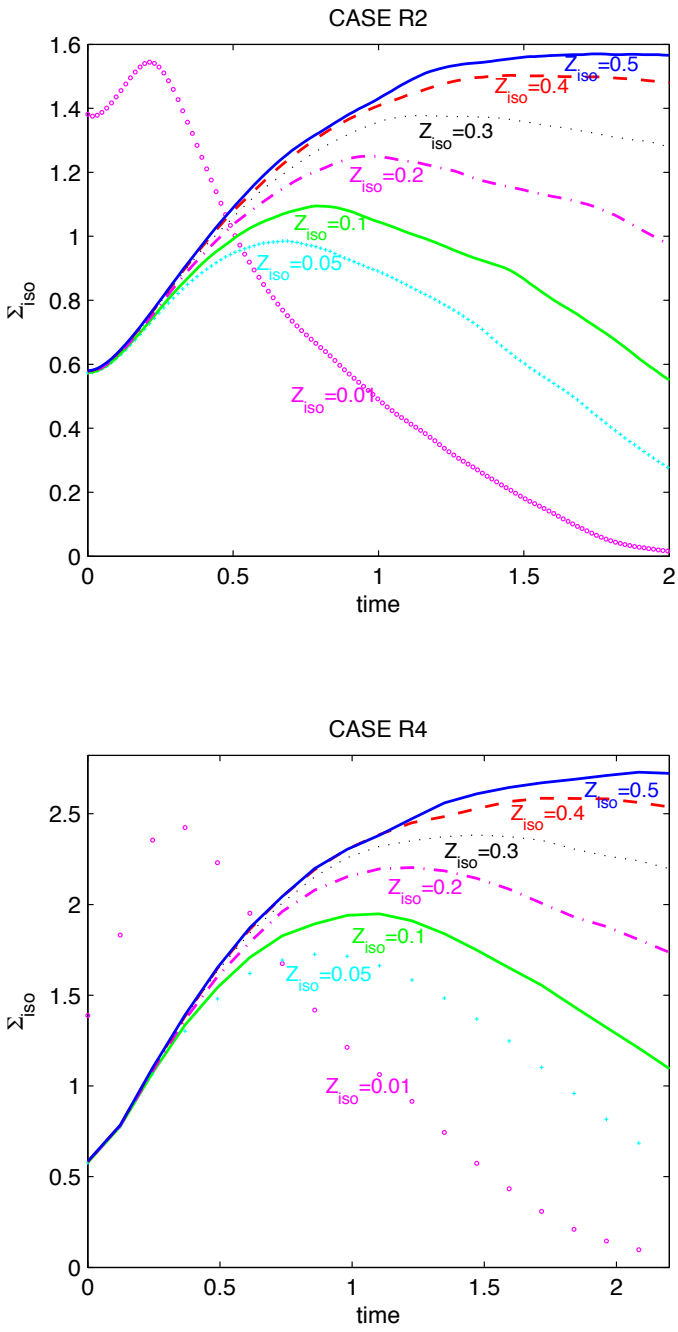

Figure 4.26: Time evolution of area density Σ_{iso} of the isosurface extracted from DNS data of case R2 (top panel) and R4 (bottom panel) corresponding to different isovalues $Z_{iso} = 0.01$(magenta circle), 0.05(cyan plus sign), 0.1(green solid line), 0.2(magenta dash-dot line), 0.3(black dotted line), 0.4(red dashed line) and 0.5(blue solid line), respectively. The curves are labelled with the isovalues.

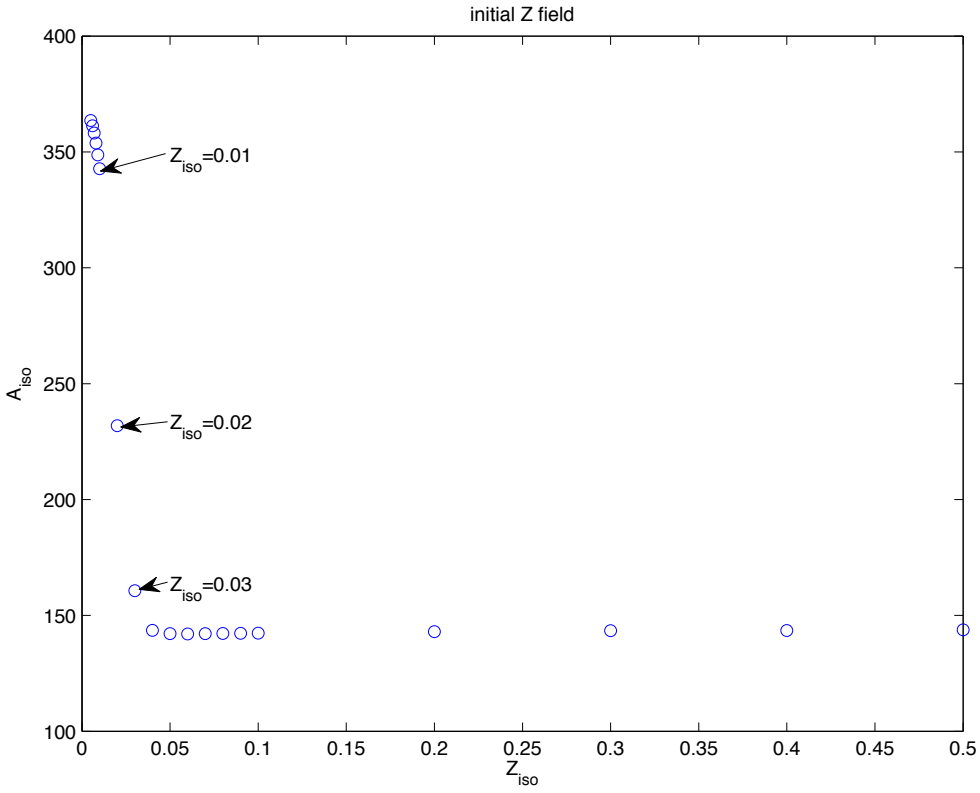

Figure 4.27: For case R2, the area A_{iso} of the isosurfaces as a function of isovalues at initial time.

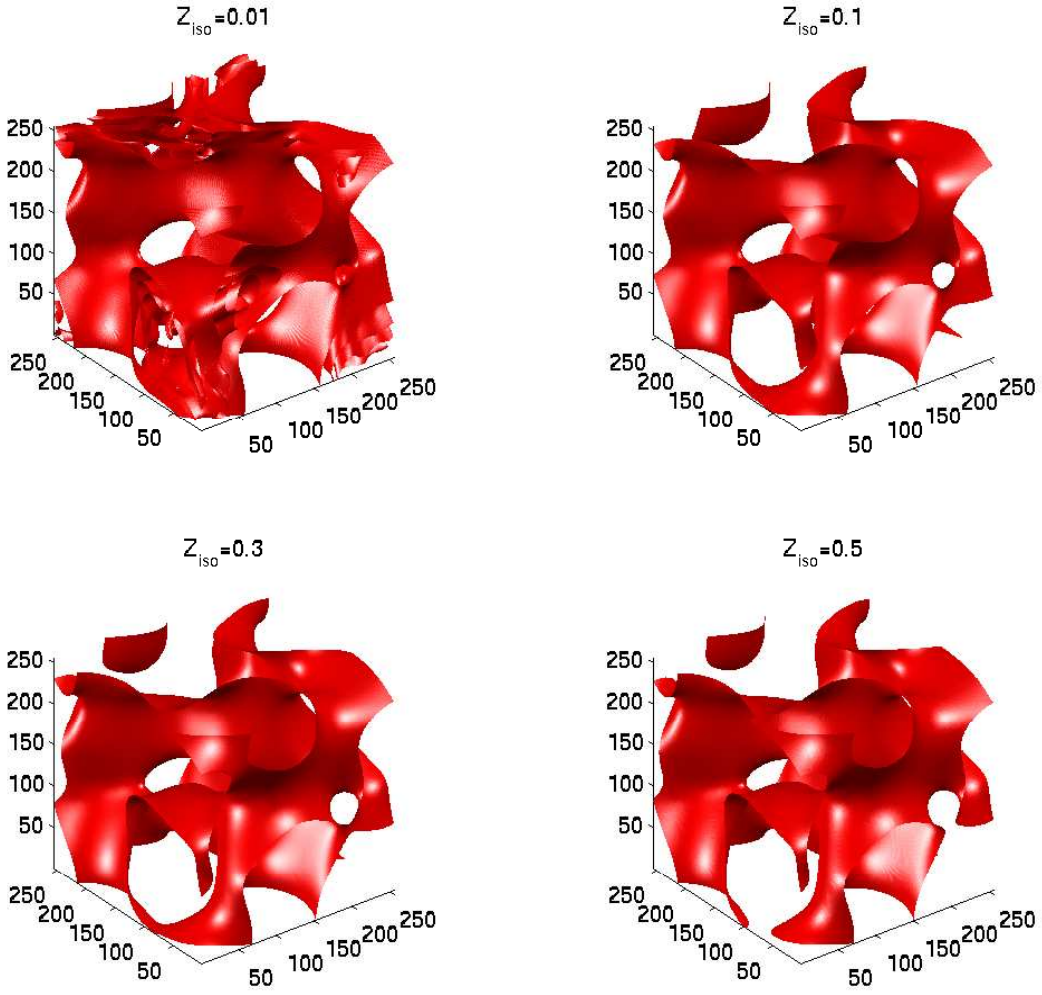

Figure 4.28: For case R2, 3D visualization of initial isosurfaces corresponding to isovalues $Z_{iso} = 0.01$(left upper), 0.1(right upper), 0.3(left bottom), and 0.5(right bottom), respectively.

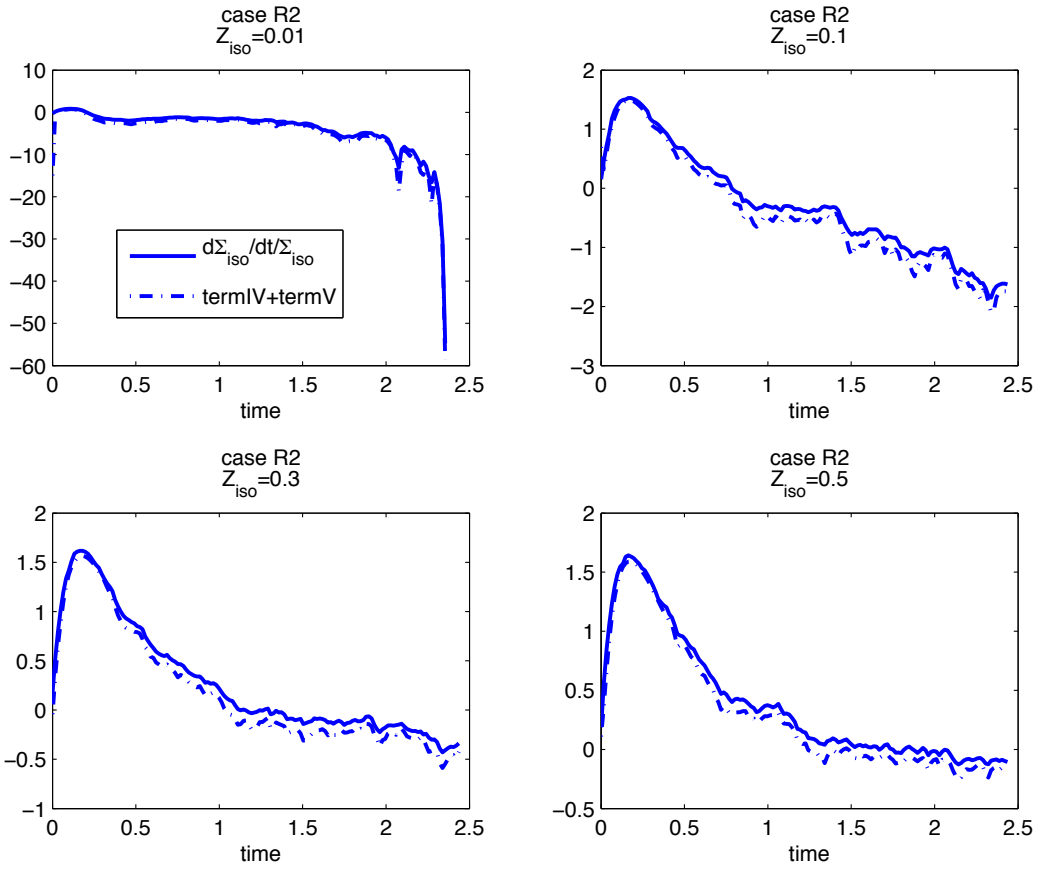

Figure 4.29: Time evolution of the LHS(solid) and the RHS(dashed) of balance equation, Eq.(4.64), for isosurface extracted from DNS data of case R2 at isovalue $Z_{iso} = 0.01$, 0.1, 0.3, and 0.5 from the top left panel to the bottom right one, as indicated in the panels.

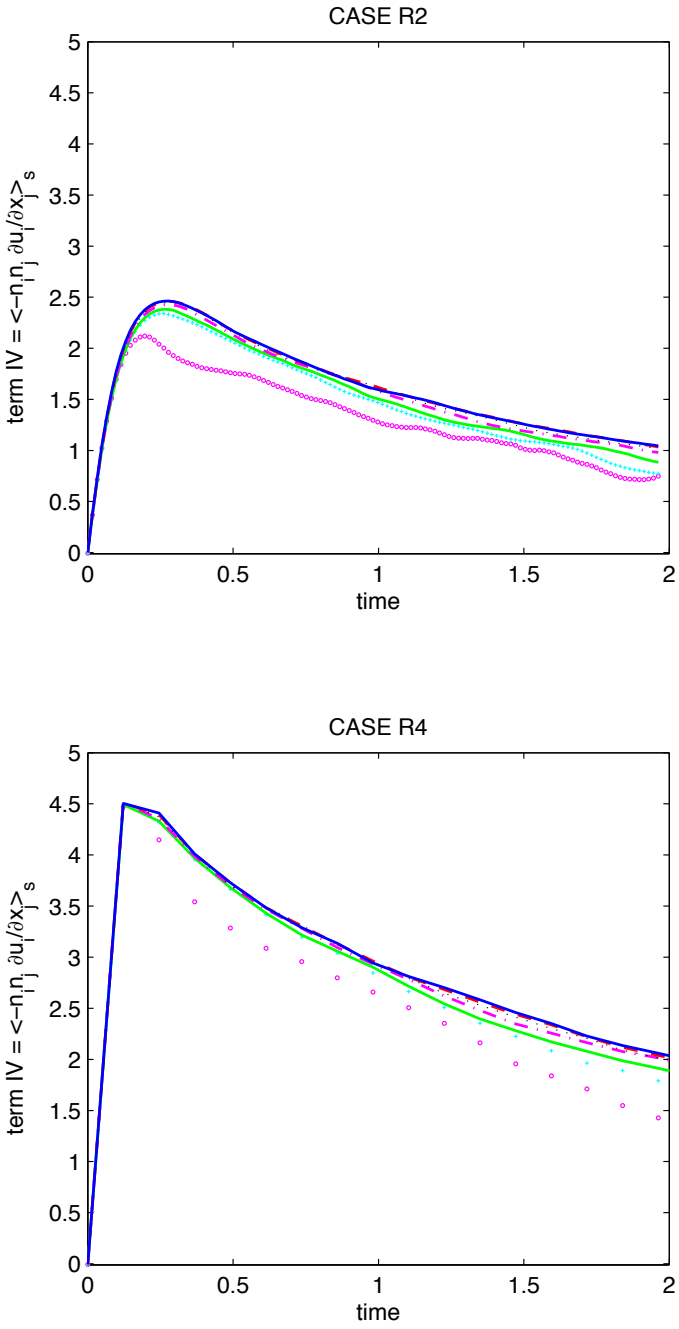

Figure 4.30: Time evolution of the strain rate term a_T calculated using DNS data of case R2 (top panel) and R4 (bottom panel) for different isosurfaces specified at isovalues Z_{iso} = 0.01(magenta circle), 0.05(cyan plus sign), 0.1(green solid line), 0.2(magenta dash-dot line), 0.3(black dotted line), 0.4(red dashed line) and 0.5(blue solid line), respectively.

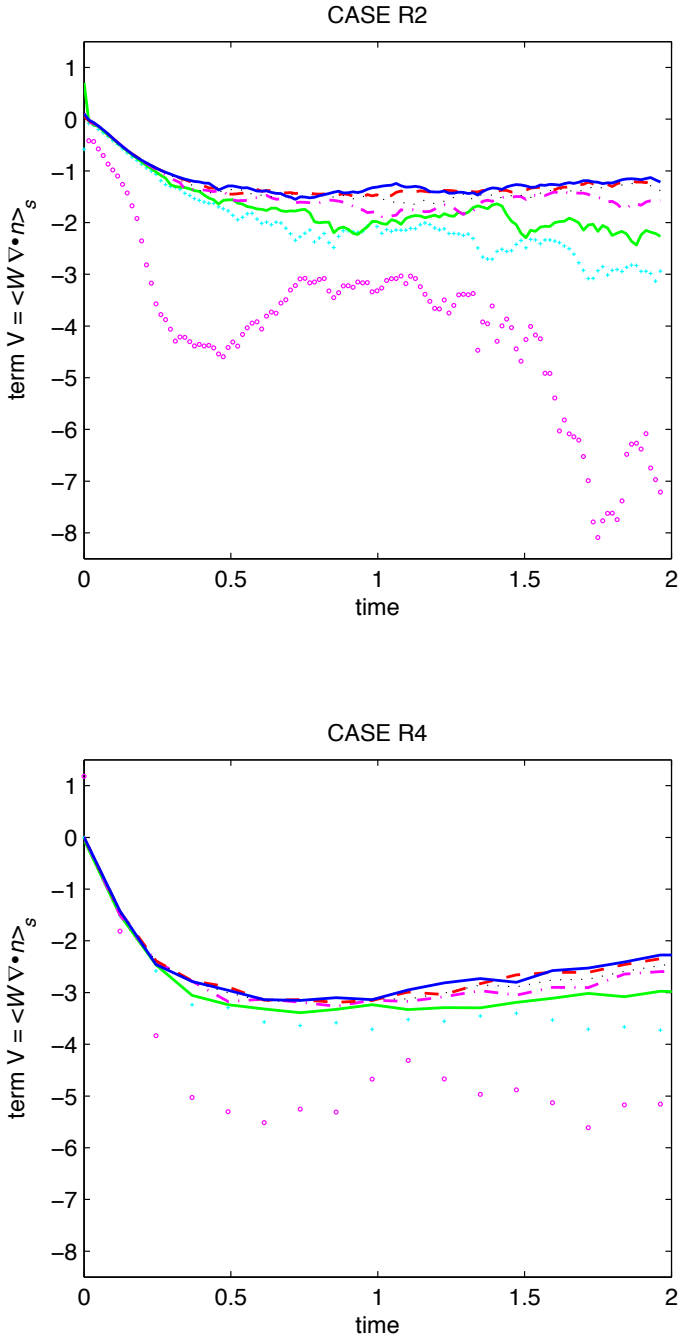

Figure 4.31: Time evolution of term(V) calculated using DNS data, plotted the same way as in Fig.(4.30).

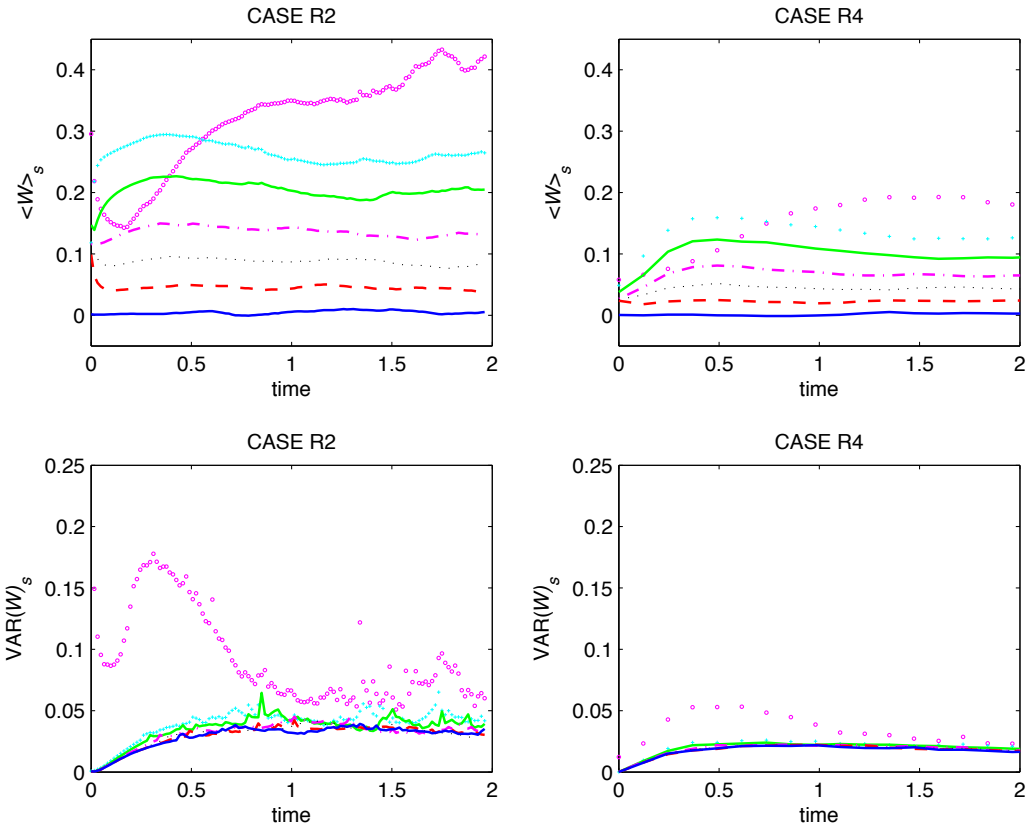

Figure 4.32: The area-weighted average (top row) and variance (bottom row) of local diffusion velocity conditioned on isosurface: $Z_{iso} = 0.01$(magenta circle), 0.05(cyan plus sign), 0.1(green solid line), 0.2(magenta dash-dot line), 0.3(black dotted line), 0.4(red dashed line) and 0.5(blue solid line), are plotted as a function of time for case R2 (left column) and case R4 (right column), respectively.

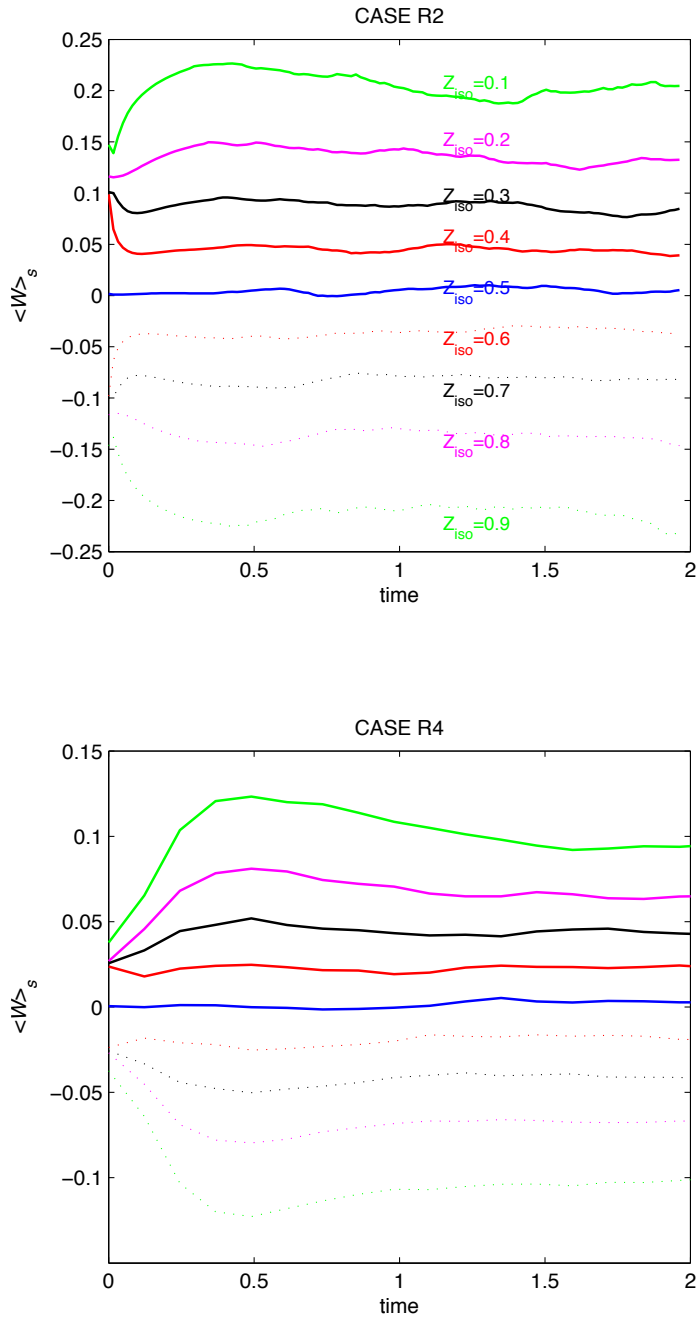

Figure 4.33: The time evolution of area-weighted average of local diffusion velocity conditioned on isosurfaces with isovalues Z_{iso} that vary in a range of 0.1 to 0.9 with uniform step size 0.1. The results for isovalues ranging from 0.6 to 0.9 are plotted with dotted line but in the same color as the ones for their symmetric counterpart isovalues ranging from 0.1 to 0.4. Top panel: case R2, bottom panel: case R4. The curves are labelled with the isovalues.

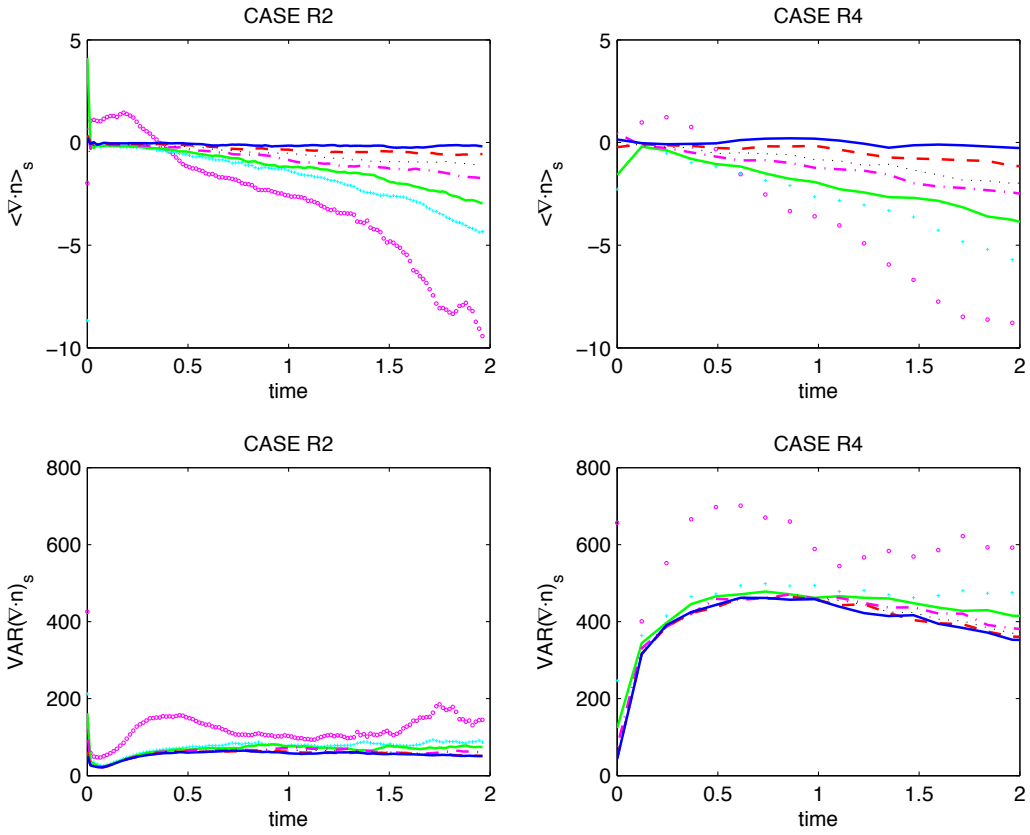

Figure 4.34: The area-weighted average (top panel) and variance (bottom panel) of local curvature conditioned on isosurface are plotted the same way as in Fig.(4.32).

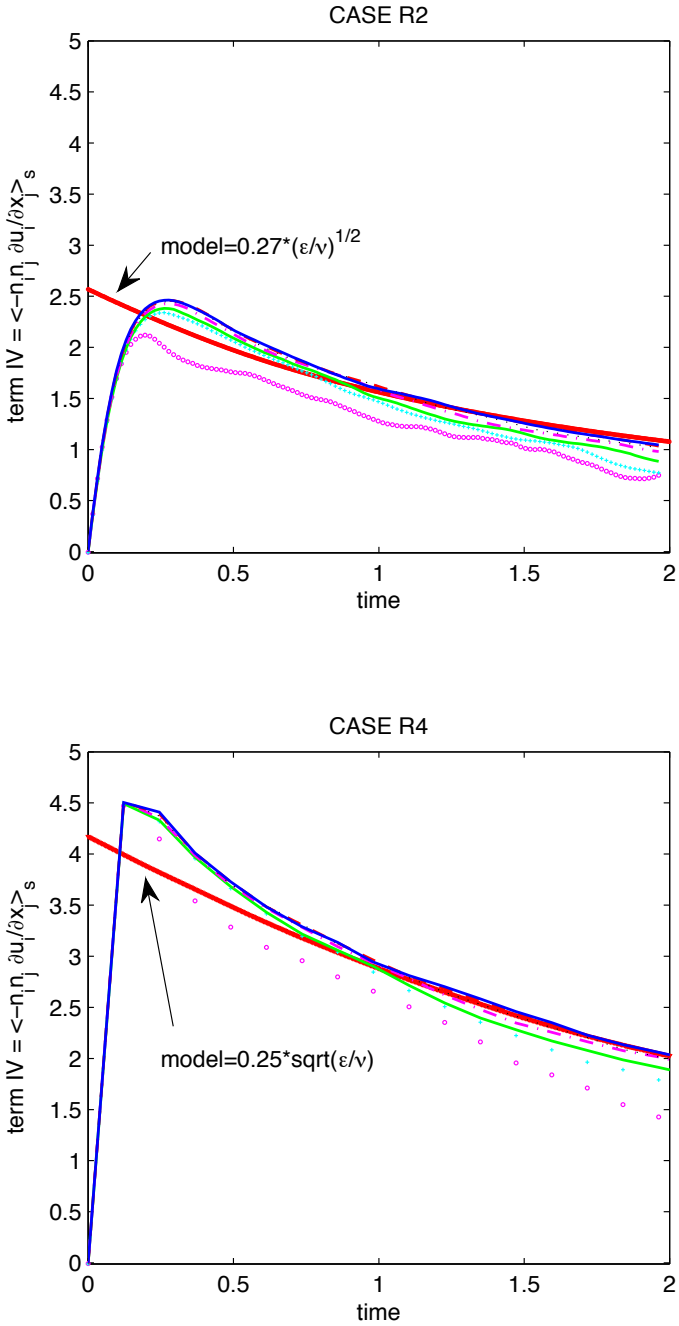

Figure 4.35: Time evolution of the strain rate term a_T from model prediction(bold red line with down-triangle) is compared with the results from DNS. The DNS results are plotted the same way as in Fig.(4.30).

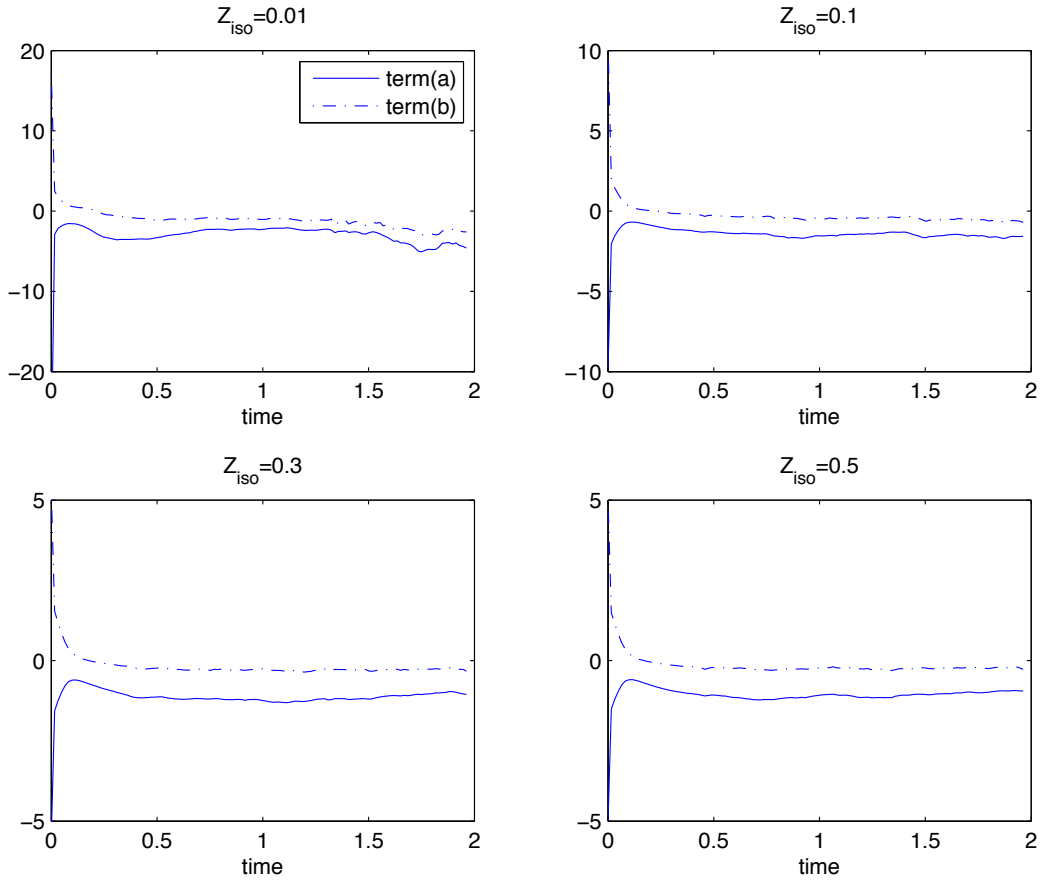

Figure 4.36: Time evolution of the term(a)(solid) and the term(b)(dash-dot) in Eq.(4.67) for isosurface extracted from DNS data at isovalue $Z_{iso} = 0.01$, 0.1, 0.3, and 0.5 from the top left panel to the bottom right one, as indicated in the panels.

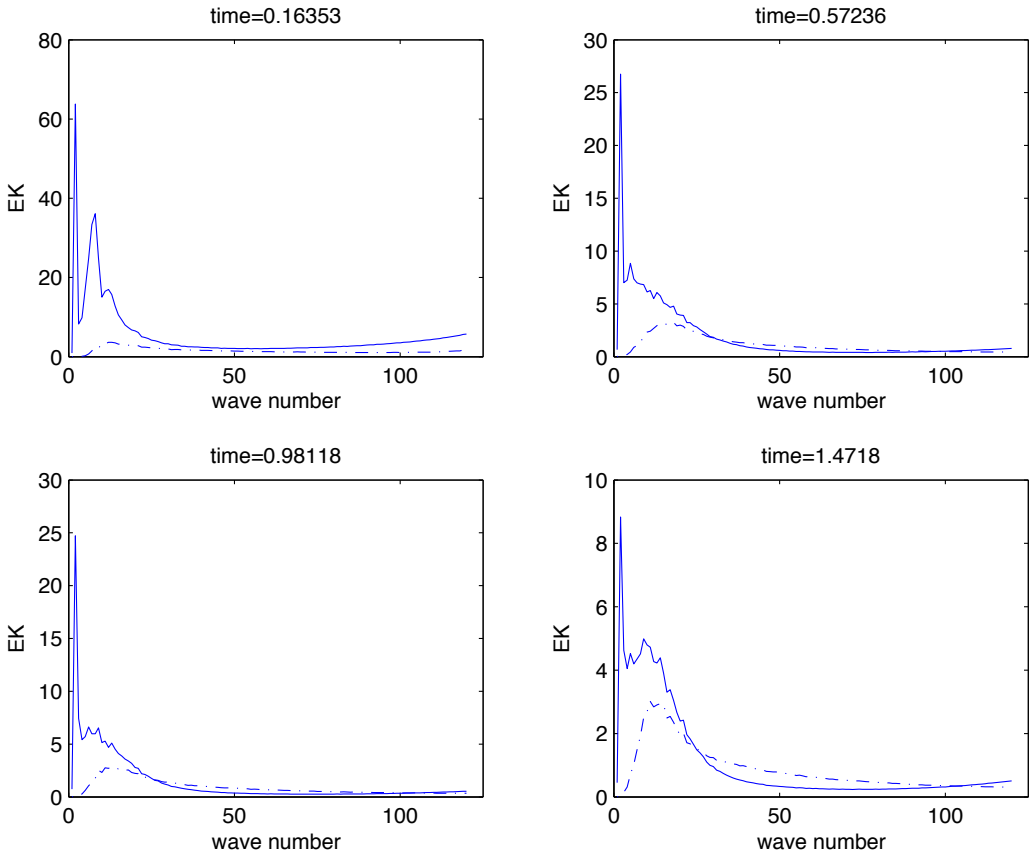

Figure 4.37: The energy spectrum of $\frac{\nabla Z \cdot \nabla |\nabla Z|}{|\nabla Z|^2}$(solid) and $\nabla \cdot \vec{n}$(dash-dot) correspond to the simulation times: time=0.16(left upper),0.57(right upper),0.98(left bottom) and 1.47(right bottom), respectively.

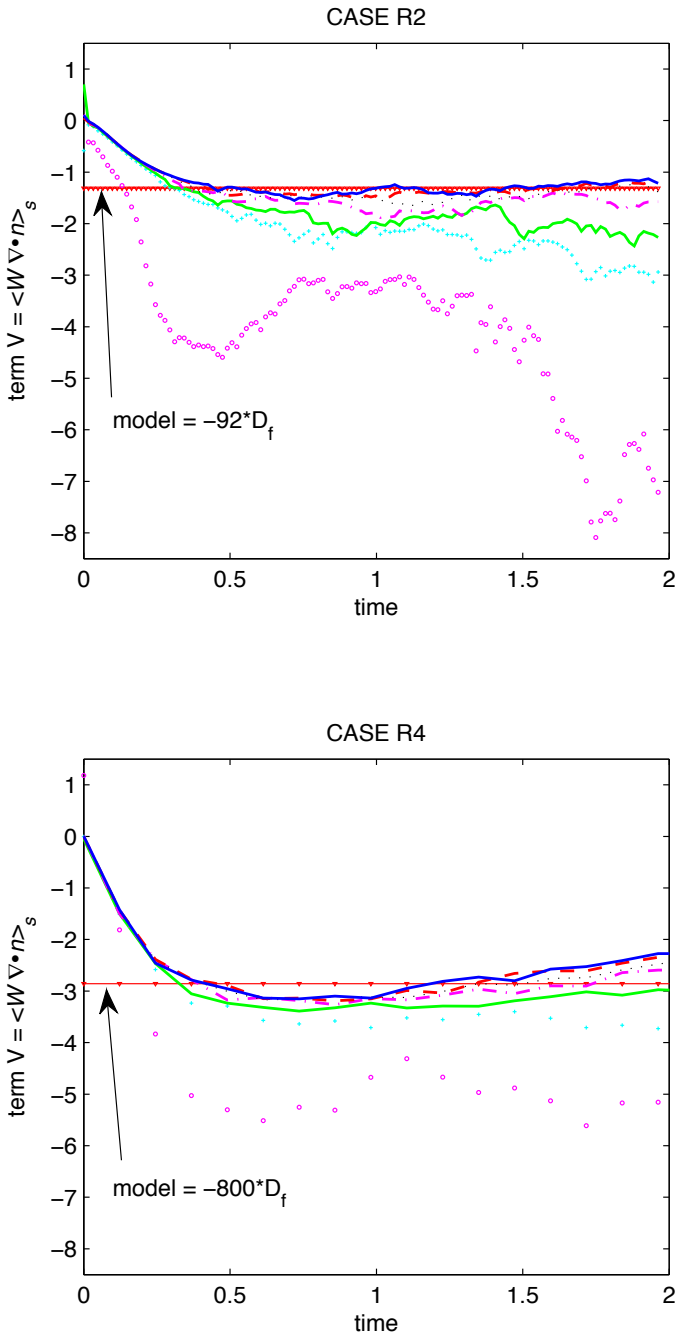

Figure 4.38: Time evolution of term(V) by model prediction(bold line with red down-triangle) is compared with the results from DNS. The DNS results are plotted the same way as in Fig.(4.31).

Chapter 5

APPLICATION OF STEADY LAMINAR FLAMELET MODEL AND KINEMATIC STUDY OF FLAME HOLE

5.1 Flamelet Model Introduction

In this section, we briefly revisit the concept of the laminar diffusion flamelet model for nonpremixed combustion which is proposed by Williams[16].

The equilibrium chemistry approach has been widely used for nonpremixed combustion since the time scale by which chemistry approaches equilibrium is generally is much shorter than the diffusion time scale. Under this assumption of fast chemistry, the equilibrium approach simplifies the problem in that all the reactive scalars can be uniquely predicted by a conserved scalar, i.e., the mixture fraction. But in hydrocarbon flames, the equilibrium model overpredicts the concentrations of intermediate products such as CO and H_2, and yields prediction errors for other major species. The reasons for this behavior involve the non-equilibirum chemistry that occurs in flames. The Steady Laminar Flamelet model(SFL) was developed to address this non-equilibirum behavior.

The model assumes that combustion occurs in relatively thin sheets on the boundary separating fuel rich from fuel lean regions. The flamelet can be described as a quasi-steady process in which the flame behavior is determined by two parameters: (1) the rate of strain at the fuel-oxidizer interface, and (2) the stoichiometry as one moves across the interface. The flame behavior can then be solved off-line in terms of these two parameters (specifically, the scalar dissipation rate χ_{st}, and the mixture fraction Z). These solutions then form a look-up library in which the temperature and the species concentration are functions of (χ_{st}, Z). A fluid dynamic calculation is performed which includes equations for the conserved scalar Z and its variance, and with Z resolved as a field variable, both Z and χ_{st} are available at each point in the calculation. The SFL look-up table is then used to find temperature and chemical species mass fractions at each point in the field.

The model predicts a critical strain rate above which the flame cannot be sustained. Under these conditions, the flame will become extinguished and the fuel and oxidizer interface will involve only mixing with no reaction. For strain rates below the extinction point, two SFL solutions are possible, one is for a steady flame, while the other is for cold mixing without reaction. The critical question is which prevails in a given situation? The answer depends on the history of the point under consideration. If the local stoichiometric surface has exceeded the extinction strain rate in the past, then it may have gone to the non-burning solution. If it subsequently relaxes below the critical strain rate, it will not spontaneously reignite; reignition occurs only via an outside source, i.e., the propagation of a flame from a neighboring burning region.

This presents difficulties for the SFL. First, one does not know what fraction of the flame surface is in the burning solution versus the non-burning solution at given instant. Second, one does not know the rate at which the non-burning regions are being reignited by flame propagation. These time-dependent and history-dependent features defeat the core purpose of the SFL, in which the local chemistry and temperature are uniquely set by χ_{st} and Z under the burning solution. These problems limit the utility of the SFL to flames where essentially no part of the flow exceeds the critical strain rate for extinction, and all stoichiometric surfaces are in the burning mode. This chapter discusses the deviations between the SFL and the DNS of a reacting flow that includes significant extinction and reignition phenomena.

5.2 Steady Flamelet Model Applied in Turbulent Nonpremixed Combustion

The applicability of the steady laminar flamelet model (SFL) to diffusion flames with local extinction and reignition will be assessed in terms of reaction rate by comparing the SFL with the DNS results in this section. Two different approaches to calculating the total reaction rate within the computational domain are utilized. These are described as follows. (1)Approach I: Directly employ the DNS data at every computational grid point. As introduced in Chapter 3, the DNS resolves all turbulent scales and generates instantaneous values of mixture fraction $Z(x_1, x_2, x_3, t)$ and product mass fraction $Y_P(x_1, x_2, x_3, t)$ at every 3D computational grid point (x_1, x_2, x_3). Accordingly, the reaction rate, denoted as

$\omega_{P,DNS}(x_1, x_2, x_3, t)$, can be determined by inserting the DNS-generated data Z and Y_p into the single-step Arrhenius-type rate expression which is given by Eq.(3.24). This rate of reaction is also an instantaneous 3D-field data and regarded as ″actual″ results for the future comparison.

(2)Approach II: Apply SFL to every computational grid point. The local chemistry at each grid point is assumed to be that of the steady state laminar flamelet and can be characterized by the mixture fraction $Z(x_1, x_2, x_3, t)$ and stoichiometric scalar dissipation rate $\chi_{st}(x_1, x_2, x_3, t)$ associated with the grid point. As introduced in Section 3.6.2, the steady flamelet solutions are compiled in a library parameterized by a series of χ_{st} and Z. To apply the SFL to each grid point within the 3D computational domain, the local instantaneous SFL temperature, denoted by $Y_{P,sfl}(x_1, x_2, x_3, t)$ can be obtained from the SFL library as a function of the known local instantaneous $Z(x_1, x_2, x_3, t)$ and $\chi_{st}(x_1, x_2, x_3, t)$, and then the reaction rate $\omega_{P,sfl}(x_1, x_2, x_3, t)$ can be calculated accordingly. Note that the instantaneous field of stoichiometric scalar dissipation rate $\chi_{st}(x_1, x_2, x_3, t)$ is obtained from the instantaneous field of scalar dissipation rate $\chi(x_1, x_2, x_3, t)$(due to Eq.(3.39)) which itself is computed directly by the instantaneous mixture fraction field from its definition.

It should be clarified that the quantity χ_{st} used in the application of SFL model pertinent to the current context and the one involved in Fig.(3.4) are estimated by different approaches. In Fig.(3.4), χ_{st} refers to the value χ of the grid point whose value of Z locates in a bin of width = 0.03 centered at Z_{st}. Whereas, in the application of SFL model, each grid point is assigned a value of χ_{st} which is modeled by Eq.(3.39)) using χ based on a counter-flow diffusion flame structure.

In Fig.(5.1), the total reaction rate (summed over all the grid points) predicted with the SFL library concept (Approach II) are compared against the actual values obtained directly from DNS (Approach I). During the whole simulation time, the SFL model underpredicts the reaction rates. The deviations at early and late simulation time will be discussed separately.

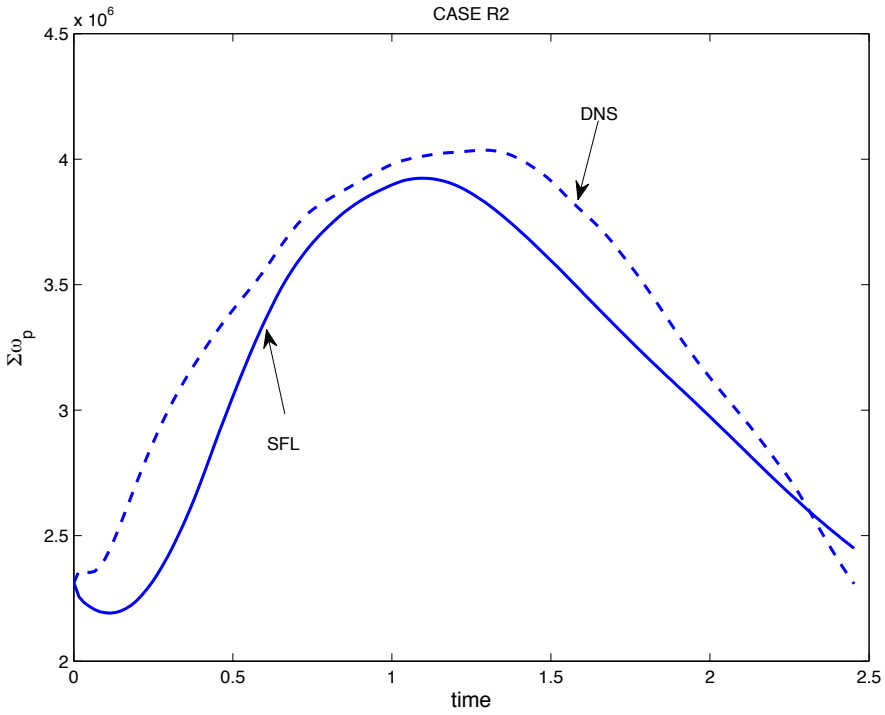

Figure 5.1: The total reaction rates summed over all grid points within computational domain as a function of time. Approach I: DNS(dashed); Approach II:SFL(solid).

5.2.1 Early Simulation Time

During early simulation time, say time $0 \sim 0.85$, the extinction process predominates. This is shown by the growth in fluctuations of χ_{st} exceeding χ_q and the corresponding decrease in $\langle Y_{P_{st}} \rangle$, as shown in Fig.(3.4) and Fig.(3.5), respectively. As described in Section 3.6.2, the stoichiometric scalar dissipation rate χ_{st} plays a key role in the application of the SFL solution. Specifically, when χ_{st} becomes greater than χ_q no burning SFL solution exists and the reaction rate for these points is set to zero.

In reality, a grid point with $\chi_{st} > \chi_q$ may still burn with a finite reaction rate especially if it only recently crossed from $\chi_{st} < \chi_q$ to $\chi_{st} > \chi_q$ and has not had time to fully extinguished yet. The DNS is capable of capturing this. This led us to classify the DNS grid points into two subsets according to whether the χ_{st} is beyond the threshold χ_q or not. The goal was to see what fraction of the total DNS reaction is attributed to points where $\chi_{st} > \chi_q$, and to

determine if this accounted for the difference in the early time behavior noted in Fig.(5.1). Fig.(5.2) shows the total DNS reaction rate divided between points where $\chi_{st} \leq \chi_q$ and $\chi_{st} > \chi_q$. It also shows the rate from the SFL model from Fig.(5.1).

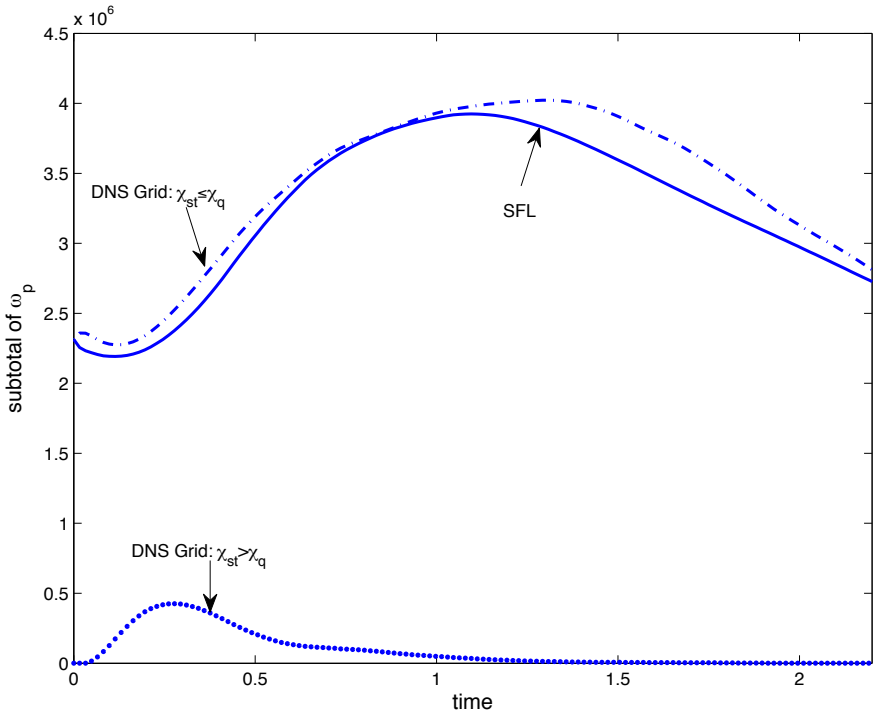

Figure 5.2: The subtotal of DNS reaction rates in each category: category $\chi_{st} \leq \chi_q$(dash-dot); category $\chi_{st} > \chi_q$(dotted), is plotted as a function of time. For comparison, the total reaction rates predicted by SFL approach is shown as solid line.

Figure (5.2) shows that during early simulation time, the SFL model predictions (solid line) are in a good agreement with the DNS results for grid points in subset $\chi_{st} \leq \chi_q$ (dash-dot line). For the grid points in subset $\chi_{st} > \chi_q$, the existence of the nonzero subtotal DNS reaction rates (dotted line) shows that the flamelet is not necessarily extinguished when $\chi_{st} > \chi_q$. This implies that assigning 0 when $\chi_{st} > \chi_q$ in the SFL model is not always correct. The plot suggests this is the source of most of the discrepancy between the reaction rates for DNS and SFL at early times.

From a theoretical viewpoint, the subtotal for a $\chi_{st} > \chi_q$ subset of DNS reaction rates

(dotted line in Fig.(5.2)) is determined not only by the number of grid points beyond χ_q, but also their DNS reaction rates distribution as well. Thus, the chronological details of this subtotal is depicted given the percentage of grid points whose χ_{st} beyond χ_q as a function of time (Fig.(5.3)) and the conditional probability density distribution of DNS reaction rates $P(\omega_{P,DNS}|\chi_{st} > \chi_q)$ for times $t = 0.15$, 0.26, 0.51, and 0.85 (Fig.(5.4)). Furthermore, the reaction rate depends on Z and $Y_{P,DNS}$ in the standard Arrhenius form. Therefore, for grid points above χ_q, the probability density distribution of their Z and the 2D histograms of their Z and $Y_{P,DNS}$ are respectively graphed in Fig.(5.5) and Fig.(5.6) for the same selected times as those of Fig.(5.4) to provide a richer illustrations.

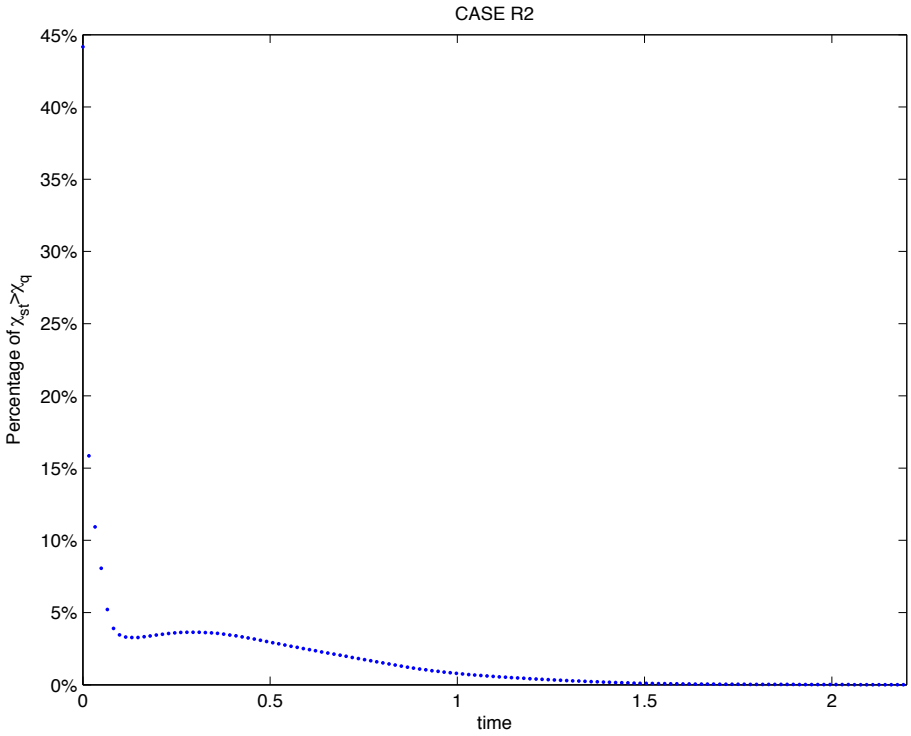

Figure 5.3: The time history of the percentage of grid points whose $\chi_{st} > \chi_q$.

These plots show that, at initial time, a high percentage of grid points above the quenching limit shown in Fig. (5.3) disagrees with the statistics pertaining to the fluctuations of χ_{st} displayed in Fig. (3.4). This is because the quantity χ_{st} is produced from a different

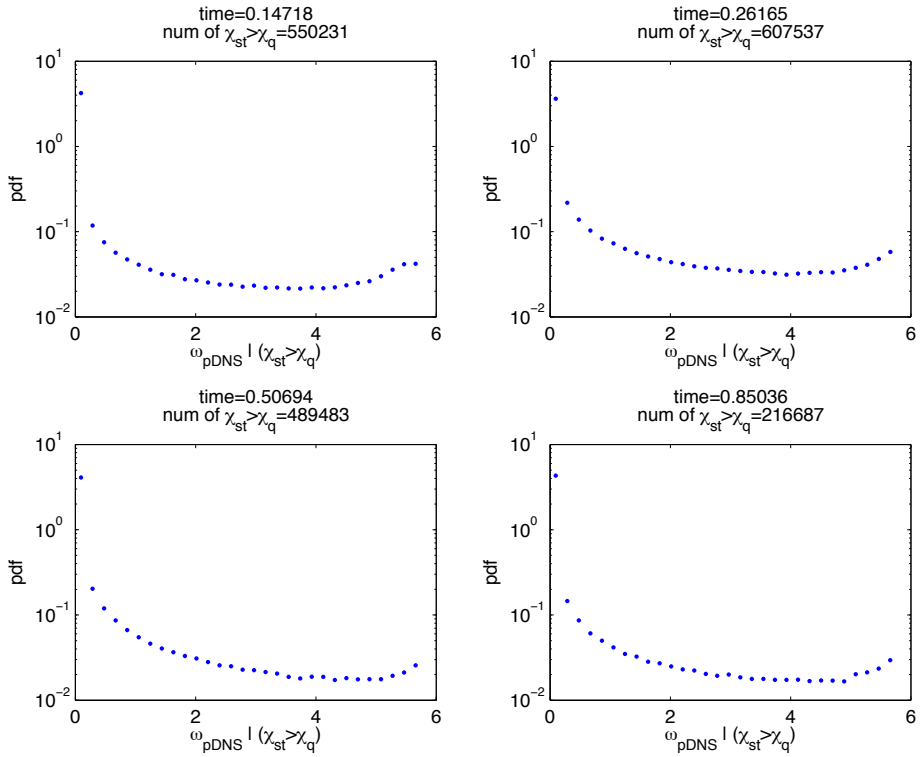

Figure 5.4: The conditional probability density distributions of reaction rates $\omega_{P,DNS}$ given $\chi_{st} > \chi_q$(on logarithmic scale for clarity) are obtained directly from DNS corresponding to simulation times: time=0.15(left upper), 0.26(right upper), 0.51(left bottom) and 0.85(right bottom), respectively. The number of grid points above χ_q is indicated in the title of each plot.

approach as described above. For the modeled approach, the value Z being close to 0 or 1 will lead to larger values of χ_{st} due to the function F intervening in Eq. (3.39)). This along with the double-delta distribution of initial mixture fraction field results in the appearance of a high proportion of χ_{st} above χ_q at the initial time. This is shown in Fig. (5.3) but not in Fig. (3.4). As time proceeds, the proportion of the fluctuations of χ_{st} beyond χ_q increases due to the larger scalar gradients caused by turbulent strain until it reaches maximum, and then gradually drops to zero as molecular mixing proceeds. In the SFL model application, the high stoichiometric scalar dissipation rate above the quenching limit is not only induced by the turbulent stretching which becomes the dominant driving force as the value of Z moves away from the two ends over time, but also results from Z being close to 0

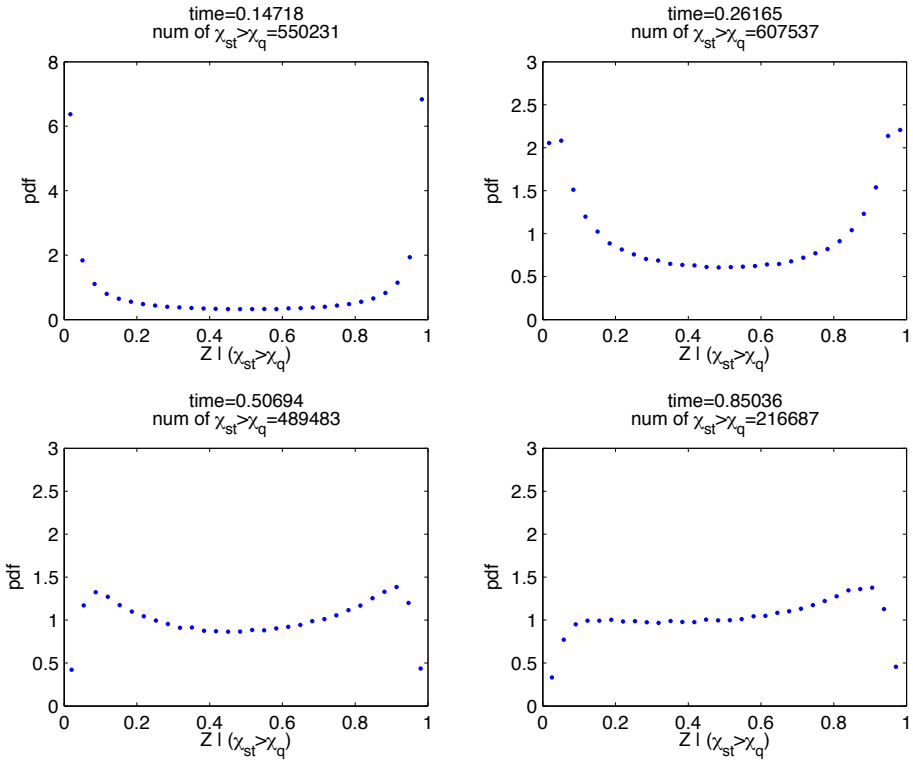

Figure 5.5: The conditional probability density distributions of Z given $\chi_{st} > \chi_q$ correspond to simulation times: time=0.15(left upper), 0.26(right upper), 0.51(left bottom) and 0.85(right bottom), respectively. The number of grid points above χ_q is indicated in the title of each plot.

or 1, especially at the beginning of simulation time when the mixture fraction distribution is close to a double-delta function.

At each selected time in Fig.(5.4), the probability of the reaction rate falling within the smallest interval $(0, 0.2)$ is the highest. Although the distribution functions at each of the four selected times appear to be similar, they are each formed through different mechanisms. At time $t = 0.15$, the appearance of low reaction rates is caused by the highest proportion of $Z = 0$ and $Z = 1$ as exhibited in Fig.(5.6) and Fig.(5.5) rather than turbulent stretch-induced extinction. The initial increase in the subtotal for $\chi_{st} > \chi_q$ (shown as dotted line in Fig.(5.2)) from time $t = 0.15$ to $t = 0.26$ results from two reasons. First, the turbulent strain gives rise to an increase in the number of grid points above χ_q as shown in Fig.(5.3).

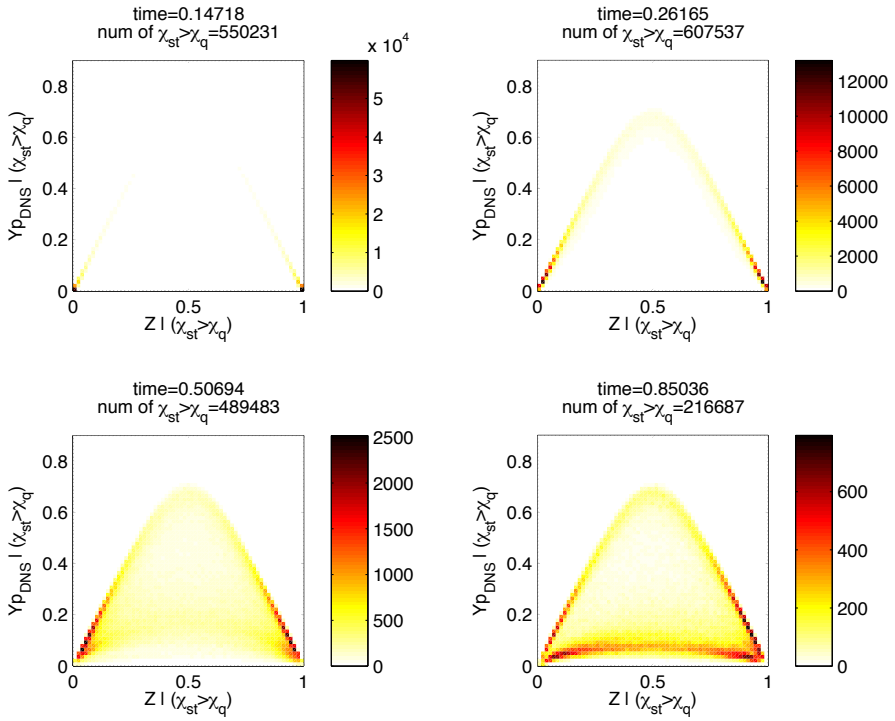

Figure 5.6: The 2D histogram is graphed to represent the joint distributions of Z and Y_P conditioned on $\chi_{st} > \chi_q$ with color intensities for four simulation times: time=0.15(left upper), 0.26(right upper), 0.51(left bottom) and 0.85(right bottom), respectively. The number of grid points above χ_q is indicated in the title of each plot.

Second, a growing percentage of grid points with values of mixture fraction approach Z_{st} are able to maintain burning solutions without significant extinction. This can be observed in the top right panel of Fig.(5.6). The levels of both Z and Y_P lead to the increase in reaction rate. The subsequent decay in this subtotal results from two reasons. First, the number of grid points above χ_q decreases with time. Second, a growing proportion of grid points reach full extinction (the corresponding temperature drops significantly) when they are constantly subjected to the large strain values for a substantial period.

In summary, during the early simulation time in which extinction prevails, Fig.(5.2) demonstrates two things. First, for those grid points with $\chi_{st} \leq \chi_q$, the SFL model provides a reasonably accurate prediction of temperature and reaction rate. Second, for those grid points with $\chi_{st} > \chi_q$, the chemistry can not response to the rapid change of χ_{st} instan-

taneously. The SFL model is capable of capturing the extinction. However it overestimates the amount of extinction because it does not take transient processes into account. In addition, for those grid points with a small and sudden excursion of χ_{st} beyond χ_q, instead of being extinguished to a very low temperature, the points are capable of returning to the fully burning state when χ_{st} decreases below χ_q without interaction with an ignition source. This spontaneous reignition process is identified as one of the three reignition mechanisms: independent flamelet scenario(IFL), in Sripakagorn[64].

5.2.2 Late Simulation Time

During late simulation time, i.e., after the onset of extinction, χ_{st} drops below the quenching limit at almost every computational grid point which is manifested by the almost zero percent of $\chi_{st} > \chi_q$ as shown in Fig.(5.3). The gradual occurrence of reignition is favored when χ_{st} is under the quenching limit. These extinguished regions can only be reignited by the three mechanisms listed by Sripakagorn[64]: (1) independent flamelet scenario(IFL); (2) edge flame propagation towards the quenched region; (3) engulfment scenario. Edge flames with a positive speed of propagation exhibit a three part structures, each with a substantially different reaction rate. Ahead of the edge flame front, the reaction is frozen. In the edge flame front, the reaction rate is highly intense. Following the edge flame front, the rate of reaction in the trailing diffusion tail is of the similar order of magnitude as the rate of the SFL burning state [28]. The deviation between the DNS and the model exhibited in Fig.(5.1) can be tentatively attributed to the existence of the intense reaction rate associated with the edge flame head. This will be further illustrated by comparing the relative quantities along the contour lines of the stoichiometric mixture fraction, which will be discussed in the following section.

5.3 Quantities Along the Z_{st} Contour Lines

The scalar quantities, e.g. temperature and reaction rate, obtained from DNS against the ones predicted by SFL model are shown plotted along the isocontour of stoichiometric mixture fraction ($Z = Z_{st} = 0.5$) to visually demonstrate the scenarios occurred in extinction and reignition as described above. To do this, the isocontour lines on some $x_1 - x_2$ plane

are generated using Matlab. The output arguments returned from Matlab contain the geometric locations of a set of points representing the isocontour lines in the form of x_1 and x_2 coordinates. The scalar quantities of the points on the contour line can then be interpolated. The times $t = 0.26$ and $t = 1.46$ are chosen for plotting to represent the early(extinction prevails) and late simulation time(reignition prevails), respectively.

At time $t = 0.26$, the temperature Y_P (top panel) and the reaction rate ω_P (bottom panel) obtained directly from DNS are compared against the ones predicted by the SFL model along two different contour lines are plotted in Fig.(5.7) and Fig.(5.8), respectively. The stoichiometric scalar dissipation rate χ_{st} along the $Z_{st}-$contour line is also included in both panels of each figure for reference. As shown in Fig.(5.7), along the contour line in the $x_1 - x_2$ plane at $x_3 = 50$, the stoichiometric dissipation rates along this contour line are all below the quenching limit. Thus, the SFL model gives very good agreement between predicted reactive scalars(temperature in top panel and reaction rate in bottom panel) and actual DNS results. In addition, as exhibited in the bottom panel, both the true and the modeled reaction rates track the trend of χ_{st} closely, indicating that the SFL model is a good predictor of behavior for $\chi_{st} < \chi_q$. This corroborates the earlier argument. Note that the reaction rates have been divided by a factor of 6, which makes them of the same order of magnitude as χ_{st}, for visualization purposes. At the same time $t = 0.26$, along another contour line in the $x_1 - x_2$ plane at $x_3 = 126$, it can be seen from Fig.(5.8) that the extinction does not necessarily coincide with the occurrence of χ_{st} beyond χ_q. The onset of extinction is related to the amplitude of the fluctuation of χ_{st} beyond the quenching limit. From Fig.(5.8), it can be seen that for a relatively smaller excursion of χ_{st} above χ_q(contour line segment between the 110th and 240th points), the flamelet is still in the burning state with a reaction rate that is of the same magnitude as the one for the SFL burning state at the quenching value of $\chi_{st} = \chi_q$. In contrast, for the sufficiently large fluctuation of χ_{st}(contour line segment between the 290th and 340th points), the flamelet experiences a transition from the burning to the completely extinguished state.

At time $t = 1.46$, as the fluctuation of χ_{st} decays to below the quenching limit, reignition occurs. The flamelet reignites through the three mechanisms which have been described previously. In present work, detailed studies of the mechanism of extinction hole reignition

via edge flame propagation are performed. The scenario of this reignition mechanism is visually demonstrated here. As seen in Fig.(5.9), the strain rates along the contour line decrease below the quenching limit, which favors a reignition process. Flame extinction is shown by the close-to-zero DNS reaction rate (the contour line segment between the 132th and 148th points). The onset of local premixing of the fuel and oxidizer within the extinction hole is indicated by a relatively large value of $f = Y_F \times Y_O = 0.197$. The edge flame front associated with the intense reaction rate at the hole edge propagates inwards along the Z_{st}-contour line, leading to reignition. The flame state exhibited in Fig.(5.10) (the contour line segment between the 85th and 115th points) corresponds to a close to completely reignited hole due to the edge flame propagation. This is manifested by a bimodal shape with a trough at the site where f attains its maximum. The reaction rate within the reignited hole is much higher than the one predicted by the SFL model. The intense reaction rate associated with the edge flame can thus be considered as a reason to cause the underprediction of the SFL model during late simulation time.

5.4 Geometric Statistics of Flame Holes on Stoichiometric Surface

5.4.1 Introduction

For studies focusing on the local structure and mechanics of extinction and reignition, a direct approach is to study the time evolution of the topological structures and properties of the local extinguished regions (i.e., flame holes, or synonymously, quenched holes). This involves examining the evolution of the number, the area distribution and the scaling behavior of flame holes during the whole simulation time. Furthermore, with the interactive 3D geometric information of each flame hole structure extracted and rendered by in-house numerical algorithm, we can provide accurate numerical predictions of the reactive properties and burning states within each flame hole and subsequently probe of the dynamics of flame holes.

A flame hole is formed due to the local quenching when and where the flame is subjected to excessive local stretching with a scalar dissipation rate exceeding the critical extinction value for a long enough time duration. It is known that the χ_{st} is a random variable in

turbulent diffusion flames, and the flame holes thus formed are randomly distributed on the stoichiometric mixture fraction isosurface.

The edge flame subsequently appears surrounding the perimeter of the flame hole that separates the extinguished and the burning region on flame surface. The propagation speed of the edge flame along the stoichiometric surface could be positive or negative with respect to the quenched hole depending on the magnitude of χ_{st} in the local quenched region. This edge flame propagation leads to the expansion or collapse of holes. Accordingly, the associated edge flame structures are distinctly different in these two situations. When propagation speed is positive, the edge flame advances toward the non-reacting premixed region to reignite and shrink the flame hole, and this regime is called the ignition mode. The edge flame may show a tribrachial structure depending on the speed and intensity of the flame. This is composed of a bending fuel-rich premixed wing locating on the fuel stream side, a bending fuel-lean premixed wing locating on the oxidizer stream side, and a trailing diffusion flame tail in which the hot unburnt fuel and oxidizer diffuse toward each other respectively from the excess residue of the leading fuel-rich and fuel-lean premixed flame. The three branches connect at triple point, where the reaction rate is highly intense. The triple flame structure is first photographically observed on a mixing layer in an experiment by Phillips[50]. When the advancing flame is less intense, the wings merge into a single high-intensity reaction zone contoured on the stoichiometric surface. When the propagation speed is negative, the edge flame retreats away from the quenched region into the burned region to extend the flame hole, this regime being called the extinction mode. The premixed wings merge with the trailing diffusion tail yielding a monobrachial structure which burns essentially as a typical diffusion flame without an excess reaction rate[28] [52] [73].

With the goal of contributing to understand the mechanics of extinction and reignition and to provide insight into the dynamics of edge flame propagation, the scaling behavior of the flame holes (i.e., the size distribution, span and temporal evolution of the flame hole) are investigated. The flame holes can be easily visualized by overlaying the temperature field onto the isosurface of stoichiometric mixture fraction. This interactive 3D visualization provides an instructive view of these complex configurations, but it cannot be used as a basis to support further numerical investigations. A numerical exploration is carried out

by developing a criteria to identify locally quenched regions, developing a new numerical algorithm to combine these locally quenched regions into contiguous flame holes, and then develop statistics on the behavior of the flame holes as they evolve in time (e.g., how the size distribution of the flame holes evolve). The procedures are as follows:

Step I: As previously introduced in Section 3.5, the stoichiometric mixture fraction isosurface is extracted from the volumetric scalar data using the triangulation algorithm based on interpolation. The resulting triangulated isosurface consists of connecting grid-scale triangular faces (equivalently, triangular meshes), each of which approximates its corresponding elemental surface area. Accordingly, the reactive scalars associated with each triangular face, denoted generally by Q_{ii} (Q as a quantity of interest may be referred to as temperature or reaction rate), are obtained by adopting the same numerical scheme as the one proposed in Section 4.8. The Q_{ii} used to characterize the local flame burning state will be compared against the criteria to determine whether or not the local triangular face is quenched. The isosurface generated in triangulated form is therefore the basis for delineating the geometric patches of flame holes.

Step II: The criterion based on chemical and physical properties of the current diffusion flame (i.e., reaction rate and temperature) are defined and applied to each individual triangular face to numerically identify whether or not a triangular face is quenched.

Step III: For those quenched triangular faces identified in the previous step, an in-house numerical algorithm is developed for connecting the neighboring quenched triangular faces (i.e., triangles that share a common edge) to form the patches of flame holes on the 3D stoichiometric isosurface.

Step IV: The accuracy of the flame hole formation algorithm is tested on two different surfaces patched with known shapes.

Step V: Using the geometric information associated with the patches of flame holes rendered in above step, the statistics of the flame hole sizes and the reactive quantities associated with the flame holes are calculated and analyzed.

The first step has already been explained in Section 4.8, so steps II, III and IV are next to be discussed.

5.4.2 Criteria for Identification of a Flame Hole

Within a flame hole, the chemical reaction is frozen because of low temperature and only pure mixing of reactants occurs, this feature is quantitatively exhibited in Fig.(5.8). The flame hole can thus be numerically characterized in terms of low reaction rate at low temperature. A criterion based on the chemical properties of quenched flame is developed as a way of identifying the quenched triangular face. The process of establishing the criteria by studying the magnitude of reactive scalars at extinguished flame state is illustrated in this section.

A necessary first step is to 1) decide which reactive scalars (either reaction rate or temperature or both) to use as a state variable in criteria for specifying the quenched flame state, and 2) describe how to apply this criteria to identify the burning state of each triangle face along the flame surface.

Before the discussion is started, the reason why the stoichiometric scalar dissipation rate χ_{st} is excluded from consideration as a criterion needs clarification. As is well known, the stoichiometric scalar dissipation rate χ_{st} plays a key role in local extinction and reignition events. Once the χ_{st} fluctuates beyond the critical value χ_q, the local extinction occurs, appearing as a flame hole. When the χ_{st} decays below the critical value, flame hole reignition takes place by the propagation of the surrounding edge flames along the flame surface and the hot flames brought into contact via diffusion and convection in the normal direction to flame surface. But, the occurrence of flame holes does not coincide temporally with the fluctuations of χ_{st} relative to χ_q. As shown in Fig.(5.8), i.e., initial occurrence of extinction during early simulation time, the flame is still in a burning state when the χ_{st} fluctuates above χ_q. And, as seen in Fig.(5.9), i.e., initial occurrence of reignition during late simulation time, the flame is still quenched while the strain rate is relaxed below the critical value. In this regard, the χ_{st} is a primary factor related to the occurrence and evolution of flame holes but not as an instant indicator.

For a single-step chemistry with Arrhenius type kinetics, the rate of reaction depends on two variables: mixture fraction Z and temperature Yp, as expressed in Eq.(3.24). Along the flame surface, the mixture fraction is a fixed constant equal to Z_{st}, the reaction rate

is thus a function depending only of temperature. The temperature on the flame surface ranges from 0 to the maximum flame temperature corresponding to the stoichiometric chemical equilibrium state $Y_{Peq} = 0.83$. Taking the chemical parameters used in the current study (listed in Table.(3.3)), with the mixture fraction being fixed at Z_{st}, the Arrhenius temperature dependence of reaction rate is analytically calculated using Eq.(3.24) and is shown in Fig.(5.11). The figure demonstrates that there exist two values of temperature for each single value of reaction rate. The temperature-dependence of reaction rate is thus a two-to-one function for all temperatures in the range $[0, Y_{Peq}]$, such that both the low and near-equilibrium temperatures can lead to the same near-zero reaction rate (these two regions of low reaction rates are marked by black circles in the figure). But, as is well known, the equilibrium state associated with zero reaction rate is not a locally quenched region. As the temperature-dependence of the reaction rate is a two-to-one function, a unique value of reaction rate can not be used to identify a unique flame state. This suggests that the use of reaction rate criteria alone to distinguish between burning versus non-burning states is inadequate. However, temperature is an adequate indicator to identify the unique burning state of each single triangular face along the triangulated flame surface. Each low temperature determines a unique low reaction rate due to the relationship exhibited in Fig.(5.11). Thus, a criterion defined by a specified low temperature is commensurable to the one defined by (low reaction rate, low temperature) pair which dictates the characteristics of quenched flame. One such criteria is

$$Y_P \leq Y_{Pcr}. \tag{5.1}$$

Here Y_{Pcr} denotes the critical value of temperature.

Along the flame surface (i.e., the reactive scalars are conditioned on stoichiometry), the temperature associated with each triangular face, denoted by $Y_{P_{ii}}$, is evaluated by comparing with the criteria Y_{Pcr} to determine if this local triangle face is quenched. The identification procedure can be exemplified for the ii-th triangle face as

$$\begin{aligned} &\text{if } Y_{P_{ii}} \leq Y_{Pcr} \quad : \quad \text{the } ii\text{-th triangle face represents a local quenched flame} \\ &\text{if } Y_{P_{ii}} > Y_{Pcr} \quad : \quad \text{the } ii\text{-th triangle face represents a local burning flame} \end{aligned} \tag{5.2}$$

Next, the critical value of temperature Y_{Pcr} needs to be determined. This critical value is

essentially a cutoff that defines the boundary between the burning and non-burning regime. It is considered to be adequate to meet the following two requirements: (1) the critical value of temperature should be low enough to be thought of as a characteristic of frozen reaction; (2) the results should be relatively insensitive to the exact value of the critical temperature selected, i.e., a minor change in the critical value will not appreciably affect the statistical results.

Starting with the first requirement, the value of the low temperature (the quenched temperature) is defined. As exhibited in Fig.(5.12), the pattern of isosurface temperature distribution demonstrates the regions of flame holes (regions of dark blue). Referring to the color-coded temperature maps, the critical value of temperature lower than 0.45 is adequate to distinguish a quenched state from a completely burning state. The specific value of Y_{Pcr} is further determined by the second requirement.

As described above, along the stoichiometric isosurface, the reactive scalars associated to each triangular face (i.e., $Y_{P_{ii}}$, $\omega_{P_{ii}}$) represents the local burning state. In Fig.(5.13), take case R2 for example, the bivariate (i.e., two-dimensional) histogram of local temperature and reaction rate (i.e., $(Y_{P_{ii}}, \omega_{P_{ii}})$ pairs) for times t = 0.54,0.72,0.9, and 1.14 is exhibited to assist in the determination of the value of Y_{Pcr}. The bivariate histogram evenly divides the domain of temperature and reaction rate dimensions into a set of bins. It then checks the local $(Y_{P_{ii}}, \omega_{P_{ii}})$ value pair at each triangular face on the stoichiometric surface and increments the appropriate bin count by one. In the figure, the color density indicates the number of joint events of $(Y_{P_{ii}}, \omega_{P_{ii}})$ data value pairs that fall within each bin. The histogram serves as a graphical representation of the burning state distribution to demonstrate the peak nonburning distribution and to facilitate the determination of Y_{Pcr}. As shown in the figure, for case R2, if the temperature of 0.35 is chosen as a critical value, almost all nonburning faces are clustered below this critical value. It implies that a minor change in Y_{Pcr} will not have appreciable effect on the statistics. The pertinent statistics on which to base assessment of critical value of 0.35 are probability density function and cumulative distribution of local temperature $Y_{P_{ii}}$, which are presented in Fig.(5.14) for four simulation times 0.54, 0.72, 0.90 and 1.14. The probability is measured in two ways: 1) counting each triangle face as 1 (left column in the figure), 2) counting the corresponding area of each

triangle face (right column in the figure). It can be seen that the statistics determined in these two ways yield the same behavior since the triangle faces used to weight the counts are about the same size. In each sub-panel, the dotted vertical line indicates the critical value of 0.35. In the low-temperature range (i.e., $Y_P < 0.45$) of probability density, the critical value of 0.35 is on the right of the peak and locates at the initial part of the off-peak tail. Correspondingly, in the plot of cumulative distribution, the critical value of 0.35 locates at the leveling-off part of the curve after initial increase. It implies that the critical value of temperature of 0.35 is appropriate to reduce the sensitivity of the statistics without violating the definition of frozen reaction.

Next the criterion determined above is applied to each triangular face over the whole triangulated flame surface to identify the quenched triangle faces. The total quenched area on the flame surface, A_h, can thus be measured by simply summing all the quenched faces. This scheme can be represented as

$$A_h = \sum_{Y_{P_{ii}} \leq Y_{Pcr}} \Delta A_{ii}, \tag{5.3}$$

where ΔA_{ii} and $Y_{P_{ii}}$ denote the area and temperature of the ii-th triangle face, respectively. Accordingly, the percentage of flame surface area identified as quenched regions is computed as

$$\frac{A_h}{A} = \frac{\sum\limits_{Y_{P_{ii}} \leq Y_{Pcr}} \Delta A_{ii}}{\sum\limits_{ii} \Delta A_{ii}}, \tag{5.4}$$

where A is the total flame surface area. For instance, in the case R2, the temporal evolution of the total quenched area A_h resulting from critical value of 0.35 is displayed in the top panel of Fig.(5.15). The total area of flame surface (i.e., stoichiometric isosurface area), A, shown by the solid red line, is also included here for reference. And, the area fraction of flame holes, A_h/A, is exhibited in the bottom panel. As shown in the figure, the total flame surface area monotonically increases due to the turbulent stretching and molecular mixing. Note that the increasing flame surface by the turbulent stretching could enlarge the hole area. The total quenched area changes in three stages: (1) during time $t = 0 \sim 0.65$, it increases rapidly due to hole expansion via extinction, (2) during time $t = 0.65 \sim 1.2$, it increases slowly and reaches peak at time $t = 1.06$ followed by a slight decrease due to the slight

imbalance between the extinction and the onset of reignition, together with the increase of flame surface by turbulent stretching, (3) after time $t = 1.2$, it gradually decreases due to hole filling by reignition. The total flame surface area A, as the denominator of quenched area fraction, is larger at the peak appearance time of the total quenched area $t = 1.06$ than at earlier time as shown in the top panel. Thus, the peak value of quenched area fraction occurs earlier in time ($t = 0.82$) than the peak value of total quenched area. During the onset of reignition, the decreasing rate of flame hole area is the result of imbalance between the increasing flame surface due to molecular mixing and the hole shrink due to reignition. Thus, the quenched area normalized by the total flame surface area provides a better way to demonstrate the role of reignition.

Subsequently, the area fractions of quenched regions identified according to a set of four different critical values, $Y_{Pcr} = [0.226, 0.3, 0.35, 0.4]$, are respectively plotted as a function of time in Fig.(5.16). For comparison, the area fraction of the stoichiometric scalar dissipation rate beyond the critical value of extinction, $Percentage(\chi_{st} > \chi_q)$, shown by the solid red line, is also included. It is measured along the triangulated stoichiometric isosurface by summing up the area of triangle faces whose associated local scalar dissipation rates are beyond χ_q. This scheme can be represented as

$$Percentage(\chi_{st} > \chi_q) = \frac{\sum\limits_{\chi_{st_{ii}} > \chi_q} \Delta A_{ii}}{\sum\limits_{ii} \Delta A_{ii}}. \tag{5.5}$$

As shown in the figure, the area fraction of the quenched regions monotonically increases with the increase of critical value, and the maximum area fraction is 13.66%, 16.67%, 18.25% and 19.58%, respectively, for the four different Y_{Pcr}. Nevertheless they follow the same trend. With respect to the relationship between A_h/A and $Percentage(\chi_{st} > \chi_q)$, it can be observed that the time evolution of A_h/A lags behind the one of $Percentage(\chi_{st} > \chi_q)$. The peak appearance time of the area fraction of quenched regions is almost invariant with respect to the critical value, but it lags behind the peak appearance time of fluctuations of χ_{st} beyond χ_q. This rightward shift in the peak time is due to the late-onset response of flame quenching to the fluctuations of χ_{st} beyond χ_q and the gradual occurrence of flame reignition resulting from the decrease of χ_{st} below χ_q. The same behavior is reported for

a piloted planar temporal $CO/H_2/N_2$ jet flame by Hewson and Kerstein[30], in which the fractions are referred to as the volume fraction of stoichiometric temperature below 1000K and the volume fraction of $\chi_{st} > \chi_q$. Because of the time lag of reignition relative to the relaxation of χ_{st}, the quenched regions are not completely reignited after χ_{st} is almost negligible.

The time rate of change of total quenched area and the fraction of the total area that is quenched are presented in Fig.(5.17) for four different critical values. Here, the second-order central difference approximation is employed for the time derivative. The hole collapse by reignition is at a lower rate than the hole growth by extinction. Combining with the behavior of the time evolution of the fluctuations of χ_{st} shown in Fig.(5.16), i.e., the mixing rate increases rapidly during extinction and then falls during reignition, it suggests that the rate of change of hole size depends on the mixing rate. During the time when extinction phase prevails, the growth rate of flame hole increases with the increase of critical value as the higher critical value expands the range of quenched hole. During the time when reignition phase prevails, the deviations between different critical values are negligible and the rate of hole collapse keeps roughly invariant over time.

5.4.3 Numerical Algorithm for Flame Hole Formation

The preceding section describes an approach for identifying individual triangular faces that represent extinguished stoichiometric surfaces. In this section we work towards collecting these faces into contiguous holes such that statistics regarding hole size can be developed over the simulation. To be specific, each of these groups is a collection of neighboring (i.e., connected) triangles. All these groups appear as multi-patches overlaid on the stoichiometric isosurface. They are the so called "flame holes".

In this section, a numerical algorithm is developed to join the neighboring selected faces together so as to form them into contiguously connected flame holes. Two triangles can be considered as neighbors and joined together to make up a patch of flame hole if they share a common edge. It is worthy to note here, that the triangular faces generated by Matlab triangulation scheme connect with each other for constructing the isosurface by sharing

common edges, but they never intersect with each other. The in-house numerical scheme is developed in the Matlab environment and comprises the following steps:

Step I: The Matlab intrinsic function *isosurface* is used to extract the isosurface from a 3D scalar data at a user-specified isovalue by triangulation. The Matlab function returns the topological data in a face-vertex format as

$$[faces, vertices] = isosurface(Xi, Yi, Zi, Z, Z_{iso}). \tag{5.6}$$

The isosurface is represented by the set of triangle faces (i.e., triangular faces) that are constructed by connecting each of the irregularly distributed data points. These spaced data points are generated by spatial interpolation at a specified isovalue and serve as the vertices of triangles. The set of all triangle faces and all vertices are indexed by contiguous integers from 1 to H and from 1 to M, respectively. The index is a label used to identify a triangle face or a vertex. Correspondingly, the returned $faces$ and $vertices$ are represented by a H-by-3 and a M-by-3 matrix. Each row of the $faces$ matrix represents a triangle face defined by three indices in the $vertices$ matrix of vertex coordinates (i.e., as the rows of indices). A more detailed description is given in Section 3.5 and Appendix A. It is worth noting that the ordering of the indices of triangle faces has no particular directional and geometrical implications, i.e., the indices of a face is not ordered according to its position.

Step II: From the triangulation rendering data (i.e., $faces$ and $vertices$) generated in Step I, the Matlab function *TriRep* creates a class of 3D triangulation representation, $trep$, that yields the topological and geometric queries for 3D triangulations in an efficient way [1]. The corresponding Matlab script is given as

$$trep = TriRep(faces, vertices). \tag{5.7}$$

Step III: Among all the triangle faces generated by the triangulation process, a quenched triangle face is individually identified according to the criteria of extinction described in Section 5.4.2. The indices of the selected triangle faces are stored in a column vector $SelectFace(N \times 1)$, where N is the number of selected faces. As mentioned in Step I, the ordering of the indices of the selected faces is irrelevant to their relative spatial positions. The selected triangle faces and their neighborhoods are displayed schematically in

Fig.(5.18). In the picture, part of the selected faces are highlighted and marked with the original face index.

Step IV: Utilizing the object of the triangulation representation *trep* generated in step II, the Matlab function *neighbors* returns the indices of neighbors of each selected triangle face. The corresponding Matlab script is given as

$$nbrs = neighbors(trep, SelectFace). \tag{5.8}$$

Here the output result $nbrs$ is a N-by-3 adjacency matrix, where N is the number of selected triangles and 3 is the maximum number of neighbors per triangle. Each row of matrix $nbrs(i,:)$ specifies the indices of the neighboring triangle faces of triangle face $SelectFace(i)$. Note that, in cases where the neighboring triangle of one side 1) is not an identified quenched triangle or 2) is nonexistent, the neighbor index is assigned NaN (Not a Number). As an example of how to interpret the output $nbrs$, the adjacency matrix for triangle faces demonstrated in schematic Fig.(5.18) is shown in the following Table.(5.1).

As shown in Table.(5.1) and Fig.(5.18), the 17th triangle face (11th row of the output) has 12th and 25th face as neighbors and has no neighbor connected at one side. So, the table means that faces 12, 15, 17, 23 and 25 are adjacent to each other and can be joined together to form a group.

Step V: The connections among these selected triangle faces have no preferential direction and are irrelevant to the ordering of their indices, the only principle of the connectivity is the common edge. The numerical algorithm for connecting the neighboring triangle faces to form flame holes is developed based on the neighboring information obtained in the above step. This algorithm is illustrated in the flowchart which is shown in Appendix D

5.4.4 The Assessment of Numerical Algorithm for Flame Hole Formation

The accuracy and adequacy of this flame hole formation strategy are assessed by (1) forming user-defined patches on a spherical surface, and (2) comparing the flame hole patterns formed by numerical algorithm against the ones visualized by a 3D temperature distribution superimposed on the flame surface.

$SelectFace(N \times 1)$	
row i	$SelectFace(i)$
row 1	5
⋮	⋮
⋮	⋮
row 9	12
row 10	15
row 11	17
⋮	⋮
⋮	⋮
row N	296250

$nbrs(N \times 3)$			
row i	$nbrs(i,1)$	$nbrs(i,2)$	$nbrs(i,3)$
row 1	7	NaN	11
⋮	⋮	⋮	⋮
⋮	⋮	⋮	⋮
row 9	17	23	15
row 10	12	NaN	NaN
row 11	NaN	12	25
⋮	⋮	⋮	⋮
⋮	⋮	⋮	⋮
row N	296179	NaN	NaN

Table 5.1: The adjacency matrix $nbrs(N \times 3)$ (right table) gives the indices of neighboring triangle faces for each selected triangle face whose index is stored in the column vector $SelectFace(N \times 1)$ (left table). The selected triangle faces and their connectivities can be visualized in schematic Fig.(5.18) as a reference.

In the first assessment, the patterns of two spatially separated patches on the surface of a sphere with radius of 30 are defined. Imagine dividing the sphere into 8 sections by coordinate planes $x = 0$, $y = 0$, and $z = 0$, the first patch is a spherical semilune covering the range from 210° to and including 240° (i.e., dihedral angle of 30° and located in the third $(-, -, +)$ spherical octant). The second patch is defined to be a spherical zone with a 45° horizontal sweep of curvature (a range from 270° to and including 315°) and a 40° vertical sweep of curvature (±20° latitude around the equator). The second patch is located in the middle of the fourth $(+, -, +)$ and eighth $(+, -, -)$ spherical octant. When the spherical surface is triangulated, each patch is then considered as a group of connected triangle faces. The indices of the triangle faces located within these two user-defined regions on the spherical surface are selected out and stored in a column vector $SelectFace$. By applying the flame hole formation algorithm, the selected triangle faces are categorized into two distinct groups. Each group of connected triangles is individually

visualized by being superimposed on the 3D spherical surface with a unique color, i.e., the first and second patch are colored green and cyan, respectively. As shown in Fig.(5.19), the configurations of the resultant regions formed by applying the numerical algorithm exactly match the defined topological patches.

In the second assessment, for the DNS scalar field of case R2 at time=0.31, the flame holes are formed and delineated by the numerical algorithm for three different critical values of extinction: $Y_{Pcr} = 0.225$, 0.35 and 0.45 are visualized by being superimposed on the 3D stoichiometric isosurface of mixture fraction with a constant black color, which are displayed in the top right, bottom left and bottom right panel of Fig.(5.20), respectively. For comparison, the isosurface of stoichiometric mixture fraction colored by the local temperature is also included (top left panel), i.e., a means to superimpose the temperature data by coloring the flame surface. The stoichiometric isosurface shows the spatial configurations of the flame surface. The color coding indicates the temperature value on the flame surface, where the dark-blue indicates the low temperature (i.e., the flame hole) referring to the temperature scale of color bar. Comparing each of the three subplots from top right to bottom right with the top left one, or equivalently, comparing the black regions (rendered numerically) with the dark-blue regions (color-coded temperature distribution), the spatial locations, distributions and patterns of the flame holes are congruent. Comparing the scales of flame holes formed by the algorithm under different critical values, the spatial locations of the flame holes are congruent, only the range of the hole increases with the increase of critical value of extinction. This implies that the temperature increases outward in the blurred border region of flame hole.

5.4.5 Statistics of Geometric Properties of Flame Holes

As previously described, the flame holes formed by the in-house neighbor-joining algorithm along the triangulated flame surface are groups of connected triangle faces. In addition the mixing and reactive scalars associated with each triangle face are available. Therefore, this numerical algorithm can yield rich geometric information on local flame hole structure and along with knowledge of the local reacting properties for each individual flame hole.

The total number of flame holes formed under a set of four different critical values, $Y_{Pcr} = [0.226, 0.3, 0.35, 0.4]$, are respectively plotted as a function of time in the top panel of Fig.(5.21). The corresponding average hole area is included in the bottom panel. As shown in the figure, both the number and average area of flame holes monotonically increase with an increase of critical value. When the critical value increases, more local regions on the flame surface are identified as quenched holes, especially capturing those going through the process of extinction (i.e., approaching complete extinction) and reignition (i.e., initial stage of reignition). Regions added due to the increase in the critical value are responsible for the increase in the number of flame holes. An increase in critical value expands the quenched region which leads to an increase in average hole area. But, the deviation between the time evolutions of the four averages is not significant. It implies that the critical value of 0.35 is adequate since the statistics of hole scales are not sensitive to the minor change in critical value. The average hole area initially increases due to the hole expansion, however, this growth trend stops after the time $t = 1$ when reignition predominates. It implies that the number and the total area of flame holes shrink at roughly the same rate. Next, this roughly time-invariant average area during the reignition scenario is illustrated with the use of the probability mass distribution of hole area.

For flame holes identified by four different critical values, $Y_{Pcr} = 0.226$, 0.3, 0.35, and 0.4, the probability mass functions of the hole areas at six selected simulation times $t = 0.33$ (i.e., peak time of area fraction of $\chi_{st} > \chi_q$), 0.82 (i.e., peak time of area fraction of flame holes), 1.06 (i.e., peak time of total area of flame holes), 1.39, 1.72 and 2.04 are shown in Fig.(5.22). Note that the flame hole size is considered as a discrete random variable by nature, so it is associated with a discrete distribution. For the purpose of comparison, the histogram of hole areas is created with fixed range ($0 \sim 5.5$) and fixed number of bins, or equivalently, fixed bin width of 0.22, such that the probability is normalized by same value for all different simulation times. Here the value of 5.5 taken as the upper limit of the range is large enough to accommodate the largest hole area during the whole simulation time with respect to all the four critical values. As seen from the probability mass function of hole area, the probability spans a narrower range at time $t = 0.33$ than at any later time. This explains the monotonic increase in average hole size from time $t = 0$ to $t = 0.82$ as

observed in Fig.(5.21), which reflects the corresponding growth of flame holes during the process of extinction. After the simulation time $t = 0.82$, while the number of flame holes decreases because of hole collapse by reignition, the probability spans a similar range and has similar distribution behavior. This is consistent with the time-invariant average hole area following the onset of reignition as observed in Fig.(5.21). Note that, at any simulation time, the most frequent hole sizes fall within the first bin, and the probability exhibits a roughly decreasing trend. When the reignition phase prevails after time $t = 0.82$, the hole area larger than 1.5 has same low weight of probability. Correspondingly, in Fig.(5.23), the shape of the cumulative percentage distribution of hole area demonstrates that the peak of distribution (i.e., around 90% of the hole areas) lies left to the hole area of 1.5 at any simulation time. As seen in the figure, the scaling distribution behavior is roughly invariant with respect to the critical value. It can explains the unnoticeable deviations between the time evolutions of average hole area and verify the appropriateness of the critical value of 0.35.

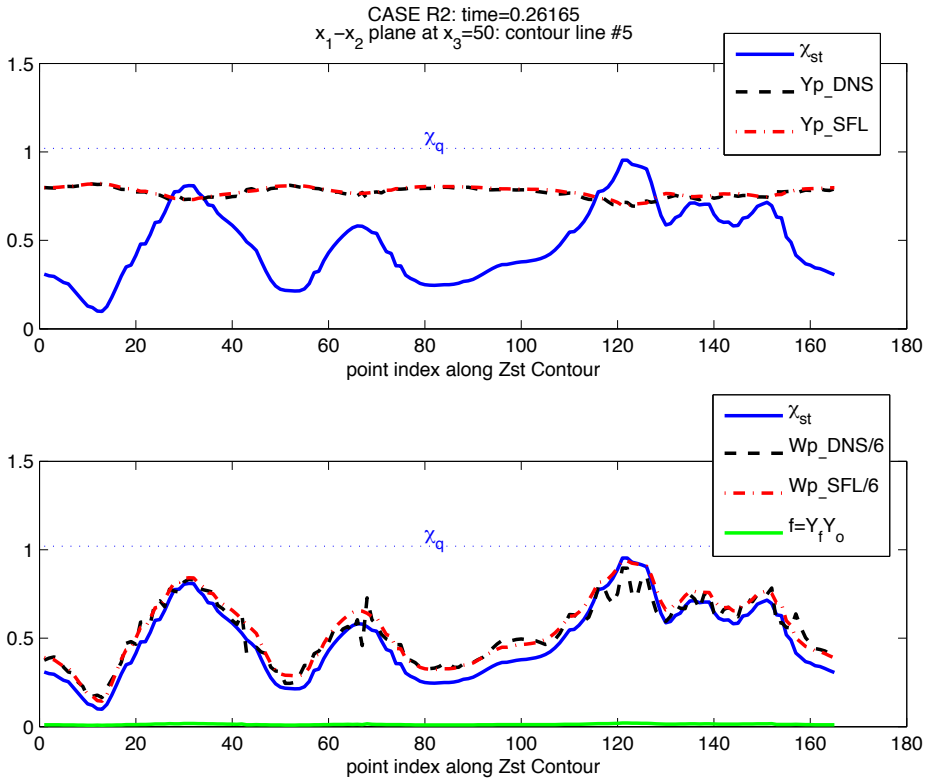

Figure 5.7: For time $t = 0.26$, the temperature Y_P(top panel) and the reaction rate ω_P(bottom panel) obtained directly from DNS(dashed) against the ones predicted by SFL model(dash-dot) are plotted along the 5th contour line in the $x_1 - x_2$ plane at $x_3 = 50$. Added to this, the $f = Y_F \times Y_O$(circle) is displayed as a predictor of premixing. The stoichiometric scalar dissipation rate χ_{st}(solid) along this contour line is also included in both panels for reference. The quenching limit value χ_q is indicated by a dotted line. Note that the reaction rates have been divided by a factor of 6, which makes them of the same order of magnitude as χ_{st}, for visualization purposes.

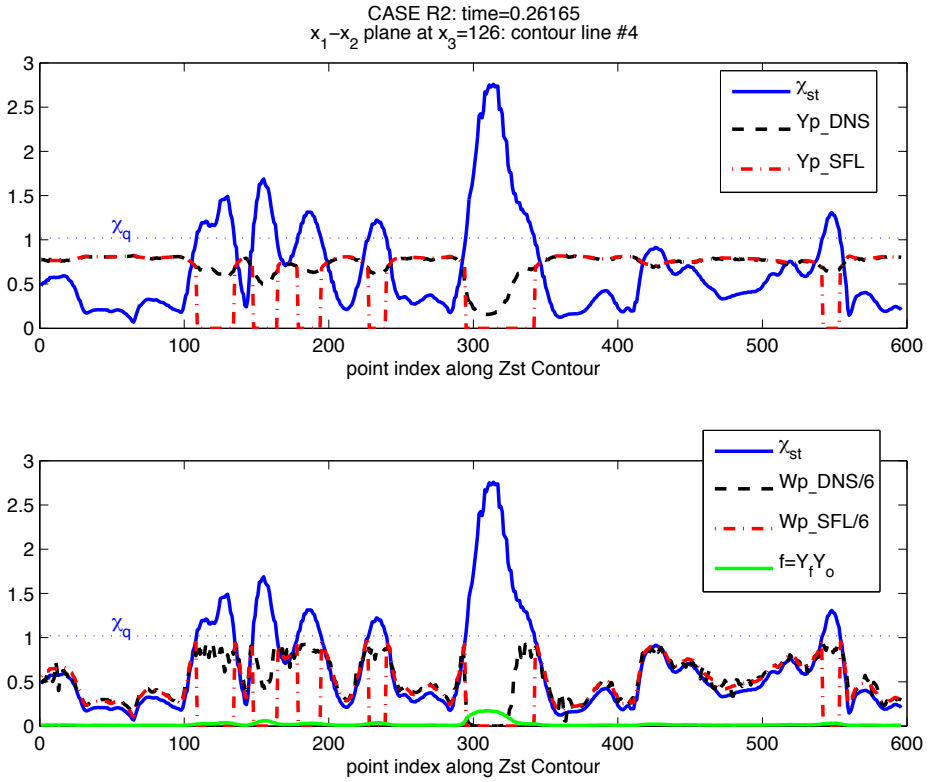

Figure 5.8: For time $t = 0.26$, the temperature Y_P(top panel) and the reaction rate ω_P(bottom panel) obtained directly from DNS(dashed) against the ones predicted by SFL model(dash-dot) along the 4th contour line in the $x_1 - x_2$ plane at $x_3 = 126$ are plotted the same way as in Fig.(5.7).

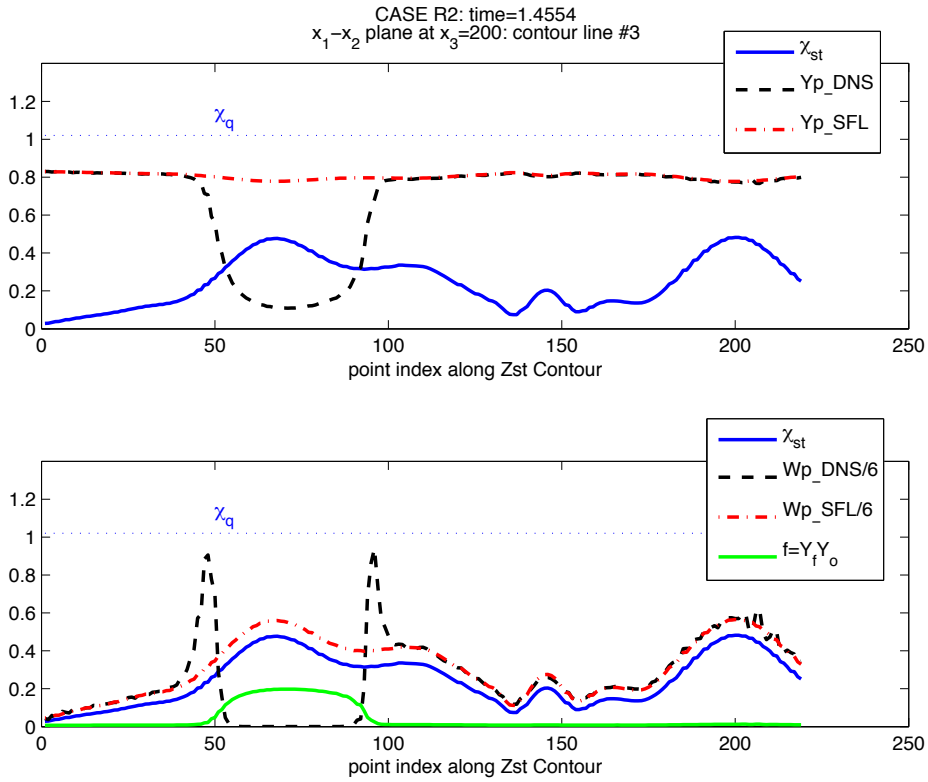

Figure 5.9: For time $t = 1.46$, the temperature Y_P(top panel) and the reaction rate ω_P(bottom panel) obtained directly from DNS(dashed) against the ones predicted by SFL model(dash-dot) are plotted along the 3rd contour line in the $x_1 - x_2$ plane at $x_3 = 200$. Added to this, the $f = Y_F \times Y_O$(circle) is displayed as a predictor of premixing. The stoichiometric scalar dissipation rate χ_{st}(solid) along this contour line is also included in both panels for reference. The quenching limit value χ_q is indicated by a dotted line. Note that the reaction rates have been divided by a factor of 6, which makes them of the same order of magnitude as χ_{st}, for visualization purposes.

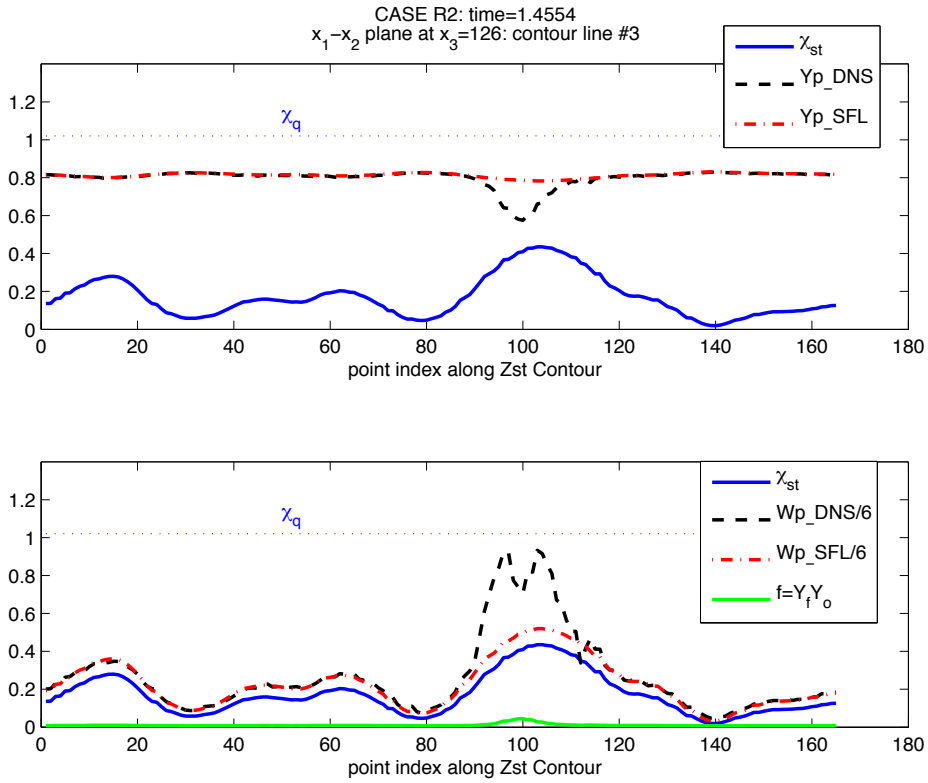

Figure 5.10: For time $t = 1.46$, the temperature Y_P(top panel) and the reaction rate ω_P(bottom panel) along the 3th contour line in the $x_1 - x_2$ plane at $x_3 = 126$ are plotted the same way as in Fig.(5.9).

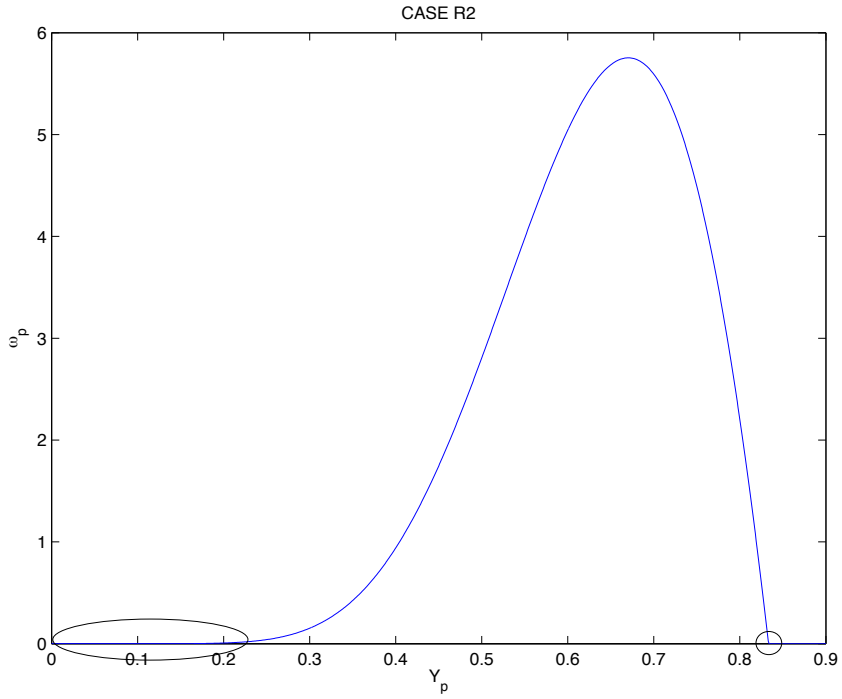

Figure 5.11: For fixed $Z = Z_{st}$, the Arrhenius type reaction rate is plotted as a function of temperature ranging from 0 to equilibrium value at stoichiometric mixture $Y_P = 0.83$.

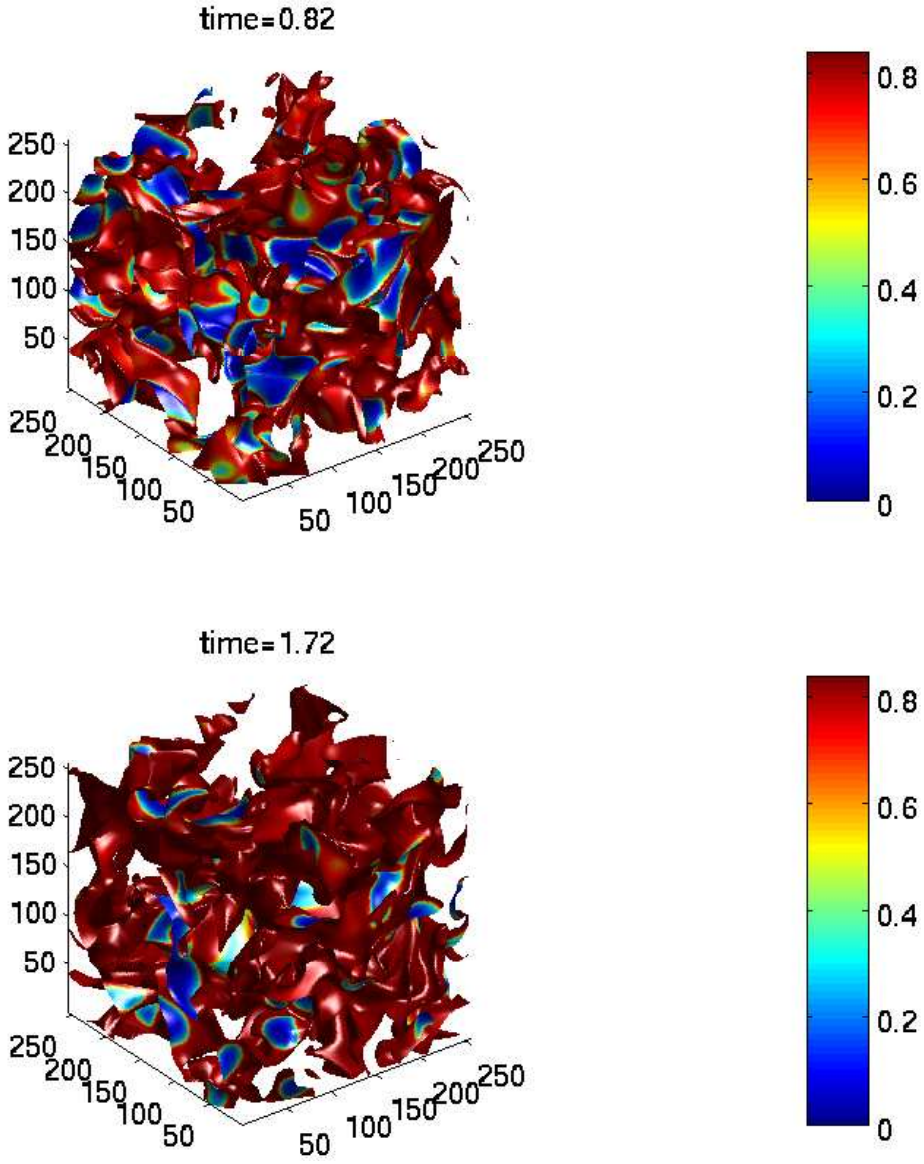

Figure 5.12: The 3D flame holes visualized by the temperature superimposed on isosurface of stoichiometric mixture fraction at simulation times: time=0.82 (i.e., peak time of area fraction of flame holes) (top panel) and 1.72 (reignition predominates) (bottom panel), respectively. The color bar indicates the temperature values. The color-coded temperature maps at two different simulation times assist in determining the critical value for identification of flame holes.

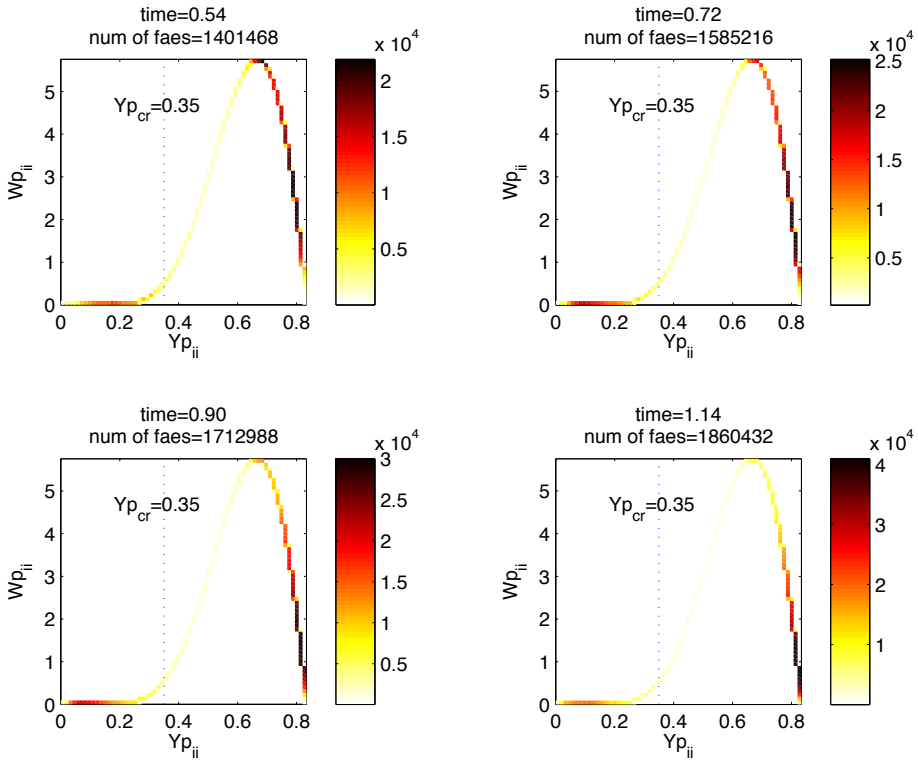

Figure 5.13: The two-dimensional histogram on pairs of $(Y_{P_{ii}}, \omega_{P_{ii}})$ data obtained from DNS data of case R2 at simulation times: time=0.54(left upper), 0.72(right upper), 0.90(left bottom) and 1.14(right bottom), respectively. The solid vertical line is added to mark the position of the critical value of temperature of $Y_{Pcr} = 0.35$.

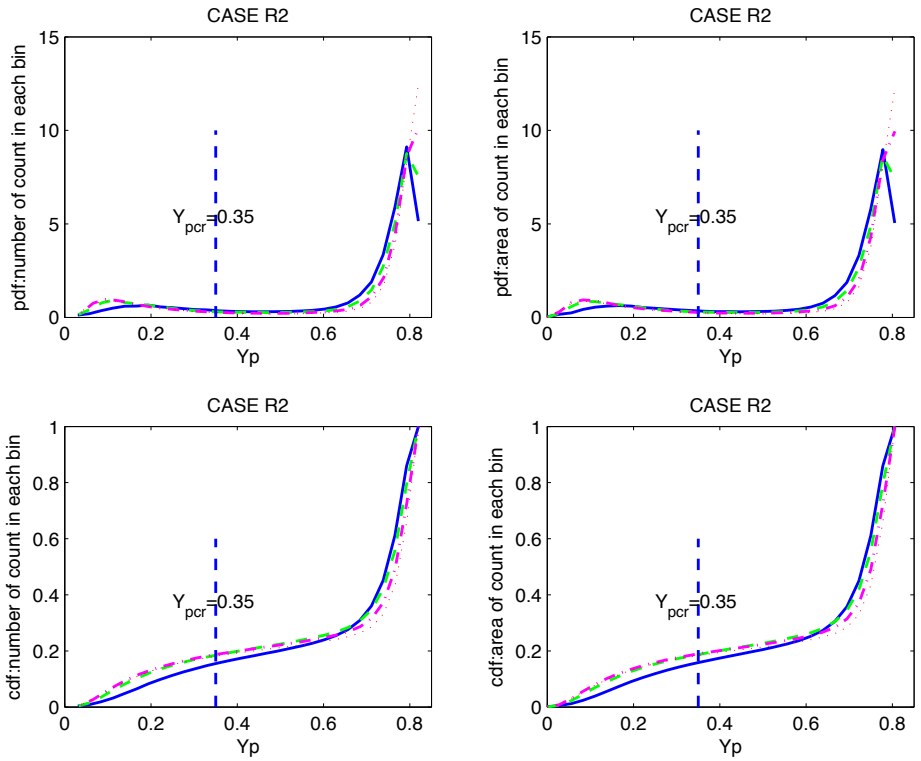

Figure 5.14: The probability density function (top row) and the cumulative distribution (bottom row) of local temperature $Y_{P_{ii}}$ for simulation times $t = 0.54$(solid blue), 0.72(dashed green), 0.9(dash-dot magenta) and 1.06(dotted red). The left and right column in the figure represent the calculations by counting the number and counting the area-weighted number, respectively.

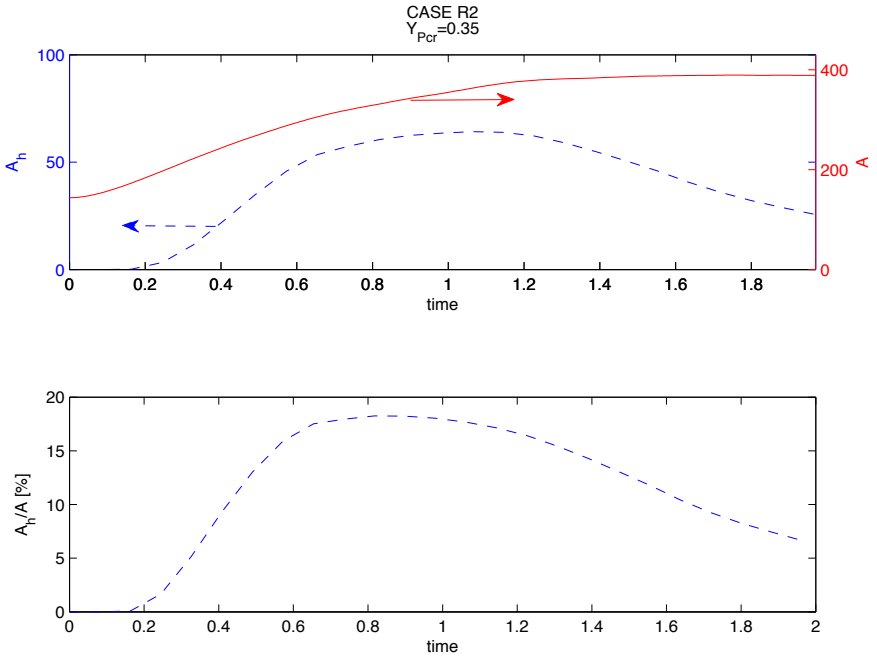

Figure 5.15: The time evolution of the total area of quenched holes on the flame surface (i.e., isosurface of stoichiometric mixture fraction) (blue dashed line, left axis in top panel) is displayed together with the total area of flame surface (red solid line, right axis in top panel) as a comparison. Correspondingly, the temporal evolution of the area fraction of flame holes (due to Eq.(5.4)) is plotted by dashed blue line in the bottom panel. Note that the scale of the area is set to 2π which is the length of computational domain in DNS.

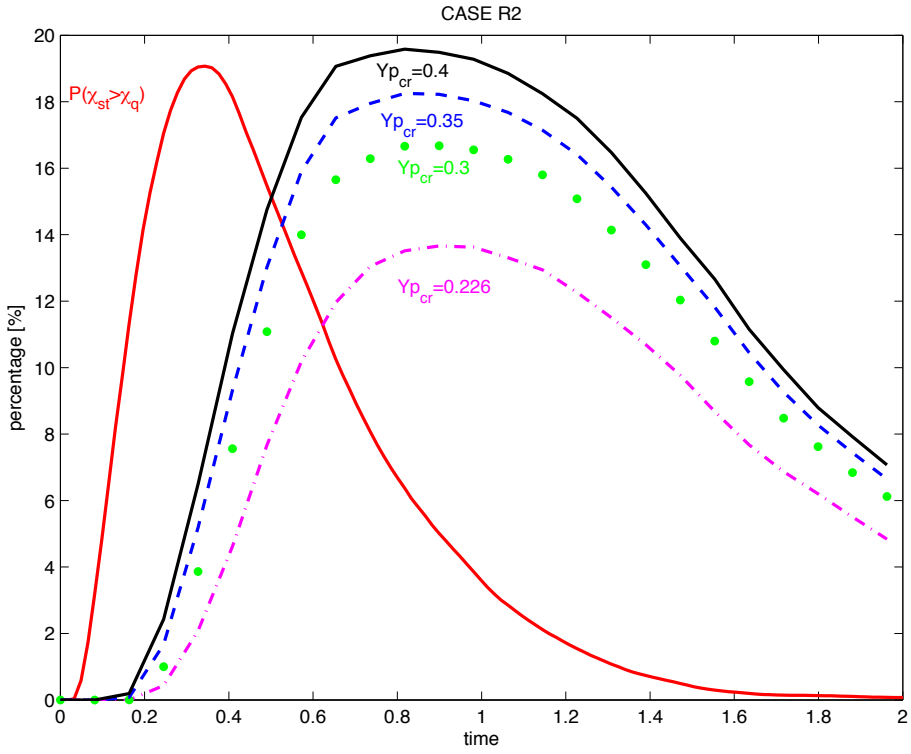

Figure 5.16: Peak time shifted. The time evolution of the percent of flame surface area identified by quenched regions according to four different critical values of extinction: $Y_{Pcr} = 0.226$(dash-dot magenta), 0.3(dotted green), 0.35(dashed blue) and 0.4(solid black), respectively. For comparison, the area fraction of the stoichiometric scalar dissipation rate beyond the critical value of extinction χ_q is plotted as a function of time(solid red).

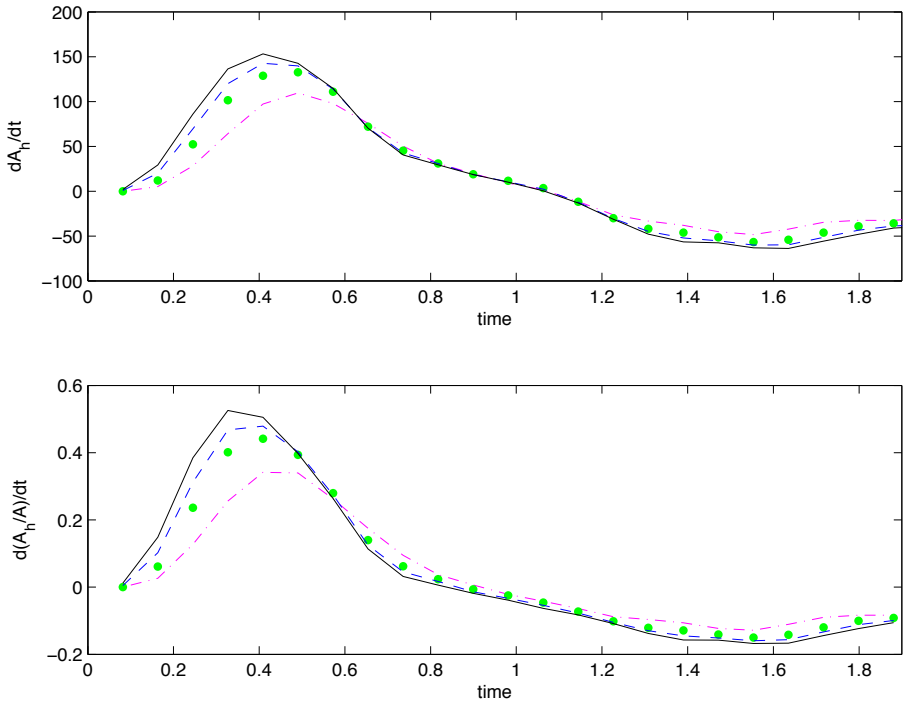

Figure 5.17: The time rate of change of total quenched area (top panel) and the one of area fraction of quenched regions (bottom panel) for four different critical values of extinction: $Y_{Pcr} = 0.226$(dash-dot magenta), 0.3(dotted green), 0.35(dashed blue) and 0.4(solid black), respectively. The time differentiation is approximated by the second-order central difference scheme.

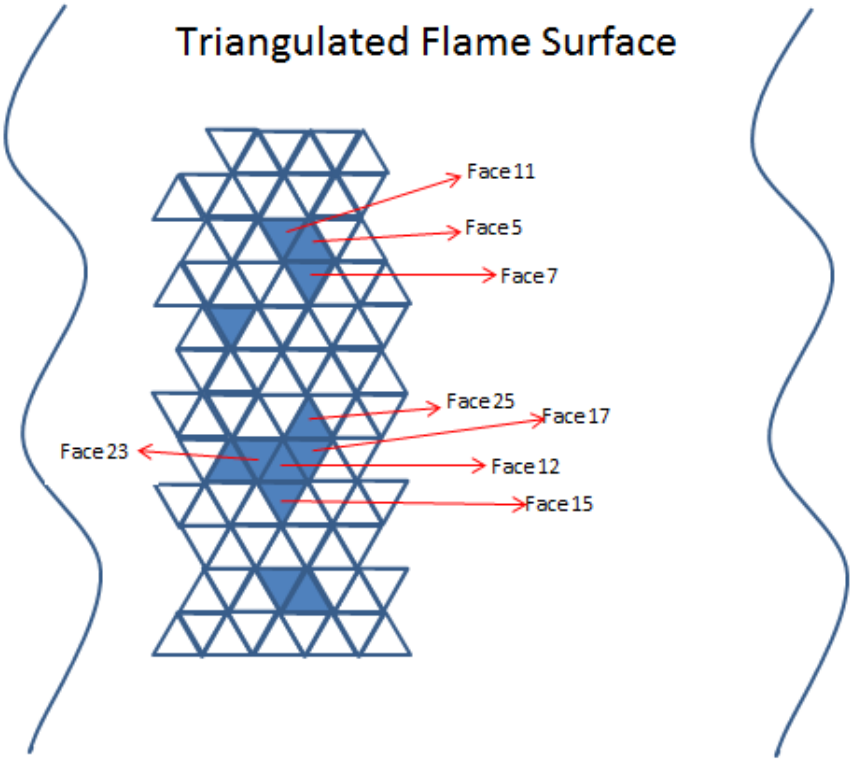

Figure 5.18: The schematic drawing of part of selected triangle faces and their neighborhoods on the flame surface. The selected faces are marked with the original face index. The blue color filled triangle faces are the identified quenched elements. The triangle faces with no fill are the burning elements.

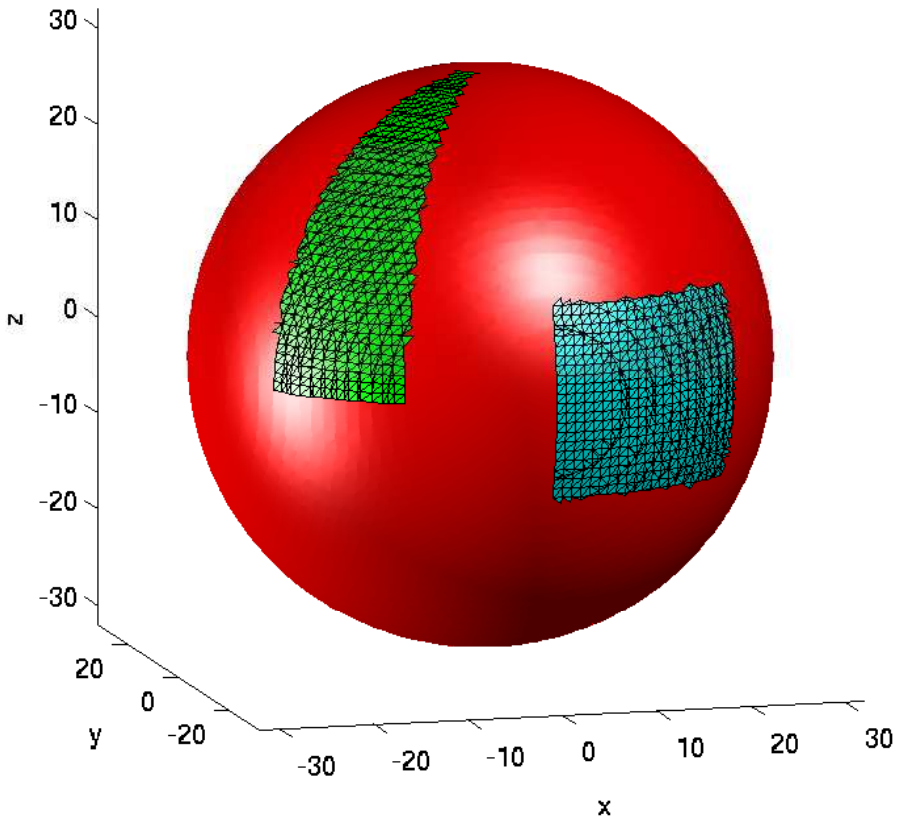

Figure 5.19: A spherical surface patched with a given-shaped hole. The topological pattern of the patched hole is formed and rendered by the in-house numerical algorithm. Each patched hole is marked by a unique color to show the individuality.

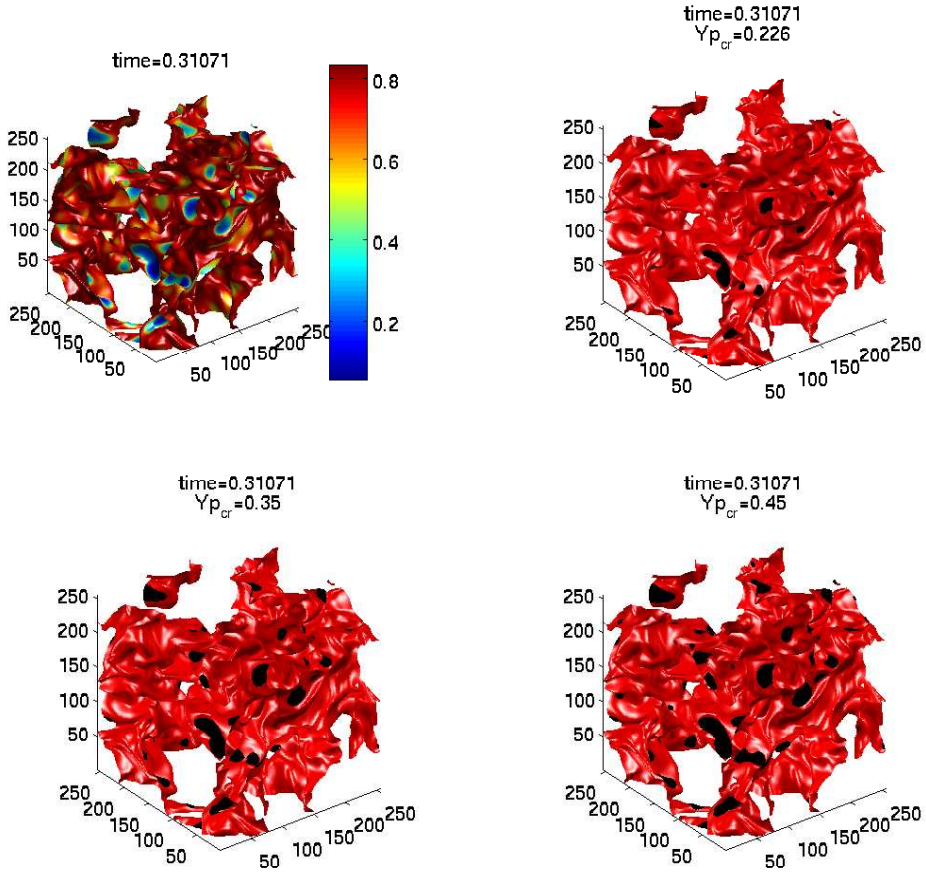

Figure 5.20: For a DNS scalar field of case R2 at simulation time=0.31, the 3D visualization of the flame holes overlaid on the isosurface of stoichiometric mixture fraction is formed and delineated by the in-house numerical algorithm for three different critical values of extinction: $Y_{Pcr} = 0.225$(right upper), 0.35(left bottom) and 0.45(right bottom), respectively. The isosurface of stoichiometric mixture fraction colored by local temperature is also included (left upper), where the color coding indicates the temperature value along the flame surface. In the top left plot, referring to the temperature scale denoted by color bar (attached to the right of the plot), the dark-blue indicates the low temperature region, i.e., flame hole. In the plot from top right to bottom right, the region marked with a constant black color represents the flame hole formed by the in-house numerical algorithm.

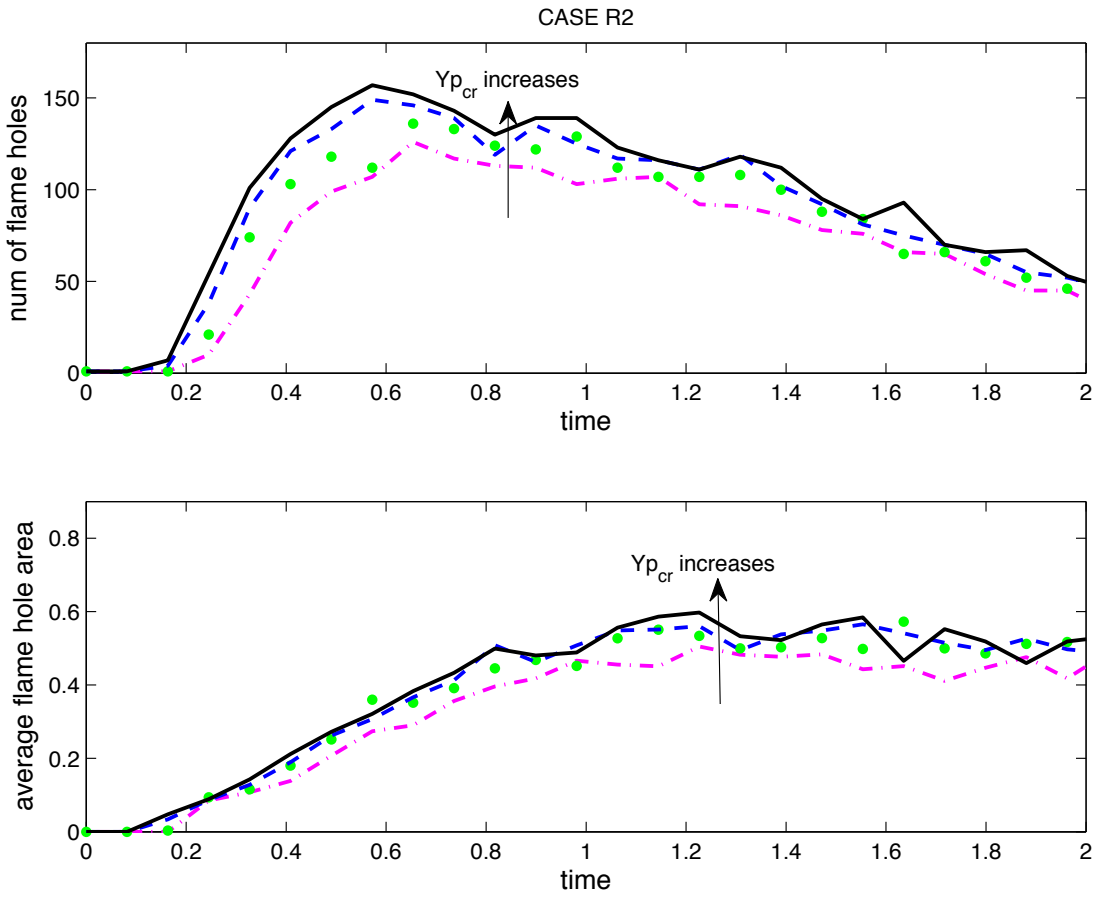

Figure 5.21: Time evolution of the number of flame holes(top panel) and the average area of flame holes(bottom panel).

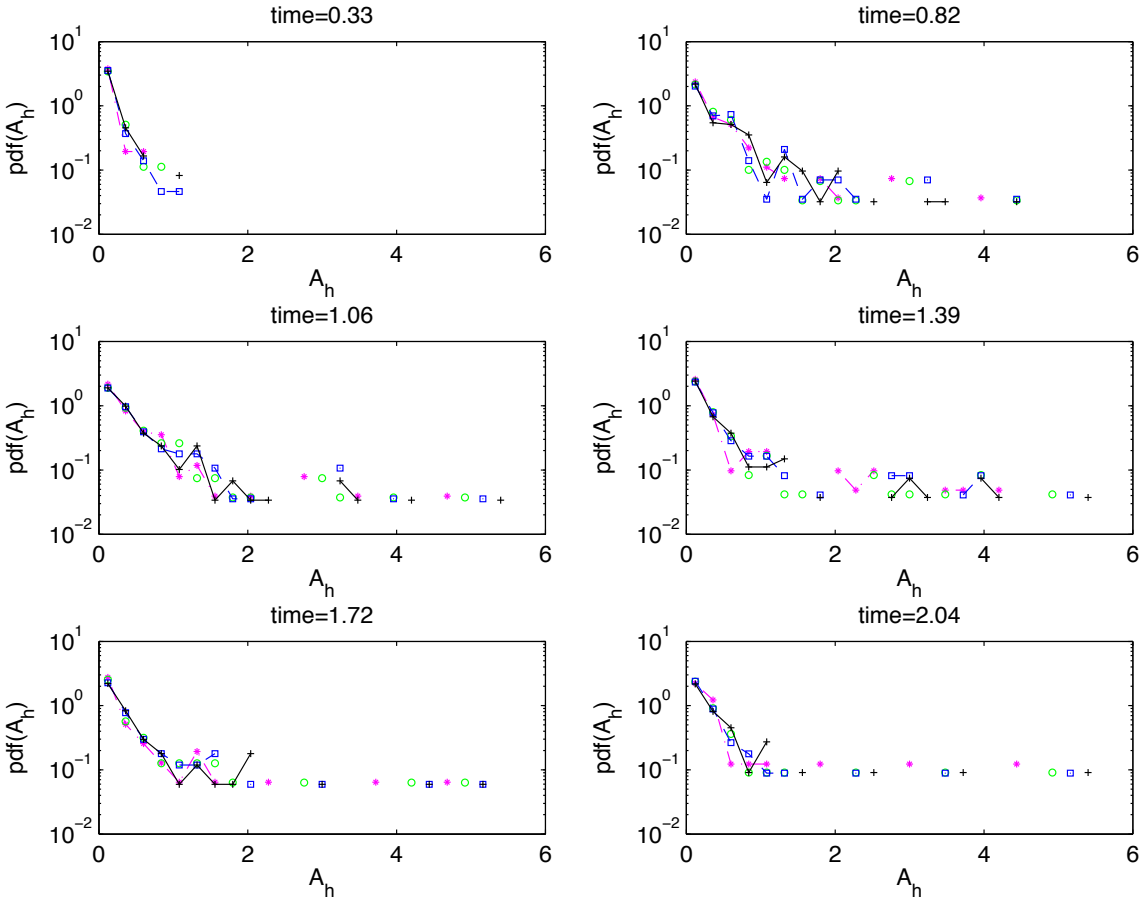

Figure 5.22: The probability mass functions of the hole areas at six selected simulation times $t = 0.33$(i.e., peak time of area fraction of $\chi_{st} > \chi_q$), 0.82(i.e., peak time of area fraction of flame holes), 1.06(i.e., peak time of total area of flame holes), 1.39, 1.72 and 2.04 are shown in panels from left to right and top to bottom, respectively. The flame holes are identified by four different critical values $Y_{Pcr} = 0.226$(dash dot magenta line marked by star), 0.3(green circle), 0.35(dashed blue line marked by square), and 0.4(solid black line marked by plus symbol), respectively.

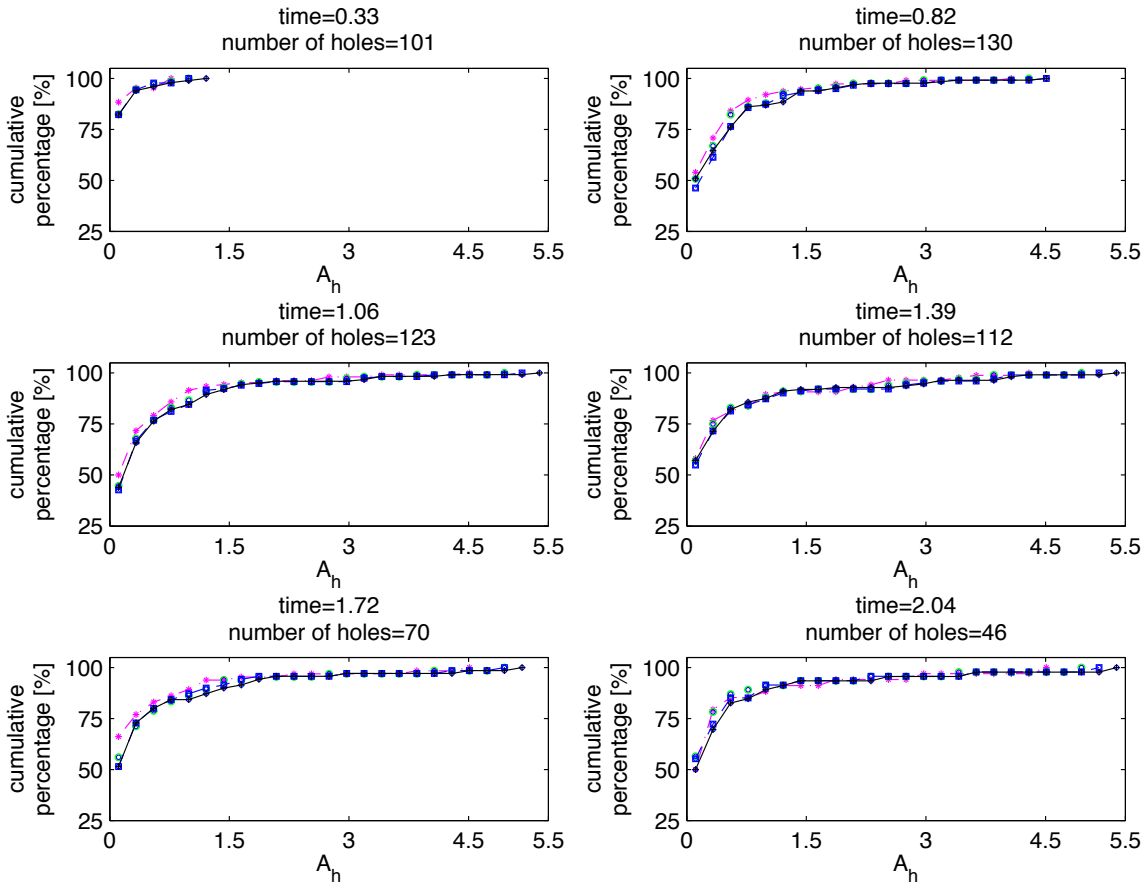

Figure 5.23: The cumulative percentage distributions of hole areas are plotted the same way as Fig.(5.22).

Chapter 6

CONCLUSIONS AND SUGGESTED FUTURE WORK

6.1 Conclusions

6.1.1 Numerical Simulation

In a turbulent diffusion flame, combustion occurs at the the flame surface where the initially separated fuel and oxidizer are in stoichiometric proportion. Thus, the flame surface is identified by the isosurface corresponding to the stoichiometric value of the mixture fraction $Z = Z_{st}$. The current study investigates the evolution and kinematics properties of flame surfaces in nonpremixed turbulent combustion with local extinction and reignition using fully resolved DNS data.

The DNS data are extracted from a series of simulations which are carried out for increasing Reynolds numbers in a cubic computational domain with periodic boundaries. The dimensions of the 3D computational domain are $L \times L \times L$, where L is taken to equal 2π. The entire domain is spatially discretized by $N \times N \times N$ grid points which are uniformly distributed in the x_1-, x_2- and x_3-directions, respectively. The required number of discrete grid points should be sufficiently large to resolve the smallest scale (i.e., the dissipation length scale), so it is proportional to the Reynolds number. For higher Reynolds number cases with the number of grid points $N > 256$, the numerical simulation is implemented on a distributed memory parallel computer. In the current research, the code developed for higher Reynolds number cases is based on a parallel scheme and invokes the Message Passing Interface (MPI) on the Fortran90 interface. The initialization and the DNS for case R4 and R5, and R6 and R7 (Table.(3.1) and (3.2)) are implemented on 32 and 128 processors on the IBM P690+/P655+ machine named ″Iceberg″ at the Arctic Region Supercomputing Center(ARSC), respectively.

The turbulent flow field is simulated to be a fully-developed, incompressible, homogeneous, decaying isotropic turbulence. The mixture fraction field (conserved scalar) is

initialized in blobs of pure fuel (Z=1) and pure oxidizer (Z=0) with a thin mixing layer in between. The average of mixture fraction $\langle Z \rangle$ remains constant at the value of stoichiometric mixture fraction Z_{st}. The temperature field (reactive scalar) is initialized using the burning state of a steady state flamelet model, thus the whole flame surface (i.e., the isosurface of stoichiometric mixture fraction) is initially fully burning. With respect to the flame structure in nonpremixed combustion, the extent of flame surface stretching by turbulence is quantified by the scalar dissipation rate χ_{st}. During early simulation times, the intense turbulence induces flame surface stretching which increases the scalar dissipation rate. Thus, flame stretching is indicated by a large value of χ_{st}. If a fluctuation of χ_{st} is beyond the set critical value the flame is locally quenched, which produces flame holes (or equivalently quenched holes). The critical quenching value of the scalar dissipation rate (χ_q) used to identify the extinction is determined from the steady flamelet model corresponding to the upper-right turning point of the S-shaped curve as shown in Fig.(2.1). As time proceeds, after the onset of local extinction, the scalar dissipation rate drops gradually below χ_q, and reignition occurs through three different scenarios: 1) reignited independently (i.e., IFL); 2) edge flame propagation along the flame surface (i.e., EDGE); 3) neighboring hot burning flames in the direction normal to the flame surface (i.e., ENGULF)[64]. During the entire simulation time, the average stoichiometric scalar dissipation rate $\langle \chi_{st} \rangle$ stays below the critical quenching value χ_q, while the fluctuation of instantaneous χ_{st} can significantly exceed the quenching limit.

6.1.2 Measurement of Flame Surface Area by Numerical, Theoretical and Modeling Approaches

In the present study, the time evolution of the flame surface area is determined in three ways: (1) numerical measurement, (2) theoretical formulation and (3) model predictions involving two different models and the balance equation. These proposed approaches are tested and evaluated with the use of DNS performed in both case R2 can R4.

Direct numerical measurement

The Matlab built-in function *isosurface* is used as an isosurface rendering technique to extract the flame surface from the gridded volumetric DNS data by triangulating it into grid-scale triangular faces. It returns a triangulated surface together with the geometric information in a face-vertex format comprising 1) which three vertices form a triangular face and 2) the 3D coordinates of all vertices along the triangulated isosurface. Consequently, the area of each grid-scale triangular face can be determined by Heron's formula and therefore the entire flame surface area is computed. The accuracy of this numerical algorithm for determining the isosurface area is assessed by comparing the numerical results with the known analytical solutions of a given shape such as spherical or prolate spheroid surfaces. The relative error of less than 3% shows that this numerical algorithm can yield very accurate numerical results which will be regarded as an 'exact solution' for further testing of theoretical formulation and evaluation of proposed models. In addition, the accuracy of this numerical scheme is improved with the decrease of surface curvature. This isosurface rendering scheme is a direct way not only to visualize the 3D flame surface but also to numerically measure the flame surface area with good accuracy.

Theoretical approach

Although the above introduced numerical measurement for flame surface area is interactive and accurate, it can not be employed as a basis for the further model development. As an alternative, the concept of level crossing is suggested as an alternative strategy for both computing and modeling purposes. The level crossing method measures how often a line through the scalar field data crosses the stoichiometric value of mixture fraction. It is intuitive to hypothesize that more frequent crossings correspond to a higher flame surface density. This suggests that the level crossing value can be utilized to quantify the area of the flame surface [60].

In the context of level-crossing, the 3D mixture fraction field $Z(x_1, x_2, x_3)$ is interpreted as a spatial random process that comprises an ensemble of one-dimensional discrete-space functions which evolve in this spatial dimension (e.g., x_1-, x_2- or x_3-direction). The scalar

field is assumed to be spatially isotropic, therefore we arbitrarily choose the axis x_1 to be the spatial argument of a 1D spatial random function denoted by $\{Z(x_1)\}$, $0 \leq x_1 \leq L$, without the explicit dependence on x_2 and x_3 for notational convenience.

The total number of crossings of a given level Z_{st} along a particular direction (say x_1-direction), $\mathbf{N}_{z_{st}}$, can be numerically calculated by comparing the value of Z at every two neighboring grid points sequentially along x_1-axis and repeating this procedure for each of N^2 x_1 axes over the entire computational domain. The resulting total number of crossings are nearly identical regardless of whether to the numerical calculations are performed along the x_1-, x_2- or x_3-axis due to the approximately isotropic property of the mixture fraction field.

The total number of crossings $N_{z_{st}}$ is hypothesized to be linearly related to the flame surface area per unit volume, (i.e., flame surface density defined as $\Sigma = A/(L^3)$), in which the coefficient of this relationship can be mathematically derived by introducing the projected area of flame surface A_P, since this can establish a link between $N_{z_{st}}$ and A. A_P is mathematically equivalent to the total number of crossings $N_{z_{st}}$ through a conversion factor that rescales their units to be interpreted on the same scale. The ratio of the surface area A to its projected area A_P can be determined with the knowledge of the statistical distribution of the local projection angles in an isotropic field. This ratio is equal to 1/2 for isotropically distributed surfaces. The proportionality constant of the linear relationship between $N_{z_{st}}$ and A is verified by a straight line with a slope proportional to the resulting coefficient which is exhibited on the plot of time-evolved flame surface area versus time-evolved total number of crossings. Thus far, the flame surface area A can be numerically predicted in terms of the total number of level crossings $N_{z_{st}}$(or equivalently, in terms of the average number of level crossings $\mathrm{E}\{\mathrm{n}_{z_{st}}(L)\}$).

Considering the 3D mixture fraction field from the perspective of a one-dimensional spatial random process defined over $[0, L = 2\pi]$, the average number of level crossings can be defined due to the theorem of S.O.Rice [62][63]. The excellent agreement when comparing the time evolution of the average number of crossings between the numerical results from DNS and the theoretical prediction from Rice's theorem confirms that the total number of crossings can be analytically predicted and thus one can infer the isosurface area. The

theoretical formulation of a model for flame surface area as given in Eq.(4.26) can thus be built by the established relation between the flame surface area and average number of crossings in conjunction with the Rice's theorem applied for predicting the average number of crossings. This theoretical formulation for A is validated extensively against the DNS results. Thus far, the theoretical expression for flame surface area A developed from the concept of level crossing is established and is necessary to be developed with the aim of providing a mathematical framework for the subsequent modeling of the flame surface area.

Modeling approaches

The theoretical formulation for A given in Eq.(4.26) leads to the following modeling approaches: 1) modeling the statistical terms intervening in the theoretical formulation; 2) develop a balance equation for isosurface area density and numerically compute the source and sink terms in the equation.

As described in Eq.(4.26), the theoretical formulation for A is composed of two terms. Accordingly, the modeling for flame surface area is performed by developing the models for the terms, $P_Z(Z_{st})$ and $\langle|Z^{'}| \mid Z = Z_{st}\rangle$, respectively. The β-distribution (Eq.(4.27)) is widely used to model the PDF of mixture fraction in nonpremixed turbulent combustion[11],[49]. The two input parameters, the mean and the variance of mixture fraction ($\langle Z\rangle$ and $\langle Z''^2\rangle$), required for defining the β-distribution are directly taken from the DNS. The comparison against numerical results shows that the β-distribution predicts almost exact results until a slight overprediction occurs at later time.

Regarding the modeling for term $\langle|Z^{'}| \mid Z = Z_{st}\rangle$ (noted by $\langle|Q|\rangle$ for simplicity), there are two models proposed in current research. The first proposed model starts with a presumed normal distribution with zero mean for conditional random variable $Q = (Z^{'} \mid Z = Z_{st})$ as presented in Eq.(4.29). Due to the isotropy, the selection of the initial conditions for Q and the choice of Z_{st}, the zero-mean assumption is invoked and is validated by the DNS data. The presumed normal distribution, in which the average and variance of Q as the required shape parameters are respectively assumed to be zero and taken directly from DNS data, appears to be a reasonable approximation when comparing against the

probability distribution function evaluated using DNS data. Nevertheless, a minor non-Gaussian tail can be observed that is attributed to the spatial intermittency effect in the turbulent velocity field. The corresponding model underpredicts the term $\langle|Q|\rangle$ during early simulation times with maximum error of 8%, and then the underprediction tends to decrease until the overprediction occurs which gives the error about 6%. As the shape parameter used to construct the normal distribution, the variance of Q, denoted by σ^2, is further modeled. Due to the definition of stoichiometric scalar dissipation rate and the isotropy of mixture fraction field, σ^2 can be estimated in terms of $\langle\chi_{st}\rangle$. This approach for σ^2 is verified against the DNS results. The model developed so far can predict the flame surface area in terms of $\langle Z\rangle$, $\langle Z''^2\rangle$ and $\langle\chi_{st}\rangle$ (Eq.(4.37)). Upon comparison with the 'exact' numerical result it is demonstrated that the model for approximating the surface area can yield a reasonable prediction. The deviations between the model and the DNS results stem mainly from the presumed normal-PDF for Q, since (1) the β-distribution can well reproduce the PDF of mixture fraction; (2) the two input parameters required for constructing the normal distribution of Q, i.e., the first and the second moments of variable Q, are accurate and independent of the PDF shape of Q. The final step in this model for surface area is to propose a model for predicting the $\langle\chi_{st}\rangle$ in terms of $\langle\chi\rangle$ by assuming locally an error-function form for mixture fraction from the flamelet perspective. Accordingly, the model for surface area is formulated in terms of $\langle Z\rangle$, $\langle Z''^2\rangle$ and $\langle\chi\rangle$ which are taken directly from DNS (Eq.(4.40)). As shown in Fig.(4.20), the difference between the model prediction Eq.(4.37) and Eq.(4.40) is negligible in comparison with the discrepancies between the models and DNS results since these two approaches are derived from the same presumed PDF shape for Q. The overprediction of surface area model becomes more pronounced during later simulation time. It can be traced back to (1) the slight overprediction of $P_Z(Z_{st})$ for later time, and (2) the overprediction of $\langle|Q|\rangle$ for later time which is mainly attributed to the presumed normal distribution for Q. As is well known, the occurrence of turbulent intermittency is evidenced by the departure from Gaussian distribution (i.e., display a non-Gaussian tail in probability density distribution).

The same modeling procedure is applied for a higher Reynolds number case R4. The flame surface area is increased by the more intense turbulence (i.e., higher Reynolds number)

with greater stretching, folding and wrinkling. The deviation between the model prediction and the numerical results increases with the increase of Reynolds number since the non-Gaussian tail in the PDF of small-scale gradients (i.e., $(Z^{'} \mid Z = Z_{st})$) caused by intermittency in the turbulent flow field become more conspicuous with increasing Reynolds number.

This motivates us to explore a better choice for the PDF of Q to improve the modeling for $\langle|Q|\rangle$. Before developing an alternative model, due to the isotropic turbulence, a relationship $\langle|\partial Z/\partial x_1| \mid Z = Z_{iso}\rangle = (1/2)\langle|\nabla Z| \mid Z = Z_{iso}\rangle$ is proposed and validated against DNS data. The constant coefficient 1/2 of the relationship is derived for the isotropic case and holds for isosurface specified by any constant value of Z_{iso} and any Reynolds number case. With respect to flame surface, the relationship is applied specifically to $Z_{iso} = Z_{st}$ and yields $\langle|Q|\rangle = (1/2)\langle|\nabla Z| \mid Z = Z_{st}\rangle$ accordingly. As a shorthand notation in subsequent derivation, R and S denote $(|\nabla Z|^2 \mid Z = Z_{st})$ and $(|\nabla Z| \mid Z = Z_{st})$, respectively, therefore this yields $\langle|Q|\rangle = (1/2)\langle|S|\rangle$. Due to the definition of R, it is proportional to the scalar dissipation rate which is commonly assumed to be lognormally distributed from both experimental observations and numerical simulations. Therefore, the modeling for $\langle|Q|\rangle$ will be developed by starting with a presumed lognormal distribution of R. In this regard, the R is assumed to be a lognormal distribution, and then $\langle S\rangle$ can be determined in terms of the statistical moments of R through applying the change-of-variable rule based on function $R = g^{-1}(S) = S^2$, which will ultimately be $\langle|Q|\rangle$. The model for approximating $\langle|Q|\rangle$ in terms of $\langle R\rangle$ and $\langle R^2\rangle$ is thus advanced. The performance of the model prediction Eq.(4.53) is compared with the previous model predictions Eq.(4.36) and Eq.(4.39) with respect to the results taken directly from DNS. The model for $\langle|Q|\rangle$ starting with a presumed lognormal distribution of R obtains an improvement over the one starting with a presumed normal distribution of Q, and this improvement is prominent in higher Reynolds number case. Consequently, the resulting alternative model for predicting the flame surface area A as given in Eq.(4.54) also shows significant advantages over the previous model.

It is noteworthy that the performance of the numerical, theoretical and model predictions are irrespective of direction because of the isotropy since the quantity involving direction has the same values regardless of the direction of measurement by using DNS data.

An additional modeling approach is the development of a balance equation for the time evolution of the isosurface area per unit volume (i.e., mean isosurface area density), where the surface corresponds to a mixture fraction isolevel with any constant value of Z_{iso}.

The theoretical formula Eq.(4.26) for the total flame surface area can be applied not only to flame surface but to an isosurface specified by any constant value of Z_{iso}, which yields the theoretical formula Eq.(4.56) for mean isosurface area per unit volume Σ_{iso}. For the purpose of deriving an exact balance equation for Σ_{iso}, the theoretical formula for mean isosurface area density is recast in terms of $\langle |\nabla Z| \mid Z_{iso} \rangle$ as given in Eq.(4.57) by applying the relationship between $\langle |\partial Z/\partial x_1| \mid Z_{iso} \rangle$ and $\langle |\nabla Z| \mid Z_{iso} \rangle$. The derivation starts with the definition Eq.(4.57) and uses the governing equation for mixture fraction followed by averaging along the isosurface [14]. The isosurface area behaves as a non-conserved property and therefore its balance equation contains terms describing sources (due to the surface stretching by intense turbulence) and sinks (due to molecular diffusion and curvature effect) of flame surface, i.e., which average by the terms $\langle -n_i n_j \partial u_i/\partial x_j \rangle_s$ and $\langle w \partial n_i/\partial x_i \rangle_s$, respectively. Here, the operator $\langle \rangle_s$ represents an area-weighted average along the isosurface with the use of geometric information generated from the isosurface extraction scheme.

Using DNS data from both case R2 and R4, the time evolution of these two terms are computed for seven different isosurfaces corresponding to isovalues $Z_{iso} = 0.01$, 0.05, 0.1, 0.2, 0.3, 0.4, and 0.5, respectively. For the source term denoted by strain rate a_T, it is larger in higher Reynolds number case due to the stronger turbulent stretching. In both cases, the maximum strain rate occurs at the stoichiometric isosurface, but the average strain rate is roughly invariant at different isolevel surfaces within mixing layer ($Z_{iso} = 0.2 \sim 0.5$), so the inverse of Kolmogorov timescale model $\gamma\sqrt{\varepsilon/\nu}$ with a universal constant $\gamma = 0.27(0.25)$ can approximately predict a_T corresponding to various isosurfaces in case R2(R4). The sink term corresponds to a curvature and molecular diffusion induced isosurface displacement. In the current study, this term stays negative over entire simulation time such that the flamelet propagation tends to smooth out the surface. It is therefore considered as a sink term that diminishes the surface area. The sink term exhibits consistent behavior across the entire mixing layer ($Z_{iso} = 0.2 \sim 0.5$) and remains invariant over time except for the initial drop. By splitting the diffusion velocity w into two components, curvature and normal

molecular diffusion, the sink term can be recast and approximated by $-D_f\langle(\nabla\cdot\vec{n})^2\rangle_s$ where D_f is diffusion coefficient. The numerical data shows that the behavior of the variance of curvature appears to be invariant with time. It implies that the mean curvature square, $\langle(\nabla\cdot\vec{n})^2\rangle_s$, can be approximated by a constant with a value of approximately 92(800) for case R2(R4). Therefore, the sink term for case R2(R4) can be predicted by a constant with a value of approximately $-92D_f(-800D_f)$.

The imbalance between the surface generation term and surface consumption term yields a surface area growth followed by a decrease. Nonetheless both the source and sink term appear to be roughly invariant across different isolevel surfaces within the mixing layer, the deviation between the curves of sink terms has relatively larger magnitude than the one of source term. It implies that deviations between the curves of sink term is the major reason to be responsible for the different behavior of the time evolutions of mean area density of isosurfaces with different isolevel values.

6.1.3 Application of Steady Flamelet Model

In first part of the current research, the evolution and properties of flame surface are investigated via numerical, theoretical and modeling approaches. In the following, the mechanisms and properties of local extinction and reignition occurring on the flame surface is investigated by comparing the steady flamelet model against DNS results, visually displaying and comparing the flamelet model prediction with DNS data along the isocontour of stoichiometric mixture fraction and studying the kinematic and topological properties of flame holes.

The steady flamelet model(SFL) is applied to the current diffusion flame. In the flamelet model, the local flame state can be characterized as a function of two parameters: (1) the rate of strain at the fuel-oxidizer interface χ_{st}, and (2) the stoichiometry as one moves across the interface Z. The SFL solutions is precomputed and tabulated in a look-up library in which the temperature and the species concentration are functions of (χ_{st}, Z). As a non-equilibrium parameter which measures the degree of departure from equilibrium state, a series of χ_{st} ranging from 0 to quenching limit χ_q corresponds to the solutions (i.e., steady

state flamelet profiles) from chemical equilibrium to extinction. As introduced previously, the DNS is performed to resolve a conserved scalar Z field, and therefore χ_{st} can be available at each point of the field. The SFL library is then used to determine the instantaneous temperature and chemical species mass fractions at each location of the field by interpolation. The advantage of the flamelet model is that it decouples the computation of the chemical process from the computation of the turbulent flow field. The SFL model predicts a critical stoichiometric scalar dissipation rate χ_q above which the flame is considered to be quenched.

The applicability of the steady laminar flamelet model (SFL) to diffusion flames with local extinction and reignition is evaluated in terms of total reaction rate within the computational domain by comparing the SFL with the DNS results. During entire simulation time, the SFL model underpredicts the reaction rate, while the reasons for discrepancies appearing at early and late simulation time are different.

During early simulation time when extinction dominates, the proportion of the fluctuations of χ_{st} beyond χ_q increases due to the larger scalar gradients caused by turbulent strain. Thus, the reason for underprediction is revealed by dividing the total DNS reaction rate between grid points where $\chi_{st} \leq \chi_q$ and $\chi_{st} > \chi_q$. The comparison shows that (1) the SFL model can accurately predict the reaction rate for grid points in subset $\chi_{st} \leq \chi_q$, and (2) the SFL model assigns zero reaction rates for grid points in subset $\chi_{st} > \chi_q$, but of which the subtotal DNS reaction rate is nonzero. For the points with quenching $\chi_{st} > \chi_q$, the SFL model is capable of capturing the extinction, but it overestimates the amount of extinction as it does not take transient processes into account. During late simulation time, the proportion of the fluctuations of χ_{st} beyond χ_q gradually drops to zero as molecular mixing proceeds. The gradual occurrence of reignition is favored when χ_{st} is under the quenching limit. The local quenched region can be reignited by the propagation of edge flames along the flame surface. The deviation between the DNS and the SFL model can be tentatively attributed to the existence of the intense reaction rate associated with the edge flame head. This behavior is further illustrated by comparing the relative quantities along the contour lines of the stoichiometric mixture fraction.

In summary, the comparisons demonstrate that the SFL model can reproduce the simu-

lated data accurately when extinction and reignition are not present. The model, in which the local reactive scalars are uniquely determined by χ_{st} and Z, can only provide two possible states: (1) an extinguished flamelet in which the fuel and oxidizer mix without reaction if the strain rate is above a critical limit $\chi_{st} > \chi_q$; (2) a steady-state burning flamelet if the strain rate is below the critical limit $\chi_{st} \leq \chi_q$. These limit the application of the SFL model which are illustrated in the following two situations:

(1) When strain rate fluctuates beyond the critical value, the true chemistry cannot respond to the rapid change of χ_{st} instantaneously such that the flamelet is still burning with a quenching χ_{st}. This transient effects cannot be taken into account in SFL modeling.

(2) When strain rate drops below the critical value, the quenched region will not spontaneously reignite; reignition occurs only via an outside source, i.e., the propagation of a neighboring burning flame along (EDGE) or across (ENGULF) the flame surface. The edge flame reignites the quenched region with intense reaction rate which is higher than the model prediction.

The onset of extinction in the form of flame hole (i.e., quenched hole) and the subsequent reignition by edge flame propagation are visually displayed by comparing the SFL model predictions with DNS results along the contour line of stoichiometric mixture fraction. The coordinates (x_1,x_2) pairs of the points representing Z_{st} isolevel contour lines on a selected $x_1 - x_2$ plane are returned by Matlab intrinsic function *contour*. The scalar quantities of the points along the contour line can thus be determined by interpolation.

At early time $t = 0.26$, for the points with χ_{st} below the quenching limit, the the SFL model gives very good agreement with the actual DNS results. In addition, both the true and the modeled reaction rates trend up χ_{st} closely. It evidences the above argument that SFL model is a good predictor for $\chi_{st} < \chi_q$. Along another segment of a contour line, it shows that the onset of extinction does not necessarily pairing the occurrence of χ_{st} beyond χ_q especially for a relatively smaller excursion of χ_{st} above χ_q. In this situation, the true reaction rate is of the same magnitude as the one of SFL burning state at quenching value $\chi_{st} = \chi_q$. But the flamelet is extinguished for sufficiently large fluctuation of χ_{st}.

At a later time $t = 1.46$, χ_{st} is relaxed below the quenching limit that favors the reig-

nition. The edge flame, as one scenario of reignition mechanism, is visually demonstrated along the contour line. The flame hole is characterized by the close-to-zero DNS reaction rate and is indicated by a relatively large value of premixing factor $f = Y_F \times Y_O$. If χ_{st} within the flame hole is below the quenching limit, the edge flame front with intense reaction rate locating at the hole edge will propagates inwards along the Z_{st}-contour line to reignite and diminish the flame hole. The flame state approaching to a complete reignition by edge flame propagation is manifested by a bimodal shape with a trough at the site where f attains its maximum. The intense reaction rate associated with edge flame (the reaction rate spikes surrounding the edge of quenched hole) is the reason for the underprediction of the SFL model during late time.

6.1.4 Kinematic Study of Flame Hole Dynamics

The previous analysis presents difficulties for the SFL model because of 1) the late response of flame extinction to the fluctuations of scalar dissipation rate, and 2) the lag if the reignition behind the relaxation of the scalar dissipation rate. First, one does not know a priori what fraction of flame surfaces are non-burning. Second, one does not know the rate at which the non-burning regions are being reignited. As is well known, local extinction induced by the fluctuation of χ_{st} appears in the form of a flame hole and the reignition favored by the relaxation of χ_{st} is manifested by the collapse of flame hole. In this sense, the investigation of the temporal evolution and geometrical properties of flame holes provides instructive information for elucidating the structure and understanding the mechanisms of extinction and reignition.

The previous described isosurface rendering technique (i.e., isosurface triangulation) has its root in the following numerical investigations where the flame holes form and evolve on the flame surface. The flame surface is extracted from volumetric data by triangulating it into connecting grid-scale triangular faces, each of which approximates its corresponding surface area. The reactive scalars associated with each triangular face, Q_{ii} (Q as a quantity of interest could be temperature or reaction rate), represent the local flamelet burning state on the flame surface.

First, the appropriate criteria for identification of each individual non-burning triangular face along the triangulated flame surface need to be set up. The χ_{st} is a key parameter related to the occurrence of local extinction and reignition, but not an instant indicator for being a criterion. The Arrhenius type temperature dependence of reaction rate (Fig.(5.11)) has a unique reaction rate for each temperature value in the left side of the S-curve. Therefore, a temperature lower than 0.6 is an appropriate indicator to identify a unique flame state. Subsequently, the critical value of temperature Y_{Pcr} is determined by two requirements: (1) Y_{Pcr} should be low enough to represent a frozen reaction state; (2) the specific value selected for Y_{Pcr} results in a statistically insensitive result. The selected value of Y_{Pcr} of 0.35 is adequate to reduce the sensitivity of the statistics without violating the definition of frozen reaction. A set of four different critical values around 0.35, $Y_{Pcr} = 0.226, 0.3, 0.35, 0.4$ are also applied to illustrate the insensitivity of the results to the choice of critical value of 0.35.

The percentages of the flame surface area identified by quenched regions due to a set of four critical values A_h/A are compared with the area fraction of the stoichiometric scalar dissipation rate beyond the quenching limit $Percentage(\chi_{st} > \chi_q)$. The area fraction of the quenched regions monotonically increases with the increase of critical value. Nevertheless they follow the same trend. The time at which the maximum fraction of surface is defined as being quenched is almost invariant with respect to the critical value, but it lags behind the peak in $Percentage(\chi_{st} > \chi_q)$. This rightward shift in the time for maximum flame hole fraction is due to a delay in flame quenching response to the fluctuations of χ_{st} beyond χ_q and the gradual occurrence of flame reignition resulting from the decrease of χ_{st} below χ_q.

Regarding the time rate of change of total quenched area and one of quenched area fraction measured under four critical values, the hole shrink by reignition is at a lower rate than the hole growth by extinction. Referring to the behavior of the time evolution of χ_{st}, it demonstrates that the rate of change of hole size depends on the mixing rate. In addition, the growth rate of hole size increases with the increase of critical value as the larger critical value expands the range of the quenched regions. But the deviations between the rate of hole collapse are roughly invariant across different critical values.

χ_{st} is a random variable in a turbulent diffusion flame, and thus the individually identified quenched triangular faces are randomly distributed along the flame surface. They are, however, actually distributed in topologically distinct groups of connected triangles. All these groups appearing as multi-patches overlaid on the flame surface are so the called "flame holes". An in-house numerical algorithm is developed for joining the neighboring quenched triangular faces to form unevenly distributed isolated flame holes. The principle for joining two quenched triangular faces is that they share a common edge. The accuracy and adequacy of this methodology are evaluated by (1) spherical surface overlaid with user-defined patches, and (2) comparing the flame hole patterns formed by numerical algorithm against the ones visualized by the 3D temperature distribution superimposed on the flame surface. These two tests verify that the numerical algorithm for flame hole formation is accurate.

With the development of numerical algorithm for forming each flame hole individually (i.e., specify which triangle faces belong to each flame hole), together with the available knowledge of the mixing and reactive scalars associated with each triangle face, it becomes possible for researchers to perform investigations with respect to the geometric scales, properties, and growth/shrinkage dynamics of the flame holes.

Both the total number and average area of flame holes increase with the increase of critical value of Y_{Pcr}. The increase of critical value identifies more local regions as quenched ones and expands the range of an identified quenched region that leads to the increase of hole number and the average hole area, respectively. Except for the smallest critical value of 0.226, the deviations between the evolutions of average hole areas are unnoticeable. It implies that the critical value of 0.35 is adequate since the statistics of hole scales are not sensitive to the minor change in critical value.

As time proceeds, the number of holes increases by extinction followed by a decrease due to reignition. The average hole area has an initial increase reflecting the hole expansion, but then levels off when reignition predominates. This implies that the number and the total area of the flame holes decay at roughly the same rate during the reignition process. Correspondingly, as shown in the probability mass function of the flame hole area, the probability at early time $t = 0.33$ spans a narrower range than the one at later time.

This potentially explains the increase in average hole area during early simulation time. After a simulation time of $t = 0.82$, while the number of flame holes decreases due to hole collapse, the probability spans a similar range and has similar distribution behavior which can explain the time-invariant average hole area since the onset of reignition. It can also be observed that the most frequent hole scales fall within the first bin and the probability exhibits a roughly decreasing trend at any simulation time. This corresponds to the shape of the cumulative percentage distribution of hole area in which the peak of distribution (i.e., around 90% of the hole areas) lies left to the hole area of 1.5 at any simulation time. For flame holes identified by four different critical values, the scaling distribution behavior is roughly invariant with respect to the critical value. This can explain the unnoticeable deviations between the time evolutions of average hole area and verify the appropriateness of the critical value of 0.35.

As is well known, the χ_{st} plays a key role in the extinction and reignition and has a significant effect on the propagation speed of the edge flame. The χ_{st} distribution pattern within any flame hole of interest is displayed in 3D by coloring the surface of flame hole with each contained triangle face's scalar dissipation rate $\chi_{st_{ii}}$ using indexed color. During early simulation time when extinction prevails, the color coded χ_{st} distribution pattern within a flame hole shows that the scalar dissipation rate decreases monotonically with increasing radius. It corresponds to the peak-like χ_{st} paired with occurrence of bowl-like temperature along the contour line of Z_{st}. At later time when reignition predominates, the majority of scalar dissipation rates drop dramatically below the χ_q with only a few slightly above the quenching limit. A relatively small hole contains a relaxed scalar dissipation rate. The scalar dissipation occurring around or slightly above the quenching limit can be found within the relatively larger hole. When the quenched χ_{st} locates at the edge of the hole, it will prohibit the propagation of surrounding edge flame or even results in a negative edge flame which advects away from the quenched hole, or equivalently, it will decrease the rate of hole collapse.

6.2 Suggested Future Work

In current study, for a 3D turbulent diffusion flame, the direct numerical measurement of flame surface area and the formation of flame holes are based on the isosurface extraction from the volumetric data. The isosurface extraction by the triangulation scheme can provide direct, rich and accurate geometric information which can easily be adopted for further investigation with any specific needs at any situations. It is thus of underlying significance for turbulent diffusion flame studies. The Matlab *isosurface* scheme for interactive isosurface extraction has high quality. The difficulties of this scheme reside in its large rendering time and the high demand for computer capacity. The current isosurface extraction technique is implemented on a sequential machine that the resolution of 512^3 is the maximum affordably performed size. With today's fast development of high performance computing techniques, the DNS carried out with grid points 1024^3 or much higher resolutions are available and can be adopted to justify the proposed isosurface area models for higher Reynolds number turbulence. This motivates the development of a parallel algorithm for isosurface extraction which can be implemented on distributed-memory computers. The parallel technique can cope with large scale data and improve the efficiency and practicality of the isourface area models.

The current theoretical approach for accurately predicting the isosurface area in 3D turbulent diffusion flames is proposed from the concept of level crossing. The concept of level crossing adopted in approximating the flame surface area is universal, requiring only some modifications due to the statistical properties of turbulence. In the current study, the theoretical formula is developed and evaluated in an incompressible and isotropic turbulent field. But it can be generalized to compressible and anisotropic case with adequate modifications. For example, the coefficient 2 which is involved in the current relationship between the number of crossings and the total isosurface area would need to be modified due to the anisotropy. The modification of this coefficient can be addressed by using appropriate probability distribution associated with the anisotropic turbulence. Accordingly, the constant coefficient 1/2 in the relationship $\langle|\partial Z/\partial x_1| \mid Z = Z_{iso}\rangle = (1/2)\langle|\nabla Z| \mid Z = Z_{iso}\rangle$ needs to be addressed to be adaptive in anisotropic case. As the theoretical formulation of A leads

to different modeling approaches, the generality of the theoretical prediction of A enables the modeling for isosurface area in compressible and anisotropic turbulent flow.

As a new methodology, the in-house developed numerical algorithm for flame hole formation on the triangulated stoichiometric mixture fraction isosurface yields contributions to the study of the dynamics of flame holes, and hence the understanding of mechanisms of local extinction and reignition. This numerical flame hole formation algorithm is advantageous to experimental schemes as it 1) has high numerical accuracy, 2) is practically unrestrained, 3) can provide more detailed topological information of each individual flame hole and 4) can be directly applied to isosurfaces with different configurations. However, the crucial point in this numerical algorithm is the efficiency, which limits the practicality for large scale data size. A more efficient algorithm needs to be developed to decrease the computation consumption and the operation time. An attempt can be made to employ the script *graphconncomp* provided by Matlab Graph Theory Toolbox in conjunction with the adjacency matrix listing the neighboring two triangle faces. The function *graphconncomp* can return the number of groups of connected triangle faces and the faces contained in each group. It is required to construct an adjacency matrix suited to be invoked by *graphconncomp* with the use of geometric information returned by isosurface extraction. An alternative to improve this numerical algorithm is to modify it to be a parallel algorithm. This modification should be easily accomplished by using message passing interface (MPI).

This numerical flame hole formation algorithm has potential to track the flame holes in three-dimensional turbulent diffusion flames. In conjunction with the flame element tracking approach[64], both the instantaneous topological properties of a flame hole and the entire spatial-temporal trajectory of the flame hole can be obtained numerically. This scheme allows the study of the evolution and dynamics of each individual flame hole. The temporal trajectory of the flame hole reignition process were tracked experimentally[3]. Therefore, the numerical hole formation algorithm combined with the flame element tracking scheme will emerge as a new, accurate and efficient numerical algorithm for tracking the flame hole and capturing the topological properties of instantaneous flame hole.

BIBLIOGRAPHY

[1] http://www.mathworks.com/help/matlab/math/triangulation-representations.html.

[2] A.Linan. The asymptotic structure of counterflow diffusion flames for large activation energies. *Acta Astronautica*, 1(7-8):1007–1039, 1974.

[3] C.M. Arndt J.H. Frank A.M. Steinberg, I. Boxx and W. Meier. Experimental study of flame-hole reignition mechanisms in a turbulent non-premixed jet flame using sustained multi-khz piv and crossed-plane oh plif. *Proc. Combust. Inst.*, 33:1663–1672, 2011.

[4] A.R.Kerstein. Linear-eddy modelling of turbulent transport. part 6. microstructure of diffusive scalar mixing fields. *J.Fluid Mech.*, 231:361–394, 1991.

[5] A.Trouve and T.J.Poinsot. The evolution equation for the flame surface density in turbulent premixed combustion. *J.Fluid Mech.*, 278:1–31, 1994.

[6] J.J.Riley A.W.Cook and G.Kosaly. A laminar flamelet approach to subgrid-scale chemistry in turbulent flows. *Combust.Flame*, 109:332–341, 1997.

[7] A.Y.Klimenko and R.W.Bilger. Conditional moment closure for turbulent combustion. *Prog. Energy Combust. Sci.*, 25:595–687, 1999.

[8] A.Y.Kuo and S.Corrsin. Experiments on internal intermittency and fine-structure distribution functions in fully turbulent fluid. *J.Fluid Mech.*, 50:285–319, 1971.

[9] Y.Gagne B.Castaing and E.J.Hopfinger. Velocity probability density functions of high reynolds number turbulence. *Phys.D*, 46:177–200, 1990.

[10] Alfio Quarteroni Claudio Canuto, M.Yousuff Hussaini and Thomas A. Zang. *Spectral Methods in Fluid Dynamics*. Springer-Verlag, NY, 1988.

[11] Soichiro Kato Dirk Riechelmann and Toshiro Fujimori. Effect of presumed pdf selection on the numerical result for turbulent diffusion flames. *JSME Int.J.B-Fluid T.*, 45(1), 2002.

[12] Dan Ebberts. http://www.motionscript.com/mastering-expressions/random-sphere.html.

[13] A.M.K.P.Taylor E.Mastorakos and J.H.Whitelaw. Extinction and temperature characteristics of turbulent counterflow diffusion flames with partial premixing. *Combust.Flame*, 91:40–54, 1992.

[14] D.Veynante E.Van Kalmthout and S.Candel. Direct numerical simulation analysis of flame surface density equation in non-premixed turbulent combustion. *26th Symp. (Int.) on Combustion, The Combustion Institute*, pages 35–42, 1996.

[15] R.S.Miller F.A.Jaberi and C.K.Madnia. Non-gaussian scalar statistics in homogeneous turbulence. *J.Fluid Mech.*, 313:241–282, 1996.

[16] F.A.Williams. *Turbulent Mixing in Non-reactive and Reactive Flows (S.N.B.Murthy,Ed.)*. Plenum Press, 1975.

[17] F.A.Williams. *Combustion Theory (2nd ed.)*. The Benjamin/Cummings Publishing Company, Inc., Menlo Park, CA, USA, 1985.

[18] F.E.Fendell. Ignition and extinction on combustion of initially unmixed reactants. *J.Fluid Mech.*, 21:281–303, 1965.

[19] F.E.Fendell. Flame structure in initially unmixed reactants under one step kinetics. *Chem.Eng.Sci.*, 22:1829–1837, 1967.

[20] F.E.Marble and J.E.Broadwell. The coherent flame model for turbulent chemical reactions. *Project squid headquarters, Chaffee Hall, Purdue Univ. Tech. Rep. TRW.*, 1977.

[21] D.Veynante F.Fichot, B.Delhaye and S.M.Candel. Strain rate modelling for a flame surface density equation with application to non-premixed turbulent combustion. *25th Symp. (Int.) on Combustion, The Combustion Institute*, pages 1273–1281, 1994.

[22] L. J. Hartley. *The structure of laminar trip-flames: implication for turbulent non-premixed combustion*. PhD thesis, University of Manchester Institute of Science and Technology, 1991.

[23] Carl H.Gibson. Fine structure of scalar fields mixed by turbulence. i. zero-gradient points and minimal gradient surfaces. *Phys.Fluids*, 11(11):2305–2315, 1968.

[24] M.Chen H.Pitsch and N.Peters. Unsteady flamelet modeling of turbulent hydrogen-air diffusion flames. *Twenty-Seventh Symposium (International) on Combustion, The Combustion Institute*, pages 1057–1064, 1998.

[25] I.Glassman. *Combustion*. Academic Press, 3rd edition, 1996.

[26] J.Buckmaster. Edge-flames and their stability. *Combust. Sci. Tech.*, 115:41–68, 1996.

[27] J.Buckmaster. Edge-flames. *Journal of Engineering Mathematics*, 31:269–284, 1997.

[28] J.Buckmaster. Edge-flames. *Prog.Energy Combust.Sci.*, 28:435–475, 2002.

[29] J.Buckmaster and T. Jackson. Holes in flames, flame isolas, and flame edges. *Proc. Combust. Inst.*, 28:1957–1964, 2000.

[30] J.C.Hewson and A.R.Kerstein. Local extinction and reignition in nonpremixed turbulent co/h2/n2 jet flames. *Combust. Sci. and Tech.*, 174(5):35–66, 2002.

[31] C.E.Frouzakis J.C.Lee and K.Boulouchos. Numerical study of opposed-jet h_2/air diffusion flame - vortex interactions. *Combust.Sci.Technol.*, 158:365–388, 2000.

[32] K. Y. Ahn J.Kim, S. H. Chung and J. S. Kim. Simulation of a diffusion flame in turbulent mixing layer by the flame hole dynamics model with level-set mouthed. *Combustion Theory and Modelling*, 10:219–240, 2006.

[33] E.Van Kalmthout and D.Veynante. Direct numerical simulation analysis of flame surface density models for nonpremixed turbulent combustion. *Phys.Fluids*, 10(9):2347–2368, 1998.

[34] K.N.C.Bray. Studies of the turbulent burning velocity. *Proc. R. Soc. London, Ser. A*, 431:315–335, 1990.

[35] K.N.C.Bray, in P.A.Libby N.Peters, Laminar flamelets in turbulent flames, and editors F.A.Williams. *Turbulent Reacting Flows*. Academic Press,London, 1994.

[36] S.M.de Bruyn Kops. *Numerical Simulation of Non-premixed Turbulent Combustion*. PhD thesis, University of Washington, 1999.

[37] S.M.de Bruyn Kops and J.J.Riley. Direct numerical simulation of laboratory experiments in isotropic turbulence. *Phys.Fluids*, 10(9):2125–2127, 1998.

[38] William E. Lorensen and Harvey E. Cline. Marching cubes: A high-resolution 3d surface construction algorithm. *Computer Graphics*, 21(3):163–169, 1987.

[39] Zhanbin Lu and Sandip Ghosal. Flame holes and flame disks on the surface of a diffusion flame. *J.Fluid Mech.*, 513:287–307, 2004.

[40] K.N.C.Bray L.Vervisch, E.Bidaux and W. Kollmann. Surface density function in premixed turbulent combustion modeling, similarities between probability density function and flame surface approaches. *Phys.Fluids*, 7(10):2496–2503, 1995.

[41] The MathWorks. Source code for the matlab isosurface function, 2007.

[42] N.Peters. Local quenching due to flame stretch in non-premixed turbulent combustion. *Combust. Sci. and Tech.*, 30:1–17, 1983.

[43] N.Peters. Laminar diffusion flamelet models in non-premixed turbulent combustion. *Prog.Energy Combust.Sci.*, 10:319–339, 1984.

[44] N.Peters. Length scales in laminar and turbulent flames,in e.s.oran and j.a.boris,editors. *Numerical Approaches to Combustion Modeling, Prog.Astronautics and Aeronautics, AIAA, Washington DC*, 135:155–182, 1991.

[45] Rodney O.Fox. *Computational Models for Turbulent Reacting Flows*. Cambridge University Press, 2003.

[46] C. Pantano and D. I. Pullin. On the dynamics of the collapse of a diffusion-flame hole. *J.Fluid Mech.*, 480:311–332, 2003.

[47] C. Pantano and D. I. Pullin. A statistical description of turbulent diffusion flame holes. *Combust.Flame*, 137:295–305, 2004.

[48] Athanasios Papoulis. *Probability, random variables, and stochastic processes*. WCB/McGraw-Hill, 3rd edition, 1980.

[49] N. Peters. *Turbulent Combustion*. Cambridge University Press,Cambridge,UK, 2000.

[50] H. Phillips. Flame in a buoyant methane layer. *Tenth Symposium (International) on Combustion, The Combustion Institute, Pittsburgh, PA*, pages 1277–1283, 1965.

[51] P.K.Yeung and S.B.Pope. An algorithm for tracking fluid particles in numerical simulations of homogeneous turbulence. *J. Comput. Phys.*, 79:373–416, 1988.

[52] K.N.C.Bray P.N.Kioni, B.Rogg and A.Linan. Flame spread in laminar mixing layers: The triple flame. *Combust.Flam*, 95:276–290, 1993.

[53] R.S.Barlow and J.-Y.Chen. On transient flamelets and their relationship to turbulent methane-air jet flames. *Twenty-Fourth Symposium (International) on Combustion, The Combustion Institute, Pittsburgh*, pages 231–237, 1992.

[54] R.S.Barlow and J.H.Frank. Effects of turbulence on species mass fractions in methane/air jet flames. *In Proceedings of the Twenty-Seventh Symposium (International) on Combustion, Pittsburgh*, pages 1087–1095, 1998.

[55] R.W.Bilger. *Turbulent Reacting Flows (P.A.Libby and F.A.Williams,eds)*. Springer, 1980.

[56] S.A.Orszag. Numerical methods for the simulation of turbulence. *Phys.Fluids, Suppl.II*, 12:250, 1969.

[57] S.B.Pope. The evolution of surfaces in turbulence. *Int.J.Engng Sci.*, 26(5):445–469, 1988.

[58] S.B.Pope. Pdf methods for turbulent reacting flows. *Prog. Energy Combust. Sci.*, 11(2):119–192, 1988.

[59] S.B.Pope. *Turbulent Flows*. Cambridge: Cambridge University Press, 2000.

[60] S.Corrsin. A measure of the area of a homogeneous random surface in space. *Quart.Appl.Math.*, 12(4):404–408, 1955.

[61] S.M.Candel and T.J.Poinsot. Flame stretch and the balance equation for the flame area. *Combust.Sci.Technol.*, 70:1–15, 1990.

[62] S.O.Rice. Mathematical analysis of random noise. *Bell Sys.Tech.J.*, 23:282–332, 1944.

[63] S.O.Rice. Mathematical analysis of random noise. *Bell Sys.Tech.J.*, 24:46–156, 1945.

[64] Paiboon Sripakagorn. *Local Extinction and Reignition in Turbulent Nonpremixed Combustion*. PhD thesis, University of Washington, 2002.

[65] J.C.Bennett S.Tavoularis and S.Corrsin. Velocity-derivative skewness in small reynolds number, nearly isotropic turbulence. *J.Fluid Mech.*, 88:63–69, 1978.

[66] John T.Barnett and Benjamin Kedem. Zero-crossing rates of mixtures and products of gaussian processes. *IEEE T.Inform.Theory*, 44(4), 1998.

[67] T.Poinsot and D.Veynante. *Theoretical and Numerical Combustion*. R.T.Edwards,Inc., 2001.

[68] T.Saitoh and Y.Otsuka. Unsteady behavior of diffusion flames and premixed flames for counter flow geometry. *Combust. Sci. Technol.*, 12:135–146, 1976.

[69] V.Eswaran and S.B.Pope. An examination of forcing in direct numerical simulations of turbulence. *Comput.Fluids*, 16:257, 1988.

[70] R Balasubramaniam V.Nayagam and P.D.Ronney. Diffusion flame-holes. *Combust.Theory Modelling*, 3:727–742, 1999.

[71] V.Nilsen. *Investigation of Differentially Diffusing Scalars in Isotropic Decaying Turbulence*. PhD thesis, University of Washington, 1998.

[72] V.Nilsen and G.Kosaly. Differential diffusion in turbulent reacting flows. *Combust.Flame*, 117(3):493–513, 1999.

[73] A.Linan V.S.Santoro and A.Gomez. Propagation of edge flames in counterflow mixing layers: Experiments and theory. *Proc.Combust.Inst.*, 28:2039–2046, 2000.

[74] W.E.Mell. *An investigation of closure models for nonpremixed turbulent reacting flow*. PhD thesis, University of Washington, 1994.

[75] Saensuk Wetchagarum. *A Numerical Study of Turbulent Two-phase Flows*. PhD thesis, University of Washington, 2008.

[76] W.P.Jones and C.H.Priddin. Predictions of the flow field and local gas composition in gas turbine combustors. *Seventeenth Symp. (Int.) on Combusiton, The Combustion Institute*, 17(1):399–409, 1979.

[77] H.Shen Y Livnat and C.R.Johnson. A near optimal isosurface extraction algorithm using the span space. *IEEE Trans.Vis.Comp.Graphics*, 2(1):73–84, 1996.

Appendix A

NUMERICAL ALGORITHM FOR COMPUTING ISOSURFACE AREA

The MATLAB built-in function *isosurface* extracts the isosurface from volume data at a specified isovalue by triangulation, it returns the geometric and topological information in a face-vertex data format. To be specific, the triangulation strategy returns a $M \times 3$ *vertices* matrix (the vertices are indexed $1, 2, \cdots, M$) and a $H \times 3$ *faces* matrix (the triangular faces are indexed $1, 2, \cdots, H$), which provide the geometric information for defining each triangle face in an efficient manner. Here, the index is a label used to identify each triangle face and each vertex. Each face represents a triangular mesh. Each row of *faces* represents a face defined by three indices into the M-by-3 *vertices* matrix of vertex 3D coordinates (i.e., as the rows of indices). This strategy can be exemplified by a simple case, as depicted in Fig.(A.1), that is composed of four faces formed by joining any three of six vertices where $M = 6$ and $H = 4$. Also, the corresponding exported *vertices* and *faces* matrices are presented in Table.(A.1). As appeared in the matrices, the $F_i (i = 1, \cdots, 4)$ and $V_j (j = 1, \cdots, 6)$ represent the i-th face and the j-th vertice, respectively. Each row of *faces* matrix contains the indices of three vertices that define each triangular face. And, each row of *vertices* matrix contains x_1, x_2, and $x_3$coordinates of each vertice.

The syntax of *isosurface* function is given as [41]

$$[faces, vertices] = isosurface(Xi, Yi, Zi, Z, Z_{iso}). \tag{A.1}$$

Here the 3D matrices Xi, Yi, and Zi generated by MATLAB *meshgrid* function denotes the coordinates of 3D cartesian grids on x_1-, x_2-, and x_3-direction at which the 3D scalar data Z is given. Z_{iso} is the user-specified isovalue.

For example, the third triangular mesh F_3 is bounded by three vertices (V_2, V_3, V_5) which are defined by the third row in *faces* matrix, and accordingly their 3D coordinates are contained in the second, third, and fifth row of *vertices* matrix. Subsequently, the area of the third triangular patch can be given by Heron's formula. The three sides opposite the

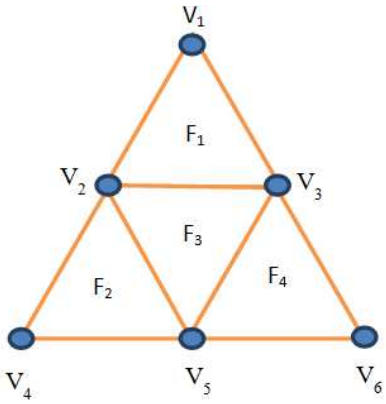

Figure A.1: An illustration of the output in faces-vertices format from 3D MATLAB *iso-surface* triangulation.

vertex V_2, V_3, V_5 are denoted by a, b, c, with these symbols also representing the lengths of the sides.

$$a = \sqrt{(Vx_3 - Vx_5)^2 + (Vy_3 - Vy_5)^2 + (Vz_3 - Vz_5)^2} \tag{A.2}$$

$$b = \sqrt{(Vx_2 - Vx_5)^2 + (Vy_2 - Vy_5)^2 + (Vz_2 - Vz_5)^2} \tag{A.3}$$

$$c = \sqrt{(Vx_2 - Vx_3)^2 + (Vy_2 - Vy_3)^2 + (Vz_2 - Vz_3)^2} \tag{A.4}$$

The semiperimeter s of the triangle is defined as half of its perimeter

$$s = \frac{1}{2}(a + b + c). \tag{A.5}$$

The area of triangle can be determined using Heron's formula as

$$\Delta A_3 = \sqrt{s(s-a)(s-b)(s-c)} \tag{A.6}$$

Then, apply the same algorithm to all four triangular faces and sum them up to give the total area.

In MATLAB, the code employed to compute the isosurface area can be something like below.

```
% generate 3D meshgird:
```

faces matrix			
triangle face index	indices of 3 bounding vertex per triangle		
F_1	V_1	V_2	V_3
F_2	V_2	V_4	V_5
F_3	V_2	V_3	V_5
F_4	V_3	V_5	V_6

vertices matrix			
vertex index	x-coordinate	y-coordinate	z-coordinate
V_1	Vx_1	Vy_1	Vz_1
V_2	Vx_2	Vy_2	Vz_2
V_3	Vx_3	Vy_3	Vz_3
V_4	Vx_4	Vy_4	Vz_4
V_5	Vx_5	Vy_5	Vz_5
V_6	Vx_6	Vy_6	Vz_6

Table A.1: The annotations of *faces*(left table) and *vertices*(right table) matrix corresponding to the surface triangulation shown in Fig.(A.1).

```
[Xi,Yi,Zi]=meshgrid([1:1:size(Z,2)],[1:1:size(Z,1)],[1:1:size(Z,3)];
% generate isosurface at isovalue Z=Zst
[faces,vertices]=isosurface(Xi,Yi,Zi,Z,Zst);
% compute the area of each triangular mesh
if size(faces,1)==0
   TriMeshArea=0;
else
   v1=vertices(faces(:,1),:);   % 3D coordinates of the 1st vertex
   v2=vertices(faces(:,2),:);   % 3D coordinates of the 2nd vertex
   v3=vertices(faces(:,3),:);   % 3D coordinates of the 3rd vertex

   a=sqrt(sum(((v2-v1).^2),2)); % length of 1st side of triangular mesh
   b=sqrt(sum(((v2-v3).^2),2)); % length of 2nd side of triangular mesh
   c=sqrt(sum(((v1-v3).^2),2)); % length of 3rd side of triangular mesh
```

```
16
17     s=(a+b+c)/2;                    % semiperimeter
18     TriMeshArea=sqrt(s.*(s-a).*(s-b).*(s-c)); % Area of triangular mesh
19 end
20 % total isosurface area
21 Area=sum(TriMeshArea);
```

Appendix B

MEAN VALUE THEOREM BY DOUBLE INTEGRAL

In a three dimensional space, on the triangulated isosurface rendered by Matlab, the three vertices that define a triangle are denoted as $A(x_1, y_1, z_1)$, $B(x_2, y_2, z_3)$ and $C(x_3, y_3, z_3)$. These three vertices are non-colinear, so they could define a closed region $\Re$ in two dimensional plane X-Y correspondingly. Then, the 3D coordinates of the three vertices are transformed in a 2D coordinate plane with origin .

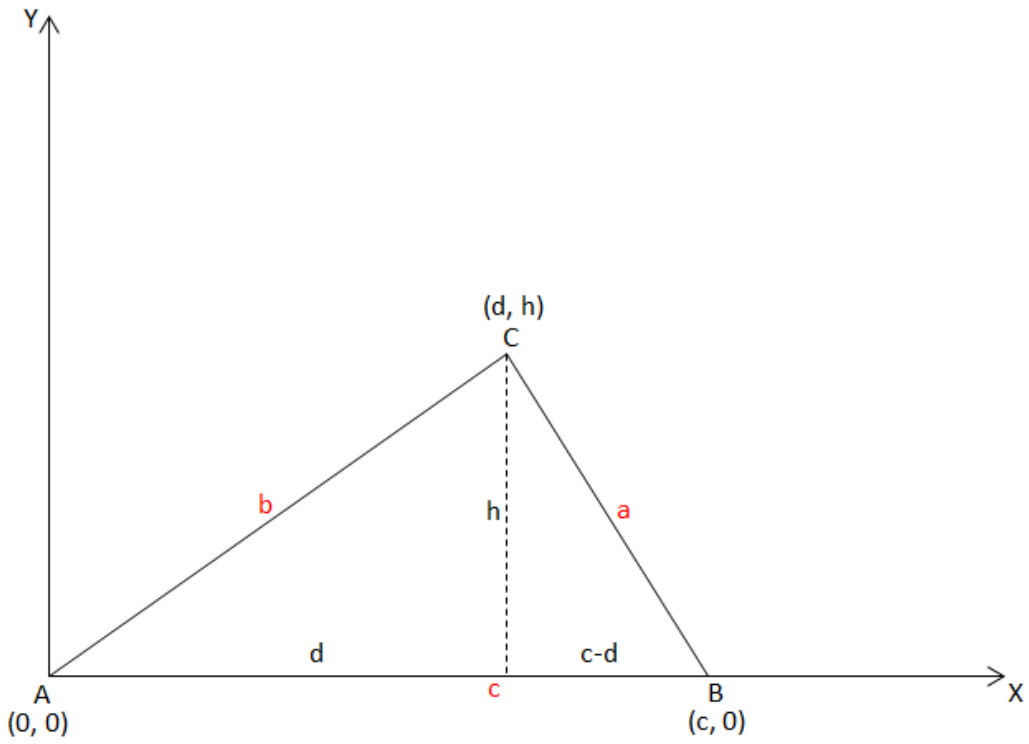

Figure B.1: An illustration of a triangular face defined by three vertices along the triangulated isosurface.

The lengths of the three sides of the triangle are determined by the 3D coordinates of

the vertices as

$$\begin{aligned} a &= \sqrt{(x_2-x_3)^2+(y_2-y_3)^2+(z_2-z_3)^2} \\ b &= \sqrt{(x_1-x_3)^2+(y_1-y_3)^2+(z_1-z_3)^2} \\ c &= \sqrt{(x_1-x_2)^2+(y_1-y_2)^2+(z_1-z_2)^2} \end{aligned} \tag{B.1}$$

If vertex A is set as the origin of two dimensional X-Y coordinate, the corresponding 2D coordinates of the three vertices are as follows:

$$\text{Vertex A:} \begin{cases} x = 0 \\ y = 0 \end{cases}$$

$$\text{Vertex B:} \begin{cases} x = c \\ y = 0 \end{cases}$$

$$\text{Vertex C:} \begin{cases} x = d = \dfrac{s(s-a)-(s-b)(s-c)}{c} \\ y = h = \dfrac{2A_h}{c} \end{cases}$$

Due to Heron's formula, s and A_h are semiperimeter and area of the triangle, respectively.

$$\begin{aligned} s &= \frac{a+b+c}{2} \\ A_h &= \sqrt{s(s-a)(s-b)(s-c)} = \frac{1}{4}\sqrt{(a^2+b^2+c^2)^2-2(a^4+b^4+c^4)} \end{aligned} \tag{B.2}$$

Suppose a function $f(x,y)$ is continuous over this closed bounded triangle region $\Re$, the general solution of this function is defined in the form of

$$f(x,y) = px + qy + l \tag{B.3}$$

The function values at the vertices A, B and C are Q_1, Q_2 and Q_3 given as

$$\begin{aligned} Q_1 &= f(x=0, y=0) \\ Q_2 &= f(x=c, y=0) \\ Q_3 &= f(x=d, y=h) \end{aligned} \tag{B.4}$$

Next, the coefficients p, q and l can be determined by the boundary conditions Q_1, Q_2 and

Q_3. Substituting the values at vertices into the general function, it yields

$$\begin{cases} Q_1 &= f(x=0,y=0) = p\cdot 0 + q\cdot 0 + l = l \\ Q_2 &= f(x=c,y=0) = p\cdot c + q\cdot 0 + l = p\cdot c + l \\ Q_3 &= f(x=d,y=h) = p\cdot d + q\cdot h + l \end{cases} \tag{B.5}$$

By solving above equations, the coefficients p, q and l in the function are determined in terms of the vertices' values Q_1, Q_2 and Q_3 as

$$\begin{cases} p &= Q_1 \\ q &= \dfrac{Q_2 - Q_1}{c} \\ l &= \dfrac{Q_3 - Q_1 - (d/c)(Q_2 - Q_1)}{h} \end{cases} \tag{B.6}$$

Consequently, the particular solution of function $f(x,y)$ is determined in terms of the function values at three vertices as

$$f(x,y) = \frac{Q_2 - Q_1}{c}\cdot x + \frac{d\cdot Q_1 - c\cdot Q_1 - d\cdot Q_2 + c\cdot Q_3}{c\cdot h}\cdot y + Q_1 \tag{B.7}$$

Next, we integrate the function $f(x,y)$ over this closed bounded triangle region $\Re$ in the X-Y plane. Before doing the double integration, the functions of the edge AC and edge CB of this closed bounded region need to be determined in terms of the geometric scales of this triangle. The function of edge AC and edge CB are determined respectively as

$$y = \frac{h}{d}\cdot x \tag{B.8}$$

$$y = \frac{h}{d-c}\cdot x - \frac{h\cdot c}{d-c} \tag{B.9}$$

Subsequently, the double integral is performed as

$$\begin{aligned} \int\int_{\Re} f(x,y)dA &= \int_{x=0}^{d}\int_{y=0}^{\frac{h}{d}x}(px+qy+l)dydx + \int_{x=d}^{c}\int_{y=0}^{\frac{h}{d-c}x-\frac{hc}{d-c}}(px+qy+l)dydx \\ &= \frac{1}{6}p\cdot h\cdot c^2 + \frac{1}{6}q\cdot h^2\cdot c + \frac{1}{6}p\cdot h\cdot c\cdot d + \frac{1}{2}l\cdot h\cdot c \end{aligned} \tag{B.10}$$

Finally, the mean value of $f(x,y)$ over this closed bounded triangle region is determined as

$$\langle f(x,y)\rangle = \frac{\frac{1}{6}p\cdot h\cdot c^2 + \frac{1}{6}q\cdot h^2\cdot c + \frac{1}{6}p\cdot h\cdot c\cdot d + \frac{1}{2}l\cdot h\cdot c}{A_h} \tag{B.11}$$

Appendix C

DISTRIBUTION PATTERN OF SCALAR DISSIPATION RATES WITHIN FLAME HOLES

As presented previously, the instantaneous scalar dissipation rate χ_{st} is not employed as a criteria for identifying quenched flame regions. However, it plays a key role in the extinction and reignition since a sufficiently large fluctuation of χ_{st} induces local quenching and later reignition following the relaxation of χ_{st}. The evolution of the flame hole, i.e. the hole could grow, collapse or remain the same, depends on the mixing rate and the hole size[70]. With the knowledge of scalar dissipation rate associated with each triangle face on the flame surface Q_{ii} (Appendix B) and the full access to the topological structure of each individual flame hole (i.e. specification of which triangle faces belong to a flame hole by the numerical algorithm), the χ_{st} distribution pattern within any flame hole of interest can easily be visualized in 3D by coloring the surface of flame hole with the triangle face's scalar dissipation rate $\chi_{st_{ii}}$ using indexed color. At time $t = 0.82$, during the process of hole growth, the distribution pattern of χ_{st} within the flame holes of area $A_h = 0.5$, 1.99, 3.3 and 4.43 (i.e. largest hole area) are respectively shown in Fig.(C.1). In the same manner, the χ_{st} distributions within four flame holes at time $t = 1.39$ are plotted in Fig.(C.2) for comparison, in which the four flame holes are selected the same way such that the area of each hole is comparable to its counterpart in Fig.(C.1). Note that the areas of these four flame holes span a large range of scales, thus their images can not be compared on the same scale and they are resized for clarity. As a reference, the value of the hole area is emphasized in the title of each subfigure.

During early time period, the fluctuation of χ_{st} grows stronger. As shown in Fig.(C.1), the color coded χ_{st} distribution pattern is warm (i.e. red or orange-red color) in the center with different shades of color. It roughly shows that the scalar dissipation rate decreases monotonically with increasing radius inside the flame hole. This corresponds to the peak-

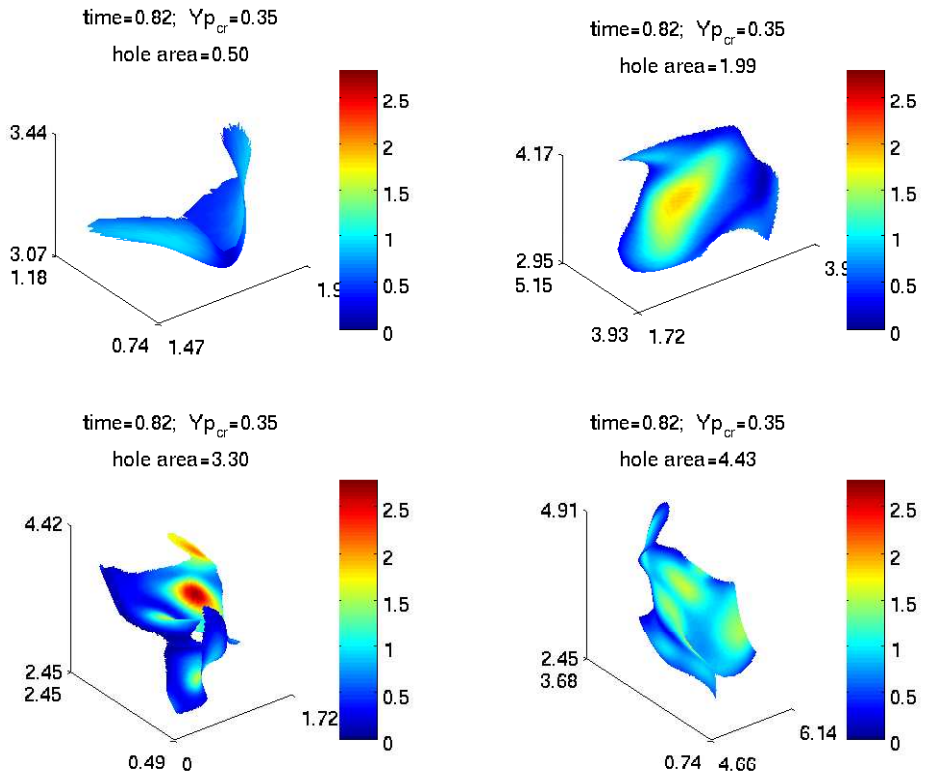

Figure C.1: At simulation time $t = 0.82$, the scalar dissipation rate is superimposed by coloring the surface of four different flame holes with areas $A_h = 0.5$(upper left), 1.99(upper left), 3.3(bottom left) and 4.43(i.e. maximum hole area at this time)(bottom right), respectively. The flame hole is configured with critical value of $Y_{Pcr} = 0.35$.

like χ_{st} paired with occurrence of bowl-like temperature along the contour line of Z_{st}, as can be observed in Fig.(5.8)(contour line segment between the 290th and 340th points). At time $t = 1.39$, majority of scalar dissipation rates dramatically drop below the χ_q with only a few are slightly above the quenching limit. As can be seen in Fig.(C.2), no quenched scalar dissipation rate is observed within the flame hole of area 0.48. This demonstrates that a relatively small size flame hole can exist in the absence of a quenched scalar dissipation rate. In other words, the flame hole in smaller size is undergoing the process of reignition which is favored by the relaxation of χ_{st}. The scalar dissipation occurs being around or slightly above the quenching limit can be found within the relatively larger hole. When the

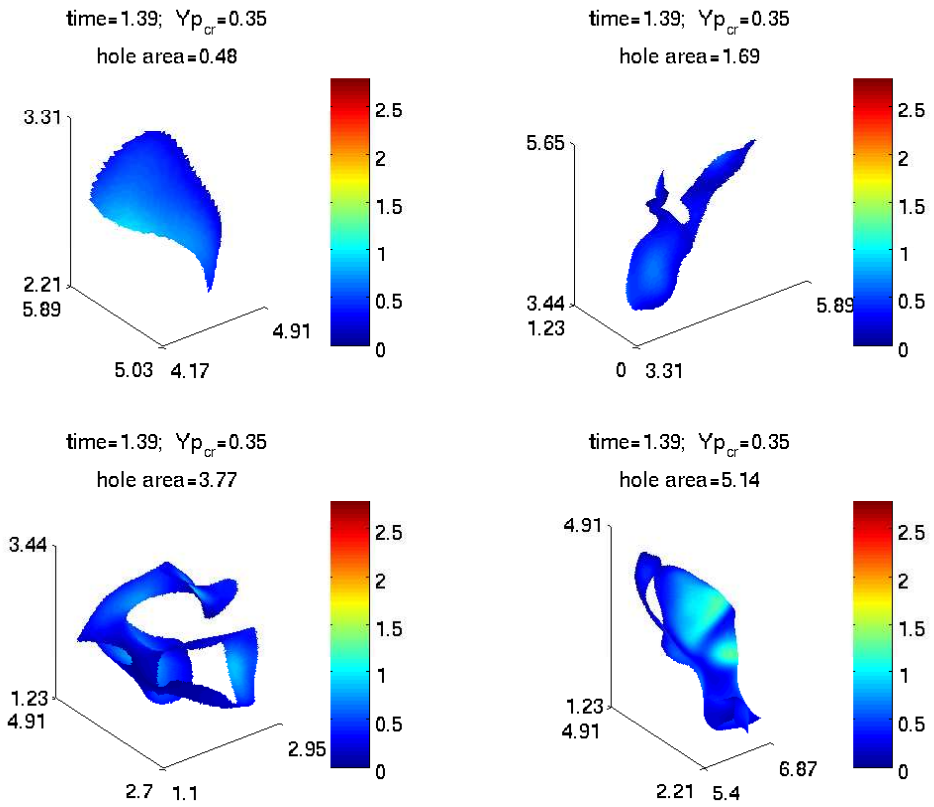

Figure C.2: At simulation time $t = 1.39$, the scalar dissipation rate is superimposed by coloring the surface of four different flame holes with areas $A_h = 0.48$(upper left), 1.69(upper left), 3.77(bottom left) and 5.14(i.e. maximum hole area at this time)(bottom right), respectively. The flame hole is configured with critical value of $Y_{Pcr} = 0.35$.

quenched χ_{st} locates at the edge of the hole, it will prohibit the propagation of surrounding edge flame or even results in a negative edge flame which advects away from the quenched hole, or equivalently, it will decrease the rate of hole collapse.

Appendix D

FLOW CHART OF NUMERICAL ALGORITHM OF FLAME HOLE FORMATION

Along the triangulated flame surface, each triangle face is individually identified to be either a quenched or a burning one due to the critical value of temperature Y_{Pcr}. A numerical algorithm is developed to join the contiguous quenched triangle faces to form the flame holes. This algorithm is performed in Matlab environment. The flow chart of this numerical algorithm is shown as follows.

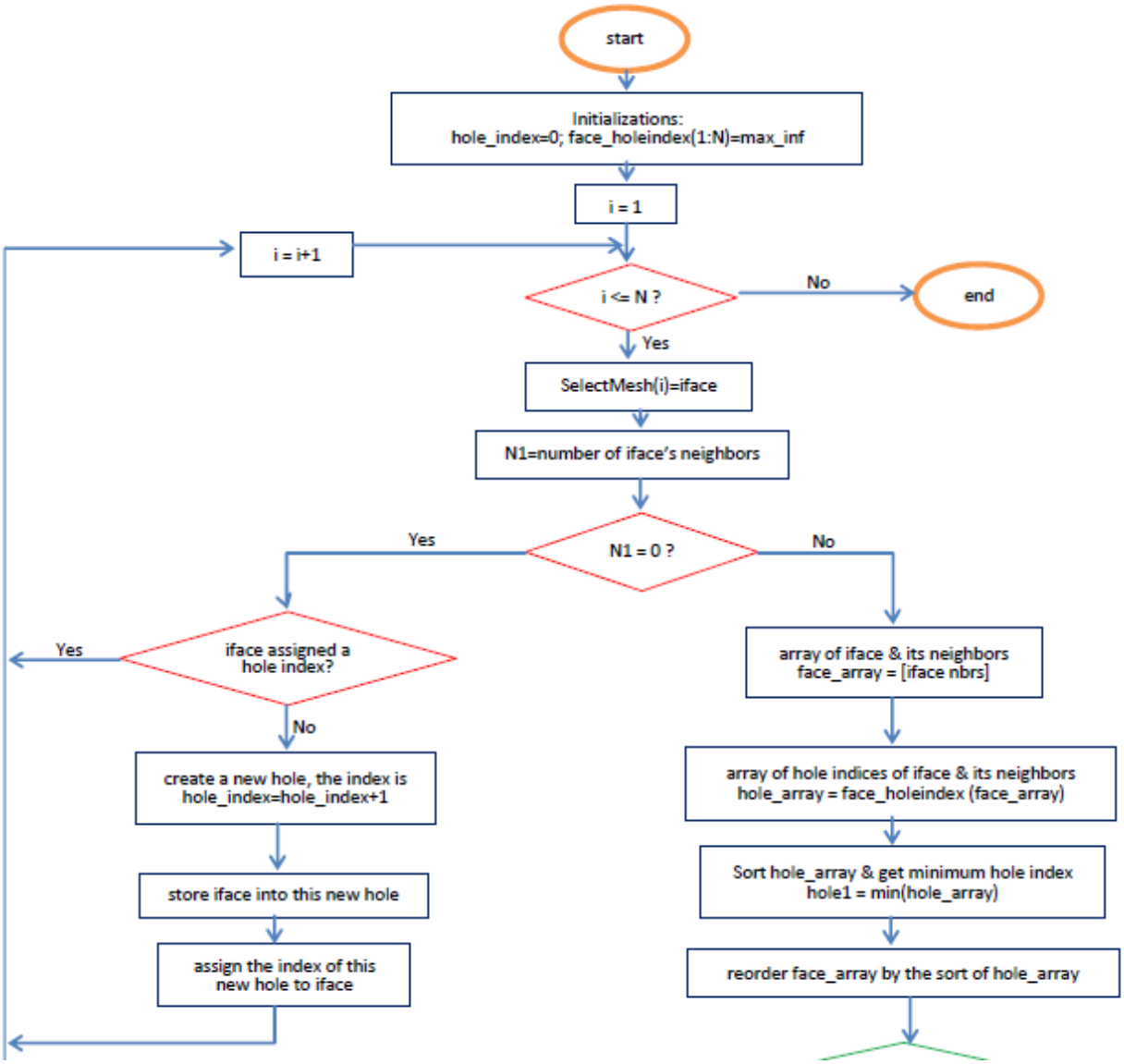

Figure D.1: The top part of the flow chart.

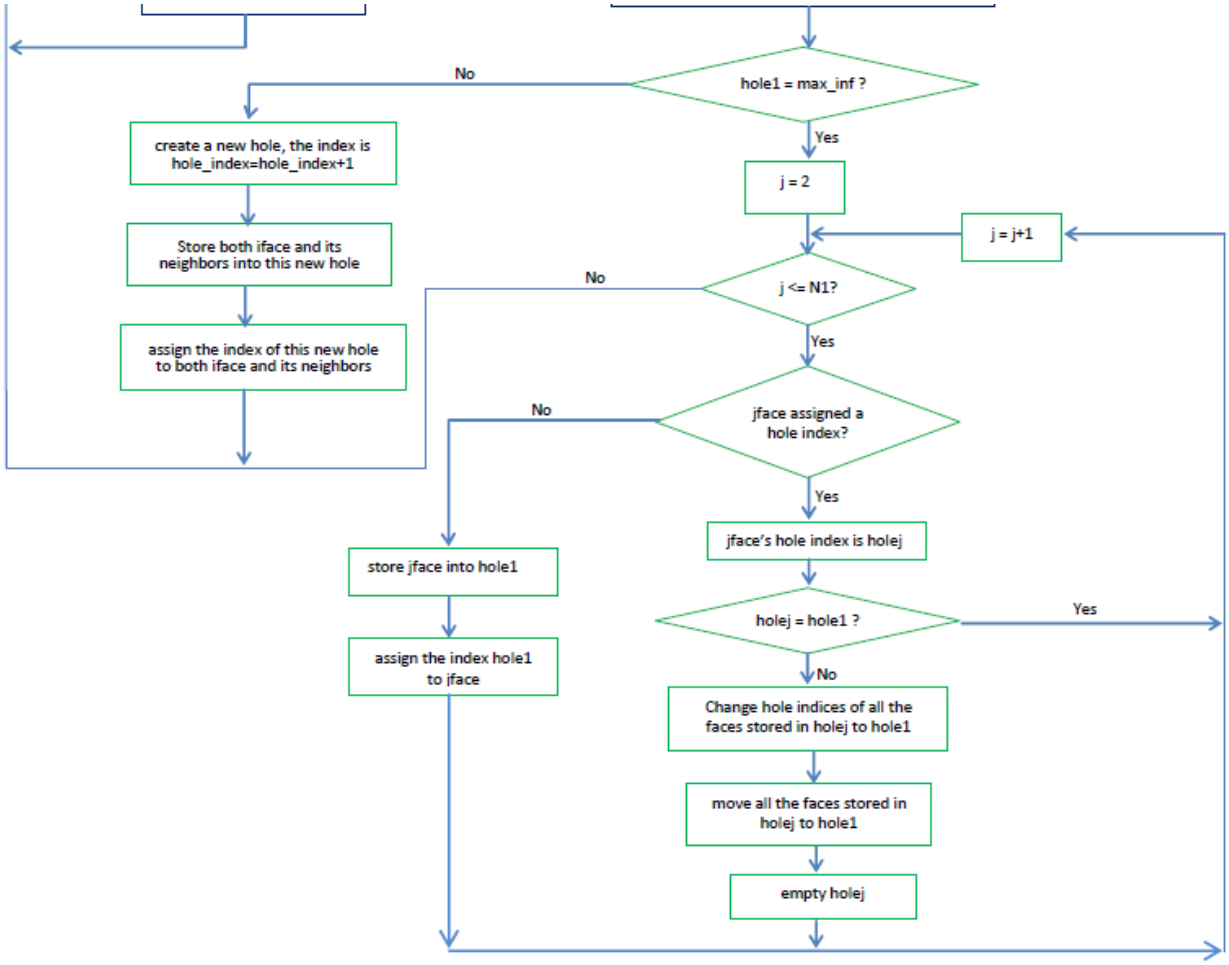

Figure D.2: The bottom part of the flow chart.